UNIVERSIDADE FEDERAL DO MARANHÃO

Centro de Ciências Exatas e Tecnologias

DEPARTAMENTO DE FÍSICA

Programa de Pós-Graduação em Física

Navadeep Shrivastava

Desenvolvimento de nanomateriais bifuncionais magnéticos-luminescentes e sua aplicação na detecção de radiação

São Luís-MA, Brasil
dezembro-2017

FEDERAL UNIVERSITY OF MARANHÃO
Center for Exact Sciences and Technologies

DEPARTMENT OF PHYSICS
Post-Graduate Program in Physics

Navadeep Shrivastava

Development of Magnetic-Luminescent Bifunctional Nanomaterials and their Application in Radiation Detection

São Luís-MA, Brazil
December-2017

Navadeep Shrivastava

Development of Magnetic-Luminescent Bifunctional Nanoparticles and their Application in Radiation Detection

Doctoral Thesis Presented to the Post-Graduate Program in Physics of Federal University of Maranhão (UFMA) as the Requirements for Obtaining the Doctorate degree in Physics
(tese de doutorado apresentada ao Programa de Pos-Graduação em Física de Universidade Federal do Maranhão como um requisitosn para obtencao do grau de doutor em fisica).

Supervisor:
Prof. Dr. Surender Kumar Sharma
Functional Nanomaterial Laboratory
Post-Graduate Program in Physics (PPGF)
Federal University of Maranhão (UFMA)
São Luís-MA, Brazil

Shrivastava, Navadeep.
Development of Magnetic-Luminescent Bifunctional
Nanomaterials and Their Application in Radiation
Detection / Navadeep Shrivastava. - 2017.
195 f.

Orientador: Surender Kumar Sharma.
Tese (Doutorado) - Programa de Pós-graduação em Física/CCET,
                    Universidade Federal do Maranhão,
                    São Luís, 2017.
1. Bifunctional materials, 2. Photoluminescence, 3. Superparamagnetic iron-oxide
nanoparticles, 4. Inorganic rare earth materials, 5. Scintillation.
I. Kumar Sharma, Surender. II. Título.

Navadeep Shrivastava

Development of Magnetic-Luminescent Bifunctional Nanomaterials and their Application in Radiation Detection

(Desenvolvimento de Nanomateriais Bifuncionais Magnéticos-Luminescentes e sua Aplicação na Detecção de Radiação)

Doctoral Thesis Presented to the Post-Graduate Program in Physics of Federal University of Maranhão as the Requirements for Obtaining the Doctorate degree in Physics (tese de doutorado apresentada ao Programa de Pós-Graduação em Física de Universidade Federal do Maranhão como um requisitosn para obtencao do grau de doutor em fisica).

**Approved On
01/12/ 2017**

Board of Examiners

_____

Prof. Dr. Surender Kumar Sharma

Functional Nanomaterial Laboratory
Post-Graduate Program in Physics-CCET,
Federal University of Maranhão, São Luís-MA, Brazil.

_____

Prof. Dr. Carlos Jacinto da Silva

Laboratory of Nanophotonics and Imaging,
Institute of Physics, Federal University of Alagoas,
Maceió-AL, Brazil.

_____

Prof. Dr. Jose Antonio H. Coaquira

Laboratory of Magnetic Materials, NFA,
Institute of Physics, University of Brasilia,
Brasilia-DF, Brazil.

_____

Prof. Dr. Alan Silva de Menezes

Department of Physics-CCET,
Federal University of Maranhão,
São Luís-MA, Brazil.

_____

Prof. Dr. Marcio Aurelio P. Almeida

Course in Science and Technology-CCET
Federal University of Maranhão,
São Luís-MA, Brazil.

गुरुर्ब्रह्मा गुरुर्विष्णुर्गुरुर्देवो महेश्वरः
गुरुः साक्षात परब्रह्म तस्मै श्रीगुरवे नमः

The Guru is Brahma (The God of Creation)
The Guru is Vishnu (The God of Sustenance)
The Guru is Shiva (The God of Annihilation)
My Salutation to such a Guru, who is verily the Supreme God.

The Almighty God, Who enlightened my mind and life with the great asset of thought.

My Parents Mrs. Sneh Lata and Mr. Brijesh Kumar for the unconditional kind support, unbounded love and affection in my life to fulfill the ambition.

My All Professors for scientific enthusiasm and moral values in me. Prof. Dr. Surender Kumar Sharma, for supporting in every hard time in life and profession and guiding me.

DEDICATED TO

My Loving Mom
Mrs. Sneh Lata Shrivastava
&
Dear Dad
Mr. Brijesh Kumar Shrivastava

Who Always Picked Me Up On Time And
Encouraged Me To Go On Every Adventure
Especially This One

Acknowledgements

Abstract

Bifunctional nanomaterials have exhibited potentially promising physico-chemical properties which can revolutionize and transform the landscape from bioclinical industry to next generation advance devices. In particular, colloidal nanoparticles have been extensively investigated as probes in biomedical and devices industries due to their unique size dependent electronic, optical, and magnetic properties amongst all possible building blocks of bifunctional materials. Superparamagentic iron-oxide nanoparticles open up a new avenue to the development and application of photonic technologies such as novel optical devices and bioclinical research by coupling with fluorescent materials especialy rare eath ions. Rare earth nanomaterials, which feature long lived intermediate energy levels and intraconfigurational 4f-4f transitions, are promising supporters for photon conversion in a wide range of fluoride hosts covering UV to IR region and are preferred over other fluorescent materials due to their large stokes shift, sharp emission spectra, long lifetime, multiphoton and up/downconversion excitation-emission preocesses. Owing to the unusual magnetic and optical properties associated with f-electrons, rare-earth elements are very suitable for creating bifunctional materials themselves at platform of nanoscale by employing the unique magnetic and up/downconversion luminescence properties integrated within single particles upon proper choices of particle matrix and dopants.

In the present thesis, we have discussed (i) bifunctionality of triply doped multicolor tuned photonic nanomaterials based on $LaF_3:Ce^{3+},Gd^{3+},Eu^{2/3+}$ prepared by polyol synthesis; (ii) green emitting triply doped bifunctional iron-oxide/ZnS@$LaF_3:Ce^{3+},Gd^{3+},Tb^{3+}$ nanocomposites with efficient optical and magnetic functionality, obtained using co-precipitation method; (iii) red/green emitting binary doped optical-magnetic up/downconverting β-$NaGdF_4:RE^{3+}$ and iron-oxide/SiO_2/$NaGdF_4:RE^{3+}$ (RE= Ce, Eu; Yb, Er) nanoparticles using microwave assisted thermolysis; and (iv) scintillating response due to neutrons for colloidal nanoparticles of $LaF_3:Ce^{3+},Gd^{3+},Eu^{2/3+}$. The prepared materials have been well characterized structurally using powder x-ray diffraction, transmission elecron microscopy techniques and Fourier transform infrared spectroscopy. The excitation/emission (photoluminescence) investigations, time decay analysis of emitting level, and proposed energy transfer mechanism for different nanomaterials have been carried out and result in exciting optical characteristics due to f-f transition (Eu^{3+}, Tb^{3+}, Er^{3+}) and f-d transitions (Ce^{3+}, Eu^{2+}) of rare earth ions. Furthermore, the magnetic characteristics of the materials were evaluated and materials containing iron-oxide as part of nanoentity displayed superparamgnetic nature whereas $LaF_3:RE^{3+}$ and $NaGdF_4:RE^{3+}$ showed their typical paramagnetic characteritcs at room temperature. Additionally, colloidal $LaF_3:Ce^{3+},Gd^{3+},Eu^{2/3+}$ nanoparticles proved to be efficient nanoscintillators for neutron detection, under irraditon of [241]AmBe source. The result encouraged to test other nanomaterials under high energy irradiation and to further design of commercial nanoscintillators. The intense optical and sufficient magnetic peculiarities of the mentioned materials are probably quite appealing for magnetic-optical imaging (X-ray/γ-ray or NIR-Laser excitation), magnetic light-converting molecular devices and smart magnetic and radiationfield detection.

Keywords: Bifunctional materials, $NaGdF_4$, LaF_3, Superparamagnetic iron-oxide nanoparticles, photoluminescence, up/downconversion, Inorganic rare earth materials, Scintillation

Resumo

Nanomateriais bifuncionais exibem propriedades fisico-químicas potencialmente promissoras que podem revolucionar e transformar o panorama da indústria bioclínica e da próxima geração de dispositivos avançados. Em particular, as nanopartículas coloidais têm sido amplamente investigadas como sondas em indústrias biomédicas e também como dispositivos devido às suas propriedades eletrônicas, ópticas e magnéticas dependentes do tamanho único entre todos as possíveis unidades básicas dos materiais bifuncionais. As nanopartículas de óxido de ferro superparamágneticas abrem uma nova via para o desenvolvimento e aplicação de tecnologias fotônicas, como novos dispositivos opticos e pesquisas bioclínicas, acoplando materiais fluorescentes, especialmente íons de terras raras. Os nanomateriais de terras raras, que apresentam níveis de energia intermediários de longa duração e transições intraconfiguracionais $4f$-$4f$, são materiais promissores para a conversão de fótons em uma ampla gama de matrizes de fluoreto que cobrem a região entre o ultra violeta e o infra-vermelho e são preferidos em relação a outros materiais fluorescentes devido ao grande deslocamento *Stokes*, acentuado espectro de emissão, longo tempo de vida, emissão multi-fotônica e processos de excitação/emissão de conversão para os modos ascendentes/descendentes. Devido as propriedades magnéticas e opticas incomuns associadas aos elétrons 4f, os elementos terras raras são muito adequados para a criação de materiais bifuncionais em nanoescala, empregando as propriedades únicas magnéticas e de luminescência por modos ascendentes/descendentes integradas em uma única partícula, dependendo da escolha apropriada da partícula matriz e dos dopantes.Neste trabalho, discutimos (i) a bifuncionalidade do nanomateriais fotônicos ajustados e dopados com multicores com base em LaF_3:Ce^{3+},Gd^{3+},$Eu^{2/3+}$ preparados pela síntese de polióis; (ii) materiais nanocompósitos triplamente dopados de óxido-de-ferro/ZnS@LaF_3:Ce^{3+},Gd^{3+},Tb^{3+} bifuncionais que emitem na cor verde com eficiente funcionalidade optica e magnética, obtidos usando o método de co-precipitação; (iii) materiais magneto-opticos dopados binários na forma de nanopartículas de β-$NaGdF_4$:RE^{3+} e óxido-de- ferro/SiO_2/$NaGdF_4$:RE^{3+} (RE = Ce, Eu, e Yb, Er) que emtem no verde e vermelho nos modos ascendente e descendente utilizando micro-ondas assistida por termólise (iv) detecção cintilante por radiação de nêutrons para nanopartículas coloidais de LaF_3:Ce^{3+},Gd^{3+},$Eu^{2/3+}$. Os materiais preparados foram caracterizados estruturalmente usando difração de Raios-X, técnicas de microscopia de eletrônica de transmissão e espectroscopia de transformada de Fourier no infra-vermelho (FTIR). As investigações de excitação/ e emissão (fotoluminescência), a análise de degradação do tempo de vida do nível de emissão e o mecanismo de transferência de energia proposto para diferentes nanomateriais foram realizados e resultaram em características opticas interessantes devido a transições f-f (Eu^{3+}, Tb^{3+}, Er^{3+}) e f-d (Ce^{3+}, Eu^{2+}) de íons de terras raras. Além disso, as características magnéticas foram avaliadas e os materiais que contêm óxido de ferro como parte da nano-unicidade apresentaram natureza superparamégnetica, enquanto que LaF_3: RE^{3+} e $NaGdF_4$: RE^{3+} mostraram características típicas paramagnéticas à temperatura ambiente. Adicionalmente, as nanopartículas coloidais LaF_3:Ce^{3+},Gd^{3+},$Eu^{2/3+}$ provaram ser nanoscintiladores eficientes para detecção de nêutrons, sob irradiação de fonte de $^{241}AmBe$. O resultado motiva a testar outros nanomateriais sob irradiação de alta energia e a posterior elaboração de nanoscintiladores comerciais. As fortes características opticas e magnéticas (excitação de Raios-X, Raios-γ e Laser), dispositivos moleculares magnéticos de conversão de luz e detecção inteligente de campo magnético e de campo de radiação.

Palavras-chave: materiais bifuncionais, $NaGdF_4$, LaF_3, nanopartículas de óxido de ferro superparamagnéticas, fotoluminescência, conversão ascendente/descendente, materiais inorgânicos de terras raras, cintilação

List of Figures and Schemes

Figure 3.9: (a) Shows a free and unpaired electron in space; (b) shows minimum and maximum spin orientations of $\bar{\mu}$ with respect to the magnetic field B_0; (c) explains the introduction of spin state energies as a function of magnetic field B_0; (d) relates spin-orbit interaction; and (e) displays the prototype EPR experiment.

Graphical Abstract Figure: Chapter 4 Color tuning (marked as A, B, C, and D) dependence on ratio of Eu^{2+}/Eu^{3+} ions in ultrasmall $LaF_3:xCe^{3+},xGd^{3+},yEu^{3+}$ (x = 5; y = 1, 5, 10 and 15 mol. %) nanoparticles and the excitation/emission spectrum for the greatest achieved emission quantum efficiency (~ 85%) of Eu^{3+} (y = 10 mol.%).

Figure 4.1: Schematic of synthesis of $LaF_3:xCe^{3+}$, xGd^{3+},yEu^{3+} (x = 5; y = 1, 5, 10 and 15mol.%) nanoparticles.

Figure 4.2: FTIR spectra of $LaF_3:xCe^{3+},xGd^{3+},yEu^{3+}$ (x = 5; y = 1, 5, 10 and 15 mol.%) nanomaterials

Figure 4.3: PXRD patterns of $LaF_3:xCe^{3+},xGd^{3+},yEu^{3+}$ (x = 5; y = 1, 5, 10 and 15 mol.%) nanoparticles and their corresponding Rietveld analyses.

Figure 4.4: (a, d) High-angle annular dark-field imaging (HAADF),(b, e) HRTEM images, and (c, f) particle size distribution obtained from TEM analysis for $LaF_3:xCe^{3+},xGd^{3+},yEu^{3+}$ (x = y =5 and 15 mol.%), respectively. Panel (c) and panel (e) show the inset region of the images analyzed by applying Fast Fourier Transforms (FFT), confirming hexagonal structure of highlighted nanoparticles.

Figure 4.5: Merged chemical maps distribution of elements and selected area electron diffraction patterns for $LaF_3:xCe^{3+},xGd^{3+},yEu^{3+}$ (x = y = 5 mol.%) (a-top/a-bottom) and (x = 5; y = 15 mol.%) (b-top/b-bottom) samples.

Figure 4.6: High angle annular dark-field (HAADF) image and EDS elemental mappings, acquired in the JEM-2100F microscope, showing the homogeneous and uniform distribution La, F, Ce, Gd and Eu elements in sample of $LaF_3:xCe^{3+},xGd^{3+},yEu^{3+}$ (x = 5; y = 15 mol.%) nanocomposite. Scale bar = 100 nm.

Figure 4.7: The Eu-$M_{5,4}$ X-ray absorption spectra of all the samples $LaF_3:xCe^{3+},xGd^{3+},yEu^{3+}$ (x = 5; y = 1, 5, 10 and 15 mol.%) along with reference Eu_2O_3 spectrum (Eu^{3+}).

Figure 4.8: Luminescence spectra of the $LaF_3:xCe^{3+},xGd^{3+},yEu^{3+}$(x = 5; y = 1, 5, 10 and 15 mol.%) nanophosphors, recorded at 300 K: (a) excitation spectra, monitoring emission at 617 nm assigned to the $^5D_0 \rightarrow {}^7F_2$ hypersensitive transition of the Eu^{3+} ion; (b) excitation spectra in the range 200-270 nm, showing the transition $4f({}^2F_{5/2}) \rightarrow 5d$ interconfigurational transitions of the Ce^{3+} ion; (c) amplified emission range for Ce^{3+} and Gd^{3+} ions; (d) emission spectra under excitation at 260 nm which corresponds to the $4f({}^2F_{5/2}) \rightarrow 5d$ interconfigurational transition of the Ce^{3+}ion.

List of Tables

Contents

Chapter 1
General Introduction and Background

1.1 Nanoscale materials

Nanoscale materials are a topic of considerable interest across a number of science, engineering and biomedical disciplines.[1] The basic rationale is that nanoscale materials, typically 1–100 nm, exhibit exceptional structural and functional properties that are not available in bulk materials or discrete molecules and have a significant commercial impact, due to their unique properties such as finite size and surface effects.[2] Finite size effects are related to manifestation of so-called quantum size effects, which arises when the size of the system is commensurable with the de-Broglie wavelengths of the electrons, phonons or excitons propagating in them. Surface effects can be related, in simplest case, to the symmetry breaking of the crystal structure at the boundary of each particle, but can also be due to different chemical and magnetic structures of internal "core" and surface "shell" parts of nanoparticles.[3,4] Few major classes of functional nanoplatforms have been extensively studied such as: (i) magnetic nanoparticles; (ii) nanophotonic materials; and (iii) plasmonic nanoparticles; and widely used in a variety of fields. **Magnetic nanoparticles,** commonly consisting of magnetic elements such as iron (Fe), cobalt (Co), Nickel (Ni) etc., and their chemical compounds, show alignment of their magnetic moment in the presence of an external magnetic field and concentrate the external magnetic flux density.[5,6] This makes the magnetic nanoparticles useful for many important applications around. **Nanophotonics** is an emerging frontier that deals with the interaction of light with matter on a nanometer scale exhibiting unique tunable optical features.[7] The design and control of the excitation dynamics in nanomaterials constitute a major area of nanophotonics; they can be utilized to produce new frequency converting (light converting) capabilities for instant using lanthanide-doped nanophosphors.[8,9] Optical nanoparticles are typically composed of quantum dots (CdSe, ZnS, ZnTe etc.), dyes or rare earth based materials. **Plasmonic nanoparticles** including gold, silver, and platinum, are highly efficient at absorbing and scattering light. By changing nanoparticle size, shape, and composition, the optical response can be tuned from the ultraviolet (UV) to the visible to the near-infrared (NIR) regions of the electromagnetic spectrum.[10] They exhibit unique localized surface plasmon resonance (LSPR), the collective oscillation of the

conduction electrons of the nanoparticles in resonance with the electric field of the incident light.

1.2 Bifunctionality at nanoscale

The design and synthesis of materials that simultaneously consists upon more than one functional part, called multifunctional or bifunctional material.[7] Bifunctional nanoparticles have exhibited potentially promising physico-chemical properties, which can revolutionize and transform the landscape from bio-clinical industry to next generation advance devices. In particular, colloidal nanoparticles have been extensively investigated as probes in biomedical/devices industries due to their unique size dependent electronic, optical, and magnetic properties amongst all possible building blocks.[11,12]

Individually, magnetic nanoparticles are one most frequent example of bifunctionality because of its several bio-medical and other industrial applications.[2,3,5] Magnetic nanoparticles can be ignited by an applied magnetic field gradient. This non-invasive approach provides several applications including transportation and confinement of nanoparticles and delivery of a package at a preferential biological component, such as cancer cure medicine to a designated part of the body. Additionally, they can respond to time altering magnetic field, as a result, transfer energy from applied field to the nanoparticles and they can heat up.[13] The most common magnetic nanoparticles are iron-oxide nanoparticles including magnetite (Fe_3O_4) or maghemite (γ-Fe_2O_3). These magnetic nanoparticles have advantages of ease-of-preparation, bio-degradability, excellent stability, and the tunability of magnetic properties through alteration in size and shape, making them the most attractive platforms. When the sizes of these magnetic nanoparticles are below a critical size (generally $\leq$ 20 nm), they are superparamagnetic, otherwise they are ferromagnetic. Superparamagnetic nanoparticles avoid the induced aggregation associated with the residual magnetization of ferromagnetic nanoparticles.[3] Magnetic nanoparticles can be spherical or anisotropic such as rods, cubes and stars and hence provide versatile structural platforms for generations of different nanostructures.[4] However, due to the high surface to volume ratio, the magnetization of bare iron-oxide nanoparticles are usually prone to aggregation. This makes them inadequate candidates for biological applications.[14,15] Therefore, they are generally functionalized with SiO_2, carbon, carboxylates, amines, diols, phosphates, phosphonates and sulfonates, in order to ensure the colloidal stability of these in an organic or aqueous medium.[15] These magnetic

nanoparticles are being exploited for applications such as data storage, spintronics, molecular cellular isolation, biosensors; hyperthermia, magnetic resonance imaging (MRI); cell manipulation etc., and contributed to an extraordinary advance in nanoengineering due to their multifunctional characteristics.[4,14]

On the other hand, lanthanides optical materials have captured attentions worldwide in the last two decades due to their versatile up or down frequency converting capabilities utilizing a low energy continuous wave excitation provided by inexpensive diode lasers or using other means of source such as xenon lamps.[7,16] Rare earth chemical elements are rich in optical and magnetic properties owing to the unique properties of 4f electrons and have widely been used in catalysis, magnets, phosphors etc. The recent accomplishments in rare earth nanoparticles synthesis with tunable shape and size have aroused great interest of researchers to further explore their biological and biomedical applications.[16,17] For example, Gd-chelates are widely used as contrast agents for MRI in clinics, promoting *in-vivo* applications of rare earth nanomaterials.[17,18] Hence rare earth based materials have great potential to be used as bifunctional materials.

However, besides possessing interesting physico-chemical properties, magnetic nanoparticles and lanthanides optical materials have several limitations e.g., in imaging application as compared in Figure 1.1. For instance, optical imaging techniques offer improved high spatial resolution allowing the visualization of cell structures, but have limited depth of imaging and poor absolute quantitative accuracy due to the absorption of light in tissues.[19,20] On the other hand, magnetic imaging has no practical limitation in terms of the depth of imaging; however, spatial resolution is worse and imaging with more than one probe is problematic.[21,22] Hence, the concept to combining (hybridizing) the two entities such as magnetic nanoparticles and luminescent nanoparticles, complements each other and provide best sensitive tool for sensitive label for imaging in cells and tissue engineering.[23] Hence, this combination of multiple imaging technique,[17,18] provides complementary and complete information about the imaged object (Figure 1.1).

Thus, hybrid nanoparticles with combined magnetic and optical properties are much more powerful and can be used in a broad range of applications.[24–29] Moreover, they offer new modalities that neither luminescence nor magnetic nanoparticles exhibit. For example, the demonstration of real field dependent luminescence phenomenon called magneto-luminescence,[30] and magnetomotive-photoacoustic phenomenon.[31–33] These novel

phenomenon shows remarkable potential in several other important applications such as high accuracy and secure communication,[34] aircraft guidance and radiation field detection and modulation of magnetic and optical field. Furthermore, these nanocomposites can be used as nanoblocks to build various nanoelectronic and photonic devices by applying an external magnetic field to manipulate or arrange the magnetic nanoparticles and optical signals.[35,36]
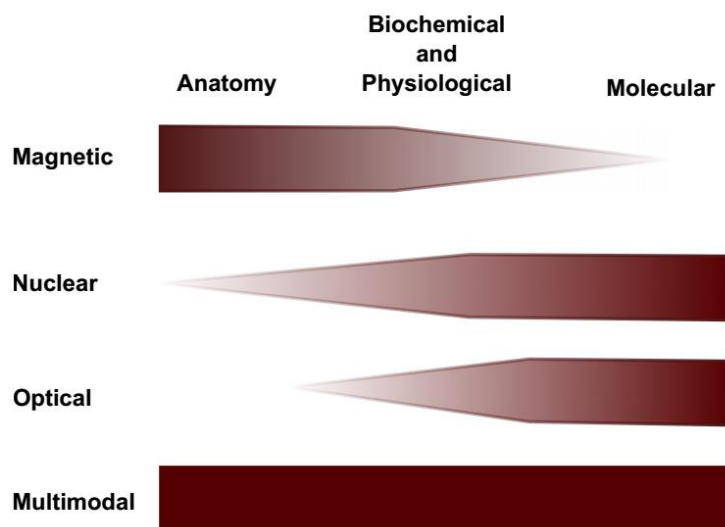
Figure 1.1: Schematic of overall information retrieved from different imaging modalities from anatomy imaging to molecular imaging and how multimodality can be used to cover limitations of each to provide more complete information.

1.3 Major challenges for magnetic-luminescent bifunctional nanoparticles

Since magnetic-luminescent bifunctional nanoparticles may provide a new and promising two-in-one characteristics, there are some challenges also to overcome in their fabrication: (i) the complexity in the preparation, which frequently involves multi-step synthesis and many purification stages leading their production is quite technical and time demanding;[37] (ii) the risk of quenching of the luminophore on the surface of the particle by the magnetic core; and (iii) quenching each other by number of fluorescent molecules attached to the surface of the particle. Although to resolve these challenges, several techniques have been proposed to integrate the luminescence and magnetic nanomaterials.[38] The fabrications of these are commonly achieved as hybrid conjugates of magnetic and luminescent entities or core-shell or composite structures using coating, layer-by-layer deposition; and optical materials (quantum

4

dots) on magnetic nanoparticles or vice-versa. Another way is the functionalization of magnetic iron-oxide with fluorescent dyes and luminescent complexes, called cross-linking attachment of molecule. Moreover, the use of SiO_2, ZnS or C as spacer between iron-oxide and luminescent materials is of great importance on the performance of nanohybrids. Table 1.1 reviews some important works related to the engineering of magnetic-luminescent nanomaterials.

Table 1.1 Examples of few magnetic-luminescent nanomaterials

Luminescent material	Magnetic material	Type	Synthesis
$NaGdF_4$: Yb^{3+}, Er^{3+}	Fe_3O_4	Core-shell	Thermolysis process[39]
LaF_3:Ce^{3+}, Tb^{3+}	Fe_3O_4	Core-shell	Coprecipitation[40]
YVO_4:Eu^{3+}	Fe_3O_4	Core-shell	Coprecipitation[41]
CdSe	Fe_3O_4	Core-shell	Thermal decomposition [42]
ZnS	Fe_3O_4	Core-shell	Thermal decomposition [43]
Gd_2O_3:Eu^{3+}	Fe_3O_4	Core-shell	Heating/calcination [44]
α-$NaYF_4$:Yb^{3+}, Er^{3+}	Fe_3O_4	Core-shell	Hydrothermal/calcination[45]
$LaPO_4$:Ce^{3+}:Tb^{3+}	Fe_3O_4	Cross linking, Calix	Coprecipitation[46]
Eu^{3+} and Tb^{3+} complexes	Fe_3O_4	Cross linking, Calix	Coprecipitation[47]
CdSe/ZnS	γ-Fe_2O_3	polymer having −SH and −COOH	Organic/water two-phase mixture [48]
	Fe_3O_4	PEG-diacid/ Polyethyleneglycol-bis-carboxymethyl ether	Covalently conjugation via amide bond formation[49]
$NaYF_4$:Yb^{3+},Er^{3+}	Fe_3O_4	1,10-Decanedicarb-oxylic acid or 11-mercaptoundecanoic acid	Crosslinker anchoring strategy[50]
Tb^{3+} *N*-(4-benzoic acid-yl),*N`*-(propyltriethoxysilyl) urea)	Fe_3O_4	SiO_2	Coprecipitation and Stöber method[51]

Core/shell structure is the most common type of bifunctional nanosystems. In this type of nanoarchitecture, generally a magnetic core is combined with fluorescent molecules, metal nanoparticles or semiconductor nanocrystals, etc.[52] and therefore exhibits unique optical, magnetic and electrical properties. However, different components in these kinds of bifunctional nanoparticles interact with each other, which generally weaken or reduce the

functionality of each unit. Recent advances in the synthesis of various functional superparamagnetic iron-oxide nanoparticles with heterostructures offer a promising solution to this problem by creating anisotropic nanoparticles. They consist of functional units with different chemistry, polarity, or other physico-chemical properties on asymmetric sides without sacrificing their own properties.[53,54] The superior properties of these heterostructured rely on synergistically enhanced magnetism and synthesis strategies on the precise control of particle size, morphology and chemical composition along with functionalization with fluorescent material, engineering like dumbbell nanoparticles. The desire to design more sophisticated nanoarchitecture with unusual properties is definitely needed. This kind of integration offers exciting opportunities for discovering new materials, processes and phenomenon. At nanoscale, these kind of bifunctional materials have their own advantage:[55,56]

(i) tuned and controlled size depending on application, (ii) nanoparticles be manipulated by external magnetic field "action at a distance", and (iii) dual mode applications, e.g., MRI contrast agents and multimodal imaging.

In spite of the growing attention paid on the bifunctional nanoparticles comprising of magnetic and luminescence materials responding to magnetic and optical excitation simultaneously,[57,58] the coupling between magnetism and luminescence of lanthanide ions in these systems remains largely ignored. From some recent reports, it has been found that the external magnetic field has direct influence on the spectral positions and luminescence intensity of lanthanide ions doped in various inorganic hosts. In Er^{3+}/Yb^{3+} doped Gd_2O_3 phosphor, for instance, optical bistability in the magnetic field dependent luminescence intensity was observed, and ascribed to the residual magnetization in the material. In several other systems, with the increase of the magnetic field, the suppression of the luminescence intensity was usually observed, accompanied by the steady shift of the spectral positions for lanthanide ions like Er^{3+} and Eu^{3+}. This is generally understood based on the interplay of field-induced Zeeman splitting. However, the exact mechanism with the application of magnetic field remains obscure. Eu^{3+} doped $NaGdF_4$ nanoparticles, where the obvious shift and splitting of the luminescence bands have been detected in the presence of magnetic field. These results can be interpreted in terms of Zeeman effects and the magnetic field induced change of local site symmetry around Eu^{3+}. Besides optical hysteresis behavior of integrated luminescence intensity for different transitions of Eu^{3+} is found when the magnetic field is scanned (from 0 to 40 T), which is connected with the magnetic ordering in the lanthanide sub-lattice.

1.4 Lanthanides and luminescence mechanism involved in bifunctional materials

Lanthanide doped nanophosphors are dilute guest host systems, where trivalent lanthanide ion emitters are dispersed as guests in an appropriate dielectric host lattice.[59] The luminescence (or magnetic) generally arises from 4f-4f orbital electronic transitions, with associated wave functions localized within a single lanthanide ion.[60] The shielding of 4f electrons by the outer complete 5s and 5p shells gives non-blinking and line-like sharp emissions, which exhibit high resistance to photobleaching and photochemical degradation. Strictly speaking, the main intra-4f electronic dipole transitions of lanthanide ions are forbidden by quantum mechanical selection rules; however, they are still manifested due to local crystal field induced intermixing of the f states with higher electronic configurations. Besides, the dipole-forbidden nature of the 4f-4f transitions yield very long lifetimes for these energy levels of lanthanide ions. These long lifetimes play an important role in increasing the probability of sequential excitations in the excited states of a single lanthanide ion, as well as in permitting favorable ion-ion interactions in the excited states to allow energy transfers between two or more lanthanide ions. Through a judicious selection of one or more lanthanide dopants, nanophosphors can display either frequency upconversion (UC) such as infrared (IR) to shorter wavelength near infrared (NIR), visible, or ultraviolet (UV), or downconversion (DC), such as IR being further red-shifted. Further, it may also happen that UV excitation can be converted into visible color lines through quantum cutting or downconversion. Unlike the quantum confined systems, the electronic energy gap of lanthanide doped nanophosphors does not change with a change in the size or shape. However, their emission properties (color, efficiency, and lifetime) are indeed dependent on nanoscale structures of nanophosphors, which influence the electron-phonon coupling, local crystal field, and nanoscopic ion-ion interactions. Manipulation of a nanoscale dielectric environment (host) to control the excitation dynamics is, therefore, of great importance in order to control their frequency-converting capabilities. Two typical energy transfer modes have been established in rare earth ion activated materials to understand the emission behavior, namely downshifting or quantum cutting, and upconversion (UC).

1.4.1 Upconversion process: Upconversion refers to a process generating higher energy emission under low-energy excitation.[61,62] Upconversion processes are mainly divided into four classes (Figure 1.2): excited-state absorption (ESA), energy transfer upconversion (ETU), photon avalanche (PA) and energy migration-mediated upconversion (EMU). All the first three mechanisms involve the sequential absorption of two or more photons by metastable, long-

lived energy states. This sequential absorption promotes the ion to high-lying excited state results in upconversion emission. A sensitizer ion (type I) first transfers its excitation energy to an acceptor ion (type II). The energy transfer from the high-lying excited state of the acceptor to a migrator ion (type III) then occurs, followed by the migration of excitation energy via the migrator ion sub-lattice through the core–shell interface. Subsequently, the migrating energy is trapped by the activator ion (type IV), resulting in upconversion emission. The 'nx' represents the occurrence of random hopping through many type-III ions.[62,63]
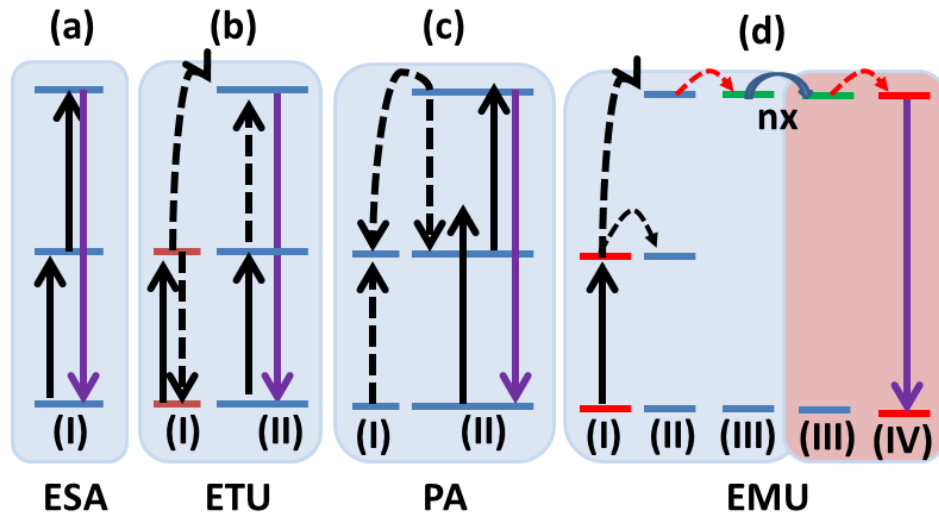
Figure 1.2: Upconversion processes (a) Excited state absorption (ESA); (b) energy transfer up-conversion (ETU); (c) photon avalanche (PA); (d) energy migration-mediated upconversion (EMU) involving four types of lanthanide ions doped in different region of core-shell nanocrystals. Note that core and shell regions are highlighted with different background colors in (d).

1.4.2 Downconversion/Quantum cutting process: The energy of a UV or vacuum UV (VUV) photon is more than twice of a visible photon. Theoretically, it is possible to generate two visible photons for a single UV/VUV photon absorbed; this two-photon luminescence phenomenon is called as quantum cutting (QC) as shown in Figure 1.3a .[64] The efficiency gain in QC materials is based on the principle that a QC phosphor can result in two visible/infra-red photons for each absorbed VUV/vis photon. QC has been demonstrated based on different mechanisms. Downconversion (DC) is a special case of quantum cutting. DC is a new route to realize visible/IR quantum cutting effect. Figure 1.3b-d illustrates the generalized energy level diagrams for three DC mechanisms involving energy transfer (ET) between two different rare-

earth ions (I and II).[64] It is not only the cross relaxation processes but also cooperative process is involved in energy transfer mechanism between rare earth ions.[65–67]
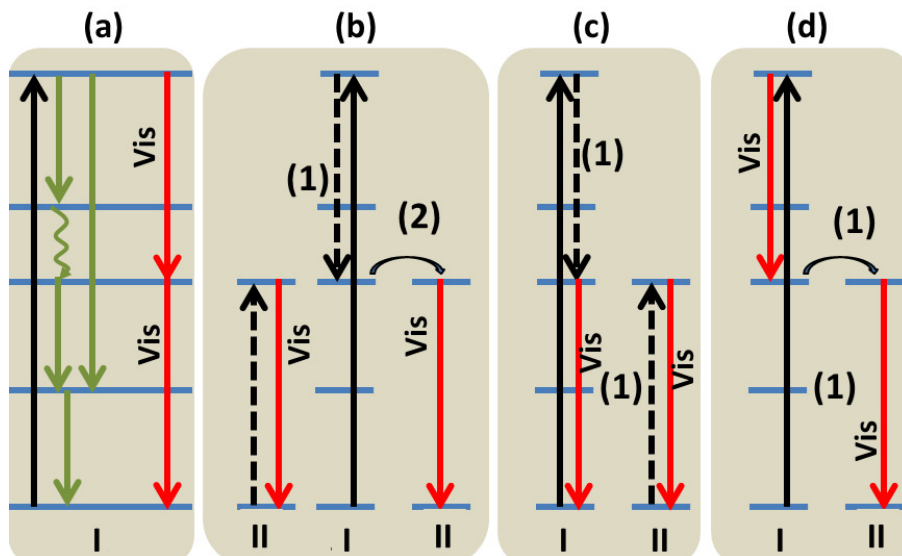
Figure 1.3: (a) QC on a single ion I by the sequential emission of two visible photons. Type I is an ion for which emission from a high energy level can occur. Type II is an ion to which ET takes place. (b) The possibility of QC by a two-step ET. In the first step (indicated by (1)), a part of the excitation energy is transferred from ion I to ion II by mainly cross-relaxation. Ion II returns to the ground state by emitting one photon of visible light. Ion I is still in an excited state and can transfer the remaining energy to a second ion of type II (indicated by (2)), which also emits a photon in the visible spectral region, giving a QE ≤ 200 %. (c and d) The remaining two possibilities involve only one ET step from ion I to ion II, sufficient to obtain visible QC if one of two visible photons can be emitted by ion I.

Figure 1.3 illustrates the energy-level diagrams for two (hypothetical) types of RE ions (I and II) showing the concept of downshifting. Efficient visible QC via two photon emission from a high energy level for a single RE ion is theoretically possible as shown in Figure 1.3a. However, competing emissions in the IR and UV (the green lines of Figure 1.3a) can also occur and prevent efficient visible QC on a single RE ion. Figure 1.3 (b–d) presents generalized energy-level diagrams for three DC mechanisms involving ET between two different RE ions I and II. Type I is an ion for which emission from a high-lying level occurs. Type II is an activator ion to which ET takes place. Figure 1.3b indicates two photon emission

from ion pairs by from ions I to II (denoted by (1)), and ET from ions I to II (denoted by (2)) with emission from ion II. Figure 1.3c and d show a cross relaxation mechanism followed by the emission of photons from both ions I and II. In all three cases, if the two step ET process is efficient, theoretical visible quantum efficiency (QE) of 200 %, can be achieved because the previous IR and UV losses existing in a single ion can be avoided.

In addition to the energy migration processes, as mentioned earlier, the size, shape, and surface of lanthanide doped nanophosphors are important in relation to a specific application, while their composition and the local dielectric environment are essential for their excitation dynamics.[68] Owing to the high surface-to-volume ratio of nanophosphors, most of the lanthanide dopants are exposed to surface deactivations caused by surface lattice defects and dangling bonds, as well as by surrounding ligands and solvents that possess high phonon energy. The deactivation can occur directly or through an indirect pathway involving energy migrations from the interior lattice points to the surface sites. Hence, the excitation dynamics is also coupled to the surface properties of nanophosphors due to these nanosize induced surface effects, which are not so pronounced in bulk crystals. These factors create interests to synthesize nanophosphors of stoichiometric composition in a precisely controlled way and to tailor their interface to generate highly efficient nanophosphors for a specific frequency conversion. Furthermore, tailoring the interface is also important for the colloidal solubility of nanophosphors.

1.5 Nanoscintillators

A scintillator is a phosphor material with the ability to absorb energetic radiation (x-ray, γ-ray, neutrons and charged particles) and to convert a fraction of the absorbed energy into photons with characteristic energies (infrared, visible or ultraviolet (UV) photons).69 A scintillation phenomenon is an example of bifunctional characteristics of luminescent materials. Detection and measurement of radiation is important in many economical activities, including mining and nuclear power generation, light emitting diodes (LEDs), biological markers, as well as in cancer treatment (radiotherapy), and medical diagnosis and imaging such as positron emission tomography (PET).[70–72] It is also very important in security applications. Available scintillators commonly correspond to high cost single crystals, many of them highly hygroscopic and of cumbersome maintenance. Additionally, glasses with intrinsic low light output, and organic scintillators that while bright, lack effective stopping power for high energy gamma radiation.

Among many varieties such as organic, plastic, and inorganic scintillators, the latter are usually known for their high stopping power, since high atomic weight inorganic compounds are available that also have high light yield. The high energy ionizing radiation detection using nanoscale materials for illustration is of particular interest and relevance to this thesis.

Researchers are interested to develop and commercializing a new optically transparent material based on specially engineered nanoparticles that, when incorporated into scintillation counters, permits sensitive and dangerous ionizing radiation detection at lower cost, even in trace amounts. In an effort to design a material suitable for detection of ionizing radiation, certain conditions have to be satisfied. Since ionizing radiation is usually of the order of high energy, firstly the material must be capable of absorbing high energy radiation. Photoelectrons or secondary electrons created in the process travel at high velocities. And, for energy transfer to take place between these particles and the atoms of the scintillating material, they must be slowed down sufficiently to allow the interaction to occur. Therefore, high atomic weight and high density material capable of attenuating the radiation is required. Most importantly, a material that characteristically emits in the UV or visible wavelength with high efficiency is required to be intrinsically situated or doped within a wider band gap material/host. Ideally, this material, known as activator, traps the excited carriers from the host and emits light after carrier relaxation in its internal energy levels. Furthermore, the time to emission or the carrier relaxation time is also important since materials that emit faster after absorption can provide higher rates of detection and therefore better accuracy. For this specific purpose, e.g., PET scanning application, a material that has a fast decay time will be useful. Essentially, a fast, single emission line, high light output activator species embedded in a high density, high molecular weight, and wide band gap host should prove to be an ideal scintillator material for ionizing radiation detection applications.[73]

The fabrication of material involves matching the refractive index of nanoparticles to the host matrix in order to reduce optical scattering, and thus enhancing optical transparency. By designing the nanoparticles in specific ways, the researchers simultaneously achieve greater surface passivation and enhanced light output. A new species of nanocrystals, where a highly luminescent ion is doped into a wide band gap host matrix is attractive for high energy ionizing radiation detection. Since lanthanides are excellent luminescent ions for the above mentioned parameters, and lanthanide halides are good wide band gap host materials, they are popularly known as lanthanide doped lanthanum halide nanocrystals, which are very good candidates for

radiation detection applications. Best single crystal LaBr$_3$(Ce) is already in the market but improvement at nanoscale is needed. The demands for high quality lanthanide containing nanocrystals are growing, as more and more problems are being solved by exploiting the unique properties of the lanthanide elements, and the way that they act when incorporated into a crystalline lattice.[20,69,74,75]

1.6 Aim of present work and thesis outlines

The broad applications of lanthanide doped up/downconversion nanomaterials in various fields have prompted the development of a new class of novel nanoparticles with desirable optical window via up/downconverting mechanism for technological applications. At the same time, the development of the subject nanomagnetism especially by considering iron-oxide improved the several perspectives in field of biomedicine/device industries. Although considerable strategies have been developed for fine tuning of up/downconversion luminescence with magnetic entity at nanoscale, this field is still immature in terms of fabrication of the material because of compromised magnetic response and tuned photoluminescence characteristics and challenging structural templates. Therefore, we have attempted to design bifunctional nanomaterials with better structural, optical and magnetic characteristics in search of their potential applications particularly in the field of scintillation. In brief, the main points of thesis are summarized below:

- To develop soft, facile and inexpensive chemical synthesis routes of new class of magnetic-luminescent bifunctional nanomaterials.
- To explore physio-chemical properties of binary and ternary rare earth ions activated luminescence materials and their alliance with iron-oxide nanoparticles for optical and magnetic functionality together.
- To investigate critically optical and magnetic behavior of the synthesized bifunctional nanomaterials for their potential applications.
- To study the photoluminescence/magnetic properties due to the rare earth dopants in inorganic matrices namely LaF$_3$ and NaGdF$_4$.
- To check their suitability for the potential application in scintillation process using ionizing radiation and low cost versatile single ternary doped rare earth fluorides primarily.

To avail motivating scientific importance and realizing aims of the present work, several materials have been synthesized and explored. All of them have been organized in the present thesis.

Chapter 2 provides a comprehensive overview of fundamental aspect of electronic, optical and magnetic behavior of rare earth ions involved in photoluminescence phenomena. The special features of superparamagnetism and magnetic characteristics of iron-oxide nanoparticles have also been discussed.

Chapter 3 contains the controlled synthesis protocols of nanoparticles by bottom up wet chemistry routes along with necessary theoretical background and experimental details for the various techniques related to structural, optical and magnetic properties of studied systems.

Chapter 4 discusses the in-depth structural, microstructural and photoluminescence studies performed for multicolor tuned $LaF_3:Ce^{3+},Gd^{3+},Eu^{3+}$ downconverting nanoparticles. Further, bifunctionality has been coined due to its paramagnetic behavior.

Chapters 5 presents the structural, magnetic and luminescence properties with proposed energy migration of the green emitting bifunctional $Fe_3O_4/ZnS@LaF_3:RE^{3+}$ (RE = Ce, Gd, Tb) nanocomposite into integration. The magntophoretic separation illustration and simultaneous green emission under UV irradiation makes these materials very appealing for high energy irradiation.

Chapter 6 investigates thoroughly a comparative structural, magnetic and up/downconversion phenomenon in between (Ce^{3+}, Eu^{3+}) and (Yb^{3+}, Er^{3+}) activated $NaGdF_4:RE^{3+}$ as well as iron-oxide/SiO_2/$NaGdF_4:RE^{3+}$ nanoparticles (where RE^{3+} = Ce^{3+}, Eu^{3+} and Yb^{3+}, Er^{3+}).

Chapter 7 contains the experimental results obtained through scintillation mechanism using ionizing irradiation emitted from [241]AmBe neutron source for $LaF_3:5\%Ce^{3+},5\%Gd^{3+},10\%Eu^{2+/3+}$ nanoparticles. This chapter provides a better understanding of the requirements needed to improve the design and fabrication of nanoscintillators.

Finally, the chapter 8 highlights the integrated conclusions drawn from the underlying work and future scope of the work. The references have been given in chapter 9.

Chapter 2
Rare Earth Spectroscopy and Magnetic Materials

2.1 Introduction

Nanostructures provide an excellent platform to integrate different functional components into one single nanoentity to exhibit multifunctional properties. To assemble different nanoparticles into a single entity as the novel building block itself is exciting and holds great potential. Materials possess luminescence and magnetism simultaneously is of great importance in many important applications.

Luminescence: The emission of light by solid bodies at relatively low temperature is called luminescence and light emission by a hot body is termed as incandescence. There are several luminescence phenomena occurring in nature such as fluorescence, phosphorescence, photoluminescence, radioluminescence, and so on. The photoluminescence is the most explored luminescence phenomenon. A general luminescence mechanism and fluorescence color can be explained using Figure 2.1a by considering crystal matrix in material acting as a (nominally inactive) host having a small quantity of impurity or activator (A). The role of the host structure or of the host activator combination is to absorb an excitation in the form of a photon of energy $h\upsilon_1$ and re-emits the excitation as a photon of energy $h\upsilon_2$. The color emitted is dependent upon the nature of the activator. Sometimes it is found that the activator containing material cannot absorb the exciting radiation directly, in which a helper species, a sensitizer (host itself or other cation), is needed as well that absorbs the exciting photons, of energy $h\upsilon_3$, and passes the energy to the activator. Irrespective of whether the luminescence is derived from an activator-sensitizer pair, or just from the activator alone, a rapid decay of light is characteristic of fluorescence. On the other hand, a slow decay is characteristic of phosphorescence (Figure 2.1b). In this case, the energy is often regarded as being stored in a reservoir from which it slowly leaks. This feature is more commonly associated with heavy atoms and is one of the reasons why the lanthanides are so much interesting.

Magnetism: The bifunctional properties come into account due to magnetic activation of rare earth ions along with other magnetic component associated with the nanostructure, e.g., ferrites, iron-oxide etc. Core-shell templates, composites, heterostructures of iron-oxide or

ferrites and luminescent materials, and doping of Fe, Co, Mn, etc., ions along with Ln^{3+} ions in rare earth matrices, lead to wide range of applications.
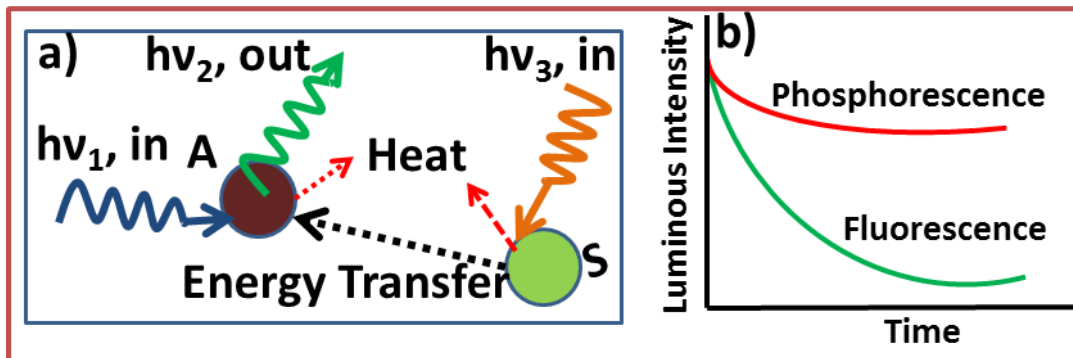
Figure 2.1: Schematic representation of energy absorption and emission processes taking place in a luminescent material. (a) Absorption of radiation. A represents an activator center and S a sensitizer center. (b) Emission of radiation.

Therefore, it becomes important to study magnetic nature of such systems to assess the real potential of bifunctional materials. In the following sections, considering bifunctionality based on the luminescence and magnetic nanoparticles, we shall first give some fundamentals concept of photoluminescence with central focus on rare earth spectroscopy. Further, magnetic properties of iron-oxide at nanoscale and magnetic characteristics of rare-earth ions will also be a central theme of this chapter.

2.2 Electronic-optical properties of lanthanides

Lanthanide ions (RE^{3+}) are important constituents in many optical materials. Lanthanides are a group of fourteen elements (La-Lu) appearing in the periodic table after lanthanum with atomic number ranging from 57 to 71 and electronic configuration [Xe] $4f^{1-14}5d^{0-1}6s^2$. The 4f electrons of lanthanide ions are strongly shielded by filled outer shell orbitals. The sharp emission lines and long excited state lifetime values from lanthanide ions have been attributed to the shielding of 4f electron from the surrounding environment by 5d and 6s electrons, leading to variety of important applications. The inorganic luminescent materials provide high luminescence efficiency and long-term chemical stability. Table 2.1 summarizes the electronic configuration, ionic radius, and main electronic transitions of trivalent ions of lanthanides.

15

Table 2.1: Electronic-optical properties of lanthanides, energy levels and transitions

Element	RE^{3+}-ground states	RE^{3+} radius (Å)	Transitions	$\lambda_{emission}$ (nm)	Energy gap (cm^{-1})
^{21}Sc	[Ar]3d^0 ($^1S_0$)	0.68	-	-	-
^{39}Y	[Kr]4d^0 ($^1S_0$)	0.88	-	-	-
^{57}La	[Xe]4f^0 ($^1S_0$)	1.06	-	-	-
^{58}Ce	**[Xe]4f^1 ($^2F_{5/2}$)**	**1.03**	**5d$\rightarrow^2F_{5/2}$**	-	-
^{59}Pr	[Xe]4f^2 ($^3H_4$)	1.01	$^3P_0\rightarrow^3H_6$	610	3910
			$^1D_2\rightarrow^3F_4$	1060	6940
			$^1G_4\rightarrow^3H_5$	1300	-
^{60}Nd	[Xe]4f^3 ($^4I_{9/2}$)	0.99	$^4F_{3/2}\rightarrow^4I_{9/2}$	1060	5400
^{61}Pm	[Xe]4f^4 ($^5I_4$)	0.98	$^5F_1\rightarrow^5I_J$	-	-
^{62}Sm	[Xe]4f^5 ($^6H_{5/2}$)	0.96	$^4G_{5/2}\rightarrow^6H_{9/2}$	590	7400
^{63}Eu	**[Xe]4f^6 ($^7F_0$)**	**0.95**	**$^5D_0\rightarrow^7F_2$**	**615**	**12300**
^{64}Gd	**[Xe]4f^7 ($^8S_{7/2}$)**	**0.94**	**$^6P_{7/2}\rightarrow^8S_{7/2}$**	**311**	**32100**
^{65}Tb	**[Xe]4f^8 ($^7F_6$)**	**0.92**	**$^5D_4\rightarrow^7F_5$**	**550**	**14800**
^{66}Dy	**[Xe]4f^9 ($^6H_{15/2}$)**	**0.91**	**$^4F_{9/2}\rightarrow^6H_{13/2}$**	**570**	**7850**
^{67}Ho	[Xe]4f^{10} ($^5I_8$)	0.89	$^5F_5\rightarrow^5I_{7,6}$	970,1450	3000
			$^5S_2\rightarrow^5I_8$	550	2200
^{68}Er	**[Xe]4f^{11} ($^4I_{15/2}$)**	**0.88**	**$^4S_{3/2}\rightarrow^4I_{15/2}$**	**545**	**3100**
			$^4I_{13/2}\rightarrow^4I_{15/2}$	**1500**	**6500**
^{69}Tm	[Xe]4f^{12} ($^3H_6$)	0.87	$^1G_4\rightarrow^3H_6$	480	6250
^{70}Yb	**[Xe]4f^{13} ($^2F_{7/2}$)**	**0.86**	**$^3F_{5/2}\rightarrow^2F_{7/2}$**	**980**	**10250**
^{71}Lu	[Xe]4f^{14} ($^1S_0$)	0.85	-	-	-

2.2.1 Electronic energy levels

2.2.1.1 4f energy levels of rare earths: Electrons in atoms are ranked in shells and subshells defined by two quantum numbers: n, the principal quantum number and l, the angular quantum number. Each subshell has $2l+1$ orbitals, with a maximum of $4l+2$ electrons. As a consequence, the 4f subshells of rare earths (n = 4 and l = 3) have seven orbitals with space for 14 electrons ($m_s = \pm 1/2$). Considering that each electron can have $+½$ or $-½$ spin, there are $\frac{(4l+2)!}{n!(4l+2-n)!}$ ways to arrange the electrons in the orbitals, and thus, as many energy levels. Then, there are 20 for

the p-electrons, 252 for the d-electrons, and 3432 energy levels for the f-electrons. This huge number explains the complexity of classifying the 4f energy levels. The interactions between electrons of a unique configuration lead to spectroscopic terms noted $^{2S+1}\Gamma$ where S is the angular moment of spin ($\vec{S} = \sum_{i=1}^{n} \vec{s_i}$) and Γ represents the L value, which is the orbital angular moment ($\vec{L} = \sum_{i=1}^{n} \vec{l_i}$). The Γ letter is written as S, P, D, F, G..., when the L value is 0, 1, 2, 3, 4... . The splitting of spectroscopic terms is made through the action of spin-orbit coupling.[76] This leads to the spectroscopic levels $^{2S+1}\Gamma_J$ with $\vec{J} \rightarrow \vec{L} + \vec{S}$, where $\vec{J}$ is the total orbital moment representing the interaction of L and S magnetic moments and 2S+1 represent the total spin multiplicity. The values of J can vary from (L+S) to (L-S). The configuration where each level is characterized by a triplet (L, S, J) is termed Russell-Saunders coupling or simply L-S coupling. The intensity of spin-orbit coupling is characterized by a constant (l).[76] l is positive if 4f is less than half filled, and negative elsewhere. In the case where 4f is half filled (n = 7), there is no coupling since S = 0. The third Hund's rule is able to give the fundamental level. If n < ($2l$ + 1), the fundamental level is the one having the minimum J. On the contrary, if n > ($2l$ + 1), the fundament level is the one with the highest J. Then, the levels are arranged with equal energy gap, the gap between two adjacent levels J and J'= J + 1 has a value of λJ'. Each of these levels has a multiplicity of 2J+1.

For each trivalent ion, the energy levels are positioned considering the electron-electron interaction of each unique configuration in a first step. In a second step, the spin-orbit coupling partially splits the degeneration of the electron-electron interaction into spectroscopic levels.[77] As we go from La^{3+} to Lu^{3+}, the 4f orbitals are filled with electrons. These electrons have little interaction with the chemical environment of the ion, as the 4f orbitals are shielded, but spatially located outside the 4f orbitals. The electronic transitions that are responsible for the line like absorption and luminescence spectra are transitions within the $5s^2\ 5p^6\ 4f^n$ configuration, and are therefore only marginally affected by the matrix. The occurrence of different energy levels belonging to the same configuration is a result of several interactions within the ion. Simply, depending on their number, there are many ways to distribute the electrons over the "7" 4f-orbitals, but some distributions are energetically more favorable. The interactions that split up the levels belonging to the [Xe] $4f^n5d^0$ configuration are clarified in Figure 2.2, where we have taken an example of Eu^{3+} ion. Of the interactions, the coulombic, representing the electron-electron repulsions (H_{ER}) within the 4f orbitals, is the largest and

yields terms with a separation in the order of $10^4 \, cm^{-1}$. These terms are in turn split into several J-levels by spin-orbit coupling, which is relatively large ($10^3 \, cm^{-1}$) because of the heavy lanthanide nucleus. We have now arrived at the free ion levels that are described earlier by the term symbols $^{2S+1}L_J$. When present in a coordinating environment, such as a crystal or an organic ligand, the individual J-levels are split up further by the electric field of the matrix, which is usually referred to as the crystal field. These splitting are usually small ($10^2 \, cm^{-1}$) and, depending on the spectral resolution of the spectrometer, appear as fine structure on the individual bands.
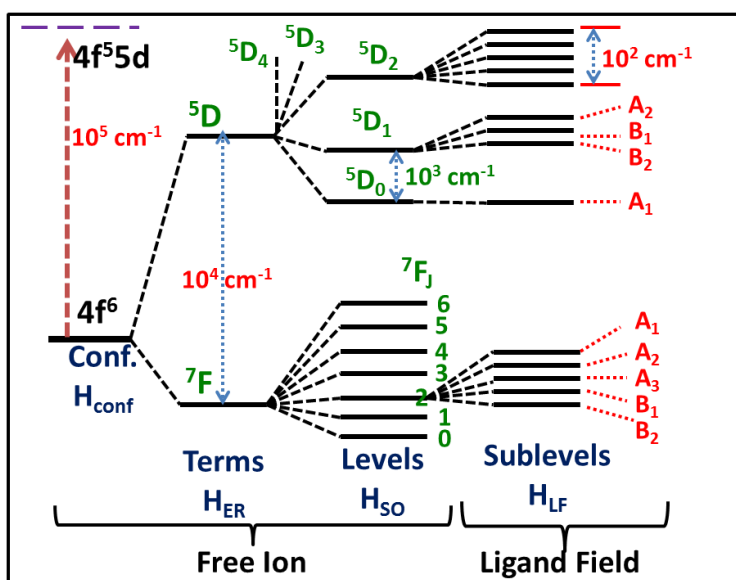
Figure 2.2: Splitting of the energy levels belonging to the $[Xe]4f^75d^0$ configuration (such as in Eu^{3+}).[78]

Throughout this work, we will largely ignore this fine structure, although it may be used to gather information about the symmetry of the coordination environment.[77] In this work, all the transitions discussed later relating to the several RE ions are due to the one of main excitation transition: 4f-4f transitions, which involve the movements of electrons between different energy levels of the 4f orbitals within the same lanthanide ion. There are three main mechanisms of the 4f-4f transitions:[79] (i) magnetic dipole transition; (ii) induced electric dipole transition and (iii) electric quadrupole transition.

(i) Magnetic dipole transition: The magnetic dipole transition is due to the interaction between the active ion (lanthanide) and magnetic field component of the light through a magnetic dipole. Intensity of the magnetic dipole transition is proportional to the square of the

18

transition dipole moment. Considering the small size of an ion, the curvature displacement will be small, thus the intensity of magnetic dipole transition is normally very weak for the most of lanthanide ions. However, it is of interest and used as intensity standards for various doping hosts, because it is independent of the environment. Magnetic dipole can be considered as a rotational displacement of charge: the sense of rotation cannot be reversed under point reversion, thus magnetic dipole transition has even parity.[79]

(ii) Induced electric dipole transition: The induced electric dipole transition is the main observed optical transition in lanthanide ions, which is due to the interaction of the active lanthanide ion and the electric field vector through an electric dipole.[80–82] The electric dipole operator has odd parity as it supposes a linear movement of charge. The intraconfigurational electric dipole transition is forbidden due to the Laporte parity rules. But in reality, weak and narrow emissions are observed, which are mainly due to the mixing of the 4f wave functions with the opposite-parity wave functions of the crystal field such as the 5d states, charge transfer states and so on. Thus, they are often called induced electric dipole transitions.

(iii) Electric quadrupole transition: The electric quadrupole transitions arise from a displacement of charge that has a quadrupole nature.[77,83] It can be considered as two electric dipoles aligned in different directions. Electrical quadrupole transition is much weaker compared with the magnetic dipole transition and induced electrical dipole transition. And it should be mentioned that no experimental evidence exists for the occurrence of quadrupole transition in lanthanide ions.

2.2.1.2 5d energy levels of rare earths: The five 5d orbitals play a big role in phosphor materials. They are empty in the normal state but could get an electron from 4f levels during excitation. In the free ion, the five 5d have the same energy. Contrary to 4f orbitals, the energy of the 5d levels will decrease when an ion lanthanide LnQ^+ is placed in a host (A). This phenomenon is called "red shift," and is illustrated by $D(Q,A)$ in Figure 2.3. The corresponding energy levels are always noted ^2D (only one electron can be excited). For cubic symmetry, there are two groups: ^2E_g and $^2T_{2g}$. The red shift is due to two phenomena:[84] (i) nephelauxetic effect, which shifts the barycenter of the 5d in arrange of $\varepsilon_c(n,Q,A)$; and (ii) crystal field (CF) splitting of the 5d orbitals in a range of $\varepsilon_{cfc}(n,Q,A)$. $\varepsilon_{cfc}(n,Q,A)$ is defined as the energy difference between the lowest and the highest 5d levels (Figure 2.3). ε_{cfc} depends upon the size of the site, the covalence of the bonds, and the coordination of the site. It increases with the charge of the ligands and decreases with their size: O > S > F >Cl> Br > I.

The emission of 4f-5d transition is also affected by Stokes shift (ΔS) which results from the electron-phonon due to host matrix vibrations. The nephelauxetic effect induces a shift of the barycenter (center of mass of two or more electrons that are orbiting each other, or the point around which they both orbit) of the d orbitals with a value of $\varepsilon_c(n,Q,A)$ compared to free ion. When the electronic cloud of the rare earth is surrounded by a ligand field, part of it is delocalized toward the ligands. This induces a global reduction of the electrostatic interaction. This value is 6.35 eV for the Ce^{3+}. This effect increases with the polarizability of the ligand $(Se^{2-}>S^{2-}>N^{3-}>O^{2-}>F^-)$ and with the charge density of the anionic ligand $(O^{2-} > AlO_4^{5-} > SiO_4^{4-} > BO_3^{3-} > PO4^{3-} > CO_3^{2-} > SO_4^{2-} > H_2O)$. This crystal field (CF) splits the 5d orbitals without modifying the barycenter position.
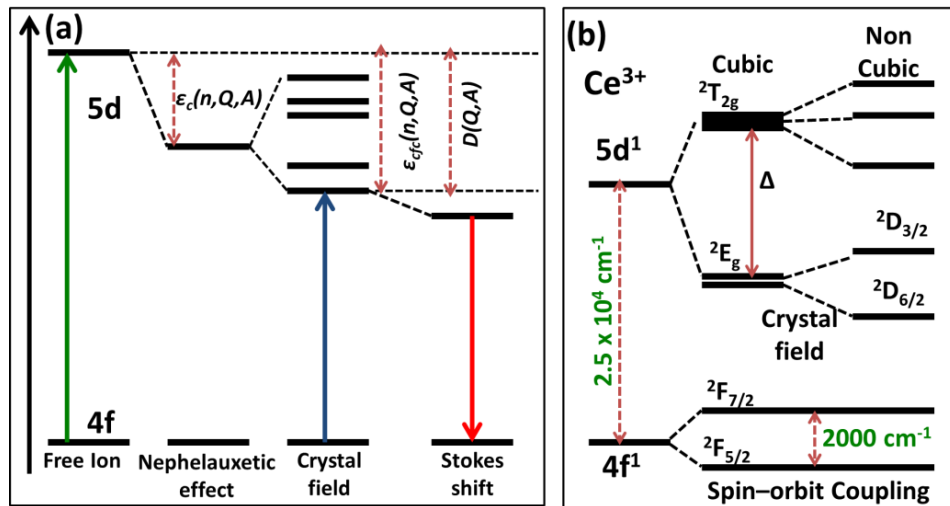
Figure 2.3: (a) Red shift diagram and transition from 4f and 5d. (b) 4f-5d transition of Ce^{3+}.

The parity allowed optical transitions of the RE^{3+} ions are interconfigurational $(4f^n \rightarrow 4f^{n-1}5d)$ and are more prevalent in the RE^{3+} ions which are most easily oxidized to their 4+ states, Ce^{3+}, Pr^{3+} and Tb^{3+}. These f-d transitions are higher in energy (Figure 2.3) than the f-f transitions, occurring mainly in the UV region as broad bands. Conversely, the f-d transitions are most energetic for those ions which are easily reduced to their 2+ states, Sm^{3+}, Eu^{3+} and Yb^{3+} and occur in the short wavelength region of the UV spectrum. The electronic absorption and emission spectra for most of the Ln^{3+} ions at wavelengths > 200 nm, involve only transitions within the $4f^n$ configuration. The f-d transitions are discussed in more detail in reference[84].

2.2.1.3 The Dieke diagram: The Dieke diagram (Figure 2.4) has been built for lanthanides in the LaF_3 matrix, but it can be applied to other matrices since the 4f levels are only slightly

dependent on the host matrix.[85] Then, depending on symmetry considerations, the most probable transitions between these levels can be identified. They are represented here by arrows. The Dieke diagram has been commonly used as a reference for estimating the absorption and emission spectra of the trivalent lanthanide ions embedded in any host matrix, as the optical characteristics are not affected much by the crystal environment.[85,86]

2.2.2 Selection Rule

Luminescence originating from electronic transitions between 4f levels is predominantly due to electric dipole or magnetic dipole interactions. Electric dipole f-f transitions in free 4f ions are parity forbidden, but become partially allowed by mixing with orbitals having different parity. Typical examples of this mechanism are demonstrated by the luminescence from the ^5D_J states of Eu^{3+} (Figure 2.2). The intensity of these transitions depends strongly on the site symmetry in a host crystal. Magnetic dipole allowed f-f transitions are not affected much by the site symmetry. The J selection rule in this case is $\Delta J = 0, \pm 1$ (except for $0 \rightarrow 0$). For electric dipole transition, the difference in the J values (ΔJ) is ± 2. Oscillator strengths are of the order of 10^{-5} to 10^{-8} for electric dipole transitions, and 10^{-8} for magnetic dipole transitions. In other words, the atomic spectra have to obey the following selection rules: $\Delta S = 0$, the overall spin is not allowed to change, because light does not affect the spin; $\Delta L = 0, 1$, with $\Delta l = 1$, the orbital angular momentum of an individual electron must change; and $\Delta J = 0, 1$, but $J = 0$ to $J = 0$ is forbidden.

2.2.3 Photoluminescence

There are two basic atomic processes that must take place during photoluminescence: (i) absorption; and (ii) emission. In addition, energy transfer between excited and non-excited states is often important and, indeed, vital when sensitizers are a necessary component of the luminescent system. Some of the fundamental luminescence characteristics can be explained as: **Emission spectrum**, gives for particular excitation energy, the intensity of photon emissionas a function of wavelength. It consists of either fine peaks (4f-4f transitions) or large bands (4f-5d transitions).[87] **Absorption spectrum,** describes the intensity of absorption, as a function of wavelength. Efficient phosphors have strong absorption resulting from specific transitions (4f-5d, charge transfer (CT) or band gap transitions) and low energy losses (minimizing the Stokes shift, multi-phonon processes, or photoionization).[87] **Excitation spectrum** is observed for a particular selected energy emission. This spectrum gives all the energies responsible for the emission as a function of wavelength.
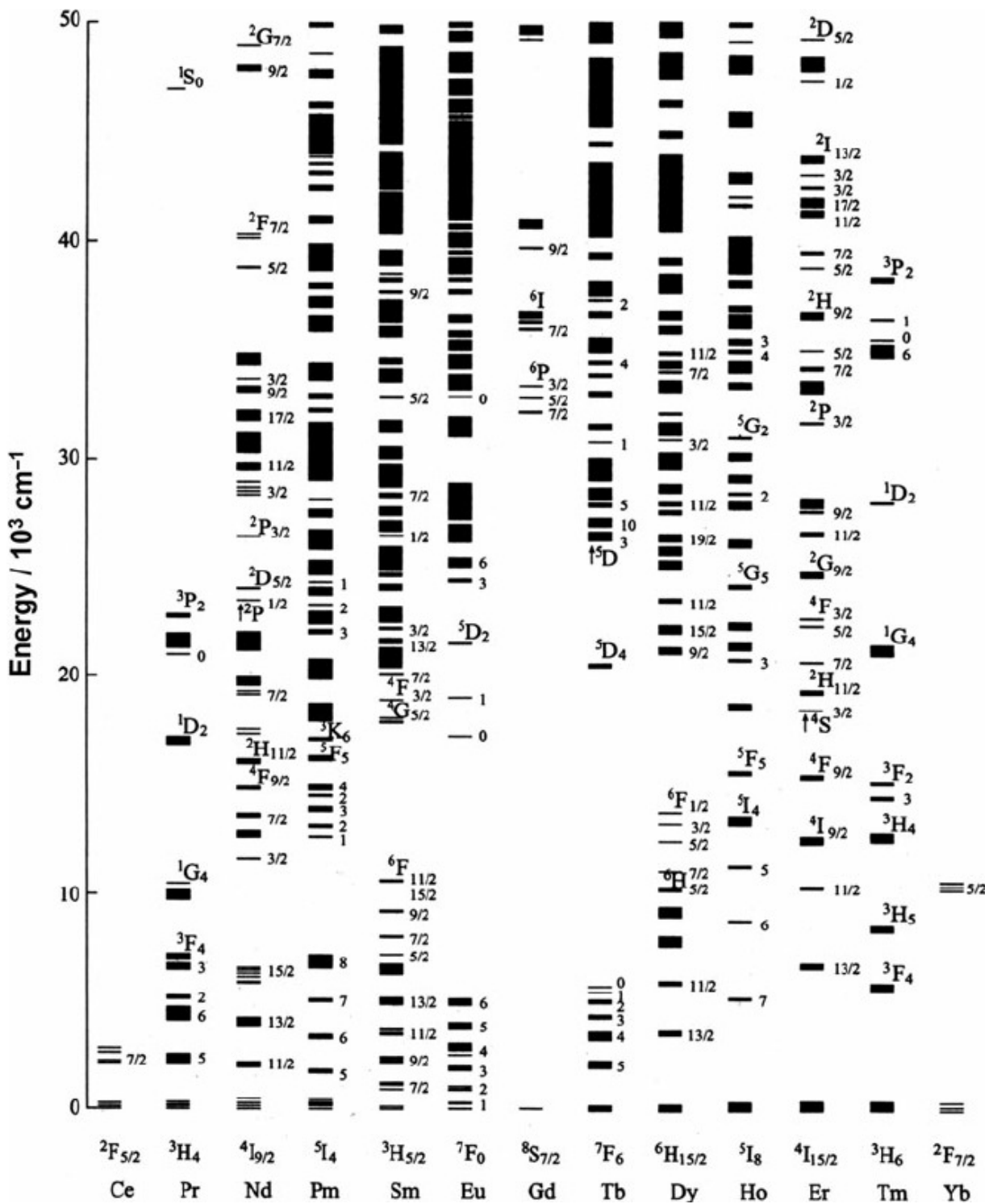
Figure 2.4: The Dieke diagram: Energy level of the $^{2S+1}L_J$ multiplet manifolds of trivalent lanthanide ions (up to 42000 cm^{-1}).[85,86]

The performance of phosphors in terms of photon generation is described in two different ways, quantum efficiency and light output (or external luminescence yield):[88]

Quantum efficiency: $\eta_{int}(\lambda) = \frac{\text{number of emitted photons}}{\text{number of absorbed photons}}$ (2.1)

External Quantum efficiency: $\eta_{ext}(\lambda) = \frac{\text{number of emitted photons}}{\text{number of incident photons}}$ (2.2)

The ratio $\frac{\eta_{ext}(\lambda)}{\eta_{int}(\lambda)}$ is the absorption $A(\lambda)$ of the material at λ wavelength. From an industrial perspective, the **external quantum efficiency** is the most important value, since it gives some indication of all optical phenomena, including incident photon absorption efficiency. The **internal yield** only explains the optical processes after absorption of the excitation source. The former value is generally given as a percentage of a calibrated reference phosphor. **The lifetime** of luminescence (decay time) is defined as the time required for the luminescence intensity to decay from some initial value to e^{-1} of that value.

2.2.3.1 Radiative and nonradiative transitions of lanthanide ions

Radiative Transition: There are several possibilities of returning of excited electron to the ground state. The observed emission from a luminescent center is a process of returning to the ground state radiatively. The processes competing with luminescence are radiative transfer to another ion and non-radiative transfers such as multi-phonon relaxation and energy transfer between different ions or ions of a similar nature. Figure 2.5 shows the configurational coordinate diagram in a broad band emission. Upon excitation, the electron is excited in a broad optical band and brought in a high vibrational level of the excited state. The center thereafter relaxes to the lowest vibrational level of the excited state and give up the excess energy to the surroundings. This relaxation usually occurs nonradiatively to the lowest excited energy state because photo-excited electrons rapidly thermalize and are captured by the states within ~ kT of the lowest energy levels. From the lowest vibrational level of the excited state, the electron returns to the ground state by means of photon emission. Therefore, the difference in energy between the maximum of the excitation band and that of the emission band is found. This difference is called the Stokes shift. The radiative transfer consists of absorption of the emitted light from a donor molecule or ion by the acceptor species. For such transfer process to takes place, the emission of the donor has to coincide with the absorption of the acceptor. The radiative transfer can be increased considerably by designing a proper geometry.

Luminescence generated from intentionally incorporated impurities is called extrinsic luminescence. These impurities create local quantum states that lie within the band gap, and result in radiative relaxation by an electron-hole recombination from conduction band to acceptor state, donor state to valence band or donor state to acceptor state, as shown in Figure 2.6(a and b). Instead of the photon energy being equal to the band gap, the Stokes shift is observed due to the localized quantum state lying in the forbidden band-gap. These transitions between the excited and lower energy states are classified as allowed or forbidden based on the Laporte and parity selection rules as explained earlier.
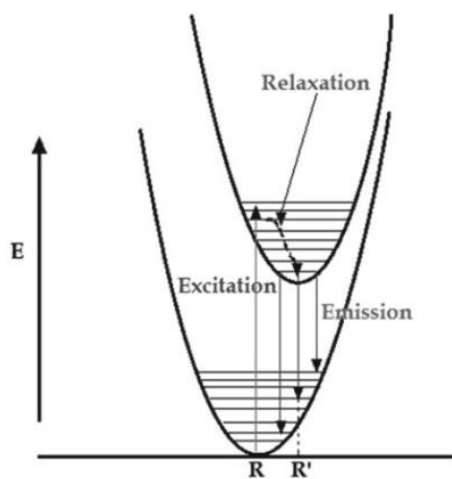
Figure 2.5: Configurational coordinate diagram in a luminescence centre.[89]

The electric dipole transition can occur between energy levels with different orbital angular momentum, $\Delta l = \pm 1$, and parity. Even though a transition may be forbidden, incorporation of activator ions in crystals may perturb the symmetry and magnitude of the crystal electric field, resulting in observation of allowed transition. Allowed transitions include s-p and f-d, while d-d and f-f are forbidden. The f-d transition processes are allowed so optical absorption is strong and observed as broad band excitation around 300 nm. The energy of f-d transition is dependent on the local crystal field; while the energy of forbidden f-f transitions from rare earth activators are constant for different hosts because of isolation of the 4f states. Luminescent 5d-4f transitions are found for some rare earth activators, e.g., Ce^{3+}, Pr^{3+}, Eu^{2+}, and are sensitive to crystal field splitting in host crystals. Trivalent rare earth ions (RE^{3+}) show f-f transition such as Tm^{3+}, Er^{3+}, Tb^{3+} and Eu^{3+}. Since the 4f energy levels over rare earth

activators are shielded by the outer 5s and 5p electron orbitals, their transition energies are largely unaffected by the host materials and the emission spectra exhibit sharp atomic-like peaks.
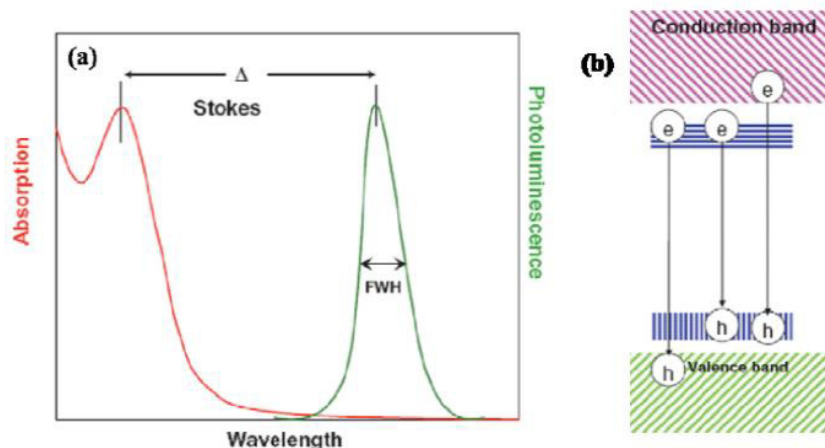
Figure 2.6: (a) Stokes shift is the energy difference between absorption and photoluminescence emission. (b) Radiative recombination processes in extrinsic luminescence.[89]

Nonradiative Relaxation: If highly excited lanthanide ions could only decay radiatively, their emission spectra would become extremely rich in lines, since in principle radiative transitions between any two states can take place.[89] Under favorable conditions, emission from 'higher' excited states is indeed observed, and that process is the basis of upconversion, in which an already excited ion is excited into a higher lying luminescent state, converting two low-energy photons into one high-energy photon, and quantum cutting in which a highly excited ion emits sequentially two photons. The excited states of lanthanide ions, however, do not decay solely by radiative processes. In glasses and crystals, the electronic excitation energy can be dissipated by vibrations of the surrounding matrix, a process known as multi-phonon relaxation. A similar process occurs also in complexes with organic ligands, and is even of bigger importance in such systems, since in organic media suitable high energy vibrations are more common.

The efficacy of matrix vibration mediated non-radiative relaxation is inversely proportional to the number of vibrational quanta that are needed to bridge the gap between a given energy level and the next-lower one. This energy gap law is a result of the overlap between the vibronic wave-functions. A semi-quantitative treatment gives a result of vibration-mediated nonradiative decay, luminescence of a given lanthanide ion occurs mainly from one state

25

indicated by the filled circles in Figure 2.7a, which is the state that has a large gap with the next lower level. More highly excited states are quickly deactivated to this state, since the higher states form a 'ladder' consisting of relatively small gaps that efficiently undergo multi-phonon relaxation.

In case of organic media and in aqueous solution,[91] where matrix vibrations of high energy are ubiquitous, the emission of lanthanide ions stem (almost) exclusively from one level, and therefore the number of emission lines is limited as emission from only one emitting state. One should, however, not expect the nonradiative decay rate to depend only on the energy gap and the number of 'fitting' matrix vibrations in organic media. Multi-phonon relaxation still involves electronic transitions in the ion without a change in parity. For this process selection rules also apply, although these only affect a few transitions, such as $^5D_1 \leftrightarrow \,^5D_0$ in Eu^{3+} (and Tb^{3+}). Indeed, even in organic media, weak luminescence from the 'higher excited' $^5D_1$ state is observed.
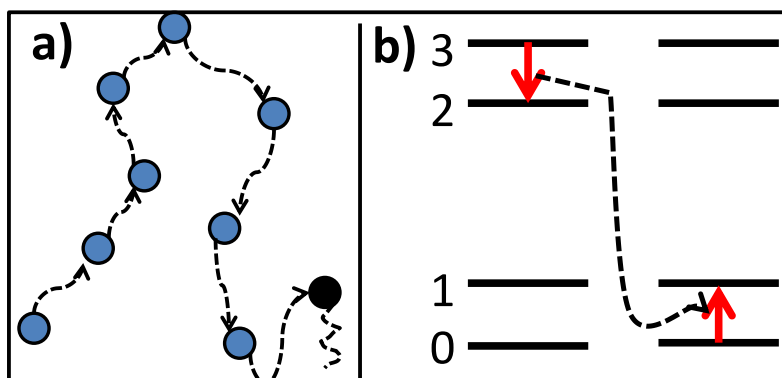
Figure 2.7: Possible mechanism for luminescence concentration quenching: (a) energy migration among donors (circles) in a chain followed by its migration to a killer site (black circle) which acts as non radiative sink; (b) cross relaxation between pairs of centers (Sinusoidal arrows indicate non-radiative decay).[90]

2.2.3.2 Luminescence Quenching

Luminescence can be quenched due to the nonradiative decay of the excited state as explained above. This nonradiative decay is brought about by different mechanisms involving energy transfer from the excited state of the donor to different types of acceptors like host lattice,

organic molecules on the surface, defect levels or nearby ions which may or may not act as activator. In the following section different types of non-radiative pathways of the excited state are given.[7,87,90]

(i) Multiphonon emission: It is clear that the extent of quenching due to phonons depends on the energy gap between the emitting states and value of phonon energy. General observation is that if the energy difference is more than 5 times the phonon energy, then luminescence is the main de-excitation process than the multi-phonon quenching. This also explains the quenching of lanthanide ions excited state by organic molecules containing functional groups with high phonon energy. Hence, efforts for the development of new efficient luminescent materials based on Ln^{3+} ions are directed towards the search for low effective phonon energy host materials. The general order of phonon energy of hosts are fluorides < sulfides < oxides < phosphates.

(ii) Concentration quenching: In principle, an increase in the concentration of a luminescent center in a given material should be accompanied by an increase in the emitted light intensity, this being due to the corresponding increase in the absorption efficiency. However, such behavior only occurs up to a certain critical concentration of the luminescent centers. Above this concentration, the luminescence intensity starts to decrease. This process is known as concentration quenching of luminescence. In general, the origin of luminescence concentration quenching lies in very efficient energy transfer among the luminescent centers. Two mechanisms are generally invoked to explain the concentration quenching of luminescence:

(a) Due to very efficient energy transfer, the excitation energy can migrate about a large number of centers before being emitted. However, even for the purest crystals, always a certain concentration of defects or trace ions can act as acceptors, so that the excitation energy can finally be transferred to them. These centers can relax to their ground state by multi-phonon emission or by infrared emission. Thus, they act as an energy sink within the transfer chain and so the luminescence becomes quenched, as illustrated in Figure 2.7a. These kinds of centers are called killers or quenching traps.

(b) Concentration quenching can also take place without actual migration of the excitation energy among the luminescent centers. This occurs when the excitation energy is lost from the emitting state via a cross relaxation mechanism. This kind of relaxation mechanism occurs by resonant energy transfer between two identical adjacent centers, brought about by the particular energy-level structure of these centers (Figure 2.7b). As the concentration quenching results

from energy transfer processes, the decay time of the emitting ions is reduced along with the luminescence quantum yield. In general, this decay time reduction is much easier to measure than the reduction in the quantum efficiency. The critical concentration is that for which the lifetime starts to be reduced.

2.2.4 Luminescence decay

The mechanism of luminescence decay from an optical center is of critical importance. In particular we have to know if there are any processes internal to the center or external to it, which reduce the luminescence efficiency. It is possible to define two decay times, τ_R, the true radiative decay time which a transition would have in absence of all nonradiative processes, and τ, the actual observed decay time, which may be temperature dependent, as will usually occur when there are internal nonradiative channels, and which may also be specimen dependent, as when there is energy transfer to other impurities in the mineral. The quantum yield may be close to unity if the radiationless decay rate is much smaller than the radiative decay. The experimentally observed decay time of the luminescence is given by equation:

$$\tau = 1/(k_r + k_i)\tag{2.3}$$

where k_r, is the probability of radiative decay and k_i is the probability of nonradiative decay processes from the same state. If k_i is much large than k_r, not only will decay time be shortened appreciably, but the luminescence intensity will be very weak. Nonradiative deactivation within a center occurs by interaction with the vibrating lattice, which depends on temperature. Thus k_i is temperature dependent. A detailed overview of decay analysis (focused on experimental facts) has been provided in chapter 3.

2.2.5 Basics of energy transfer (ET) between rare earth ions

Energy transfer (ET) between rare earth ions finds wide range of applications in sensitizing solid state lasers, infrared quantum counters as well as infrared to visible convertors.[92] ET between RE ions also plays important role in quantum cutting (QC) processes.[93] In this section, the basic processes of ET are presented between rare earth ions. Aside from ET by movement of charge transports, there remain four basic mechanisms involved in ET processes between RE ions: (a) resonant radiative transfer through emission of sensitizer (S) and re-absorption by activator (A); (b) non-radiative transfer associated with resonance between absorber (sensitizer, S) and emitter (activator, A); (c) multiphonon-assisted ET; and (d) cross-relaxation (CR) between two identical ions.
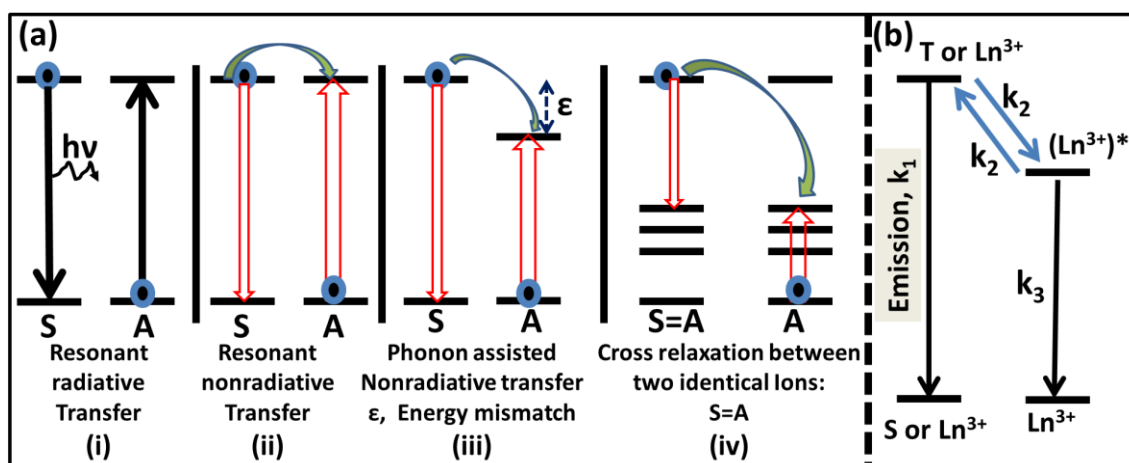
Figure 2.8: A schematic diagram for various basic energy transfer processes between two ions (a). Note that activator ion (A) receiving the energy from the sensitizer (S) is initially in its ground state. Cross-relaxation is the special case where S is identical to A. Doubled arrows symbolizes the Coulombic interaction: (i) radiative resonant transfer; (ii) resonant nonradiative transfer; (iii) phonon-assisted nonradiative transfer; (iv) cross relaxation as a special case of nonradiative transfer. (b) Back energy transfer mechanism among organic complex (singlet/triplet state) and lanthanides (Ln^{3+}).

A schematic diagram to illuminate the different ET processes between two ions is presented in Figure 2.8.[94] The efficiency of radiative transfer (Figure 2.8a) depends on how efficiently the activator fluorescence is excited by the sensitizer emission. It requires a significant spectral overlap of the emission region of sensitizer and the absorption region of activator and an appreciable intensity of the absorption of activator. If the radiative ET takes place predominantly, then the decay time of sensitizer fluorescence does not vary with the activator concentration. In contrast to the non-radiative ET (Figure 2.8b), the radiative ET accompanies the significant decrease in decay time of sensitizer fluorescence with the activator concentration. Because of the requirement for a considerable absorption capability of activator, the radiative ET can usually be neglected relative to non-radiative ET in most inorganic systems. Only in a few cases, the requirements for radiative ET are satisfied. ET may occur if the energy difference between the ground and excited states of donor (or sensitizer) is equal to that of acceptor (or activator) and there exists a suitable interaction between systems. Non-resonant ET can also take place by the assistance of phonon unless the difference between the ground and excited states of donor and acceptor is large. The ET rate between a donor and an acceptor is derived by Dexter as follows:[95]

29

$$W_{DA} = \frac{2\pi}{\hbar} [|\langle a'b|H_{DA}|ab'\rangle|]^2 \int g_D(E) \, g_A(E) dE \tag{2.4}$$

where D and A are a donor and an acceptor, respectively. The factors $g_D(E)$ and $g_A(E)$ represent the normalized shape of the donor emission and acceptor absorption spectra, respectively. The matrix elements in eq. (2.4) can be expressed as a function of the distance between donor and acceptor, so that the ET probability depends upon the distance between donor and acceptor. The distance varies with the interaction type. For exchange interaction, this distance is exponential, while it is of the type R^{-n} for the multipolar interactions.[93]

If two RE ions are with different excited states, as shown in Figure 2.8a(iii), the probability for ET should drop to zero, where the overlap integral $\int g_D(E) \, g_A(E) dE$ vanishes. However, it is experimentally found that ET can take place without phonon-broadened electronic overlap provided that overall energy conservation is maintained by production or annihilation of phonons with energies approaching $k\Theta_d$, where Θ_d is the Debye temperature of the host matrix. Then for small energy mismatch (100 cm^{-1}), ET assisted by one or two phonons can take place. However, in ET between RE ions, energy mismatches as high as several thousand reciprocal centimeters are encountered. This is much higher than the Debye cut off frequency found in normally encountered hosts, so that multi-phonon phenomena have to be considered. In their theoretical analysis of multi-phonon processes, Miyakawa and Dexter derived a comparative relaxation analogue of the multi-phonon gap dependence. According to their theory, the probability of phonon assisted transfer (PAT) is expressed by,[93]

$$W_{PAT}(\Delta E) = W_{PAT}(0) \exp(-\beta \Delta E) \tag{2.5}$$

where ΔE is the energy gap between the electronic levels of donor and acceptor ions and β is a parameter determined by the strength of electron–lattice coupling as well as by the nature of the phonon involved. The above equation has the same form as that for the energy gap dependence of the multi-phonon relaxation (MPR) rate, which is also given by the Miyakawa–Dexter theory as,[96]

$$W_{MPR}(\Delta E) = W_{MPR}(0) \exp(-\beta \Delta E) \tag{2.6}$$

It is further indicated that the parameter β is given by: $\beta = \alpha - \gamma$; which is further defined as $\alpha = \frac{1}{\hbar\omega} [\ln\{\frac{N}{G(n+1)}\} - 1]$ and $\gamma = \frac{1}{\hbar\omega} [\ln(1 + g_s/g_A)]$; where g is the electron–lattice coupling constant, suffixes S and A are sensitizer and activator ions, respectively, n is the number of phonons excited at the temperature of the system, $\hbar\omega$ is the phonon energy which contributes dominantly to these multiphonon processes and N is the number of phonons

emitted in the processes, namely, N = $\Delta E/\hbar\omega$. Non-resonant phonon-assisted ET between various trivalent RE ions in yttrium oxide crystals were thoroughly studied by Yamada and coworkers.[92] In their experiments the energy gap between the sensitizer and activator system varied in a wide range of energies upto 4000 cm^{-1}. The probability of phonon-assisted ET was observed to obtain the exponential dependence on energy gap predicted by the Miyakawa– Dexter theory. It was revealed that the phonons of about 400 cm^{-1} which produce the highest intensity in the vibronic side bands of yttrium oxide contribute dominantly to the phonon-assisted process. Cross relaxation terminology usually refers to all types of downconversion ET between identical ions. In such a case the same kind of ion is both a sensitizer and an activator. As shown in Figure 2.8a(iv), cross relaxation may give rise to the diffusion process already considered between sensitizers when the levels involved are identical or to self-quenching when they are different. In the first case there is no loss of energy, whereas in the second there is a loss or a change in the energy of the emitted photons.[85,93,94] Since the major focus of the present work is the downshift luminescence process, but a detailed energy transfer mechanism of upconversion process can be found in review by Auzel.[92]

Back energy transfer: One of the factors that can limit the energy transfer efficiency in sensitizer-activator lanthanide systems are the thermally activated energy back transfer from the lanthanide ion to other lanthanide ion (Figure 2.8 b). This process occurs when the energy difference between the excited state of one ion and the main receiving lanthanide state is less than 1500 cm^{-1}, and can be recognized if the lanthanide luminescence lifetimes are temperature dependent. This may quench the radiative transition of higher excited state energy ions. As a result the energy back-transfer rate is increased relative to the forward transfer, which leads to an increased deactivation of the lanthanide luminescent state. Rising of the temperature also increases the (endothermic) energy back-transfer rate relative to the forward transfer.

2.2.6 Judd-Ofelt theory

The Judd-Ofelt (J-O) theory was built independently by Judd and Ofelt in 1962.[96] The idea that an admixture of the opposite parity can relax the $4f^n$ dipole transitions is the basis of the Judd-Ofelt theory. Judd-Ofelt has been commonly used to predict the 4f-4f optical transition properties of the lanthanide ions within a crystal structure for branching ratios, especially for the spontaneous radiative emission rates and lifetimes. The radiative decay rate A_r of the electronic transition from an initial state $^{2S+1}L_J$ to final state $^{2S'+1}L'_{J'}$ can be calculated as per

31

the Judd-Ofelt theory using equation 2.7:

$$A_r = A_{ED} + A_{MD} = \frac{8\pi^2 e^2}{mc\lambda^2} f_{ED} + \frac{8\pi^2 e^2}{mc\lambda^2} f_{MD} \tag{2.7}$$

where A_{ED} and A_{MD} are the spontaneous transition probability for electric dipole transitions and magnetic dipole transitions, and are determined by the oscillator strength f_{ED} and f_{MD} separately, m is the mass of the electron, c is the speed of light in vacuum, λ is the average transition wavelength, e is electronic charge.

It should be mentioned that the strength of the magnetic dipole transition (f_{MD}) is only 10^{-6} of that of an electric dipole transition (f). Thus, f_{MD} is excluded from the discussion below. For the electric dipole transitions, f_{ED} is related to the dipole strength D by,

$$f_{ED} = \frac{8\pi^2 mc}{3he^2\lambda} D \tag{2.8}$$

And the dipole strength D is defined by,

$$D = \left| < \psi_i | \hat{O} | \psi_f > \right|^2 \tag{2.9}$$

where ψ_i and ψ_f are the initial and final wave functions and ô is the electric dipole operator. In order to compare the calculated dipole strength with the experimental one, the correction factor for the dielectric medium and the degeneracy of the initial levels have to be considered:

$$\chi_{ED} = \frac{n(n^2 + 2)^2}{9} \tag{2.10}$$

In summary, the spontaneous radiative decay rate A_r can be calculated using:

$$A_r = \frac{64\pi^4}{3h\lambda^3 (2J+1)} \chi_{ED} \left| < \psi_i | \hat{O} | \psi_f > \right|^2 \tag{2.11}$$

The radiative lifetime τ of an emitting state $^{2S'+1}L'_{J'}$ is related to the spontaneous emission probabilities of all transition from this state to the underlying states $^{2S+1}L_J$;

$$\tau = \frac{1}{\Sigma_J A_r (J'-J)} \tag{2.12}$$

2.3 Lanthanide Luminescence Characteristics

2.3.1 Selection of fluoride matrices

Due to the high optical quality of crystals and their wide transmission range, fluorides are well suited for the study of spectroscopic properties. They have brought a major contribution to the knowledge of luminescence processes. Fluorides possess specific characteristics mentioned below which influence luminescent properties.

(i) Wide band gap: The wide band gap makes possible emission from high energy levels. For

instance for Nd^{3+}, Er^{3+} and Tm^{3+} an allowed 5d→4f emission has been observed in various fluorides around 170 nm in the vacuum UV.[97,98] It allows the existence of the scintillating properties of BaF_2 crystals:[99] a wide forbidden band is necessary for avoiding re-absorption of the ultraviolet 2pF → 5pBa emission produced when holes are formed in the 5pBa core levels by x-rays or γ-rays (cross-luminescence).

(ii) Low nephelauxetic effect and moderate crystal field splitting: Because of its high electronegativity, fluorine is the element inducing the lowest nephelauxetic effect. The crystal field in fluorides is lower than in oxides but stronger than in other halides. In oxides the nephelauxetic effect and crystal field splitting strongly displace the position of levels formed from external orbitals. In fluorides the higher energy of the first 5d level of lanthanide ions allows the existence of line emissions from 4f levels usually located in the 5d bands. So in fluorides with high coordination number such as $BaLiF_3$, BaY_2F_5, $BaSiF_6$, Eu^{2+} substituted for barium shows an emission from the first excited $4f^7$ level ($6p_{7/2}$) instead of the usual 5d-4f band. Similarly in Pr^{3+} doped LaF_3, YF_3 and α-$NaYF_4$ materials, excitation in the 5d states of Pr^{3+} leads to population of the upper $4f^2$ level ($^1S_0$) at 46,700 cm^{-1} (214 nm). YF_3:Pr has the peculiarity to exhibit a visible luminescence from this level with a quantum efficiency exceeding 1: a two-photon emission occurs by a cascade process ($^1S_0$→$^1I_6$, followed after non-radiative decay to $^3P_0$ by $^3P_0$→^3H_J, ^3F_J).

(iii) Long lifetimes of excited levels of nd^N and $4f^N$ configurations: Electric dipole transitions are allowed if the initial and final states are made up of orbitals of opposite parity ($\Delta l = 1, 3$; l: orbital angular momentum quantum) and if the spin remains unchanged ($\Delta S = 0$). However parity forbidden transitions can occur as a result of mixing with states of opposite parity. Because of the high ionicity of the bonds formed by fluorine, the probability of the nd→nd transitions of transition element ions and 4f→4f transitions of lanthanide ions are lower than in oxides. This gives result in lower absorption properties and longer lifetimes of excited states ($r = 1/P_{rad}$, P_{rad}: sum of the radiative rates of transitions from the excited state). The lifetime of the $^4F_{3/2}$ Nd^{3+} state from which the 1.06 µm laser emission originates, amounts to 700 µs in LaF_3, compared to 260 µs in Y_2O_3, 220 µs in $LaCl_3$ and 60 µs in γ-La_2S_3. Long lifetimes are favorable for upconversion processes which are used for instance for infrared-to-visible conversion.

(iv) Low phonon energies: The thermal stability of luminescence depends on the energy of the emitting level, the change in equilibrium cation-anion distance induced by the electronic

transition and phonon energies. In fluorides phonon energies are lower than in oxides and higher than in other halides. Typically for most host lattices the highest phonon energies lie in the 400-500 cm^{-1} range (CaF$_2$: 465 cm^{-1}, LiYF$_4$: 490 cm^{-1}). The relatively low phonon energies in fluorides are favorable for a high stability. Quenching of the 5d→4f emission of Ce^{3+} in LiYF$_4$ (λ_{max} = 320 nm) starts only at about 900 K. The probability of nonradiative transitions between the 4f levels of lanthanide ions (multiphonon transitions) diminishes with increasing gap with the next lower level and decreasing phonon energies. Typically the probability for non-radiative decay becomes negligible when the energy gap exceeds 4-5 times the highest phonon energies of the host. Because of the lower phonon energy and smaller crystal field splitting of J levels, in fluorides for Ln^{3+} ions with closely spaced levels such as Ho^{3+} and Er^{3+} this condition is filled for various levels which in oxides decay essentially nonradiatively. This is the case of the green emitting level $^4S_{3/2}$ of erbium which is separated from the next lower level by 3000 cm^{-1}. The highest efficiencies for conversion of infrared radiation to visible (up-conversion) have been obtained with YF$_3$ and NaYF$_4$ doped with Yb^{3+} and Er^{3+}: the energy of two IR photons (λ = 970 nm) absorbed by ytterbium is transferred to an erbium ion which is excited into the $^2H_{11/2}$, $^4S_{3/2}$ states.

2.3.2 Selection of dopants

2.4.2.1 Division of rare earth: We consider the 4f–4f luminescence of RE^{3+}ions can be divided into four groups depending on their photonic features:

(i) Sc^{3+}(3d^0), Y^{3+}(4d^0), La^{3+}(4f^0) and Lu^{3+}(4f^{14}) ions exhibit no luminescence because they contain no optically active electrons.

(ii) Gd^{3+}(4f^7) ion presents a special case, since there is a large energy gap between the $^8S_{7/2}$ ground state and first $^6P_{7/2}$ excited state (~32000 cm^{-1}), that can emits in the ultraviolet region. In general, it cannot accept energy from the lower line excited states of the organic ligands *via* intramolecular ligand to metal energy transfer.

(iii) Sm^{3+}(4f^5), Eu^{3+}(4f^6), Tb^{3+}(4f^8) and Dy^{3+}(4f^9) ions have relatively large energy gaps between their excited and ground states. Complexes of these ions generally show strong luminescence because the excited energy levels of the ion lie just below that of the ligand triplet state.

(iv) Ce^{3+}(4f^1), Pr^{3+}(4f^2), Nd^{3+}(4f^3), Ho^{3+}(4f^{10}), Er^{3+}(4f^{11}), Tm^{3+}(4f^{12}) and Yb^{3+}(4f^{13}), the complexes of which usually show only weak 4f–4f luminescence, as a consequence of the

small energy gap between their emitting and lower energy levels; this increases the probability of nonradiative transitions through coupling with vibrational modes in the ligands.

The remarkable feature of RE^{3+} ions is their photoluminescence behavior; some of them show luminescence in the visible or near-infrared spectral regions under UV irradiation lamp. The color of the emitted light depends on the RE^{3+} ion. For instance, Eu^{3+} emits in red, Tb^{3+} green, Sm^{3+} orange and Tm^{3+} blue light. The Yb^{3+}, Nd^{3+}, and Er^{3+} are well known for their near-infrared luminescence. In addition, the Pr^{3+}, Sm^{3+}, Dy^{3+}, Ho^{3+} and Tm^{3+} ions also show transitions in the near-infrared region as well as Gd^{3+} emits in the UV region.

2.4.2.2 Specific selection of rare earth ions

(i) Ce^{3+}, a versatile candidate for phosphor materials: Ce^{3+} ions with the configuration $4f^1$ do not have any 4f-4f transitions. The transition observed is purely an interconfigurational 4f-5d type. The lifetime is in the range of 20 ns, much shorter than divalent europium (micro to millisecond). The 4f level splits into two levels due to spin-orbit coupling, and the 4f-5d band shape is different from the one of Eu^{2+}, as shown in Figure 2.9: two large bands appear in the case of Ce^{3+}.[100,101]
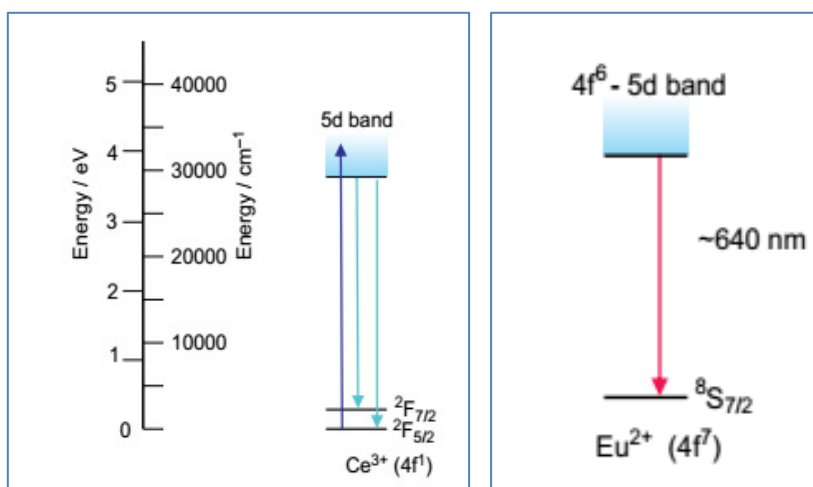
Figure 2.9: (Left panel)- The energy-level diagram for Ce^{3+}. The transitions shown correspond to the absorption of blue light of wavelength approximately 466 nm and emission at approximately 537 nm. (Right panel)- The energy-level diagram for Eu^{2+}.

(ii) Eu^{2+}, the blue emitter: Due to their strong dependence on the crystal field, Eu^{2+} ions give color emission from the UV to red spectral range. This aspect is illustrated in Figure 2.9 (right panel). In all cases, a band is observed due to the strong phonon coupling with the host matrix.

The intensity is high due to the strong permitted transition from the lowest 5d levels to fundamental 4f level (singlet $^8S_{7/2}$). Eu^{2+} ions generally absorb light strongly through the 4f-5d permitted transitions. As emission, excitation bands also strongly depend on crystal field. Absorption from vacuum ultraviolet (VUV) to yellow can be observed with Eu^{2+}based phosphors.

(iii) Tb^{3+} luminescence: The luminescence of Tb^{3+} is characterized by emission from the $^5D_4$ state resulting in green luminescence. The $^5D_4 \rightarrow ^7F_5$ emission band at 545 nm is hypersensitive, but is not as sensitive to the changes in the environment as the $^5D_0 \rightarrow ^7F_2$ emission of Eu^{3+}. The spectra show some structuring within the emission bands, but do not provide the basis for a reliable diagnostic probe of the symmetry of the complex, as is the case for the Eu^{3+} spectra. This is caused by the fact that the J-values of the levels involved in the transitions are high, resulting in splitting of the J-levels into many sublevels.

(iv) Eu^{3+}, best spectroscopic probe: The luminescence originating from the Eu^{3+} ion can be used as a probe for the coordination environment, and to obtain information concerning the symmetry of the first coordination sphere. The optical transitions of Eu^{3+} are a special case in the theory of induced electric dipole transitions. The induced electric dipole transitions have an additional selection rule if the initial level has J = 0, as is the case for Eu^{3+} ($^5D_0$): transitions to odd J are forbidden. This generally results in the following emission spectrum: $^5D_0 \rightarrow ^7F_0$ (~ 580 nm): extremely weak, induced electric dipole (J = 0 to J = 0 is forbidden). $^5D_0 \rightarrow ^7F_1$ (~ 590 nm): magnetic dipole emission. $^5D_0 \rightarrow ^7F_2$ (~ 613 nm): hypersensitive induced electric dipole emission, which is usually dominating.$^5D_0 \rightarrow ^7F_3$ (~ 650 nm): extremely weak, induced electric dipole emission.$^5D_0 \rightarrow ^7F_4$ (~700 nm): weak, induced electric dipole emission.[100]

(v) Yb^{3+} and Er^{3+}, a perfect couple for upconversion: According to the definition and requirement of upconverting materials,[90] a strong IR excitation source is used (solid-state laser diode). The IR light is absorbed by the Yb^{3+}ions (4f-4f transition). If the dopant concentration is high enough, the energy will be transferred to Er^{3+} ions by a cross relaxation process directly in the excited state. As the lifetime of the excited state in Er^{3+} ion is long enough, IR photons are also absorbed by the excited level and promote the ion to a higher energy emitting level. Finally, the system relaxes by emitting green and red light. All these processes have a low efficiency. To improve the efficiency, matrices with low energy phonons are preferred, such as fluoride materials.

(vi) Gd^{3+} ions, a bridge: Due to highest stable cross section, highest energy (> 32000 cm^{-1})

and no intermediate energy level, Gd^{3+} ions become very special candidate and used as support in energy transfer mechanism. Also, it has a highest neutron captor cross-section.

2.4 Electronic and Magnetic studies of Lanthanides

2.4.1 Magnetic Moment in Metals

A most amazing effect arises, when several electrons are put together and are treated as one many-particle system. [102,103] By virtue of their Fermionic character, an additional interaction called exchange is a consequence of the fact, that two identical particles cannot be distinguished in quantum physics. For a system of electrons, out of the set of solutions of Schrodinger`s equation, only the anti-symmetric ones (in terms of particle exchange) are allowed states. Those states can be expressed by the Slater determinant. The heuristic formulation of the Pauli's exclusion principle then follows easily from the general properties of the determinant. Exchange interaction between electrons, on the other hand, is a straightforward consequence of the exclusion principle. The probability density in space depends on the relative orientation of the spins, and different spatial wave functions correspond to different energy eigen values, due to coulomb repulsion. In the shape of Hund's rules, the Pauli principle governs the electronic and magnetic structure within the atom (see Table 2.2). In solid state, it is responsible for band structure and magnetic ordering. Magnetic properties of the rare earth metals differ, in many aspects, from those of other metals in the periodic table of elements.

2.4.2 Stable (+3) ionic core and paramagnetism of free rare earth ions

In the metallic state, rare earths use to occur as trivalent ion cores, each of the atoms contributing with three electrons to the metallic bonding. One of the inner 4f electrons is promoted to a band state and participates in the metallic bonding, together with the two 6s (and the 5d, if present) electrons. Exceptions are cerium (Ce^{4+}), europium (Eu^{2+}) and ytterbium (Yb^{2+}). They step out of the line, as a completely empty or a completely filled 4f shell is energetically most favorable (Hund's Rules). For magnetism,[104] the closed inner shells are of no importance, as their net magnetic moments cancel out. Valence electrons only account for a small fraction of magnetic susceptibility, although they are the essential mediators of exchange in the ordered states. Thus, the 4f electron shells are protagonists in terms of the magnetic moment. Their occupation with increasing atomic number within the period of the rare earth elements perfectly displays the validity of the Pauli principle and Hund's rules. The total

angular momentum of the 4f electrons can be determined according to Russel-Saunders coupling explained earlier in section 2.2.1.

Table 2.2 Rare earth ions, quantum numbers (L, S and J), and magnetic moment

$4f^n$	3+ Ion	L	S	J	g	$g\sqrt{J(J+1)}$	$\mu_{para}^{exp} = (\mu_B)$
0	La	0	0	0			
1	Ce	3	1/2	5/2	6/7	2.54	2.51
2	Pr	5	1	4	5/4	3.58	2.56
3	Nd	6	3/2	9/2	8/11	3.62	3.4
4	Pm	6	2	4	3/5	2.68	
5	Sm	5	5/2	5/2	2/7	0.85	1.74
6	Eu	3	3	0	-		
7	Gd	0	7/2	7/2	2	7.94	7.98
8	Tb	3	3	6	3/2	9.72	9.77
9	Dy	5	5/2	15/2	4/3	10.65	10.83
10	Ho	6	2	8	5/4	10.61	11.02
11	Er	6	3/2	15/2	6/5	9.85	9.9
12	Tm	5	1	6	7/6	7.56	7.61
13	Yb	3	1/2	7/2	8/7		
14	Lu	0	0	0			

Table 2.2 shows the respective quantum numbers for the rare earth metal series. The Landé factor in the case of Russel-Saunders coupling is;

$$g = \frac{3}{2} + \frac{S(S+1)-L(l+1)}{2J(J+1)} \tag{2.13}$$

The energetic distance of the lowest lying multiplet to the next higher one is large. At room temperature only the ground state is occupied. Thus the contribution of Van Vleck paramagnetism to the total paramagnetic moment, i.e., the admixture of the ground state multiplet with higher ones, is negligible (exceptions: samarium and europium).

Paramagnetism of the free rare earth ions: Let us consider the interaction between the "free" RE ion with an external magnetic field H. An interaction Hamiltonian of the ion with an external magnetic field (denoted the Zeeman Hamiltonian) is usually written as,

$$\widehat{H_z} = \mu_B\left(\hat{L} + 2\hat{S}\right)\vec{H} = \mu_B\left(\hat{J} + \hat{S}\right)\vec{H} \tag{2.14}$$

If the field H is directed along the z-axis of the coordinate system, the Hamiltonian can be written in the following form,

$$\widehat{H_z} = \mu_B \left(\widehat{J_z} + \widehat{S_z}\right)H \tag{2.15}$$

Based on the state wave functions, $|LSJM_J>$, that are distinct for each state, we can write the matrix elements for this Hamiltonian as,[105]

$$\langle LSJM_J|\widehat{H_J}|LSJM_J\rangle = g_J\mu_B M_J H; \tag{2.16}$$

where, $g_J = 1 + \frac{J(J+1)+S(S+1)-L(L+1)}{2J(J+1)}$ is the Lande' factor for the multiplet of the RE ion; and

$$\langle LS(J+1)M_J|\widehat{H_J}|LSJM_J\rangle = -g'_J\mu_B H\left[(J+1)^2 - M_J^2\right]^{1/2} \tag{2.17}$$

Where, $\quad g'_J = \left[\frac{(J+L+S+2)(L-J+S)(J+L-S+1)}{4(J+1)^2(2J+1)(2J+3)}\right]^{1/2}$

Let us consider now the behavior of an ensemble of free RE ions in an external magnetic field. In this case, the magnetic field tends to orient the magnetic moments $\overrightarrow{M}$ of the ions, whereas the thermal motion tends to disorient them. As $\overrightarrow{M}$ is spatially quantized, the energy of the interaction between the magnetic moment $\overrightarrow{M}$ of the RE ion with the magnetic field must also be quantized. This additional interaction energy W_H is given by the expression,

$$W_H = -g_J\mu_B M_J H \tag{2.18}$$

As the projection M_J of the angular momentum $\vec{J}$ takes on $(2J+1)$ values, with $-J \leq M_J \leq J$, W_H splits the (initially degenerate) energy level (multiplet) of the ion into sublevels located above and below the unperturbed energy level. These sublevels are equally spaced in the energy spectrum, with the energy separation between the magnetic (or Zeeman) sublevels equal to $\Delta_H = g_J\mu_B H$.

The magnetization of N ion ensembles, each having similar equidistant structure in the energy spectrum, is isotropic and can be represented as,[105,106]

$$I = I_0 B_J(x) \tag{2.19}$$

where $B_J(x)$ is the Brillouin function.

$$B_J(x) = \frac{2J+1}{2J}\coth\left(\frac{2J+1}{2J}x\right) - \frac{1}{2J}\coth(\frac{1}{2J}x) \tag{2.20}$$

And $x = \frac{g_J\mu_B JH}{kT}$; $I_0 = Ng_J\mu_B J$ is the saturation magnetization of N ion ensembles at T = 0 K (for example, for the RE ion Gd^{3+}, $I_0 = 7\ \mu_B$).

Keeping only the first terms in the series expansions of $\coth(x)$ terms in equation (2.20) allows

39

us to simplify equation (2.19) for high T and a low H (i.e., x << 1) as,

$$I = \frac{NJ\,(J+1)g_J^2\mu_B^2}{3kT}H \qquad\qquad (2.21)$$

where k is the Boltzmann constant. "I" corresponds to the expression for the paramagnetic susceptibility χ, which can be written as; $\qquad \chi = \frac{C}{T} \qquad\qquad (2.22)$

where C is the Curie constant, $C = \frac{NJ\,(J+1)g_J^2\mu_B^2}{3k} = \frac{NM_J^2}{3k}$ and M_J is the atomic magnetic momentum. Equation (2.22) is called the Curie law, and is used in this text for several compounds in which the RE ions can be considered as free ions. For the most part, rare earth compounds obey the Curie-Weiss law

$$\chi = \frac{C}{T-\Theta} \qquad\qquad (2.23)$$

Where, Θ is the Weiss constant, often called the paramagnetic or Curie temperature, which takes into account both magnetic and electric interactions between magnetic ions in paramagnets. In addition to the orientation-dependent paramagnetism, we also encounter Van Vleck paramagnetism,[105] caused by the mixing of wave functions of closely spaced electronic states of certain RE ions by an external magnetic field *H*. This situation is especially common in compounds containing the RE ions Eu^{3+} and Sm^{3+}.

2.5 Magnetism and iron oxide nanoparticles

2.5.1 Magnetism: Magnetism is a physical behavior of the magnetic materials which originates from electron orbital motion or intrinsic spin from the presence of unpaired electrons. Iron and certain iron containing materials can have unpaired electrons necessary to show magnetic behavior. Due to the large number of electrons in materials, magnetic solids are more easily viewed as a collection of magnetic dipole moments. Generally, the magnitude of a magnetic dipole moment increases with the number of unpaired electrons and is given by,

$$\mu = -g_s\mu_0\left(\frac{s}{\hbar}\right)...\text{(i)} \qquad \text{and} \qquad \mu|g| = -g_s\mu_0\sqrt{s\,(s+1)}...\text{ (ii)} \qquad (2.24)$$

where *s* is the total spin quantum number from unpaired electrons, g_s is the electron "g factor" predicted by quantum electrodynamics and μ_0 and $\hbar$ are the Bohr magneton and the Planck constant, respectively.

The potential energy U and force F on a magnetic dipole in a magnetic field are,

$$U = -\bar{\mu}.\bar{B} \qquad ... \quad \text{(iii)} \qquad\qquad \text{and} \quad F = -\nabla(-\bar{\mu}.\bar{B}) = \bar{\mu}.\bar{B}...\text{(iv)} \qquad (2.25)$$

Equation 2.25 (iv) implies that magnetic dipoles are attracted to regions where the density of

magnetic field lines is greater. In order to minimize energy according to eq. 2.25 (iii), dipoles close to each other will tend to line up in the same direction.[106]

2.5.2 Iron-oxide at nanoscale

2.5.2.1 Structure of iron oxide

Iron oxides are a group of minerals widespread in nature and readily synthesized in the laboratory. There are three major types of iron oxide: hematite (α-Fe_2O_3), maghemite (γ-Fe_2O_3) and magnetite (Fe_3O_4). The α-Fe_2O_3 is a blood red iron oxide found widespread in rocks and soils. Crystal structure of α-Fe_2O_3 is corundum (Al_2O_3), which can be described as rhombohedral or hexagonal with the space group D_{3d}^6. The γ-Fe_2O_3 occurs naturally in soils as a weathering product of Fe_3O_4, to which it is structurally related. Both γ-Fe_2O_3 and Fe_3O_4 exhibit a spinel crystal structure, wherein the oxygen atoms form a *fcc* closed packed orientation and the iron cations occupy the interstitial tetrahedral and octahedral sites. Bulk magnetite consists of both Fe^{2+} and Fe^{3+} atoms and exhibits ferrimagnetic behavior. Large ferrimagnetic crystals of Fe_3O_4 are comprised of multiple magnetic domains that exhibit magnetic moments and these are aligned within a domain, but between domains magnetic moments are oriented in random directions.

2.5.2.2 Magnetic characteristics of iron oxide nanoparticles and superparamagnetism

The most common and easy approach to understand the magnetism of material is dc magnetic measurement where we determine the equilibrium, quasi-static magnetic properties. Mainly following two properties are evaluated.

(i) Magnetization curves: In simple terms, when we measure the irreversible changes in the magnetization of a sample as a result of applying cyclic positive and negative values of magnetic fields, we obtain a hysteresis loop (Figure 2.10a). The path initially followed by the magnetization as the field is increased is given by the so-called virgin curve, since the sample comes from an unmagnetized or virgin state; then the magnetic structure of the material will be irreversibly altered precluding this virgin curve to be retraced during the experiment. Among the different parameters that can be extracted from this peculiar graph, there are three that provide us with the basic information needed to describe the magnetic behavior of a given material in a general fashion. The saturation magnetization (M_S) is essentially the limit value to which the curve tends within the high field region, and is reached when all the magnetic moments in the material are aligned with the external field. Upon field decreasing, the sample

does not recover its unmagnetized state, retaining a certain amount of magnetization at zero field: the remanence or remanent magnetization (M_r). The third parameter is also a consequence of the irreversible character of magnetic hysteresis; the coercivity or coercive field (H_c) represents the field we need to apply to completely demagnetize the sample. This parameter is very important, for example, in designing materials required to be in a non-magnetized state at a certain moment for a specific application or to be subjected to cycles of demagnetization and remagnetization, like magnetic recording media.
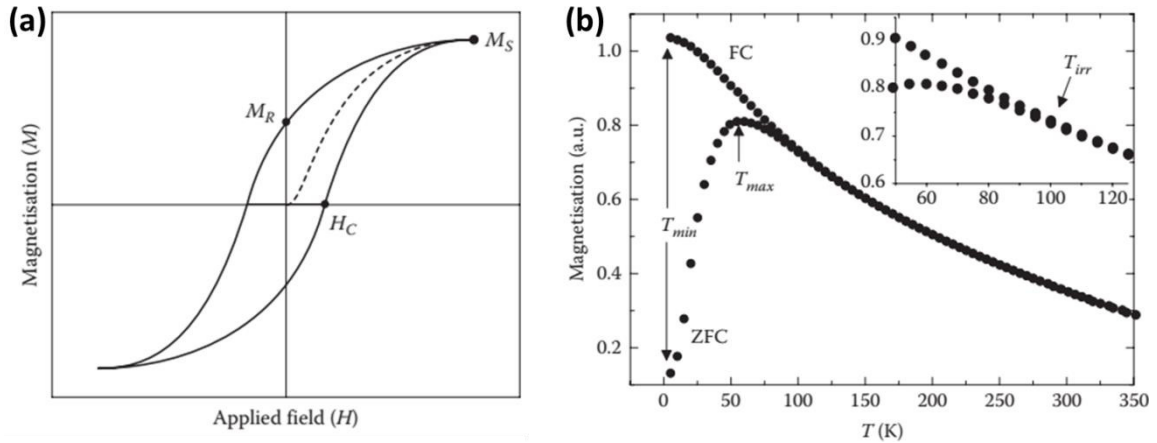
Figure 2.10: (a) Main parameters of interest in a generic hysteresis loop. Virgin curve is indicated by the dashed line; and (b) Generic ZFC and FC magnetization curves for a system of nanoparticles.

(ii) Zero field cooling and field cooling curves: In a typical zero-field cooling/field-cooling (ZFC/FC) curves (Figure 2.10b),[104] the sample is initially heated up to a temperature high enough as to ensure that it is in a superparamagnetic regime prior to the start of the measurement; in such a way, we ensure that the initial magnetic state is known. Then the sample is subsequently cooled without magnetic field down to lowest achievable temperature in the magnetometer (T_{min}). From that point, the magnetization (M_{ZFC}) is measured by heating up the sample under the action of an external field giving the ZFC branch of the experiment. The usual tendency of this curve is the same for most of the nanoparticle systems: at low temperatures, all the magnetic moments are blocked in random directions eventually leading to a (nearly) zero magnetization. In practice, this will depend on the magnetic history of the material and the initial conditions of the experiments. As the temperature is further increased from T_{min}, M_{ZFC} rises to a maximum at the temperature T_{max} and then decreases again. T_{max} is related but not necessarily equal to the average blocking temperature (T_B), for which both the

42

magnetic relaxation time of the nanoparticles and the measuring time coincide. The FC measurement is carried out in a similar fashion to the one already described for the ZFC experiments, although in this case the sample is cooled down under a constant magnetic field until T_{min} is reached again. Again as in the ZFC branch, the measurement, properly speaking, will begin when the system is heated up from T_{min} to room temperature or its surroundings. This process can be considered as reversible from a thermal point of view, since both the heating and cooling rates are the same. In ZFC/FC experiments, the irreversibility temperature (T_{irr}), where the condition $M_{FC} - M_{ZFC} \neq 0$ is met–is that for which the separation between the two branches takes place, and represents the blocking temperature of those particles that must overcome a higher energy barrier in their magnetic relaxation process.

(iii) Superparamagnetism: Magnetic property of iron oxide is significantly size-dependent and is intrinsically different from bulk magnetic particles. [107,108]In large sized magnetic particles, it is well known that there is a multi-domain structure, where regions of uniform magnetization are separated by domain walls. According to magnetic domain theory, the formation of a domain wall inside a magnetic particle is not thermodynamically favored when the size decreases to a certain level called critical diameter (D_s). Under this condition, magnetic moments are aligned in the same direction within only one magnetic domain. The superparamagnetism can be understood by considering the behavior of a well-isolated single-domain particle. The magnetic anisotropy energy per particle which is responsible for holding the magnetic moments along a certain direction can be expressed as follows: $K(\theta) = k_{eff} V \sin^2\theta$, where θ is the angle between the magnetization and the easy axis. The energy barrier $K_{eff}V$ separates the two energetically equivalent easy directions of magnetization. Under certain temperature, bulk materials have magnetic anisotropic energies much larger than the thermal energy $k_B T$ (Figure 2.11, green line). The thermal energy of the nanoparticles is sufficient to invert the magnetic spin direction. For single domain nanoparticles, the thermal energy $k_B T$ exceeds the energy barrier $K_{eff}V$ and the magnetization is easily flipped (Figure 2.11 (a), blue line). For $k_B T > K_{eff}V$, the system behaves like a paramagnet. This system is named a superparamagnet. Superparamagnetic system has no hysteresis and the data of different temperatures superimpose onto a universal curve of M versus H/T.

The relaxation time of the moment of a particle (τ) is given by the Nëel-Brown expression, $\tau = \tau_0 \exp(\frac{KV}{k_B T})$, where k_B is the Boltzmann's constant and $\tau_0 = 10^{-9}$ s. If the particle magnetic

moment reverse at times shorter than the experimental time scales, the system is in a superparamagnetic state, if not, it is in the so called blocked state. The temperature, which separates these two regimes, is called blocking temperature (T_B) and measured through ZFC/FC set of measurement as mentioned before. In ZFC curve, the peak temperature is normally related to the blocking temperature T_B.
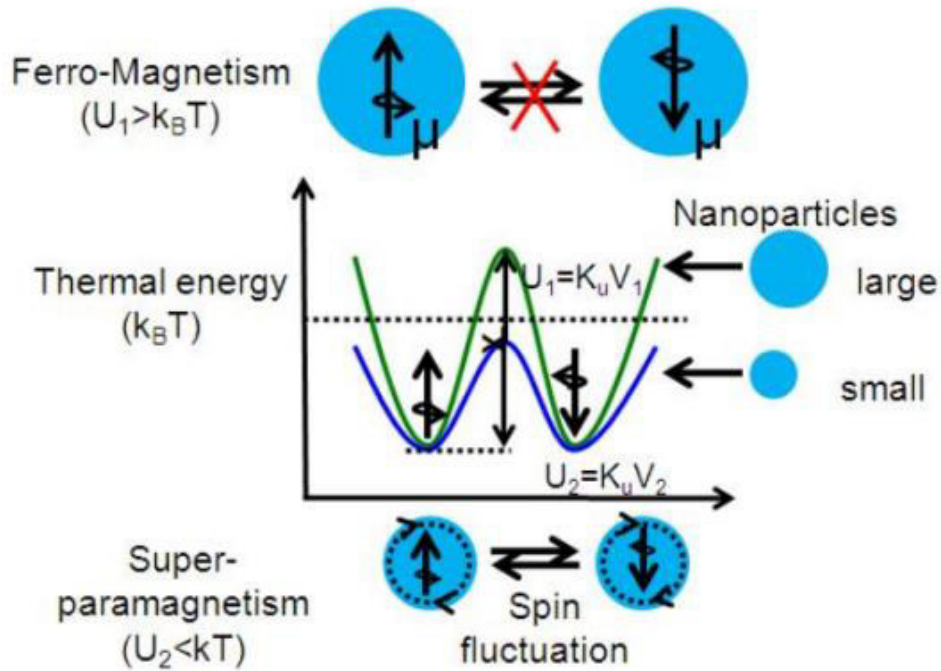
Figure 2.11 Nanoscale transitions of magnetic nanoparticles from ferromagnetism to superparamagnetism: energy diagram of magnetic nanoparticles with different magnetic spin alignment, showing ferromagnetism in a large particle (top) and superparamagnetism in a small nanoparticle (bottom).[104]

Further, as the particles size decreases, the fraction of atoms that lies near or on the surface increases, making the surface effect more and more important. It is estimated that in a 3 nm diameter nanoparticles 80% are surface atoms. Surface effects can also be observed not only in small particles, but also in larger particle systems, depending on the chemical composition of the nanoparticles and their crystalline state.[108] The magnetocrystalline anisotropy reflects the symmetry of the neighbors of each atom. The large perturbations to the crystal symmetry at surfaces should lead to magnetocrystalline anisotropy of different magnitude and symmetry for

surface sites. In fact, surface anisotropy has a crystal-field nature and it comes from the symmetry breaking at the boundaries of the particle. Accordingly, the surface effects result from the breaking of symmetry of the lattice at the surface of the particles, which leads to site-specific surface anisotropy of unidirectional character, from the broken exchange bonds.[107,108]

Many of the systems that exhibit surface effects could be described by a core–shell model. This model considers each particle as a nanosystem composed of internal magnetic ordered core (with ferro- or antiferromagnetic ordering) that can be described by the Stoner-Wohlfarth relaxation model; and a disordered shell of spins, that interact among them and the particle core. For small nanoparticles, the surface effect must be considered to estimate the size dependence of the effective anisotropy. Usually, it has been considered as an effective anisotropy term given approximately by the following phenomenological expression:[109]

$$K_{eff} = K_V + \frac{6}{\langle D \rangle} K_S \tag{2.26}$$

Eq. 2.26 has been extensively applied in to take into account the effect of the surface on nanostructured systems, with rather good success in most of the cases. In fact, surface effects can be important even when dealing with larger particles, and a careful analysis is necessary to properly separate the effects of structural disorder, interparticle interactions and surface contributions.

Chapter 3
Experimental Details

3.1 Materials and Synthesis

Bottom-up wet chemistry approach has been adopted throughout this work for the preparation of bifunctional nanomaterials. This procedure promotes the preparation of nanoparticles by assembling the individual atoms or molecules in the presence of stabilizer or protecting agents. They prevent the agglomeration of nanoparticles by either steric or electrostatic repulsion among nanoparticles, as agglomeration is a key issue in nano-regime. Several chemical methods have been reported for the synthesis of nanomaterials via bottom-up approach, such as co-precipitation, thermal decomposition, hydrothermal and microemulsion etc.[110–112] Wet chemical synthesis permits the manipulation of matter at the molecular level. Also, by understanding the relationship between how matter is assembled on an atomic and molecular level and the material's macroscopic properties, molecular synthetic chemistry can be designed to prepare novel starting components. Better control of particle size, shape, and size distribution can be achieved in particle synthesis.

3.1.1. Chemicals: The commercially available chemical reagents have been used for the syntheses of nanomaterials in present work and are summarized in Table 3.1. All rare earth chlorides ($RECl_3 \cdot 6H_2O$; RE^{3+} = La^{3+}, Ce^{3+}, Gd^{3+}, Eu^{3+}, Tb^{3+}, Yb^{3+}, Er^{3+}) were synthesized from their respective oxides by treatment with concentrated hydrochloric acid.

Table 3.1: Commercially available chemicals used for synthesis

Chemicals	Comapany
$FeCl_2 \cdot 4H_2O$, $FeCl_3 \cdot 6H_2O$, $NH_3 \cdot H_2O$, Ethanol, Methanol, Acetone, Octanol, Isopropanol, Hydrogenperoxide, NaOH	Synth
Oleic acid, 1-Octadecene, Oleylamine, Toluene, Diethyline Glycol (DEG), Cetyltrimethylammonium Bromide (CTAB), Tetraethyl orthosilicate (TEOS), NH_4F, HCl	Sigma-Aldrich
$Zn(O_2CCH_3)_2(H_2O)_2$, Thioacetamide	Alfa Aesar
Rare Earth Oxides (99.99%)	Rhodia

3.1.2 Synthesis

Before discussing the synthesis procedures and protocols to prepare different bifunctional nanomaterials, it is important to understand the general synthesis procedure for hydro (solvo) thermal, microemulsion, co-precipitation method, polyol and microwave assisted approach to provide a better idea about the synthesis protocol.

3.1.2.1 Hydro (solvo)thermal synthesis: The heterogeneous/homogeneous chemical reaction in water (hydro) or non-aqueous medium, under constant pressure and temperature is known as hydro (solvo) thermal synthesis (Figure 3.1 (a)). Usually reaction takes place in an autoclave (a sealed thick-walled steel vessel with teflon cup) at high temperature (150 to 220 ^{0}C) and high vapor pressure (> 1 bar), allowing subsequent growth of single crystals or crystallization of substances from the solution. By tuning the reaction conditions (temperature, pressure, pH, reaction timing etc.) and choosing a solvent (reaction medium) are the key issues to tune the size, shape, phase composition, crystallinity etc. of nanomaterials.[112] The solvent selection varies from water to different organics depending upon the need and specification of reaction, although the water is still remained the most widely used solvent. In hydro (solvo) thermal synthesis, some organic additives or surfactants with specific functional groups e.g., oleic acid (OA), polyethylenimine (PEI), cetyltrimethylammonium bromide (CTAB) etc., are generally added along with the reaction precursors to achieve simultaneous control over the crystalline phases, sizes, and morphologies as well as the surface functional groups for the resulting nanoparticles. The broad range of nanomaterials can be synthesized with the hydro (solvo) thermal method, using optimized reaction conditions such as temperature, pressure, and pH.

3.1.2.2 Micro-emulsion synthesis: A micro-emulsion is a thermodynamically stable dispersion of two immiscible liquids (e.g., water and oil) with the aid of surfactant. Small size droplets of one liquid are stabilized in the other liquid by an interfacial film of surfactant molecules. In the water-in-oil microemulsions, the aqueous phase forms droplets (~ 1-50 nm in diameter) in a continuous hydrocarbon phase. Consequently, this system can impose kinetic and thermodynamic constraints on particle formation, such as a nanoreactor. The surfactant-stabilized nanoreactor provides a confinement that limits particle nucleation and growth. By mixing two identical water-in-oil emulsions containing the desired reactants, the droplets will collide, coalesce and split and induce the formation of precipitates (Figure 3.1b). Adding a solvent like ethanol to the microemulsion, allows extraction of the precipitate by filtering or centrifuging the mixture. The main advantage of the reverse micelle or emulsion method is

better control over nanoparticles size by varying the nature and amount of surfactant and co-surfactant, the oil phase or the other reacting conditions. The working window for synthesis in micro-emulsions is usually quite narrow and the yield of nanoparticles is low compared to other methods, such as hydrothermal and co-precipitation methods. Furthermore, because large amounts of solvent are necessary to synthesize appreciable amounts of material, micro-emulsion is not a very efficient process and is rather difficult to scale-up.[113–115]
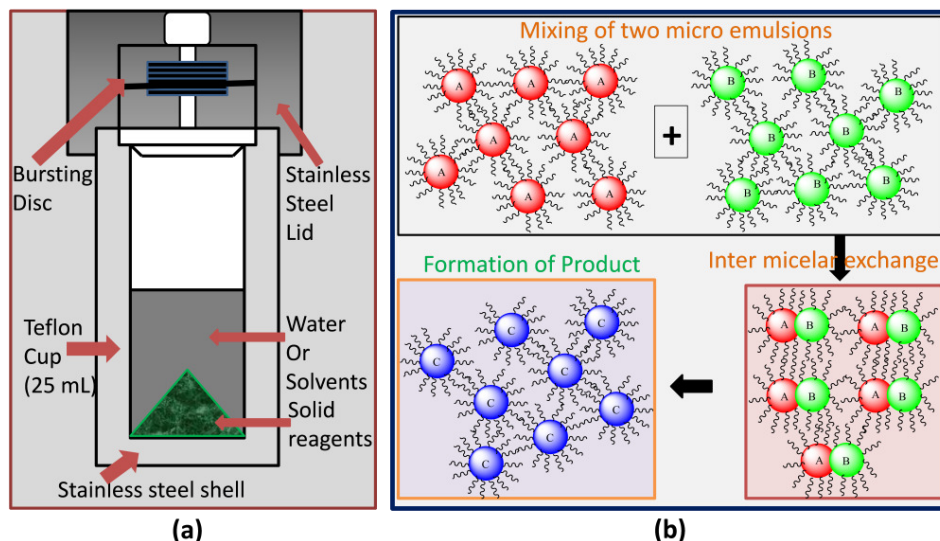
Figure 3.1: Schematic explanation of synthesis mechanism for the formation of nanoparticles by (a) hydrothermal and (b) micro-emulsion method.

3.1.2.3 Co-precipitation method: Generally, co-precipitation can be defined as "the simultaneous precipitation of more than one substances from homogeneous solution", which results in formation of crystal structure of single phase (e.g., Fe_3O_4). The co-precipitation is probably the convenient and most efficient chemical pathway to synthesize broad range of nanomaterials including magnetic nanoparticles[112,116–118] due to relatively mild reaction conditions, low cost of required equipment, simple protocols and short reaction time. Therefore, this method is not only a preferred route to synthesize magnetic iron-oxide nanoparticles, but it is also commonly used to prepare wide range of rare earth ions (RE^{3+}) doped luminescent nanomaterials, such as alkaline-earth tungstate's: $MWO_4:RE^{3+}$ (M^{2+}: Ca, Sr and Ba), rare earth fluorides: $NaYF_4:RE^{3+}$, $LaF_3:RE^{3+}$ etc. The great advantage of the co-precipitation method is to obtain a large amount of nanoparticles. However, polydisperse and wide particle size distribution are usually obtained with this method due to the kinetic factors

that control the growth of the crystal. Generally, two processes are involved in the growth and formation of the particles: a rapid nucleation (aggregation of nanometric building blocks such as pre-nucleation clusters), which occurs when the concentration of the species reaches critical supersaturation. The other one is the slow growth of the nuclei by diffusion of the solutes to the surface of the crystal. Therefore, to produce monodisperse nanoparticles, controlling of these processes are very important. In a supersaturated solution when the nuclei form at the same time, subsequent growth of these nuclei results in the formation of particles with a very narrow size distribution.

3.1.2.4 Polyol synthesis: Polyol synthesis (a special kind of sol-gel synthesis) is an excellent method for the synthesis of nanoparticles from metallic salts by using a poly-alcohol, which acts as amphiprotic solvents, as well as complexing, reducing and surfactant agents, depending on the studied system.[119,120] The poly-alcohols used in this process are ethylene glycol (EG), diethylene glycol (DEG), 1,2-propanediol, tetraethylene glycol and glycerol. Owing to the high boiling point and high dielectric constant of these solvents, they offer a wide range of reaction temperature.[119]

Hydrolysis and reduction reactions can be performed in these liquids, allowing the production of a wide variety of size and shape-controlled inorganic nanoparticles from nano to micro regime. In this method, the precursor compound is suspended in liquid polyol and heated to the boiling point of polyol at constant stirring. During this process, the precursor gets dissolved in the polyol leading to the formation of an intermediate followed by reduction to form nanoparticles.[120] This method allows preparation of water based nanoparticles by coating hydrophilic polyol over the nanoparticles, producing particles with higher crystallinity that leads to a better saturation magnetization and narrow particle size distribution compared to the traditional methods. This process is heralded for its self-seeding mechanism and lack of required "hard" or "soft" templating materials, making it an ideal process for industrial scale-up owing to the low cost of processing.

3.1.2.5 Microwave assisted method: In recent years, microwave assisted synthesis method is widely used over conventional heating methods to produce nanomaterials with higher yield. Specially designed microwave synthesis reactor allows an exquisite control on reaction temperature, stirring rate and pressure inside the reaction vessel, which is the unique feature of microwave apparatus over conventional heating principles. The heating effect in the microwave arises from the interaction of the electric field component of the microwave with

49

charged particles in the material through both conduction and polarization. The use of microwave heating as a non-classical energy source has been shown to dramatically reduce reaction times, increase product yields and enhance purity or material properties compared to conventionally processed experiments. In conventional methods, heating chemical reactions have been achieved using mantles, oil baths, hot plates, reflux set-up where the highest reaction temperature achievable is dictated by the boiling point of the solvent used. This traditional form of heating is rather slow and has low efficiency for transferring energy to a reaction mixture as it depends on convective currents and on the thermal conductivity of various compounds or materials that have to be penetrated. This often results in the temperature of the reaction vessel being higher than that of the reaction solution. In contrast, microwave irradiation produces efficient volumetric heating by raising the temperature uniformly throughout the whole liquid volume by direct coupling of microwave energy to the molecules that are present in the reaction mixture.

A single mode microwave reactor closed-vessel microwave synthesis, purchased from Synth-wave has been utilzed in this work. It consists of single reaction chamber (SRC) is a large, pressurized stainless steel reaction chamber into which all reactions mixture are placed and performed simultaneously. The pressurized chamber in SRC serves as the reaction vessel and the microwave cavity and the reaction vessel, enabling the intensity and distribution of the microwave energy to be optimized with the shape and size of the reaction vessel.[121] There are several benefits using SRC. Some of them are: (i) it can run multiple parameters or reactions simultaneously; (ii) since all reactions are in the same vessel, nearly any reaction type can be processed simultaneously; (iii) large range of temperature and pressure; (iv) several stoichiometry combinations and element changes can be modified for inorganic hydrothermal syntheses in a single run, saving weeks of research labor; and (v) control of every reaction is made possible by direct pressure and temperature control.

3.1.2.6 Silica coating over magnetic nanoparticles: Silica is the most common coating material for magnetic iron oxide nanoparticles. A silica shell not only prevent the aggregation, but can also prevents the direct contact of the magnetic core with additional agent linked to the surface of the silica thus prevent the unwanted interaction. For example, the direct attachment of the luminescence materials on the surface of magnetic nanoparticles reduces the luminescence properties. In order to deal with this issue, magnetic nanoparticles were first coated by silica and then luminescence materials were grafted on silica shell.[116,118,122] Silica

coated magnetic nanoparticles have advantages such as improved chemical stability, good biocompatibility, ease in surface modification and a controlled interparticle interaction through varying the thickness of the shell. In order to generate the magnetic silica sphere different processes have been explored such as Stöber process, sol-gel process and aerosol pyrolysis. Stöber process is a well-known process, in which silica is formed *in-situ* through the hydrolysis and condensation of a sol-gel precursor, such as tetraethyl orthosilicate (TEOS). The thickness of the silica shell can be tuned by varying the concentration of NH_4OH and the ratio of TEOS to H_2O. Furthermore, silica contains free silanol groups that can be subsequently reacted with additional appropriate functional groups through relevant salinization reactions.

3.1.3 Material preparation protocols used in thesis
3.1.3.1 Synthesis of $LaF_3:xCe^{3+},xGd^{3+},yEu^{3+}$ nanoparticles

The polyol synthesis procedure[27,115] based on mild temperature is described following with the protocol for 1 mol.% doped europium precursor and total 2.4381 mmol of RE precursors. Hexahydrate rare earth chlorides have been prepared by using rare earth oxides precursors given in the table 3.1, after treating them by HCl acid. These chloride precursors were used in synthesis. 2.170 mmol (0.767 g) of $LaCl_3 \cdot 6H_2O$, 0.1219 mmol (0.0453 g) of $GdCl_3 \cdot 6H_2O$, 0.1219 mmol (0.053 g) of $Ce(NO_3)_3 \cdot 6H_2O$ and 0.0243 mmol (0.00893 g) of $EuCl_3 \cdot 6H_2O$ were dissolved together in 25 mL of DEG in a three neck round-bottom flask under magnetic stirring and 10 mL oleic acid (OA) was added. The reaction mixture was heated at 115°C under stirring in a silicon oil bath until a clear solution was formed and the moisture in the solvent was allowed to evaporate by keeping the round bottomed flask open. Thereafter, the solution was cooled down near 70°C, by closing the round-bottom flask under continuous flow of N_2, and a solution of 7.29 mmol (0.28 g) of NH_4F in DEG (25 mL) was injected. The temperature of the reaction mixture was further increased to 215°C and vigorously stirred under the same temperature for 2 hours under refluxing conditions. Then, the obtained suspension was cooled to room temperature, diluted with 70 mL of methanol, stored overnight and the supernatant was decanted. The solid particles were further separated by centrifugation. To remove the residual DEG, the solid powders were dispersed in methanol three times, centrifuged, and dried in oven at 115°C to get 0.62 g powder product. Further, using the same procedure, nanomaterials with varying stoichiometric concentrations of Eu precursor (5, 10, and 15 mol.%) were prepared.

3.1.3.2 Synthesis of Fe_3O_4/ZnS@LaF_3:xCe^{3+},xGd^{3+},yTb^{3+} nanocomposites

The following three step synthesis procedure has been used to prepare green emitting magnetic optical nanocomposites. The final product is synthesized using co-precipitation method. The stepwise approach to synthesize Fe_3O_4/ZnS@LaF_3:xCe^{3+},xGd^{3+},yTb^{3+} nanocomposites is given in following steps:

Step1: Iron-oxide nanoparticles by hydrothermal method - The hydrothermal method was used to prepare oleic acid coated magnetic core nanoparticles, according to the previous report published elsewhere.[123,124] The 3.0 g (75 mmol) of NaOH and 30.0 g (95.4 mmol) of oleic acid (90 wt. %) were mixed in 40.0 mL of ethanol and stirred at room temperature till the formation of white viscous solution. Further, a dark brown color suspension was appeared immediately after pouring 60 mL aqueous solution of $FeCl_2 \cdot 4H_2O$ (0.1 mol L^{-1}) into the above solution. This solution was vigorously stirred for 30 minutes and brown precipitate was formed. Then, the reaction mixture was transferred into a 150 mL autoclave. It was sealed and heated at 180°C for 10 hours. After that the system was allowed to cool to room temperature. The product was collected at the bottom of the vessel and washed first with n-butanol and after by water and ethanol. The washed material was dried under reduced pressure in a vacuum desiccator.

Step 2: Fe_3O_4/ZnS nanoparticles - In a typical procedure,[125] 0.3 g (1.29 mmol) of as prepared Fe_3O_4 nanoparticles were dispersed in 100 mL n-propanol by adding the solution of 0.44 g (2.0 mmol) of $Zn(O_2CCH_3)_2(H_2O)_2$ in 60 mL n-propanol. This reaction mixture was stirred at room temperature for 24 hours. Thereafter, 60 mL solution of 0.2 g (2.66 mmol) thioacetamide in milli-Q water was added dropwise in above solution. Simultaneously, the resulting solution was heated at 65°C under vigorous stirring for 5 hours. Then, the reaction mixture was cooled to room temperature and gently stirred for overnight. The solid product was collected by magnetic separation method and washed with water and ethanol for five times to remove the excess ZnS nanoparticles. Finally, it was dried under reduced pressure for 12 hours and stored in a vacuum desiccator.

Step 3: Fe_3O_4/ZnS@LaF_3:xCe^{3+},xGd^{3+},yTb^{3+} nanocomposites - Fe_3O_4/ZnS@LaF_3:RE^{3+} nanomaterials were prepared by chitosan assisted co-precipitation method through general procedure[58] using specific amount of Fe_3O_4/ZnS nanoparticles as seeds and stoichiometric amounts of $LaCl_3 \cdot 6H_2O$, $Ce(NO_3)_3 \cdot 6H_2O$, $GdCl_3 \cdot 6H_2O$ and $TbCl_3 \cdot 6H_2O$ precursors[126]. In this procedure, 0.1 g of Fe_3O_4/ZnS nanoparticles was dispersed in 20 mL milli-Q water through

ultra-sonication. Further, 4 mL (0.1 mol L^{-1}) aqueous solution of CTAB was added in above mixture and stirred for 1 hour to obtain $Fe_3O_4/ZnS@CTAB$ dispersion (solution A). Thereafter, 0.4876 g (1.3792 mmol) $LaCl_3\cdot6H_2O$, 0.0302 g (0.0812 mmol) $GdCl_3\cdot6H_2O$, 0.0352 g (0.0812 mmol) $Ce(NO_3)_3\cdot6H_2O$ and 0.0303 g (0.0812 mmol) $TbCl_3\cdot6H_2O$ were dissolved together in 25 mL solution of 0.2 g of chitosan in acetic acid/milli-Q water (5 v/v%) in a three neck round-bottom flask under magnetic stirring. The pH of the solution was adjusted to 7 by drop-wise addition of $NH_3\cdot H_2O$ (28 v/v%) (solution B). The 20 mL aqueous dispersion of $Fe_3O_4/ZnS@CTAB$ (solution A) was directly added to solution B and stirred under continuous N_2 atmosphere. The 15 mL aqueous NH_4F solution (0.1802 g; 4.86 mmol) was injected slowly to the reaction mixture. Finally, it was heated at refluxing condition for 3 hours under continuous N_2 flow. The brown color suspension was cooled to room temperature and the solid sample was separated from the aqueous suspension using magnetic separation. The collected solid material was washed with milli-Q water and methanol. The brown $Fe_3O_4/ZnS@LaF_3:xCe^{3+},xGd^{3+},yTb^{3+}$ (x = y = 5 mol.%) was dried in a vacuum desiccator and heated in oven at 80^oC. The other two bifunctional nanomaterials with concentration at x = 5; y = 10 and 15 mol.% were also prepared by same procedure by changing stoichiometric values. The products were found to be water dispersible.

3.1.3.3. Synthesis of $NaGdF_4:RE^{3+}$ and iron-oxide/SiO_2/$NaGdF_4:RE^{3+}$ nanomaterials

The multistep synthesis procedure has been used to prepare up/down converting nanocomposites. The final product was synthesized using microwave assisted thermolysis synthesis protocol (Figure 3.2). The stepwise protocols are given below:

Step 1: $NaGdF_4:RE^{3+}$ - In the modified synthesis,[127,128] 0.90 mmol $GdCl_3\cdot6H_2O$, 0.05 mmol $CeCl_3\cdot7H_2O$, 0.05 mmol $EuCl_3\cdot6H_2O$ was added into a solution containing 16 mL OA and 8 mL of 1-ODE, and the mixture was left under stirring at ambient temperature for 30 minutes. This forms solution (A). Separately, 2.5 mmol NaOH were added to 15 mL methanol, followed by addition of 8 mL OA. The resultant solution was stirred for 20 minutes at room temperature. This forms solution (B). The two solutions (A + B) were finally mixed very quickly together, and stirred for additional 10 minutes. A third separate solution (C) obtained by mixing 4 mmol NH_4F in 15 mL methanol was added to the above solution (A+B). This mixture (A+B+C) was transferred into a reaction vessel in a Synth's microwave reactor, with an output power of 1000 W. The working cycle of the microwave reactor was set as (i) 3 minutes at 50^0C from room

temperature, (ii) 20 ^{0}C per minute rapid heating until 200 ^{0}C from 50°C, and (iii) 60 minutes at 200 ^{0}C. The system was then allowed to cool down to room temperature, and the final material (NaGdF$_4$:RE^{3+} (RE^{3+} = Ce^{3+}, Eu^{3+})) was washed sequentially with methanol and ethanol, and then dried in an oven at 50°C for 8 hours. Other samples (with dopants 20 mol.% Yb, 2 mol.% Er) were prepared similarly.

Step 2: Iron-oxide nanoparticles - A chemical co-precipitation method was used to prepare iron-oxide (Fe$_3$O$_4$/γFe$_2$O$_3$), according to the procedure reported elsewhere.[23,47] Solutions of FeCl$_2$·4H$_2$O (1mol L^{-1}, 50 mL) and FeCl$_3$·6H$_2$O (2mol L^{-1}, 50 mL) in milli-Q water were prepared separately and transferred together into a 250 mL three neck flask under N$_2$gas flow and stirring. The reaction mixture was then heated at 50^{0}C and NH$_4$OH was added drop-wise until pH reached 11, and the solution turned black, indicating the formation of iron oxide nanoparticles. The reaction mixture was heated at 80^{0}C for 1 hour. The black solid precipitate was isolated from the reaction mixture by magnetic separation, washed three times with milli-Q water, dried in vacuum, and stored in a desiccator.

Step 3: Iron-oxide/SiO$_2$ nanoparticles - Iron-oxide/SiO$_2$ nanoparticles were prepared using a modified microemulsion method.[45,129] In a typical procedure, 50 mg of above prepared iron-oxide nanoparticles were dispersed in 60 mL of n-hexane by sonication, and then were added 15 mL of octanol as surfactant. The resulting solution was stirred at room temperature for 10 minutes. Thereafter, 1.3 ml of 28 wt% NH$_4$OH and 1 mL H$_2$O was added to induce formation of a reverse microemulsion solution. After stirring for 30 minutes, 0.15 mL TEOS was added to the solution and stirred at 500 rpm at room temperature for 24 hours. The final product was isolated by centrifugation, washed with ethanol and water and dried under vacuum and stored in a desiccator for further use.

Step 4: Iron-oxide/SiO$_2$/NaGdF$_4$:RE^{3+} - Iron-oxide/SiO$_2$/NaGdF$_4$:RE^{3+} (RE^{3+} = Ce^{3+}, Eu^{3+} and Yb^{3+}, Er^{3+}) nanoparticles were synthesized by using 20 mg of iron-oxide/SiO$_2$ nanoseeds dissolved in 7 mL of 1-ODE and the shell solution of NaGdF$_4$:RE^{3+} (RE = Ce^{3+}, Eu^{3+}) was prepared as described above in step 1. Solution A and solution B were prepared and mixed. Further, the solution of iron-oxide/SiO$_2$ seed was poured in above mixture of (A+B) solution slowly and stirred for 5 minutes at room temperature. Further, a separate solution C as described above was prepared and mixed in solution containing iron-oxide/silica and solution (A+B).

The mixture was transferred into the reaction vessel following exactly the same procedure as described for the preparation of $NaGdF_4:RE^{3+}$. The same procedure was applied to prepare other samples with dopants 20 mol.% Yb, 2 mol.% Er.
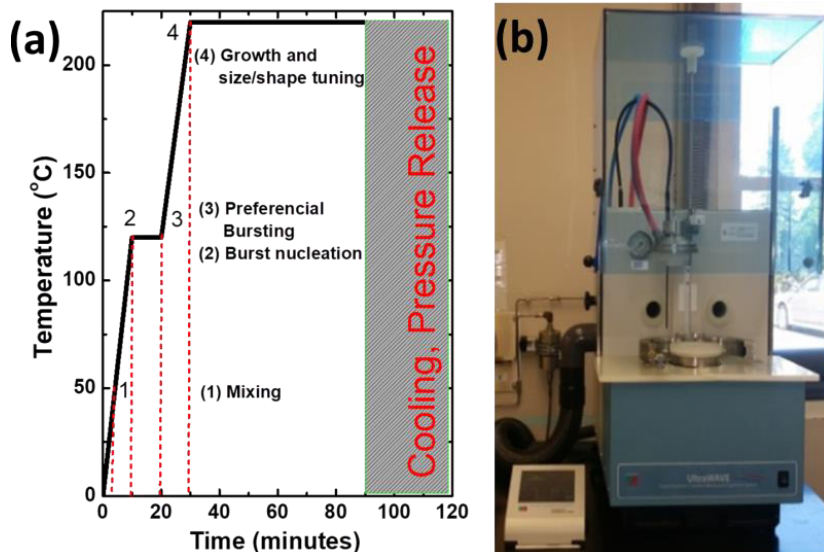
Figure 3.2: (a) Shows temperature and time scheme adopted during synthesis; (b) displays the commercial Microwave instrument used for the synthesis available at Federal University of Maranhão.

3.2 Instrumental techniques

The characterization of nanoparticles is necessary for establishing understanding and control of synthesis and their applications. The synthesized nanoparticles have been thoroughly characterized for their structural, optical and magnetic properties using different techniques and are given in the next sections.

3.2.1 Powder X-Ray Diffraction (PXRD)

X-ray diffraction (XRD) is a very important characterization tool to identify the crystallographic phase formation of any material.[130] Since all the nanomaterials synthesized in the present thesis are in powder form, therefore a standard powder x-ray diffractogram has been utilized to determine the size, phase composition, crystal structure and crystallinity. XRD exploits the wave nature of electromagnetic radiation and as x-rays interact with a sample, they interfere with each other (Figure 3.3b). Most of the x-rays undergo destructive interference; however, the x-rays that interact with the sample at a specific angle θ_B undergo constructive interference, which results in a signal for that particular angle. The condition for the

constructive interference between the scattered x-ray is given by Bragg's condition[131].
Constructive interference of the x-ray from successive planes occurs when the path difference
is an integral multiple of wavelength:

$$n\lambda = 2d_{hkl}\ sin\ \theta_B; \tag{3.1}$$

 where 'd_{hkl}' is the interplaner spacing and θ_B is the angle of incidence also known as the
Bragg`s angle. The observed peaks correspond to basic Bragg's reflection belonging to a
particular family of planes. For the XRD taken in the θ-2θ scan mode, a monochromatic beam
of x-ray is incident on the material at an angle θ and the detector motion is coupled with the x-
ray source in such a way that it always makes an angle 2θ with the incident direction of the x-
ray beam. The resultant pattern can be plotted between the intensity and the 2θ.
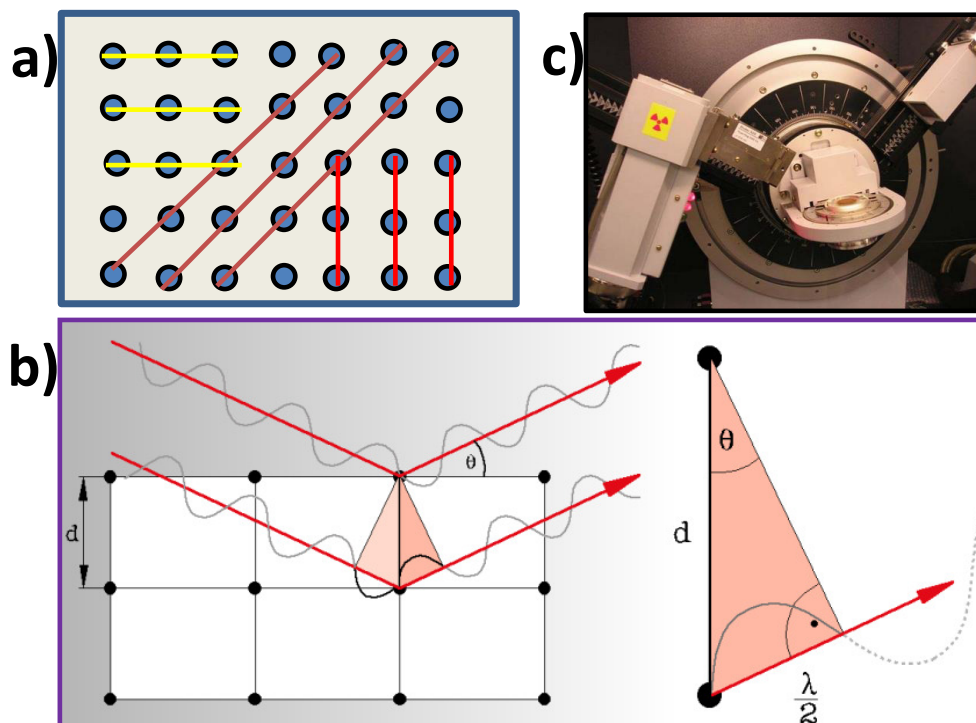
Figure 3.3: Schematic showing (a) lattice fringes, (b) diffraction of X-ray from scattering centers
(atoms) in the crystal, and (c) diagram of goniometer of Brucker's D8 Advance diffractometer.

XRD investigations also provide additional valuable information on nanocrystals such as size,
lattice strain, and morphology. Appreciable line broadening in diffraction peaks typically
indicates a decrease in the size of the particles. Scherrer's equation is usually applied to

estimate the average size of nanocrystals when the strain in crystallites is not taken into consideration.

$$D = \frac{k\lambda}{\beta \cos\theta}$$ (3.2)

Here, k is the crystallite shape factor (0.89 for spherical nanoparticles), λ is the wavelength of the incident x-ray, β is the corrected half width of the diffraction peak and θ is the diffraction angle. Note that the equation is only applicable to nanocrystals with a size less than 100 nm as the size-dependent line broadening is negligible when the size is over this threshold. Williamson–Hall theorem is required for the estimation of effective particle size and lattice strain when the lattice strain contributes to the effects of diffraction line broadening as well through relation:

$$\frac{\beta \cos\theta}{\lambda} = \frac{1}{D} + \frac{\eta \sin\theta}{\lambda}$$ (3.3)

where D and η are the effective particle size and strain, respectively. The strain and effective size from nanocrystals are deduced from the slope and the intercept of a plot of $\frac{\beta \cos\theta}{\lambda}$ against $\frac{\sin\theta}{\lambda}$. It should be noted that a number of factors, including doping, thermal annealing and shell-coating, can induce lattice strain in the nanosized crystals.

Usually, Rietveld refinement technique is used for quantitative phase analysis of crystalline nanomaterials by refining neutron or X-ray diffraction patterns.[132,133] A theoretical pattern is computed based on the crystal structure parameters of all phases in the material, parameters used to model peak shape for each phase, and instrument parameters (specimen height offset, for example). This theoretical pattern is refined until it best fits the measured pattern, using a least squares approach. The technique may be used to refine the crystal structure parameters in a single phase or simple mixture or to determine the mass fraction of each phase in a complex mixture. The Rietveld refinement requires detailed crystal structure information for all phases in the sample. The parameters include the space group and unit cell parameters and the position in the unit cell of all atoms in the phase. If any phase is not included in the refinement, the mass fraction results are biased even for the phases included. For this reason, use of the technique must be preceded by careful qualitative phase analysis. There are several programs available for Rietveld refinement such as Generalized Structure Analysis System (GSAS) and TOPAS.[132,133]Quantitative Phase Analysis (sometimes called also Standardless Phase Analysis,

Multiphase Rietveld Phase Quantification, Rietveld Quantitative Analysis or Rietveld XRD Quantification) relies on the simple relationship:

$$W_p = S_p (ZMV)_p / \sum_{i=1}^{n} S_i (ZMV)_i \qquad (3.4)$$

where W is the relative weight fraction of phase p in a mixture of n phases, and S, Z, M, and V are, respectively, the Rietveld scale factor, the number of formula units per cell, the mass of the formula unit (in atomic mass units) and the unit cell volume (in Å^3).

The analysis of the XRD pattern is of vital importance, as the lattice volume of a material is very sensitive to nanoparticle sizes, depending on which the character of a material changes drastically. For example, it has been reported that size reduction of nanoparticles leads to the broadening of Bragg peaks; in other instances, size reduction can lead to an entirely new crystallographic phase in the nanoform, which is completely different from their bulk counterpart. Anisotropic line broadening observed in the XRD characterization of nanomaterials can provide useful information on the morphology of the nanocrystals.

Instrument - In the present work, two different PXRD instruments were used with Cu $K_{\alpha 1}$ radiation ($\lambda = 1.5405$ Å) operating in the range 10^0- 90^0 with a step size of $\Delta 2\theta = 0.02°$. Bruker's D8 Advance diffractometer available in Federal University of Maranhão has been used to evaluate the crystal structure of $Fe_3O_4/ZnS@LaF_3:xCe^{3+},xGd^{3+},yTb^{3+}$ (x = 5; y = 5, 10 and 15 mol.%), $NaGdF_4:RE^{3+}$ and $Fe_3O_4@SiO_2@NaGdF_4:RE^{3+}$, (RE = Ce, Eu and Yb, Er), whereas XRD data for triply doped $LaF_3:RE^{3+}$ were recorded on a Rigaku Miniflex II diffractometer in University of São Paulo, São Paulo. Further, the XRD patterns were analyzed by Rietveld refinement utilizing General Structure Analysis System (GSAS) and TOPAS software.[132,133]

3.2.2 Transmission Electron Microscopy (TEM)

TEM is a sole instrument capable of imaging inside of a specimen directly and at the atomic level.[131] Recent advance TEM has the capability of analyzing the samples elemental distribution at the nanometer level.[131] By using TEM, we can have following general information: (i) average size of the particles, (ii) element contrast between core-shell structure using High Resolution TEM, scanning TEM (STEM) and High Angle Annular Dark Field (HAADF) and (iii) elemental variance using energy dispersive spectroscopy (EDS) and electron energy loss spectroscopy (EELS).

3.2.2.1 TEM and STEM: TEM exploits three different interactions of electron beam specimen i.e., unscattered electrons (transmitted beam), elastically scattered electrons (diffracted beam) and inelastically scattered electrons. The intensity of transmitted electrons is inversely proportional to the specimen thickness. Areas of the specimen that are thicker will have fewer transmitted electrons and so will appear darker; conversely the thinner areas will appear lighter due to more transmission. The scattered part of the incident beam is transmitted through the remaining portions of the specimen. All incident electrons have the same energy and enter the specimen normal to its surface. All incidents that are scattered by the same atomic spacing will be scattered by the same angle. These scattered electrons can be collimated using magnetic lenses to form a pattern of spots, each spot corresponding to a specific atomic spacing (or plane). This pattern can then yield information about the orientation, atomic arrangements and crystal phases. Also, incident electrons can interact with the specimen inelastically and loose its energy during the interaction. These electrons are then transmitted through the rest of the specimen.

Typically, a TEM consists of three stages of lensing (Figure 3.4). The stages are the condenser lenses, the objective lenses, and the projector lenses. The condenser lenses are responsible for primary beam formation, whilst the objective lenses focus the beam that comes through the sample itself (in STEM mode, there are also objective lenses above the sample to make the incident electron beam convergent). The projector lenses are used to expand the beam onto the phosphor screen or other imaging device, such as film. The magnification of the TEM is due to the ratio of the distances between the specimen and the objective lens' image plane. Additional quad or hexapole lenses allow for the correction of asymmetrical beam distortions, known as astigmatism. It is noted that TEM optical configurations differ significantly with implementation, with manufacturers using custom lens configurations, such as in spherical aberration corrected instruments or TEMs utilizing energy filtering to correct electron chromatic aberration. In a TEM, an electron gun, located at the top of it, emits the electrons by thermionic or field emission. These electrons travel through vacuum in the column of the microscope where electromagnetic lenses focus them into a very thin beam. The electron beam then travels through the specimen under study. At the bottom of the microscope, the image is formed on the image plane of objective lens from the unscattered electrons. Then, projector lenses form the images on a screen or charge coupled device (CCD) camera.

TEM can be used as a direct tool to reveal the morphology, and precise growth habits by screening morphology changes imaging. The diffraction contrast (brightness) from crystalline interfaces due to incident electron scattering difference often contains rows of one-dimensional bands or fringes, which can be used to examine the formation of nanoheterostructures. Under a high resolution imaging mode, the crystallographic structures of nanocrystals, including crystalline defects and crystallite domains, can be inspected at an atomic level. Also, TEM provides imaging capability of selected area electron diffraction (SAED) on individual nanocrystals by taking advantage of electromagnetic lens and physical apertures. Phase-specific patterns of dots in single crystal structures are observed in the SAED measurement of nanomaterials. Moreover, combining the results of HRTEM with SAED data performed on single nanocrystals can provide valuable information
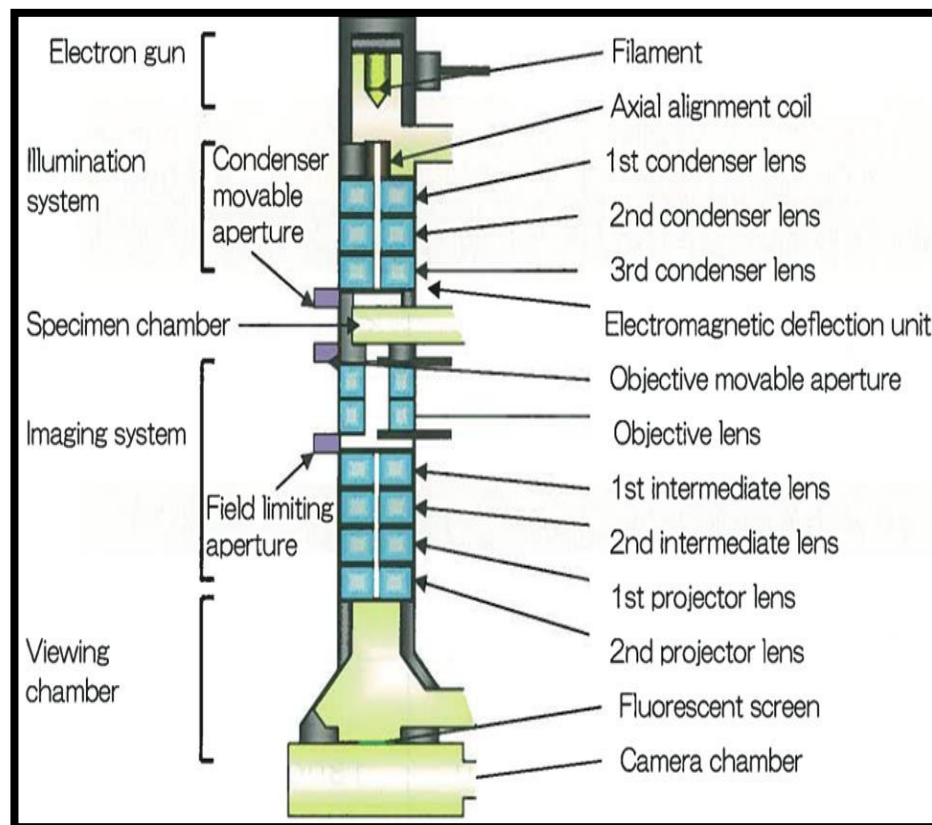
Figure 3.4: Cross sectional view of column of TEM.

STEM: Apart from high imaging resolution, STEM in a high angle annular dark field (HAADF) imaging mode is terrific techniques that can be used to distinguish the interfacial

region of a core-shell nanocomposite. This capability stems from the fact that heavy atoms tend to generate high angle scattered electrons and the contrast difference obtained by HAADF-TEM imaging of different components in a nanocrystal is proportional to the square of Z (Z = atomic number). Different layers in a variety of core–shell or multilayer core–shell or composite nanoparticles have been characterized by the HAADF-STEM imaging technique. Despite a number of excellent capabilities, the STEM imaging technique has inherent limitations and problems, some of which are associated with the low thermal stability of nanomaterials such as lanthanide doped nanocrystals in response to electron beam irradiation. Notably, the scanning mode of STEM is attractive in analyzing the spatial distribution of elements in a nanocrystal and is given in the next section.

3.2.2.2 Energy dispersive x-ray spectroscopy (EDS): EDS is an x-ray micro analytical technique that can provide information on the elemental composition of a sample upon bombarding of high energy electron beam by atomic and weight percent[131] which is a separate merit to TEM imaging. When the sample is bombarded by the electron beam of the STEM, electrons are ejected from the atoms on the specimen surface. A resulting electron vacancy is filled by an electron from a higher shell and an x-ray is emitted to balance the energy difference between the two electrons. The x-ray detector measures the number of emitted x-rays versus their energy. The energy of the x-ray is characteristic of the element from which the x-ray was emitted. A spectrum of the energy versus relative counts of the detected x-ray is obtained and evaluated for qualitative and quantitative determinations of the elements present. The energies of the characteristic x-rays allow the elements making up the nanomaterials sample to be identified, while the intensities of the x-ray peaks allow the quantification of dopant concentrations. EDS in line scanning mode is particularly useful in the characterization of core–shell nanoparticles.

Instrument - TEM and EDS measurements were performed using the TEM-FEG (JEM 2100F) at Laboratory of electronic microscopy (LME), LNNano-CNPEM, Brazil, for all the nanomaterials. The samples $LaF_3:xCe^{3+},xGd^{3+},yEu^{3+}$ (x = 5; y = 1, 5, 10 and 15 mol%) were dissolved in isopropyl alcohol (IPA). For $Fe_3O_4/ZnS@LaF_3:RE^{3+}$; the samples were prepared by dissolving dry powders of Fe_3O_4 in toluene, Fe_3O_4/ZnS in IPA and $Fe_3O_4/ZnS@LaF_3:RE^{3+}$ in distilled water. $NaGdF_4:RE^{3+}$ and iron-oxide/SiO_2/$NaGdF_4:RE^{3+}$ (RE^{3+} = Ce^{3+} and Eu^{3+}) samples were prepared in IPA. Further, the samples were followed by ultrasonification for 15 minutes. The dispersion of each sample was deposited drop wise on the 400 mesh copper grids

of with ultrathin carbon film with Lacey Carbon and dried in open atmosphere. The images were acquired with the sample on a single-tilt sample holder and a Gatan ES-500W TV camera. The EDS measurement of $LaF_3:xCe^{3+},xGd^{3+},yEu^{3+}$ was performed using TEM-FEG (JEM 2100F) in STEM mode. The EDS analysis of $Fe_3O_4/ZnS@LaF_3:RE^{3+}$ and $NaGdF_4:RE^{3+}$ and iron-oxide/$SiO_2/NaGdF_4:RE^{3+}$ ($RE^{3+} = Ce^{3+}$ and Eu^{3+}) samples were done at newly installed state of art machine Titan at LNNano, CNPEM, Brazil.

3.2.3 Fourier Transforms Infrared (FTIR) Spectroscopy

FTIR is a technique which is used to determine the chemical functional groups in the sample. In IR spectroscopy, IR radiation is passed through a sample. Some of the infrared radiation is absorbed by the sample and some of it is passed through (transmitted). The resulting spectrum represents the molecular absorption and transmission creating a molecular fingerprint of the sample. Like a fingerprint no two unique molecular structures produce the same infrared spectrum. This makes infrared spectroscopy useful for several types of analyses. The block diagram of FTIR principle is summarized in Figure 3.5.
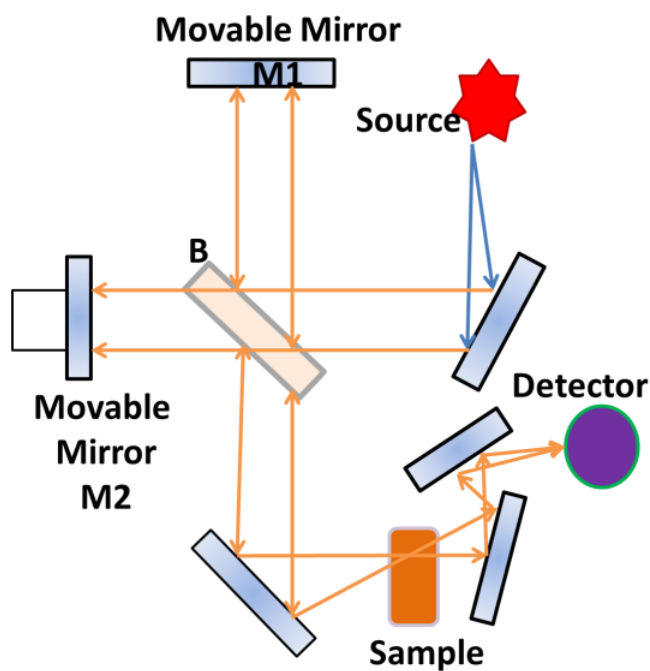
Figure 3.5: Schematic diagram of FTIR Spectrometer.

FTIR spectroscopy can also be applied to the characterization of inorganic coatings made of silicon oxide and carbon on the basis of their characteristic absorptions in the IR region. IR analysis can be utilized to understand abnormal indirect surface related properties of nanocrystals by monitoring the chemical reactions between the ligands. Although valuable for qualitative and structural analysis, the IR-based technique is seldom used for quantitative analysis of surface ligands on the nanocrystals, partly because it is difficult to obtain accuracy of intensity measurement. The IR technique is also insensitive to chemical environment, implying the difficulty in unraveling the origin of absorption peaks.

Instrument-FTIR spectra were measured using KBr pellet method with a Bomem MB100 FTIR from 400 to 4000 cm^{-1} available at the Analytical Center of the Federal University of Maranhão.

3.2.4 DC magnetic measurements

Superconducting Quantum Interference Devices (SQUID) are very sensitive magnetometers used to measure extremely small magnetic fields,[134] based on superconducting loops containing Josephson junctions (Figure 3.6).
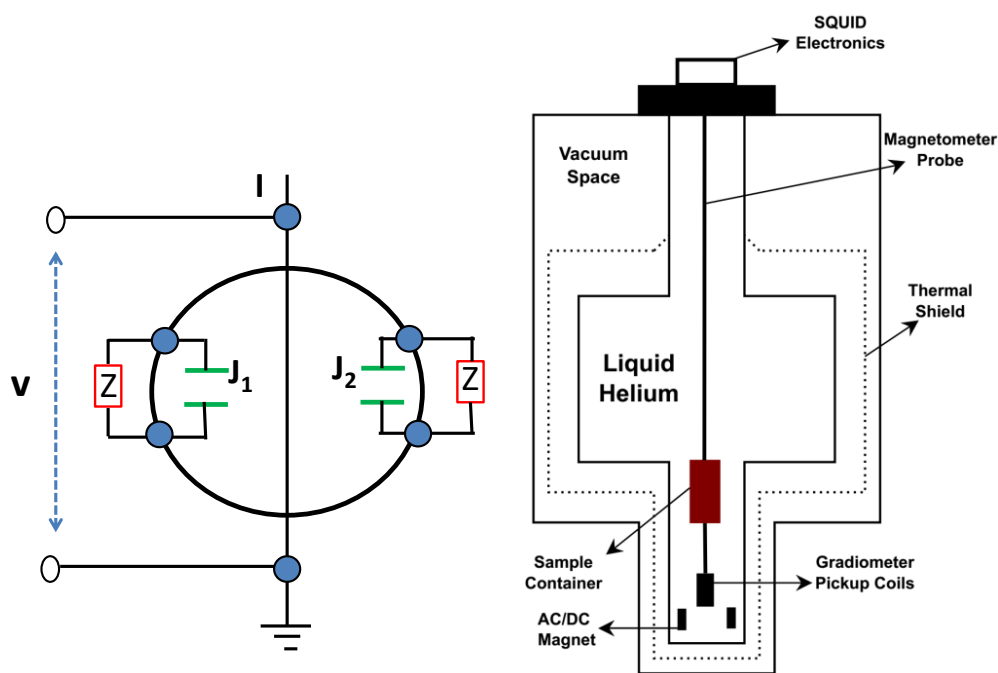
Figure 3.6: Schematic diagram of SQUID sensing device (left panel) and cross sectional schematic diagram of a simple SQUID magnetometer (right panel).

It is a very sensitive magnetometer capable of measuring extremely small magnetic fields typically of the order of 10^{-7} T. They are based on superconducting loops containing Josephson junctions. Noise levels in a SQUID are extremely low. A Josephson junction is made up of two superconductors, separated by an insulating layer so thin that electrons can pass through it. A SQUID consists of tiny loops of superconductors employing Josephson junctions to achieve superposition: each electron moves simultaneously in both directions. Because the current is moving in two opposite directions, the electrons have the ability to perform as qubits (that theoretically could be used to enable quantum computing). The direct current superconducting SQUID consists of two Josephson junctions connected in parallel. When the SQUID is biased with a current greater than the critical current, the voltage across the SQUID is modulated with the flux treading the SQUID at a period of one flux quantum, $\Phi_0 = h/2e$. Therefore, SQUID is a flux-to-voltage transducer. This special flux-to-voltage characteristic has enabled researchers to use the device to detect small magnetic field, current, voltage, inductance and magnetic susceptibility. Low-T_c SQUID has been used in a wide range of applications.

Instrument- The dc magnetic properties of the samples were studied using a Quantum Design, MPMS XL, SQUID magnetometer available at State University of Campinas and University of Brasilia, Brazil. The ZFC and FC magnetization versus temperature measurements were carried out as follows: the sample was first cooled down from 300 to 5 K (or 2 K) in a zero magnetic field, then a static magnetic field of 50 Oe was applied and the magnetization was measured increasing the temperature up to 300 K. Subsequently, the samples were cooled down to 5 K (or 2 K) under the same applied magnetic field (50 Oe) and the magnetization was measured while warming up the samples from 5 (or 2 K) to 300 K. The magnetization as a function of the applied field (M-H hysteresis loops) in a magnetic field of $\pm$ 7 T or ± 2 T was measured at 5 (or 2K) or 300 K.

3.2.5 Photoluminescence (PL) Study

PL is the spontaneous emission of light from a material under optical excitation.[134] The excitation energy and intensity are chosen to probe different regions and excitation concentrations in the sample. PL investigations can be used to characterize a variety of material parameters and provides electrical (as opposed to mechanical) characterization, and moreover it is a selective and extremely sensitive probe of discrete electronic states.[135] Features of the

emission spectrum can be used to identify surface, interface, and impurity levels and to gauge alloy disorder and interface roughness. Under pulsed excitation, the transient PL intensity yields the lifetime of non-equilibrium interface and bulk states. Variation of the PL intensity under an applied bias can be used to map the electric field at the surface of a sample. In addition, thermally activated processes cause changes in PL intensity with temperature. PL analysis is non-destructive tool. Indeed, the technique requires very little sample manipulation or environmental control. Because the sample is excited optically, electrical contacts and junctions are unnecessary and high-resistivity materials pose no practical difficulty. The fundamental limitation of PL analysis is its reliance on radiative events. Materials with poor radiative efficiency, such as low-quality indirect band-gap semiconductors, are difficult to study via ordinary PL. Similarly, identification of impurity and defect states depends on their optical activity. Although PL is a very sensitive probe of radiative levels, one must rely on secondary evidence to study states that couple weakly with light. Photoluminescence proceeds via following three steps[135]:

(i) Excitation: Excitation of electrons from lower energy state to higher energy state by absorption of energy from external sources, such as lasers, arc-discharge lamps and xenon lamp and in this process electron-hole pairs are created.

(ii) Thermalization: Excited pairs relax towards quasi-thermal equilibrium distributions.

(iii) Recombination: The energy can subsequently be released, in the form of a lower energy photon, when the electron falls back to the original ground state. This process can occur radiatively or non-radiatively.

The most common starting point in the characterization of luminescent lanthanide systems is UV-visible-NIR electronic absorption spectroscopy. The UV-visible-NIR spectrum, in which absorption (or diffuse reflectance in optically opaque samples) is measured as a function of the wavelength of the incident light, is used to determine the wavelength (energy) and optical density (i.e., the molar absorbance) of the electronic absorption bands in the sample of interest. This information provides the basis on which luminescence spectral data acquisition is planned. Luminescence spectroscopy typically entails a number of different yet complementary experiments. The most common experiments employed to characterize luminescent systems are intensity versus wavelength (or energy) scans of: (i) the emission spectrum and/or (ii) the excitation spectrum using a continuous wave light source. If a pulsed light source and a time-gated detection system are part of the instrumental arrangement, then luminescence lifetime

measurements (emission intensity versus time for a single excitation wavelength and at a single emission wavelength) are also possible. Similarly, if these time-resolved instrumental components are available, it is also common to measure and compare time-resolved emission and excitation scans to those collected with a continuous light source. Each of these basic experiments is described with examples below. This suite of experiments establishes the required instrumental hardware and configurations to perform these investigations.

3.2.5.1 Luminescence emission spectra: In the emission spectral mode the wavelength of the exciting light (λ_{ex}) is selected to coincide with an electronic absorption band in the sample and is held constant at this wavelength. The emission spectrum is generated by measuring the intensity of the emitted light as a function of wavelength. Most commonly the spectral range for an emission spectrum is chosen to begin at a wavelength longer than the excitation wavelength and to extend to even longer wavelengths to cover the region in which emission from the excited state(s) of the luminescent lanthanide are anticipated. Its value is same as emission spectral data at multiple excitation wavelengths corresponding to differing optical absorption bands in the sample to evaluate the degree of electronic coupling between the differing electronic excited states. In particular case of rare earth spectroscopy, the excitation wavelength could coincide with: (i) direct population of the emissive f-f manifold; (ii) higher lying states derived from the f-electronic configuration; (iii) charge-transfer states; and/or (iv) ligand localized states.

Commonly the measured intensity in an emission spectral band as a function of the excitation wavelength should correlate with the magnitude of the absorbance in the optical absorption spectrum at the excitation wavelengths indicating that there is good electronic communication among the different states in the excited state manifold(s). Conversely, if a relatively more intense absorption band gives rise to an emission spectrum that is weaker than one obtained by exciting into a less strongly absorbing band, this suggests that the more strongly absorbing excited state is not strongly coupled to the emissive excited state. This can happen, for example, when systems of lanthanides contain multiple discrete chromophores that are either spatially or electronically isolated from each other.

3.2.5.2 Luminescence excitation spectra: In an excitation spectrum a single emission detection wavelength (λ_{em}) is chosen that coincides with an observed band in the emission spectrum. The excitation source is then scanned through the wavelength region in which the sample absorbs light, and the intensity of emission at the single selected wavelength is

recorded versus the excitation wavelength. The wavelength range of the excitation spectrum is typically chosen to begin at the short wavelength end of the instrument's capability and extend to a wavelength just short of that of the emission band being monitored. The excitation spectrum is analogous to a UV-visible-NIR absorption spectrum, but instead of measuring the diminution in transmitted light as the samples absorbs energy, the excitation spectrum measures the light given off from an emissive excited state. Thus, the excitation spectrum not only maps out the electronic absorption bands in the sample, but through relative intensity variations as noted above between the absorption spectrum and the excitation spectrum, it also provides information about the extent to which the higher lying, absorbing excited states are coupled to the emissive excited state(s). The acquisition of an excitation spectrum requires a tunable broadband light source such as an arc lamp or flash lamp. Further, because excitation sources typically have a variable intensity output versus wavelength, it is essential that the excitation spectrum be corrected for this intensity variation so that any observed peak intensity variations in the excitation spectrum reflect effects intrinsic to the electronic excited state processes in the sample and not simple instrumental factors attributable to source intensity variations. This correction is most easily and commonly done by diverting a very small fraction of the excitation source intensity (using a simple beam splitter such as a glass slide) onto an ancillary detector. The output from this ancillary detector, which corresponds to the intensity spectrum of the source, is then used to normalize the emission intensity signal from the sample.

3.2.5.3 Luminescence lifetime measurements: Luminescence lifetime measurements are an essential ingredient in characterizing the luminescence properties of lanthanide ions. They form the basis for a number of analytically important determinations regarding electronic structure and coordination environment in lanthanide systems including quantum yields for radiative and nonradiative transitions (chapter 2), estimation of the number of coordinated water molecules and other ligands, and enumeration of multiple structurally distinct emissive species in complex samples. Lifetime measurements require a pulsed excitation source such as a flash lamp or pulsed laser with a pulse duration that is sufficiently short to enable discrimination of the light emitted from the sample from that due to the excitation source itself. In practice, with commercially available sources, the pulse duration ranges from the micro second regime for flash lamps to the picoseconds regime for pulsed laser sources, while measured lanthanide luminescence lifetimes in the range from milliseconds to nanoseconds are common. The actual experiment typically entails the use of an excitation wavelength (λ_{ex}) that

corresponds to an electronic absorption band in the sample of interest. The decay in the intensity of the emitted light is measured as a function of time from arrival of the light pulse on the sample to generate the emission decay curve. In most cases, the emitted light is dispersed and the wavelength selected to coincide with a specific band in the emission spectrum (λ_{em}). For a pure single emissive species the decay in luminescence intensity I(t) should follow simple first-order exponential decay kinetics, described by equation

$$I(t) = I_0 \exp(-t/\tau) \tag{3.5}$$

τ is the measured luminescence lifetime and I_0 is the intensity at t = 0. In general the emission decay curves are analyzed according to this model to extract the measured lifetime values. Deviations from this simple, single-exponential decay behavior then reflect the presence of multiple emissive species in the sample, sample inhomogeneity, and/or more complex excited state decay processes.
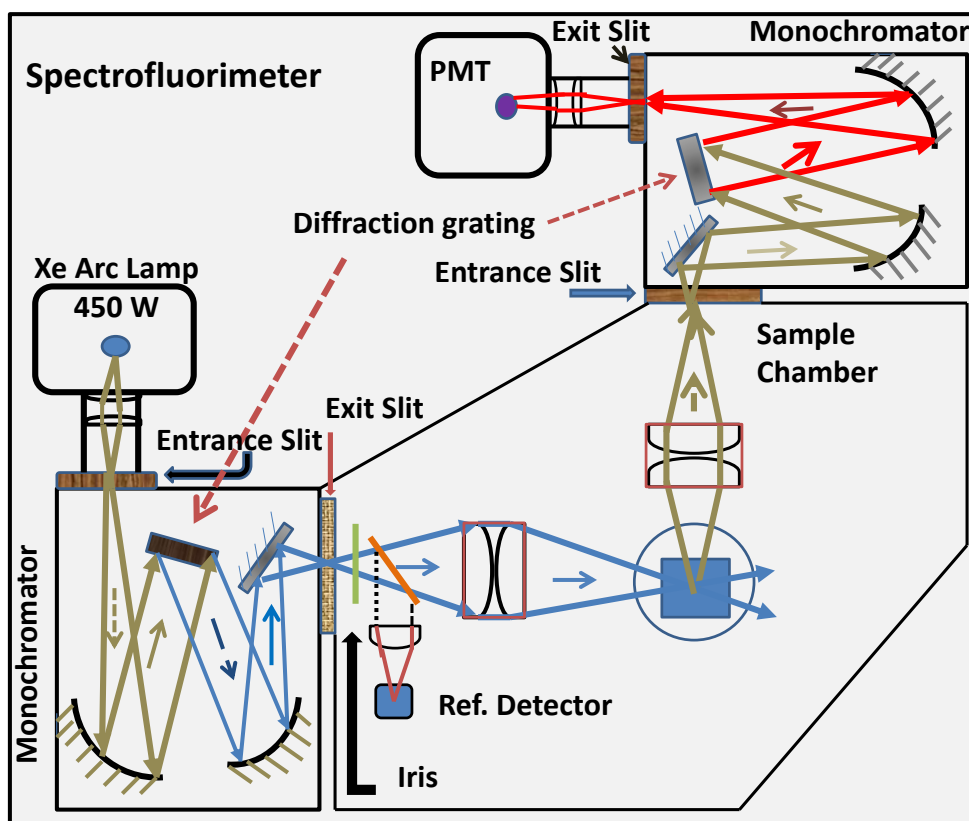
Figure 3.7: Schematic instrumental setup of a PL experiment.

The schematic representation of spectrofluorimeter can be seen in Figure 3.7. The light from an excitation source passes through a monochromator, and strikes the sample. A proportion of the incident light is absorbed by the sample and some of the molecules in the sample fluorescence. The fluorescent light is emitted in all directions. Some of this fluorescent light passes through a second monochromator and reaches a detector, which is usually placed at 90° to the incident light beam to minimize the risk of transmitted or reflected incident light reaching the detector. Various light sources may be used as excitation sources, including lasers, photodiodes and lamps (Xenon arcs and mercury-vapor lamps).

Instrument- The excitation and emission spectra of all the samples were recorded with a Horiba`s Nanolog UV-Vis-NIR spectrofluorometer, by using a 450 W Xenon lamp and an external laser source of 980 nm as an excitation source, connected to a Spectracq2 data acquisition module. The measurements were performed at University of São Paulo, SP and Federal University of Alagoas, Maceió, AL. All spectra were recorded for the dried powders and automatically corrected for the instrumental and photomultiplier (PMT) response. The entire luminescence setup was fully controlled by a DM3000F spectroscopic computer program. In order to describe the dynamics of the emitted wavelengths, time-resolved spectroscopy was carried out using the same equipment using a pulsed lamp (Xenon flash tube) mode and an external laser source of 980 nm for NIR region. Data Station v3.1 software was used to collect the time decay spectra and further to process the experimental traces. As detectors, two Hamamatsu photomultiplier tubes (PMT) were used: the R928P PMT, to measure the visible and NIR bands, and the R5509-73 PMT, cooled with liquid nitrogen, for the IR measurements.

CIE chromaticity: The Commission International de l'Eclairage (CIE) is defined as a standard system for color representation. The CIE system characterizes colors by a luminance parameter Y and two color coordinates x and y which specify the point on the chromaticity diagram. This system offers precision in color measurement because the parameters are based on the spectral power distribution (SPD) of the light emitted from a colored object and are factored by sensitivity curves which have been measured for the human eye.

3.2.6 X-ray Absorption Spectroscopy (XAS)

XAS is a core-level spectroscopy and refers to the details of how x-rays are absorbed by an atom at energies near and above its core level binding energies. Thus, it provides sensitivity to

a specific chemical element by tuning the x-rays to the resonance energy of the core to valence transition. The absorbing process is illustrated in Figure 3.8a. An x-ray photon strikes the absorbing atom (in pink) and disappears. Whenever the energy of an x-ray is greater than the binding energy of one of the absorbing atom's core electrons, a photoelectron is emitted. Depending on the energy of the incident x-ray photon, different processes occur. If the binding energy (ionization potential E_0) of certain electron in the absorbing atom is equal to the x-ray photon energy E, there is a sharp increase in the absorption cross-section, called absorbing edge, corresponding to an emission of the photoelectron to the continuum states, as indicated in Figure 3.8b.
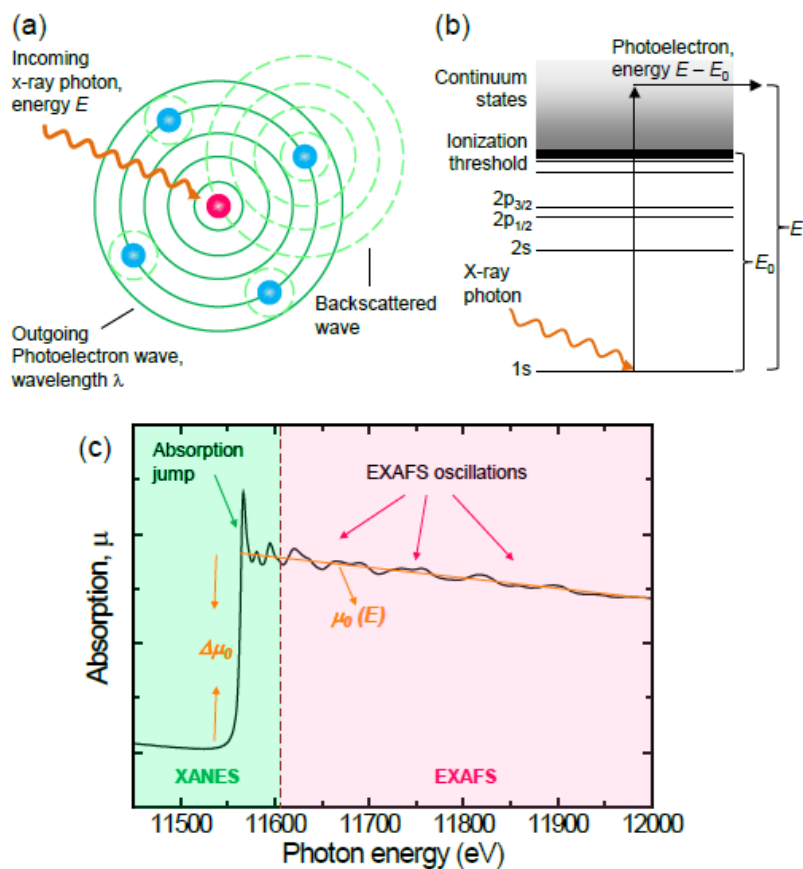
Figure 3.8: (a) Schematics of the x-ray absorption process.[136] An absorbing atom (pink) is shown here surrounded by several other atoms (blue). (b) Energy level diagrams of an absorbing atom showing the atom's first few core electron orbitals: 1s, 2s, $2p_{1/2}$, and $2p_{3/2}$ (c) XAFS spectrum recorded at the Pt L_3 edge for a Pt foil at 300 K. The main regions of the spectrum are depicted. The background function μ_0, and the measured jump at the absorption at the threshold energy E_0, $\Delta\mu_0$, are also shown.

With the absorption of a photon of energy, the electron undergoes a transition to an unbound state in the continuum and, by conservation of energy, acquires a kinetic energy ($E-E_0$). The absorption edges are named according to the principle quantum number of the electron that is excited, i.e., K, L, M, N, O refers to n = 1, 2, 3, 4, 5, respectively. The subscript 1, 2, 3, 4, 5, 6, 7, corresponds to the electronic orbital shells as $s_{1/2}$, $p_{1/2}$, $p_{3/2}$, $d_{3/2}$, $d_{5/2}$, $f_{5/2}$, $f_{7/2}$, respectively. The energies at which edges appear are unique for each element, which is the key for its element selectivity nature. Figure 3.8(c) shows the spectrum for a Pt foil measured at the Pt L_3 edge, which corresponds to $p_{3/2}\rightarrow$5d transitions.

X-rays have energies ranging from less than 1 keV to greater than 100 keV. Hard x-rays are the highest energy x-rays, while the lower energy ones are referred to as soft x-rays, with the boundary between both regions being around 2-3 keV. Soft x-rays cover the 3d transition metal $L_{2,3}$ (2p$\rightarrow$3d), 4d and 5d transition metal $M_{2,3}$ (3p$\rightarrow$d), and lanthanide $M_{2,3}$ (3p$\rightarrow$5d) and $M_{4,5}$ (3d$\rightarrow$4 f) edges. Hard x-rays cover the 3d and 4d transition metal K (1s$\rightarrow$p), 4d and 5d transition metal and lanthanide $L_{2,\,3}$ (2p$\rightarrow$d) edges. Intense absorption jumps at the edge are known as 'white lines', which refers to the sharp lines observed on photographic plates used in the early days of x-ray spectroscopy.

XAS can be detected in transmission, fluorescence, or electron yield mode. Each of these methods is suited to different sample types. Transmission mode is traditionally used for the analysis of thin layers of solid samples, or solvated analyte in solution. For thicker samples, fluorescent photons are measured from the relaxation of the excited atom after photoionization. To analyze surface species, detection of the Auger electron is especially useful.

Instrument- The XAS across Eu M-edges were collected for the LaF_3:xCe^{3+},xGd^{3+},yEu^{3+} (x = 5; y = 1, 5, 10 and 15 mol.%) samples along with reference compound Eu_2O_3. The measurements were performed at soft x-ray absorption spectroscopy (SXAS) beam line BL-01, at Indus-2, RRCAT, Indore, India in total electron yield (TEY) mode. BL-01 operates in the energy range 100-1200 eV.

3.2.7 Electron Paramagnetic Resonance (EPR)

EPR is a spectroscopic technique that detects species that have unpaired electrons.[137] Surprisingly a large number of materials have unpaired electrons. These include free radicals,

many transition metal ions, and defects in materials. Free electrons are often short-lived, but still play crucial roles in many processes such as photosynthesis, oxidation, catalysis, and polymerization reactions. EPR spectroscopy is similar to any other technique that depends on the absorption of electromagnetic radiation[138]. A molecule or atom has discrete (or separate) states, each with a corresponding energy. This difference in energy can be measured according to Planck's law "$\Delta E = h\nu$," where h is Planck's constant and ν is the frequency of the radiation. The absorption of energy causes a transition from a lower energy state to a higher energy state. It differs in EPR measurement, which uses high frequencies lying in microwave region (X-Band, GHz range).
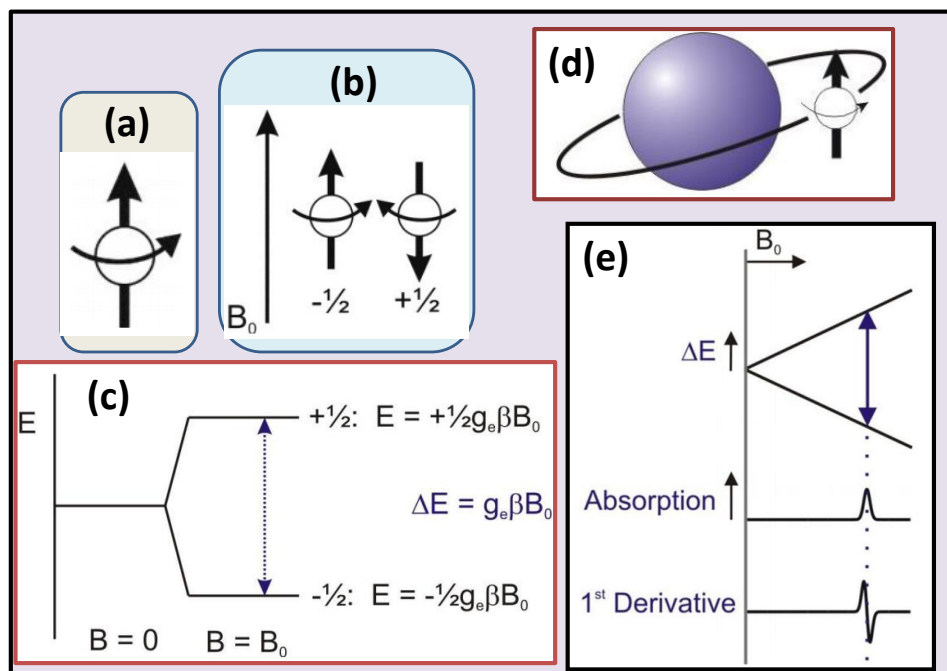
Figure 3.9: (a) Shows a free and unpaired electron in space; (b) shows minimum and maximum spin orientations of $\bar{\mu}$ with respect to the magnetic field B_0; (c) explains the introduction of spin state energies as a function of magnetic field B_0; (d) relates spin-orbit interaction; and (e) displays the prototype EPR experiment.

The energy differences studied in EPR spectroscopy are predominately due to the interaction of unpaired electrons in the sample with a magnetic field produced by a magnet in the laboratory. This effect is called the Zeeman Effect. The two states are labeled by the projection of the electron spin, m_s, on the direction of the magnetic field. Because the electron is a spin ½ particle, the parallel state is designated as $m_s = -1/2$ and the antiparallel state is $m_s = +1/2$

(Figure 3.9b and c). The energy of each orientation is the product of μ and B_0. For an electron μ = $m_s g_e \beta$, where β is a conversion constant called the Bohr magneton and g_e is the spectroscopic g-factor of the free electron and equals 2.0023192778 (≈ 2.00). Therefore, the energies for an electron with m_s = +1/2 and m_s = -1/2 are, respectively, given by

$E_{1/2}$ = ½ $g_e \beta B_0$ and $E_{-1/2}$ = - ½ $g_e \beta B_0$ (3.6)

As a result there are two energy levels for the electron in a magnetic field. When we take an electron in space with no outside forces on it and place it on to a molecule, its total angular momentum changes because, in addition to the intrinsic spin angular momentum ($\bar{S}$), it also possesses some orbital angular momentum (L). An electron with orbital angular momentum is in effect a circulating current, and so there is also a magnetic moment arising from the orbital angular momentum. These two magnetic moments interact, and the energy of this spin orbit interaction depends on their relative orientations.

Electron in space-

$\bar{\mu} \ \alpha \ g_e \bar{S}$ (3.7)

And electron in a molecule-

$\bar{\mu} \ \alpha \ g_e \bar{S} + \bar{L}.$ (3.8)

In general, the orbital angular momentum is approximately zero for an electron in the ground state (s electron). Interaction between the ground state and excited states, however, admixes small amounts of orbital angular momentum to the ground state: spin-orbit coupling contribution. It gives rise to $\bar{\mu} \ \alpha \ g_e \bar{S}$ + Spin orbit coupling contribution. Usually the spin-orbit coupling term is proportional to ($\bar{S}$),which means we can simply combine both terms on the right and just change the value of g_e to g, or

$\bar{\mu} \ \alpha \ g \ \bar{S}$ and ΔE = $g \beta B_0$ (3.9)

The magnitude of the spin-orbit coupling contribution depends on the size of the nucleus containing the unpaired electron. Therefore, the g factors of much larger elements, such as metals, may be significantly different from g_e. The value of g can be taken as a fingerprint of the molecule. In an EPR spectrometer, a paramagnetic sample is placed in a large uniform magnetic field which, as shown above, splits the energy levels of the ground state by an amount ΔE where,

ΔE = $g \beta B_0$ = hν (3.10)

Since β is a constant and the magnitude of B_0 can be measured, all we have to do to calculate g

73

is determine the value of ΔE, the energy between the two spin levels. This is done by irradiating the sample with microwaves with a set frequency and sweeping the magnetic field (Figure 3.9e). The whole process can be summarized in following way. Initially, there will be more electrons in the lower energy level (i.e., parallel to the field) than in the upper level (antiparallel). A fixed frequency of microwave irradiation is used to excite some of the electrons in the lower energy level to the upper energy level. In order for the transition to occur, the external magnetic field at a specific strength should be applied, such that the energy level separation between the lower and upper states is exactly matched by applied microwave frequency. In order to achieve this condition, the external magnet's field is swept while exposing the sample to a fixed frequency of microwave irradiation. The condition where the magnetic field and the microwave frequency are "just right" to produce an EPR resonance (or absorption) is known as the resonance condition and is described by the equation shown in the Figure 3.9, c and e.

Instrument- EPR spectra were recorded on JEOL JES-X-320 operating at X-band frequency (~ 9.1 GHz), equipped with a variable temperature control ES 13060DVT5 apparatus or a ES-CT470/AT Liquid Helium Variable Temperature System, and were performed on the powder samples. The cavity Q quality factor was kept above 6500 in all measurements, and highly-pure quartz tubes were employed (Suprasil, Wilmad, ≤ 0.5 OD). The measurements were done at Regional Centre for Advanced Technologies and Materials, Palacky University, Czech Republic.

Chapter 4
Tuned photoluminescence and Magnetic Investigation of Ternary doped LaF$_3$
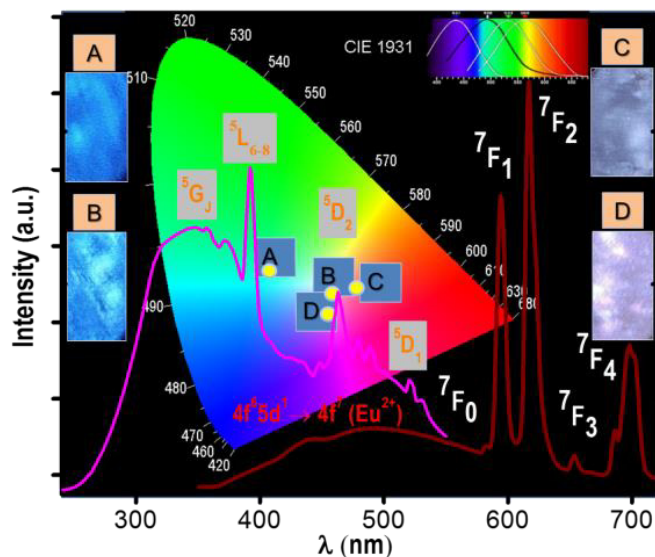
Color tuning (marked as A, B, C, and D) dependence on ratio of Eu^{2+}/Eu^{3+} ions in ultrasmall LaF$_3$:xCe^{3+},xGd^{3+},yEu^{3+} (x = 5; y = 1, 5, 10 and 15 mol. %) nanoparticles and the excitation/emission spectrum for the greatest achieved emission quantum efficiency (~ 85%) of Eu^{3+} (y = 10 mol.%).

Luminescence tunable multicolored LaF$_3$:xCe^{3+},xGd^{3+},yEu^{3+} (x = 5; y = 1, 5, 10, and 15 mol.%) nanoparticles have been synthesized via a low cost polyol method. Powder x-ray diffraction and high resolution transmission electron microscopy studies confirm the hexagonal phase of the LaF$_3$:xCe^{3+},xGd^{3+},yEu^{3+} nanophosphors with average sizes (oval shape) ranging from 5 to 7 nm. Energy dispersive x-ray spectroscopy analyses show the uniform distribution of Ce^{3+}, Gd^{3+}, and Eu^{3+} dopants in the LaF$_3$ host matrix. The photoluminescence spectra and electron paramagnetic resonance measurements guarantee the presence of Eu^{2+}, corroborated through dc susceptibility measurements of the samples displaying paramagnetic behavior at 300 K, whereas weak ferromagnetic ordering is shown at 2 K. The nonradiative energy transfer processes from the 4f(^{2}F$_{5/2}$)-5d state (Ce^{3+}) to the intraconfigurational 4f excited levels of rare earth ions and simultaneous emissions in the visible region from the 4f^{6}5d^1 (Eu^{2+}) and ^{5}D$_0$ (Eu^{3+}) emitting levels, leading to overlapped broad and narrow emission bands, have been proclaimed. The energy transfer mechanism proposes involvement of the Gd^{3+} ion sub-lattice as the bridge and finally trapping by Eu$^{2+/3+}$, upon excitation of the Ce^{3+} ion. The calculation of experimental intensity parameters ($\Omega_{2,4}$) has been discussed and the highest emission quantum efficiency (η = 85%) of the Eu^{3+} ion for the y = 10 mol.% sample is reported. The advantageous existence of the Eu^{2+}/Eu^{3+} ratio along with variously doped nanomaterials described in this work, results in tunable emission color in the blue-white-red regions, highlighting the potential application of the samples in solid-state lighting devices, scintillation devices, and multiplex detection.

4.1 Introduction

Optical materials containing rare earth halides have been used extensively in a variety of industrial/electronic and medically oriented applications. The technological implementation of rare earth based materials can be found in biomedical probes,[139] in cathode ray tubes,[140] radiation scintillations devices,[70,72,126,141] back-light unit (BLU) displays,[142] in tunable lasers,[143,144] in photo-conversion molecular devices[145] and in MRI agents.[146] So far, highly studied systems tailored for optical uses are based on the LaX_3 (X = F, Br, Cl) inorganic matrices.[60,147–151] Materials formed by La^{3+} ion as the sole rare earth element are not straightforwardly used; the reasoning stems from the fact that La^{3+} is optically inactive, having the frontier 4f orbitals completely filled.[64,150,152–154] However, the benefit of using La^{3+} inorganic matrices (hexagonal LaF_3) resides in the structural flexibility, a key factor that allows within the synthetic assembly to easily host in the matrix diverse type of dopants, especially other rare earth ions (RE^{3+}). In La-RE doped materials, the optical properties become strongly dependent on the type/s of dopant/s and the optical performances can be tailored to convert *via* a multi-photon processes high energy photons (UV, x-ray, gamma ray)[126,155,156] and low energy photons (near-infrared-NIR) to output light that falls in the visible region.[152,157–159] Moreover, depending on the chemical nature and relative amount of the dopant used, the nanostructured material can feature low phonon energy (~350 cm^{-1}),[149] minimal quenching,[72,160] low refractive index,[158] high ionicity,[161] wide band gap,[162,163] adequate thermal and environmental stability along with large solid/liquid solubility.[149] All these properties generate easily processable materials for industrial applications. One type of rare earth element often added to the La^{3+} matrix is the Ce^{3+} ion. Cerium imprints exceptional photoemission efficiency and coherency,[164] high energy resolution potential with fast response scan,[165] large stokes shift,[166] and broad emission bands.[167] Binary or even ternary doped materials have also been synthesized in a way to further enhance the absorption cross-section of the rare earth ions.[168] In these nanocomposites, the multicolor emission via up/down conversion are achieved by (i) selected combination of the dopants (e.g., sensitizers as Ce^{3+}, Yb^{3+} and activators as Eu^{3+}, Tb^{3+} or Er^{3+}), (ii) the doping percentage of RE^{3+} ions, and (iii) the careful control of the structure (lattice/symmetry organization) emerging from the synthetic process.[9,169–171] The emission of lanthanide ions ranges from the UV to IR region of the electromagnetic spectra. For example, Eu^{3+} ion displays red sharp emission from $4f^6$-$4f^6$ transitions and is used as an activator.[81] The

allowed magnetic dipole $^5D_0\rightarrow{}^7F_1$ transition has its intensity almost unaffected by symmetry variation. Due to forced electric dipole from the $^5D_0\rightarrow{}^7F_2$ hypersensitive transition, Eu^{3+} is considered one of the best spectroscopic probes. The $^5D_0\rightarrow{}^7F_2$ transition is responsible for change in optical intensity of the system and depends on the symmetry of the chemical environment around the ion.[81] The comparison in intensity between these two transitions ($^5D_0\rightarrow{}^7F_1$ and $^5D_0\rightarrow{}^7F_2$) reveals the symmetry of charge distribution around the Eu^{3+} ion. During doping processes, Eu^{3+} ion can partially reduce to Eu^{2+}. When present, the parity allowed electric dipole $4f^7\rightarrow 4f^65d^1$ transition gives broad band and highly intense luminescence of Eu^{2+} in absorption as well in emission.[167,172] The Gd^{3+} ($4f^7$) ion displays ultraviolet emission having large energy gap (> 32000 cm^{-1}) between the ground ($^8S_{7/2}$) and first excited ($^6P_{7/2}$) energy levels and can be employed as an intermediate sub-lattice to convert more high energetic photons (UV) to the visible region,[173–175] i.e., it favors energy transfer processes from sensitizer cations (e.g., Ce^{3+}/Eu^{2+}) to activator cations such as Eu^{3+}, Dy^{3+}, Tb^{3+}, Yb^{3+}, Sm^{3+}.[80,147] Therefore, by selecting Ce^{3+}, Eu^{3+}, Gd^{3+} with the coexistence of Eu^{2+} in LaF_3 host lattice,[72,165] the so formed triply doped hybrid can, in principle, provide access to flexible color tuning through excitation of Ce^{3+}, Eu^{3+} and Eu^{2+}.[169,176,177]

In this chapter, we illustrate the synthesis and properties of novel multicolor triply doped oleic acid coated LaF_3:xCe^{3+},xGd^{3+},$yEu^{2+/3+}$ ($x = 5$; $y = 1, 5, 10$ and 15 mol.%) nanoparticles. The presence of Eu^{2+} ions, due to auto-reduction of Eu^{3+} ions in diethylglycol (DEG), was validated by photoluminescence (PL) spectra and electron paramagnetic resonance (EPR). We found that the color tuning was easily achieved in these nanoparticles, from the blue-white to red region of the visible spectrum, and the phenomenon was correlated with the doping concentration of Eu^{3+} and the ratio Eu^{3+}/Eu^{2+}. We describe in detail the nanoparticles structure, morphologies, optical and magnetic properties, showing the true potential of these types of triply doped nanomaterials to be employed in a variety of applications, from multiplex detection, solid state lighting to scintillating devices.

4.2 Experimental Section

4.2.1 Synthesis: A detailed synthesis has been explained in the section 3.1.3.1 of chapter 3. The following schematic diagram (Figure 4.1) explains the synthesis procedure. Four samples were prepared namely, LaF_3:xCe^{3+},xGd^{3+},$yEu^{2+/3+}$ ($x = 5$; $y = 1, 5, 10$ and 15 mol.%) by varying concentration of Eu precursors.

4.2.2. Instrumentation: The presence of oleic acid coating and organics was confirmed by Fourier transform infrared (FTIR) spectroscopy The phase structure of the synthesized materials was determined by powder x-ray diffraction and General Structure Analysis System (GSAS) program was used to perform Rietveld refinement.[178] The morphology and elemental analysis were analyzed by transmission electron microscopy (TEM), scanning TEM (STEM) and energy-dispersive x-ray spectroscopy (EDS). The excitation and emission spectra of the LaF_3:xCe^{3+},xGd^{3+},yEu^{3+}(x = 5; y = 1, 5, 10 and 15 mol.%) nanoparticles and luminescence decay profiles for Eu^{3+} were measured. The dc magnetic studies were carried out with field range +/-7 T and temperatures from 2 to 300 K. Electronic paramagnetic resonance (EPR) spectra were recorded to confirm existence of rare earth ions. Complete experimental details have been provided in chapter 3.2.
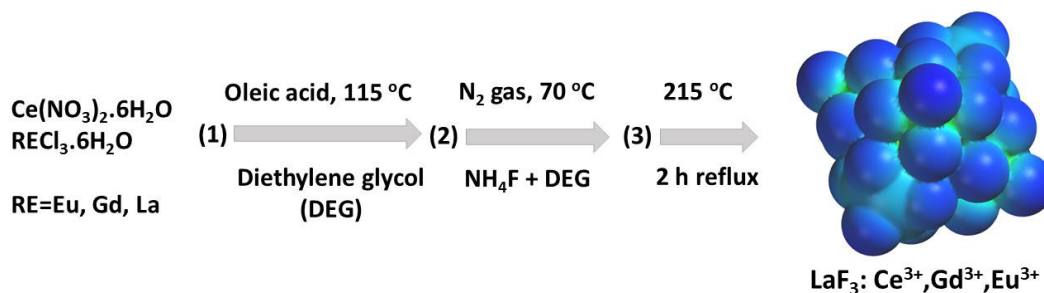
Figure 4.1: Schematic of synthesis of LaF_3:xCe^{3+}, xGd^{3+},yEu^{3+} (x = 5; y = 1, 5, 10 and 15 mol.%) nanoparticles.

4.3 Result and Discussion

4.3.1 Determination of the phase, structure and morphologies

4.3.1.1 Fourier transfer infrared (FTIR) spectroscopy: FTIR was used as an effective probe to validate the presence of the oleic acid (OA) acting as a canopy for the nanoparticle surfaces.[179,180] The observed spectra for the variously doped systems are collected together in Figure 4.2. The broad and intensive band corresponding to the O-H stretching (υ) vibrations (asymmetric υ_{as} and symmetric υ_s) is observed around 3400 cm^{-1} in all systems together with the additional characteristic O-H deformation (σ) around 1640 cm^{-1}. These signatures correspond to the adsorbed water molecules.[179] The absorption bands~2930 and 1390 cm^{-1} are attributed to the C-H group. The two bands at 2922 and 2856 cm^{-1} are assigned to the CH_2 asymmetric and symmetric stretching vibration, respectively. These fingerprints clearly reveal

the presence of organic surfactant on the surfaces of $LaF_3:xCe^{3+},xGd^{3+},yEu^{3+}$ nanoparticles. Furthermore, two absorption peaks around 1582 and 1546 cm^{-1} are the characteristic asymmetric (COO-) and symmetric (COO-) stretching modes, respectively. Below 1300 cm^{-1}, the absorption bands developing around 721 cm^{-1} highlight the presence of the $(CH_2)_n$ (n ≥ 4) alkyl chains.[155] Finally, the strong absorption at 1710 cm^{-1} is attributed to the stretching vibrations of the C=O group. Therefore, taken these fingerprints all together, indicated that the oleic acid is not physically adsorbed on the surface of the nanoparticle but rather chemisorbed.[155]
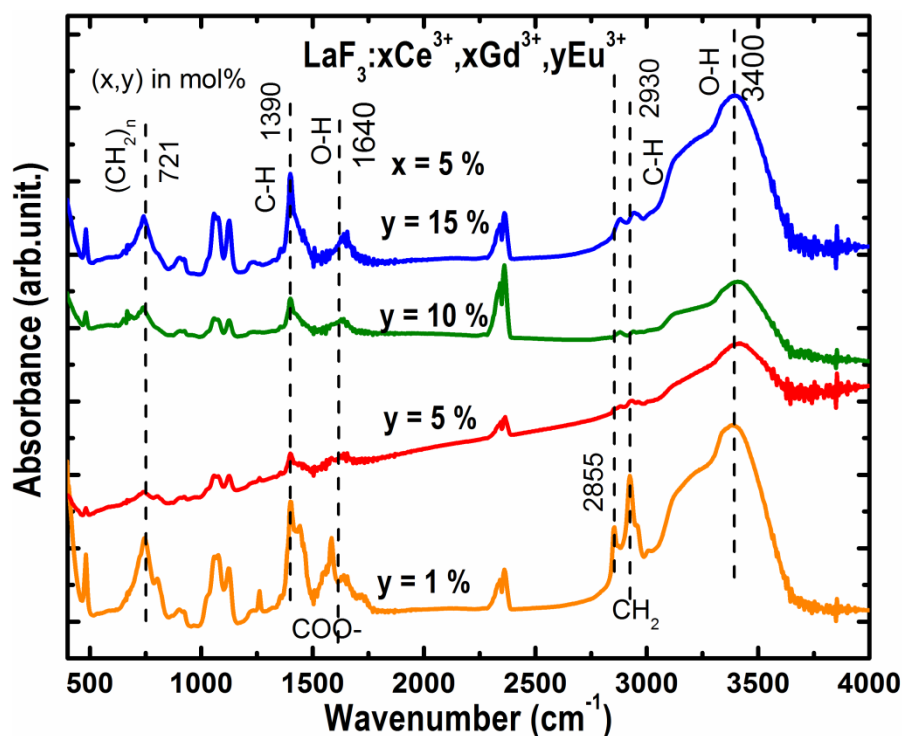
Figure 4.2: FTIR spectra of $LaF_3:xCe^{3+},xGd^{3+},yEu^{3+}$ (x = 5; y = 1, 5, 10 and 15 mol.%) nanomaterials.

4.3.1.2 Powder x-ray diffraction (PXRD): PXRD measurements were performed for better evaluating the structural organization of the various $LaF_3:xCe^{3+},xGd^{3+},yEu^{3+}$ nanoparticles. We found that all diffraction peaks emerging in the diffraction spectra matched well with the ICDD PDF no. 01- 076-0510 (Figure 4.3). The Rietveld analysis suggested the formation of hexagonal structure (P63/mmc) of nanoparticles, and main peak is indexed against plane (101). All PXRD patterns show broadening suggesting ultrasmall formation of nanoparticles. A small peak shifting is due to substitution effect of La ions by ionic doping, with different intrinsic

ionic volumes; and surface effects such as the crystalline lattice relaxation effect at the interface, following the *Vegard's Law*.[147]. It indicates that the Ce^{3+}, Gd^{3+} and Eu^{3+} ions were well incorporated in the LaF_3 lattice. Further, Rietveld refinement for these samples suggested anisotropic elongation in crystallite size observed along [110] direction. Lattice parameters, volumes, crystallite size and strain, calculated from Rietveld refinement have been tabulated in the Tables 4.1 and 4.2.
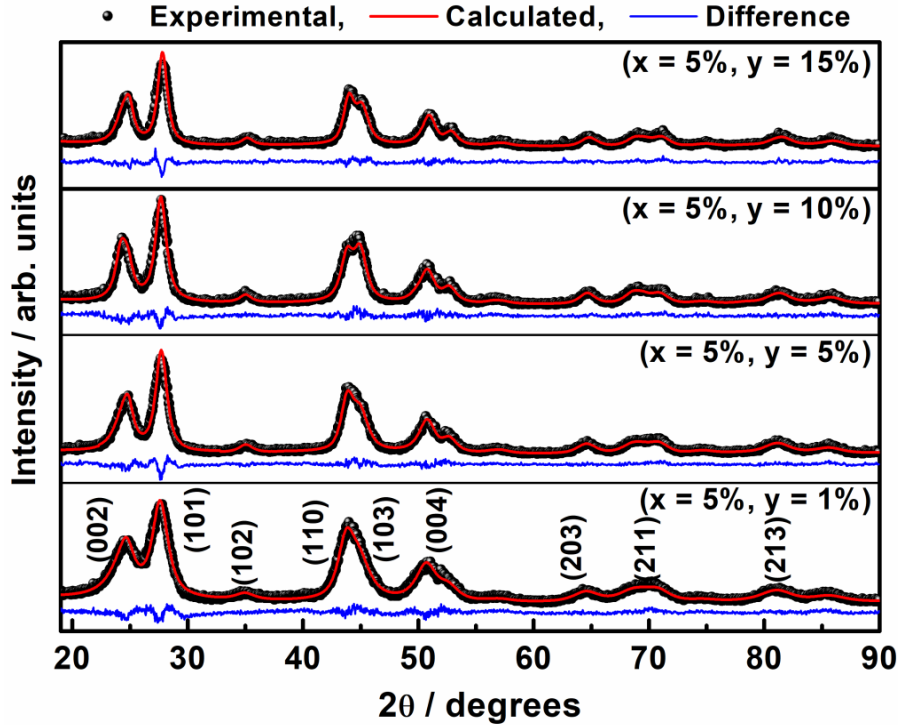
Figure 4.3: PXRD patterns of $LaF_3:xCe^{3+},xGd^{3+},yEu^{3+}$ (x = 5; y = 1, 5, 10 and 15 mol.%) nanoparticles and their corresponding Rietveld analyses.

Table 4.1: Anisotropic crystallite size and microstrain analyses in $LaF_3:xCe^{3+},xGd^{3+},yEu^{3+}$.

Samples	Crystallite size d (nm)		Strain
$LaF_3:xCe^{3+},xGd^{3+},yEu^{3+}$	‖ to [110]	⊥ to [110]	(%)
(x = 5, y =1 mol.%)	8.22	3.43	0.94
(x = 5, y =5 mol.%)	12.1	5.36	0.80
(x = 5, y =10 mol.%)	8.96	8.77	0.57
(x = 5, y =15 mol.%)	13.3	6.78	0.65

80

Table 4.2: Lattice parameters (a, c), volume (V), R_{wp}, and chi-square (χ^2)

Samples	Lattice Parameters (Å)		Volume	R_{wp}	χ^2
LaF_3:xCe^{3+},xGd^{3+},yEu^{3+}	a = b	c	V ($Å^3$)	(%)	
(x = 5, y =1 mol.%)	4.133 (3)	7.323 (6)	108.3 (2)	8.45	1.56
(x = 5, y =5 mol.%)	4.135 (3)	7.332 (5)	108.6 (2)	9.12	1.22
(x = 5, y =10 mol.%)	4.126 (3)	7.313 (5)	107.8 (2)	10.01	1.14
(x = 5, y =15 mol.%)	4.122 (3)	7.304 (5)	107.5 (2)	10.33	1.28

4.3.1.3 Transmission electron microscopy (TEM): The morphology and size distribution of LaF_3:xCe^{3+},xGd^{3+},yEu^{3+} (x = y= 5 and 15 mol.%) nanoparticles are shown by HRTEM images illustrated in Figure 4.4 (a, b) (LaF_3:xCe^{3+},xGd^{3+},yEu^{3+} with x = y = 5 mol.%) and Figure 4.4 (d, e) (LaF_3:xCe^{3+},xGd^{3+},yEu^{3+} with x = 5, y = 15 mol.%). Ovoid shape like nanoparticles for both samples were observed in STEM and HRTEM modes, with an average size of 6.1 ± 1.4 nm (Figure 4.4 (b, c)) for the former and 7.1 ± 1.1 nm (Figure 4.4 (e, f)) for the latter, which agree with PXRD. Selected area electron diffraction (SAED) patterns showed the diffraction of crystallographic planes with d-spacings of the hexagonal crystalline structure, according to the ICDD PDF no. 01-076-0510 (Figure 4.5). The Fast Fourier Transform (FFT) analyses show the hexagonal structure of LaF_3 along the [100] and near the [211] zone axis, with presence of the ($\bar{3}$30), ($\bar{1}$20) and (110) planes (inset, Figure 4.4b) and (1$\bar{2}$0), (0$\bar{1}$1) and (1$\bar{1}\bar{1}$) planes (inset, Figure 4.4e), respectively.

The elemental maps distribution for the LaF_3:xCe^{3+},xGd^{3+},yEu^{3+} (x = y = 5 and 15 mol.%) samples is shown in Figure 4.5. The top of the Figure 4.5 shows the EDS layered images of samples, and the bottom, its respective SAED patterns, highlighting three major crystallographic planes.EDS mappings for LaF_3:xCe^{3+},xGd^{3+},yEu^{3+} (x = 5; y = 15 mol.%) sample have been acquired by focusing electron beam on agglomerated particles (Figure 4.6). The element selective scanning confirmed the existence of La, F, Ce, Gd and Eu elements. Tables 4.3 show the average % elemental composition measured at different spots of the samples LaF_3:xCe^{3+},xGd^{3+},yEu^{3+} (x = 5; y = 5 and 15 mol.%).
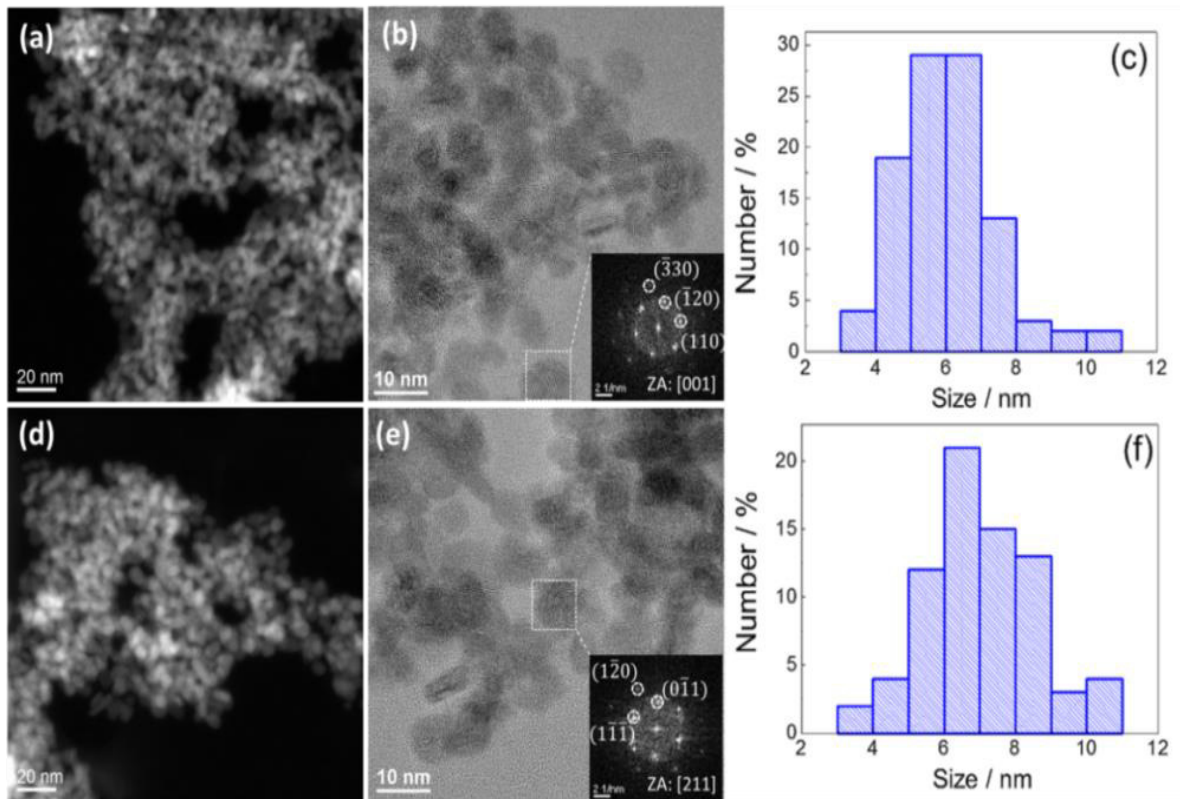
Figure 4.4: (a, d) HAADF), (b, e) HRTEM images, and (c, f) particle size distribution obtained from TEM analysis for LaF$_3$:xCe^{3+},xGd^{3+},yEu^{3+} (x = y =5 and 15 mol.%), respectively. Panel (b and e) show the inset region of the images analyzed by applying Fast Fourier Transforms (FFT), confirming hexagonal structure of highlighted nanoparticles along the [001] and near the [211] zone axis.
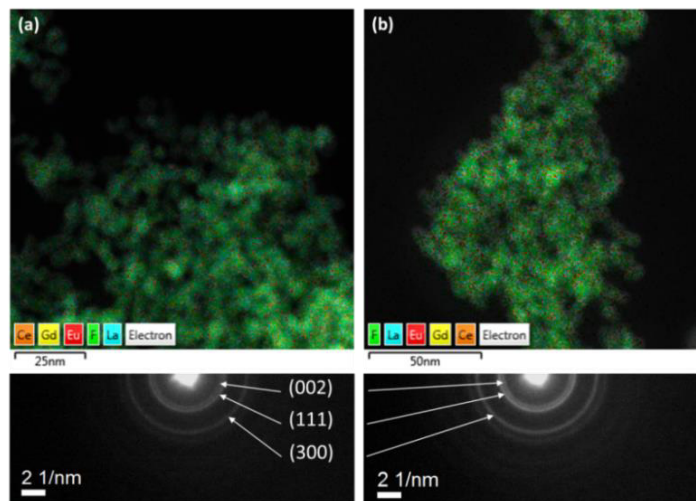
Figure 4.5: Merged chemical maps distribution of elements and selected area electron diffraction patterns for LaF$_3$:xCe^{3+},xGd^{3+},yEu^{3+}(x = y = 5 mol.%) (a-top/a-bottom) and (x = 5; y = 15 mol.%) (b-top/b-bottom) samples.
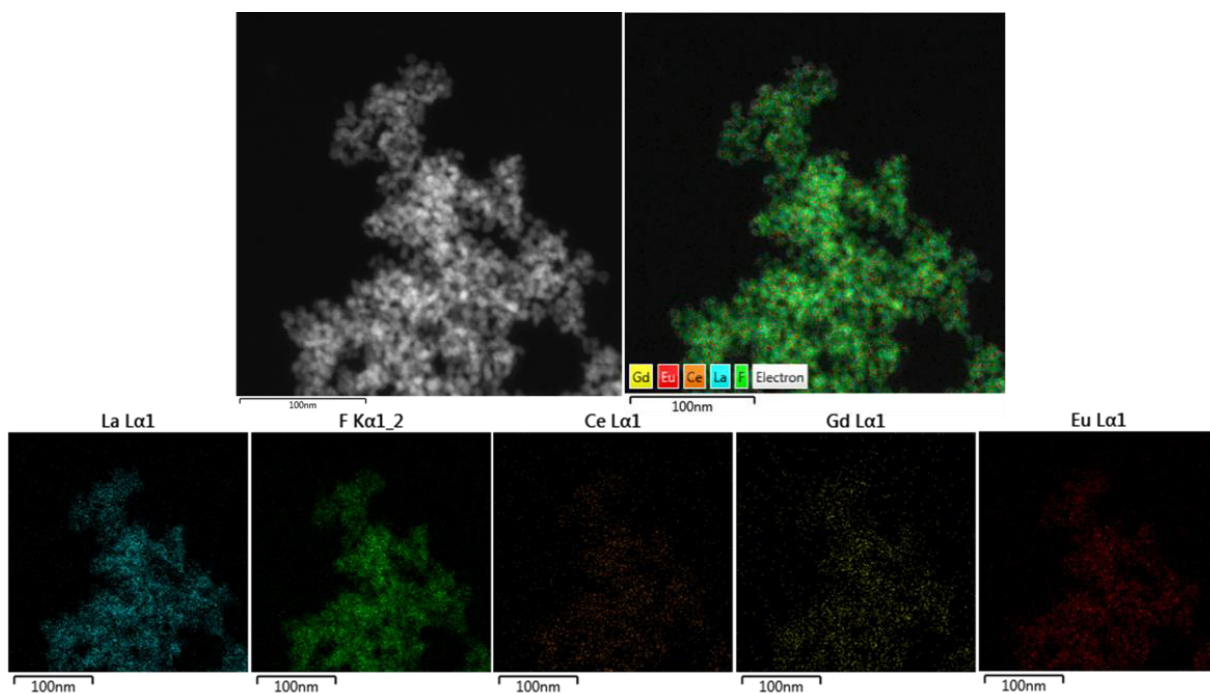
Figure 4.6: High angle annular dark field (HAADF) image and EDS elemental mappings, acquired in the JEM-2100F microscope, showing the homogeneous and uniform distribution La, F, Ce, Gd and Eu elements in sample of $LaF_3:xCe^{3+},xGd^{3+},yEu^{3+}$ (x = 5; y = 15 mol.%) nanocomposite. Scale bar = 100 nm.

Table 4.3: Chemical distribution of $LaF_3:xCe^{3+},xGd^{3+},yEu^{3+}$ (x = 5; y = 5 and 15 mol.%) samples.

	Spectrum 1 (y = 5 mol.%)		Spectrum 2 (y = 5 mol.%)		Spectrum 3 (y = 5 mol/%)		Spectrum 4 (y = 15 mol.%)		Spectrum 5 (y = 15 mol.%)	
Element	Wt%	Wt% Sigma	Wt%	Wt% Sigma	Wt %	Wt% Sigma	Wt%	Wt% Sigma	Wt%	Wt% Sigma
F	31.62	0.33	30.45	0.31	32.43	0.33	15.36	0.28	31.07	0.58
La	58.5	0.42	59.15	0.41	57.55	0.42	60.87	0.55	51.76	0.72
Ce	3.52	0.35	3.12	0.35	3.36	0.35	3.6	0.44	3.48	0.59
Eu	3.48	0.25	3.83	0.24	3.96	0.27	15.19	0.40	10.42	0.52
Gd	2.88	0.24	3.45	0.23	2.71	0.25	4.99	0.36	3.30	0.48

4.3.1.4 X-ray absorption spectroscopy (XAS): XAS across Eu M-edges were collected for all the samples along with reference compound Eu_2O_3 at soft X-ray absorption spectroscopy (SXAS) beam line of RRCAT, India. The detail of the experiment is explained in chapter 3.
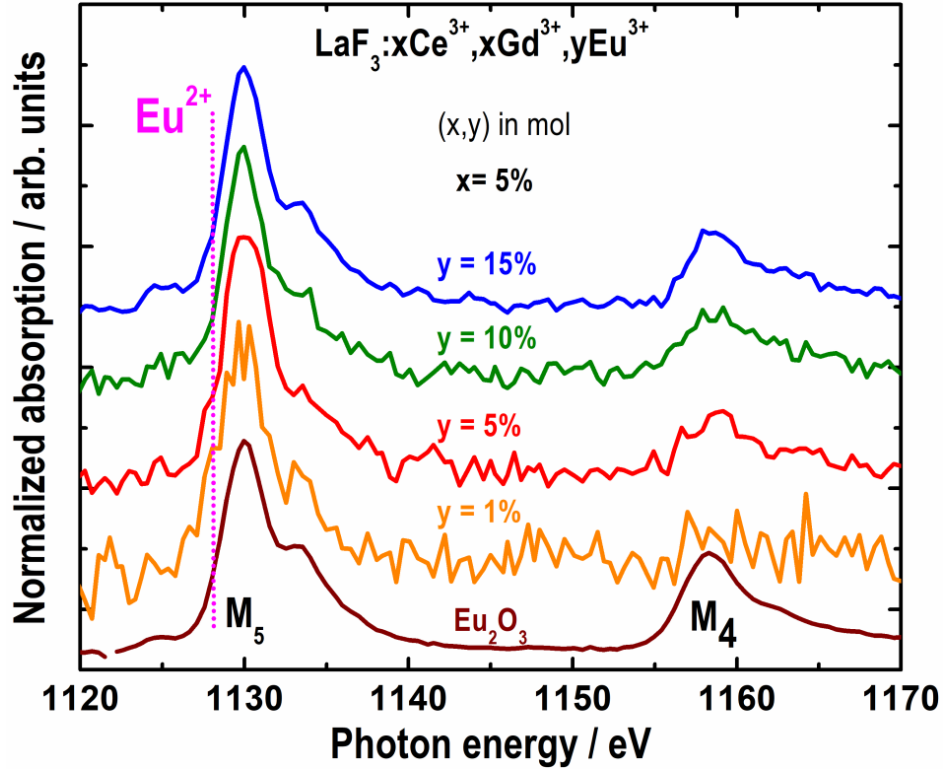
Figure 4.7: The Eu-$M_{5,4}$ X-ray absorption spectra of all the samples LaF_3:xCe^{3+},xGd^{3+},yEu^{3+} (x = 5; y = 1, 5, 10 and 15 mol.%) along with reference Eu_2O_3 spectrum (Eu^{3+}). The spectra were divided by their respective maxima and vertically shifted to enhance direct comparison.

This technique has been employed to determine more thoroughly the valence state of Eu cations as well as to study the local geometrical structure. Figure 4.7 shows the Eu $M_{5,4}$ edge XAS of all doped samples, along with the reference compound, Eu_2O_3. These spectra show two clear features marked as M_5 and M_4, signatures that arise to spin-orbit splitting. For a symmetrical molecule, XAS is dominated by dipolar transitions. The M_5 fingerprint is associated to transitions from $3d_{5/2}$ to 4f states, while M_4 arises from $3d_{3/2}$ to 4f states. The dotted line in Figure 4.7 shows the expected $3d_{5/2}$ to 4f transition peak position for Eu^{2+} cation, which falls around 2 eV. These results indicate that all the investigated samples certainly possess Eu in (3+) valence state, but remains unclear the presence of Eu^{2+}, because only

shoulders around 1128 eV were detected. Stronger evidences of the presence of Eu^{2+} cations in the samples emerged indeed from analysis of the photoluminescence spectra.

4.3.2 Photoluminescence Investigation

The excitation spectra (Figure 4.8a and 4.8b) of the $LaF_3:xCe^{3+},xGd^{3+},yEu^{3+}$ (x = 5; y = 1, 5, 10 and 15 mol.%) nanophosphors were recorded at 300 K in spectral range of 200-550 nm, under the emission monitored at 617 nm, assigned to the $^5D_0\rightarrow^7F_2$ hypersensitive transition of the Eu^{3+} ion. These spectra contain overlapped broad absorption bands centered at 260 nm and 335 nm, which are assigned to the $4f(^2F_{5/2})\rightarrow5d$ and $4f^7(^8S_{7/2})\rightarrow4f^65d^1$ interconfigurational transitions of the Ce^{3+} and Eu^{2+} ions, respectively (Figure 4.8b). In addition, narrow absorption lines have also been observed that are assigned to the intraconfigurational 4f transitions, originating from the $^7F_0$ ground state to the following excited states of Eu^{3+} ion: $^5D_4$ (~361 nm), $^5L_7$ (~374 nm), $^5L_6$ (~394 nm), $^5D_2$ (~464 nm) and $^5D_1$ (~525 nm).[81] However, the intensities of the broad absorption bands are comparably higher than those of the 4f–4f narrow lines (Figure 4.8a). The results indicate that the indirect excitation process of the Eu^{3+} ion *via* $4f(^2F_{5/2})\rightarrow5d$ and $4f^7(^8S_{7/2})\rightarrow4f^65d^1$ interconfigurational transitions of the Ce^{3+} and Eu^{2+} ions, respectively, is less operative than under direct $4f^6$-$4f^6$ transitions of the Eu^{3+} ion in the nanophosphors.[176,167]

The emission spectra (Figure 4.8c and 4.8d) of the $LaF_3:xCe^{3+},xGd^{3+},yEu^{3+}$ (x = 5; y = 1, 5, 10 and 15 mol.%) nanophosphors were recorded at 300 K in the range from 290-750 nm, under excitation monitored at $4f(^2F_{5/2})\rightarrow5d$ (260 nm) along the interconfigurational transitions of the Ce^{3+} ion. All of these spectra exhibit narrow emission bands assigned to $^5D_0\rightarrow^7F_J$ transitions (where J = 1, 2, 3, 4), with the $^5D_0\rightarrow^7F_2$ hypersensitive one (617 nm) for the $LaF_3:xCe^{3+},xGd^{3+},yEu^{3+}$ nanophosphors (Figure 4.8d). Additionally, the emission spectra of these nanomaterials show broad emission band from the $4f^65d^1\rightarrow4f^7$ interconfigurational transition of the Eu^{2+} ion, suggesting that Ce^{3+} (luminescence sensitizer) ions have transferred energy to Eu^{2+} ions (luminescence activator).[167] A further confirmation for the existence of Eu^{2+} ions is obtained from EPR and magnetic susceptibility measurements and the details are given in the later section. Two main features observed in the emission spectra of $LaF_3:xCe^{3+},xGd^{3+},yEu^{3+}$ (x = 5; y = 1, 5, 10 and 15 mol.%) nanophosphors are most notable. The first one is the practically negligible intensity of the $^5D_0\rightarrow^7F_0$ transition, when it is allowed by symmetry, it

"borrows intensity" mainly from the $^5D_0{\to}^7F_2$ transition through the *J*-mixing effect.[174] The second feature is the lower or weak intensity of the $^5D_0{\to}^7F_2$ transition when compared to the $^5D_0{\to}^7F_1$ transition intensity. These findings suggest that the Eu^{3+} ion may occupy high symmetry site (D_{3h}) in LaF_3 matrix, or distorted high symmetry corroborated through XRD analysis.

Figure 4.8: Luminescence spectra of the $LaF_3{:}xCe^{3+},xGd^{3+},yEu^{3+}$(x = 5; y = 1, 5, 10 and 15 mol.%) nanophosphors, recorded at 300 K: (a) excitation spectra, monitoring emission at 617 nm assigned to the $^5D_0{\to}^7F_2$ hypersensitive transition of the Eu^{3+} ion; (b) excitation spectra in the range 200-270 nm, showing the transition 4f($^2F_{5/2}$)$\to$5d interconfigurational transitions of the Ce^{3+} ion; (c) amplified emission range for Ce^{3+} and Gd^{3+} ions; (d) emission spectra under excitation at 260 nm which corresponds to the 4f($^2F_{5/2}$)$\to$5d interconfigurational transition of the Ce^{3+}ion.

However, the weak intensity of the $^5D_0\rightarrow{}^7F_2$ transition might be due to the low polarizability of the fluoride ligand for the LaF_3:xCe^{3+},xGd^{3+},yEu^{3+}(x = 5; y = 1, 5, 10 and 15 mol.%) nanophosphors. This transition is always weak for compounds with fluoride ligands such as Eu^{3+} doped lanthanum fluoride, and is independent of the shape and symmetry of the coordination polyhedron. This typical feature of fluoride ligands might be due to their low polarizability.[81]

4.3.2.1 Calculation of Judd-Ofelt parameters: In order to interpret this result further and to probe the local chemical environment of the Eu^{3+} ion, the experimental intensity parameters Ω_λ (λ = 2 and 4) have been determined for the LaF_3:xCe^{3+},xGd^{3+},yEu^{3+}(x = 5; y = 1, 5, 10 and 15 mol.%) nanoparticles from their emission data recorded at 300 K. The Ω_λ (Judd-Ofelt) parameters, are determined by the intensities of the $^5D_0\rightarrow{}^7F_J$ transitions (J = 2 and 4) of the Eu^{3+} ion, and the forced electric dipole and dynamic coupling mechanisms are considered simultaneously. Under normal excitation conditions, the emission intensities (I) of the bands may be given by the expression:[145]

$$A_{0\rightarrow J'} = \hbar\omega_0 A_{0\rightarrow J}N_0 \tag{4.1}$$

where, $\hbar\omega_0$ is the energy of the transition (in cm^{-1}), N_0 is the population of the emitting $^5D_0$ level and $A_{0\rightarrow J}$ are the coefficients of spontaneous emission. For the experimental determination of the $A_{0\rightarrow J}$ emission coefficients from the emission spectra the special character of the magnetic dipole allowed $^5D_0\rightarrow{}^7F_1$ transition was exploited. This 4f-4f transition is formally insensitive to the chemical environment around the Eu^{3+} ion and consequently, can be used as a reference.[145] The values of Ω_λ are obtained from equation 4.2 as follow:

$$A_{0\rightarrow J'} = \frac{4e^2\omega^3}{3\hbar c^3}\frac{1}{2J+1}\chi\sum_{\lambda=2,4,6}\Omega_\lambda\left\langle{}^5D_0\left\|U^{(\lambda)}\right\|{}^7F_J\right\rangle^2 \tag{4.2}$$

where, $\chi = \frac{n_0(n_0^2+2)^2}{9}$ is the Lorentz local field correction and n_0 is the refractive index of the medium (n_0 assumed to be equal to 1.6).[179] The squared reduced matrix elements $\left\langle{}^5D_0\left\|U^{(\lambda)}\right\|{}^7F_J\right\rangle^2$ have values of 0.0032 and 0.0023 for J = 2 and 4, respectively. The coefficients of spontaneous emission ($A_{0\rightarrow J'}$) are then obtained from equation 4.3:

$$A_{0\rightarrow J} = \left(\frac{\sigma_{0\rightarrow1}}{S_{0\rightarrow1}}\right)\left(\frac{S_{0\rightarrow J}}{\sigma_{0\rightarrow J}}\right)A_{0\rightarrow1} \tag{4.3}$$

where, the $S_{0 \to J}$ factors correspond to the integrated area under the curve related to the $^5D_0 \to {}^7F_J$ transition and $\sigma_{0 \to J}$ are the energy barycenters of the transitions. The emission quantum efficiency (η) of the emitting $^5D_0$ level is determined according to the equation 4.4:[47]

$$\eta = \frac{A_{rad}}{A_{rad} + A_{nrad}}$$

(4.4)

The total decay rate corresponds to, $A_{tot} = \frac{1}{\tau} = A_{rad} + A_{nrad}$, where $A_{rad}(= \sum_J A_{0 \to J})$ and A_{nrad} are the total radiative and nonradiative rates, respectively.

Table 4.4: Experimental intensity parameters (Ω_λ), lifetimes τ (Figure 4.11, given later), emission coefficient rates A_{rad} and A_{nrad} as well as emission quantum efficiencies η for the $LaF_3:xCe^{3+},xGd^{3+},yEu^{3+}$ nanophosphors.

Materials $LaF_3:xCe^{3+},xGd^{3+},yEu^{3+}$	Ω_2 $(10^{-20}$ $cm^2)$	Ω_4 $(10^{-20}$ $cm^2)$	A_{rad} (s^{-1})	A_{nrad} (s^{-1})	A_{tot} (s^{-1})	τ (ms)	η (%)
x = 5; y = 1 mol%	2.1	2.9	158	51	209	4.77	75
x = 5; y = 5 mol%	2.1	3.2	165	43	208	4.80	79
x = 5; y = 10 mol%	2.7	3.7	191	32	223	4.48	85
x = 5; y = 15 mol%	2.1	3.5	169	81	250	4.00	67

On the basis of theoretical considerations,[81] the Ω_2 intensity parameter is by far mostly influenced by small angular changes in the local coordination geometry, while Ω_4 and mainly Ω_6 are by far the most sensitive to lanthanide-ligating atom bond distances.[47] This fact together with changes in the ligating atoms polarizabilities (α) have been used to rationalize the hypersensitive character of certain 4f intraconfigurational transitions to changes in the chemical environment. The fact that the Ω_2 and Ω_4 experimental parameters of all the $LaF_3:xCe^{3+},xGd^{3+},yEu^{3+}$(x = 5; y = 1, 5, 10 and 15 mol.%) nanophosphors (Table 4.4) have quite similar values with each other, is an indication of similar chemical environments and bond distances around the Eu^{3+} ion. However, the lower values of the Ω_2 experimental

intensity parameter of all the LaF$_3$:xCe^{3+},xGd^{3+},yEu^{3+} nanophosphors (Table 4.4) reflect the lower intensity of the $^5D_0 \rightarrow ^7F_2$ transition in these nanomaterials when compared to the $^5D_0 \rightarrow ^7F_1$ transition intensity.[81,181]

The considerably high values of the emission quantum efficiency of the $^5D_0$ level for the LaF$_3$:xCe^{3+},xGd^{3+},yEu^{3+} (x = 5; y = 1, 5 and 10 mol.%) nanophosphors (η = 75, 79 and 85%) are usually consistent with the LaF$_3$ matrix that shows relatively low phonon cutoff energy, reflecting from the considerably low nonradiative (A$_{nrad}$ = 51, 43 and 32 s^{-1}) contribution to the total decay rate (Table 4.4). The emission quantum efficiency of these nanophosphors was increased from η = 75 to η = 85 % as the concentration of the dopant Eu^{3+} ion was increased from 1 to 10 mol.%, respectively. However, the emission quantum efficiency was further decreased to η = 67%, as the concentration of the dopant Eu^{3+} ion was increased to 15 mol. %. This result may be attributed to the increased lattice distortion around Eu^{3+} ion and more defect state, leading to higher nonradiative decay rate (A$_{nrad}$ = 81 s^{-1}). Nevertheless, these nanophosphors yield efficient luminescence intensity and show multicolor emission, indicating they may be good candidates for the solid state lighting e.g., white light emitting diodes (WLEDs).

The presence of the emission bands assigned to the rare earth dopants, namely Ce, Gd and Eu ions, with excitation at 260 nm assigned as 4f($^2F_{5/2}$)$\rightarrow$5d interconfigurational transitions of Ce^{3+} suggests clear evidence of nonradiative energy transfer from $^6P_{7/2}$ (Gd^{3+}), 4f^7($^8S_{7/2}$)$\rightarrow$4f^{6}5d^1 (Eu^{2+}) and $^5D_0$ (Eu^{3+}) emitter states (Figure 4.8c and Figure 4.8d). This energy transfer process is due to the fact that the energy level structures of these RE ions exhibit very similar emitter levels, within only a few hundred cm^{-1} (see Figure 4.9).

4.3.2.2 Energy transfer mechanism: A simplified energy transfer process (Figure 4.9) for these nanophosphors can be described as follows: (i) a strong absorption from the $^2F_{5/2}$ ground state to the 5d excited state of the Ce^{3+} ion leading to a weak emission from 5d to $^2F_{5/2}$ states; (ii) nonradiative energy transfer pathway from the 5d state of the cerium ion to $^6I_{7/2}$ excited state of the Gd^{3+} ion that decays nonradiatively to $^6P_{7/2}$ emitting level resulting weak UV emission assigned to the $^6P_{7/2} \rightarrow ^8S_{7/2}$ transition; (iii) a probable weak absorption from the $^8S_{7/2}$ ground state to the 4f^{6}5d^1$\rightarrow$4f^7 excited state of the Eu^{2+} ion leading to a emission from 5d to $^8S_{7/2}$ states and energy transfer to $^5D_0$ energy level of Eu^{3+} through nonradiative decay process; and (iv) a direct energy transfer from the 5d (Ce^{3+}) and $^6P_{7/2}$ (Gd^{3+}) states to the 4f-4f

intraconfigurational excited states of the Eu^{3+} and Eu^{2+} ions. In this energy transfer process, the Gd^{3+} ion provides another energy transfer pathway between sensitizer (Ce^{3+}) and activator (Eu^{3+}) ions along with Eu^{2+}. Further, a close energy level of excited states of Ce^{3+}, Gd^{3+} and Eu^{2+} may produce inter-energy circulation (see, Figure 4.9). However, the high intensity white-blue-red emission lines are seen due to co-existence of Eu^{2+} and Eu^{3+} in different ratios of Eu^{2+}/Eu^{3+} in all samples.
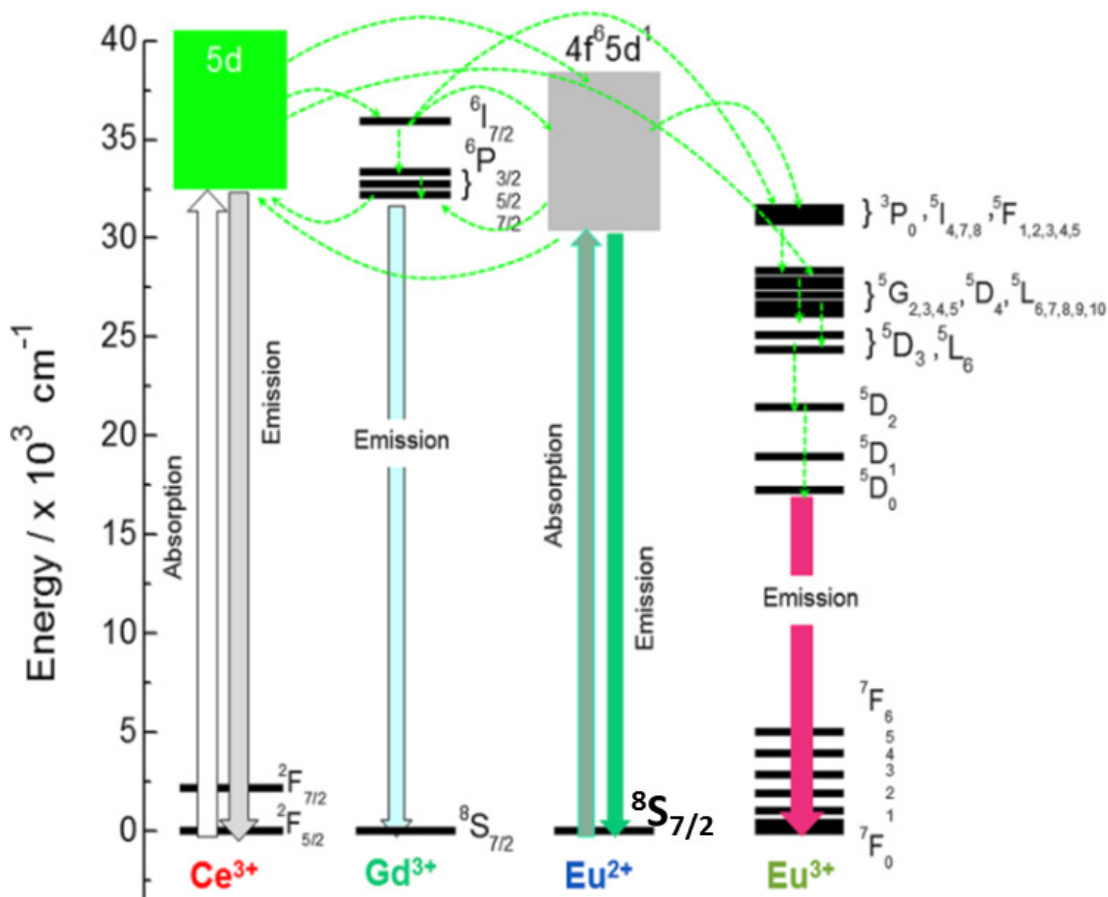
Figure 4.9: Proposed energy transfer mechanism in triply doped multicolor tuned $LaF_3:xCe^{3+},xGd^{3+},yEu^{2+/3+}$ (x = 5; y = 1, 5, 10 and 15 mol.%) nanophosphors.

4.3.2.3 Time decay analysis: The lifetime values (τ) of the emitting $^5D_0$ level of Eu^{3+} ions were determined from the luminescence decay curves of the nanophosphors, which were measured at 300 K by monitoring emission at 617 nm of the $^5D_4 \rightarrow ^7F_2$ transition of Eu^{3+} ion and excitation at 260 nm of Ce^{3+} ion (Figure 4.10). By fitting the curves with exponential function of $I(t) = I_0 \exp(^{-t}/\tau)$, it displays mono exponential decay behavior. The lifetime of

long lived component is relatively long as for Eu^{3+} luminescence, maximum 15 ms.[172] The lifetime coming from Eu^{3+} ions present on the surface of the nanoparticles is 4.77, 4.80, 4.48, and 4.00 ms for LaF_3:xCe^{3+},xGd^{3+},yEu^{3+}(x = 5; y = 1, 5, 10 and 15 mol.%), respectively (Figure 4.10). As the concentration is increased from 10 mol.% to 15 mol.% of Eu ions in matrix LaF_3, quenching of luminescence was observed probably due to cross relaxation mechanism. Since there exists Eu^{2+} ion due to reduction of Eu^{3+} ions and duration of Eu^{2+} luminescence is usually 0.2 to 2 microseconds.[176] It was undetectable over the luminescence decay curves recorded.
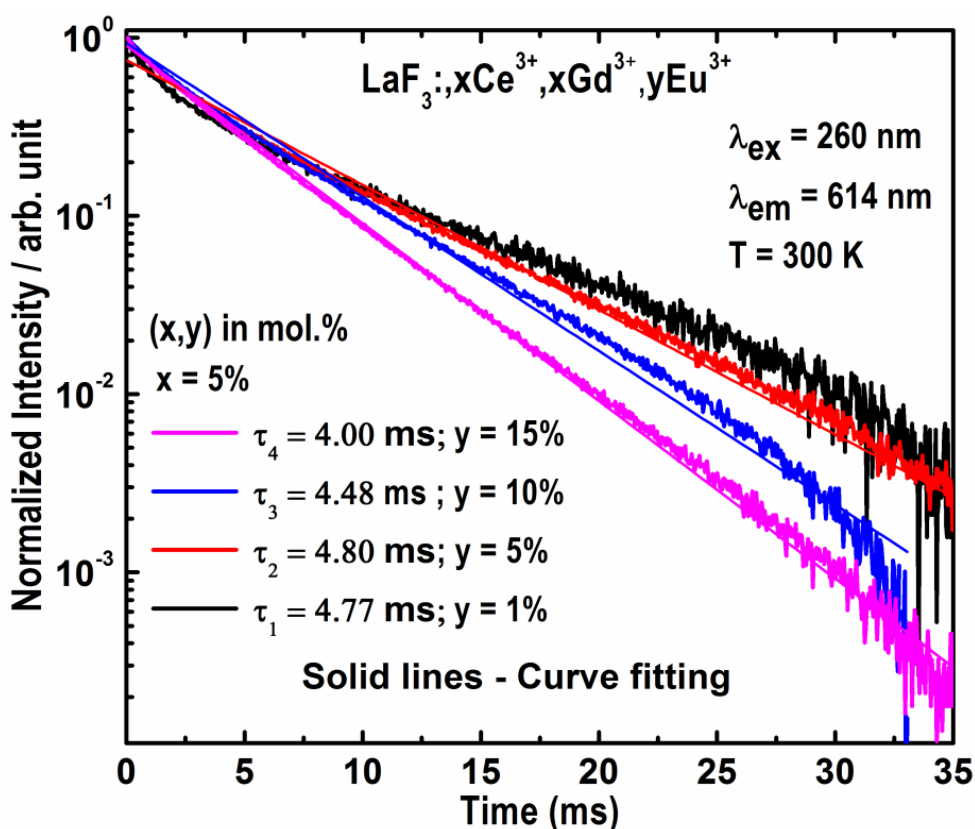
Figure 4.10: Normalized luminescence decay curves of the LaF_3:xCe^{3+},xGd^{3+},yEu^{3+} (x = 5; y = 1, 5, 10 and 15 mol.%) nanophosphors, monitoring excitation at 260 nm corresponding to the 4f($^2F_{5/2}$)→5d interconfigurational transition of the Ce^{3+} ion and emission at 617 nm, assigned to the $^5D_4$→$^7F_2$ transition of Eu^{3+} ion.

In general, the existence of Eu^{2+} ions in the structure force creation of the fluorine vacancies may result in shortening Eu^{3+} lifetimes as the local environment of these ions is more distorted

and defected. Direct interaction between Eu^{2+} and Eu^{3+} ions usually results in the quenching of Eu^{2+} emission because of energy transfer between these ions.[176] The cross relaxation mechanism due to Eu^{3+} ions may occur as following:

$$Eu^{3+} (^5D_1) + Eu^{3+} (^7F_0) \rightarrow Eu^{3+} (^5D_0) + Eu^{3+} (^7F_3).$$
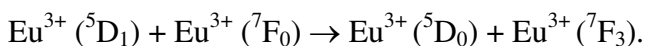
4.3.2.4 CIE chromaticity diagram: The emission color of green emitting nanomaterials evaluated by *Commission Internationale de l'éclairage* -CIE chromaticity diagram, is presented in Figure 4.11. The overall emission color is expressed according to (x, y) CIE color coordinates, which are marked as A(0.2433, 0.3638), B(0.3715, 0.3160), C(0.4234, 0.3240) and D(0.3640, 0.2764), respectively for samples $LaF_3:xCe^{3+},xGd^{3+},yEu^{3+}$ (x = 5; y = 1, 5, 10 and 15 mol%). Upon increasing the concentration of Eu precursor, observed shifting of color is caused by the self-reduction of Eu^{3+} into Eu^{2+} in improper ratio. From blue-green region to white to red region shifting is due to increasing dominancy of Eu^{3+} ions which is corroborated through efficiency given in Table 4.4. The dramatic color change in sample $LaF_3:xCe^{3+},xGd^{3+},yEu^{3+}$ (x = 5; y = 15 mol) is due to lowering in efficiency of Eu^{3+} and probably lower ratio of Eu^{3+}/Eu^{2+}.
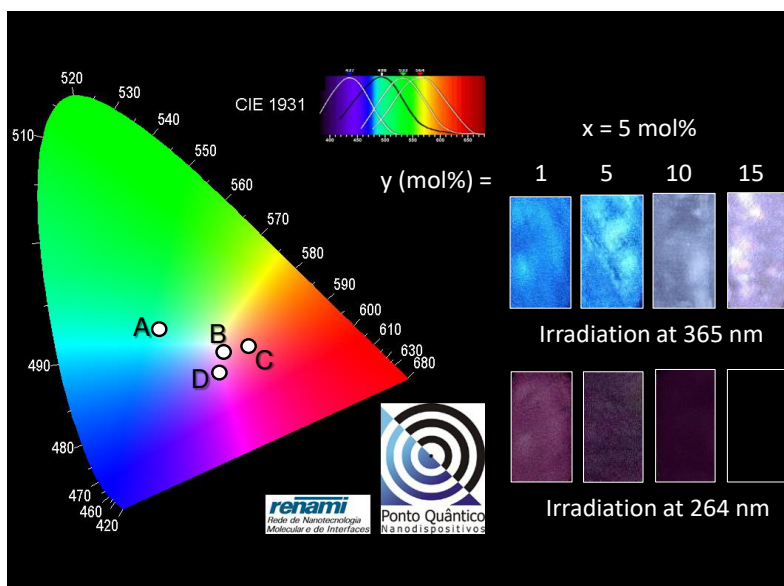
Figure 4.11: The CIE chromaticity diagram of tuned color $LaF_3:xCe^{3+},xGd^{3+},yEu^{3+}$ (x = 5; y = 1, 5, 10 and 15 mol.%) nanophosphors. Photographs of (inset), taken by a digital camera, display the blue-white-red under UV irradiation lamp at 254 and 365 nm.

4.3.3. Magnetic Properties

The magnetic properties of LaF_3: xCe^{3+},xGd^{3+},yEu^{3+} (x = 5 mol.%; y = 1, 5, 10, 15 mol.%) samples were measured as a function of applied field ($\pm$ 7 T) (Figure 4.12). The result showed a linear correlation with the magnetization value in range of 0.40-0.56 emu/g at 7 T and suggests a paramagnetic nature of nanoparticles at 300 K. The host matrix (LaF_3) is diamagnetic in nature. The paramagnetic property is originated mainly due to intrinsic magnetic moment of Ce^{3+}, Gd^{3+} and $Eu^{2/3+}$ ions having non-interacting and localized nature. This characteristic should help the samples to act as multifunctional materials that combine the benefit of multicolor fluorescent probe and probable MRI contrast agents.[152,182]
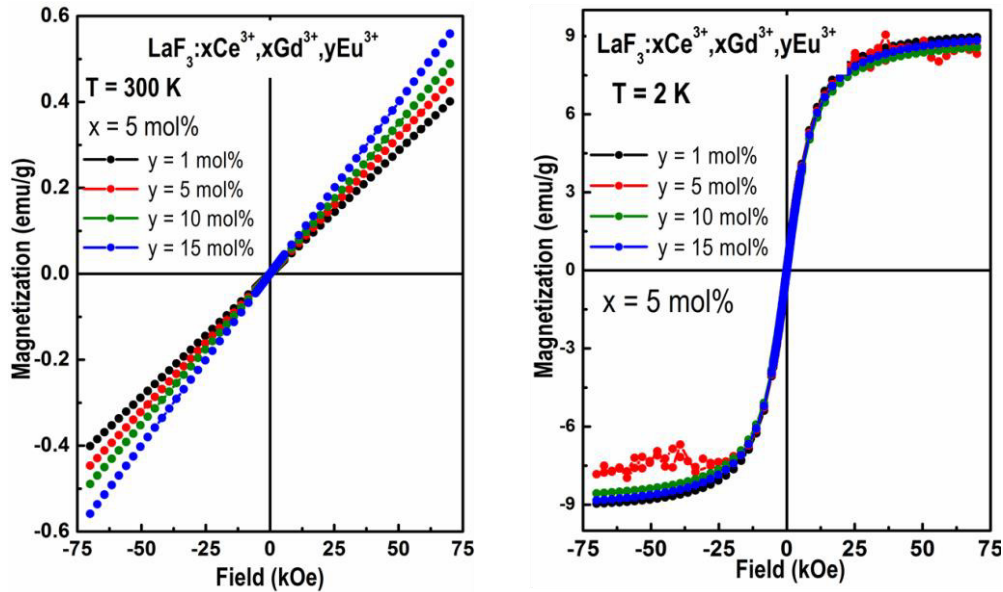
Figure 4.12: Magnetization as a function of magnetic field for LaF_3:xCe^{3+},xGd^{3+},yEu^{3+} (x = 5; y = 1, 5, 10 and 15 mol.%) samples at 300 and 2 K.

From Figure 4.12, it can be observed that nanoluminophores display a paramagnetic nature. Whereas the luminophores at 2K show non-zero hysteretic magnetic curves with a magnetization values of ~ 9 emu/g. The increase in magnetic susceptibility at low temperature might be due to reduction in thermal fluctuation, which is a typical behavior in paramagnetic materials described by Curie's Law.[173] The inorganic compounds containing Gd atoms usually show paramagnetic properties.[147,173] The seven unpaired electrons in inner 4f subshells of Gd^{3+} ions are tightly bounded to the nucleus and shielded by the outer closed shell $5d^1 6s^2$ electrons from the crystal fields. These are responsible for the magnetic characteristic of the Gd^{3+} ions.

The magnetic moment related to Gd^{3+} ions are all localized and non-interacting, which led to paramagnetism of Gd^{3+} ions. Hence the prepared material $LaF_3:xCe^{3+},xGd^{3+},yEu^{3+}$(x = 5; y = 1, 5, 10, 15 mol.%) not only exhibit luminescence properties but also show magnetic properties.

The dc susceptibility (χ_{DC}) as a function of the temperature (T) was obtained in a field of H = 1 kOe for all the investigated samples (Figure 4.13). A typical paramagnetic behavior can be seen for all the $LaF_3:xCe^{3+},xGd^{3+},yEu^{3+}$(x = 5; y = 1, 5, 10, 15 mol.%) samples. The thermal dependence of the susceptibility can be simulated by the Curie–Weiss law given by:

$$\chi_{DC} = \chi_0 + \frac{C}{T-\theta} \qquad (4.5)$$

where χ_0 represents any temperature independent contribution, θ is the Curie–Weiss temperature, C is the Curie constant which is given by

$$C = N\mu_{eff}^2/3k_B, \qquad (4.6)$$

N is the number of doped rare earth ions, μ_{eff} is their effective magnetic moment, which is given by:

$$\mu_{eff} = 2\mu_B[J(J + 1)]^{1/2}, \qquad (4.7)$$

where J is the total angular momentum quantum number of RE^{3+} ions, and μ_B is the Bohr magneton.[173,183] Various magnetic parameters are calculated and summarized in Table 4.5. It is observed that Curie-Weiss temperature is very small and having negative values. These values suggest that the dopants (Ce^{3+}, Gd^{3+} Eu^{2+} and Eu^{3+}) ions show weak ferromagnetic behavior at low temperature. The positive value of χ_0 could be assigned to other temperature independent contributions.

Since LaF_3 is a diamagnetic host matrix and concentration of doped ions of Ce and Gd atoms are here fixed, the only expected effects for the witnessed changes in the magnetic susceptibility can be ascribed to the presence of Eu^{2+} and Eu^{3+} ions. However, the theoretical magnetic moment for Eu^{3+} is zero and, hence, the presence of Eu^{2+} is the key factor that drives the observed modifications of the magnetic responses.[184,185] The co-existence of $Eu^{2/3+}$ is not uniform in all the samples, however XAS and PL data suggest that upon increasing the concentration of Eu dopant, a decrease the ratio of Eu^{2+}/Eu^{3+} ions in the samples is induced (x = 5 mol.%; y = 1, 5, 10 mol.%). This effect leads to a small decrease of the Curie constant, as shown in Table 4.5, upon taking into accounts other effects due to the diamagnetic contributions of LaF_3 along with the van Vleck paramagnetic for Gd^{3+}.[176]
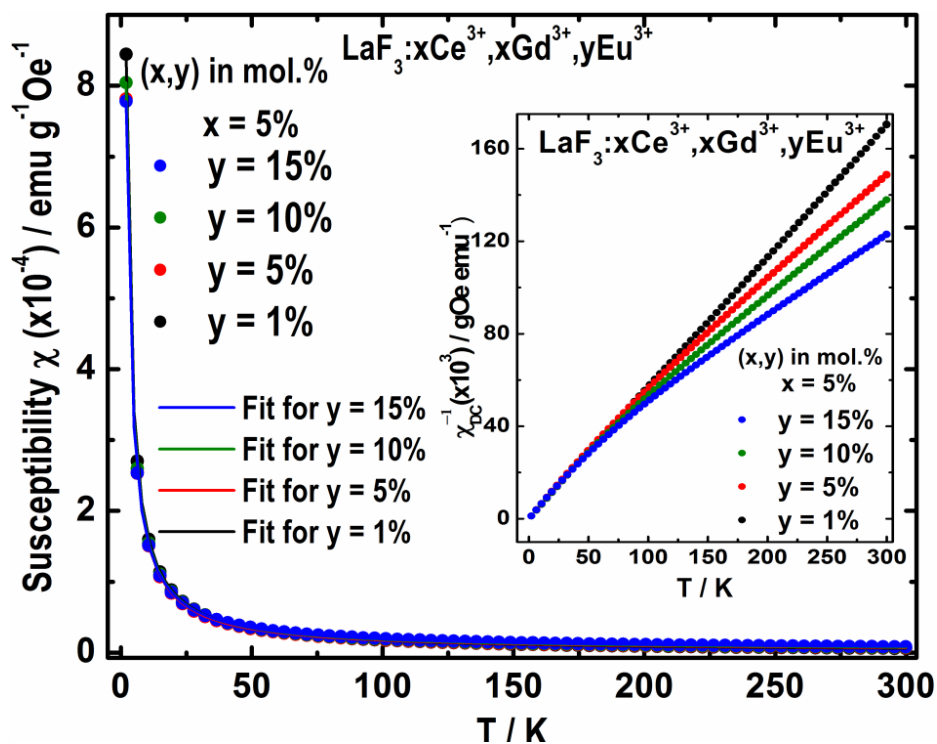
Figure 4.13: The dc magnetic susceptibility measurement performed from 2-300 K for all samples LaF$_3$:xCe^{3+},xGd^{3+},yEu^{3+}(x = 5 mol.%; y = 1, 5, 10, 15 mol.%) in a magnetic field of 1kOe. Inset in Figure shows the inverse susceptibility versus temperature plot.

Table 4.5: List of parameters obtained from experimental dc susceptibility versus temperature curves along with Curie–Weiss fitting.

Eu content (mol%)	χ_0 (emu/gOe)		C (emu K/gOe)		Θ (K)	
	Value (x10^{-6})	Error (x10^{-8})	Value (x10^{-4})	Error (x10^{-6})	Value (x10^{-1})	Error (x10^{-2})
1	0.30	1.87	17.0	0.878	-0.19	0.12
5	1.57	2.90	16.0	1.365	-0.53	0.19
10	2.22	2.93	16.3	1.374	-0.29	0.19
15	3.41	3.52	15.9	1.657	-049	0.24

The paramagnetic behavior observed at 300 K in all the samples is mainly due to Eu^{2+} and Gd^{3+}, which are responsible for the deviation of magnetization as a function of temperature M(T) manifested as an upward bending of magnetization curves at low temperature. This

95

property could also indicate the presence of a magnetically ordered component embedded in the LaF_3 matrix, with exchange coupled Eu magnetic moments that emerge in the low temperature region.[176]

4.3.4 Electronic paramagnetic resonance (EPR)

The X-band (~ 9.1 GHz) EPR spectra of the powder $LaF_3:xCe^{3+}$, xGd^{3+}, yEu^{3+} (x = 5; y = 1, 5, 10 and 15 mol.%) samples are shown together in Figure 4.14. Irrespective of the probed temperature (Figure 4.14a, T= 300 K; Figure 4.14b, T = 10 K) the overall resonances are dominated by a strong and broad derivative line centered at $g \sim 2$ ($\Delta B_{pp} \sim 60$-74 mT).
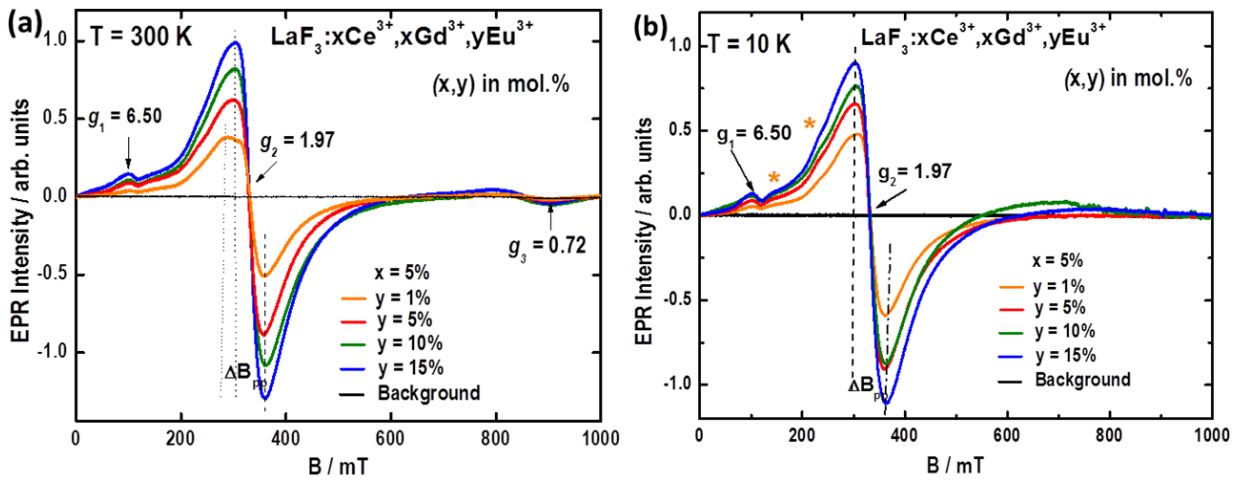
Figure 4.14: The X-band (~9.1 GHz) EPR spectra of $LaF_3:xCe^{3+},xGd^{3+},yEu^{3+}$ (x = 5; y = 1, 5, 10 and 15 mol.%) samples recorded at T = 300 K (a) and T = 10 K (b). Experimental conditions for panel (a) and panel (b), 100 kHz modulation frequency, 1.0 mT of modulation amplitude, 0.03 s of time constant, 30 minutes sweep time. Applied microwave power was 2.6 mW for the traces recorded in panel (a) and 0.1 mW for those shown in panel (b).

At high temperature, additional EPR resonances are clearly visible at low field (*g* = 6.50) and high field (*g* = 0.72). All features appear to increase in intensity upon increasing the effective $Eu^{2+/3+}$ doping. Upon lowering the temperature down to 10 K, additional weak resonances emerge in the low field regions of the spectra, and those are evidenced by stars placed along the EPR lines in Figure 4.14b. While the *g* = 6.50 and *g* ~ 2 components remained well resolved, the high field component becomes undetectable in all the samples.

The EPR spectra of $LaF_3:xCe^{3+}$, xGd^{3+}, yEu^{3+} (x = 5; y = 1, 5, 10 and 15 mol.%) are interpreted as being dominated by resonances arising from both Gd and Eu cations. The Ce^{3+} ion, with its $4f^1$ spin configuration, is expected to show very weak EPR features that become here indiscernible and small g values ($g << 2.0023$). The trivalent Gd^{3+} with the free-ion $S_{7/2}$ ground state is known to exhibit relatively long relaxation time and similarly behaves the Eu^{2+} cation with pure $S_{7/2}$ state.[81,186] Gd^{3+} and Eu^{2+} are Kramer rare earth ions that express features observable by X-band EPR even at room temperature, thus, the recorded fingerprints validate the existence of Eu^{2+} ions in the powder samples, in agreement with PL data.

4.4 Conclusion

In this chapter, the polyol synthesis of triply doped LaF_3 along with in-depth investigation of energy transfer mechanism, photoluminescence and magnetic characteristics have been described. The three step single synthesis allowed obtaining ultrasmall and oleic acid coated nanoparticles, with structural organization confirmed via FTIR, PXRD, HRTEM and EDS mappings. The existence of Eu^{2+} cation along with Eu^{3+} ions was due to the partial reduction of Eu^{3+} cations in diethylene glycol (DEG) and had an advantageous impact on the emission property of $LaF_3:xCe^{3+},xGd^{3+},yEu^{3+}$ nanomaterials. The presence of Eu^{2+} cations on the increasingly doped system, $LaF_3:xCe^{3+},xGd^{3+},yEu^{3+,}$ had a profound effect on the witnessed color of the fluoride luminescence, which spread from blue-white to red as a result of the band $4f^65d^1/4f^7$ transitions of Eu^{2+}. The Judd-Ofelt parameters were fully calculated and showed the greatest efficiency (85%) of the $LaF_3:xCe^{3+},xGd^{3+},yEu^{3+}$ (x= 5,y= 10 mol.%) system. Besides optical properties, the reported materials were magnetically active, and exhibited paramagnetic behaviors in the range of temperatures from 2 to 300 K. A sharp increase in the magnetization at low temperature was also observed, with feature suggesting magnetic ordering when doping exceeded the 5% threshold. The multicolor tuning of these systems may therefore find true applications as scintillating materials in high energy radiation detection. The reasoning behind, apart from their easy access by synthesis, stems from the fact that Ce^{3+}/Eu^{2+} are both gamma ray sensitizer, Gd^{3+} encodes the highest stable cross-section of neutron captor and Eu^{2+}/Eu^{3+} behaves as luminescence activator or wavelength shifter in the visible region. Along with this they are potential candidate for solid state lighting applications such as tuned light emitting diode.

Chapter 5
Green Emitting Magnetic-Luminescent Nanomaterials
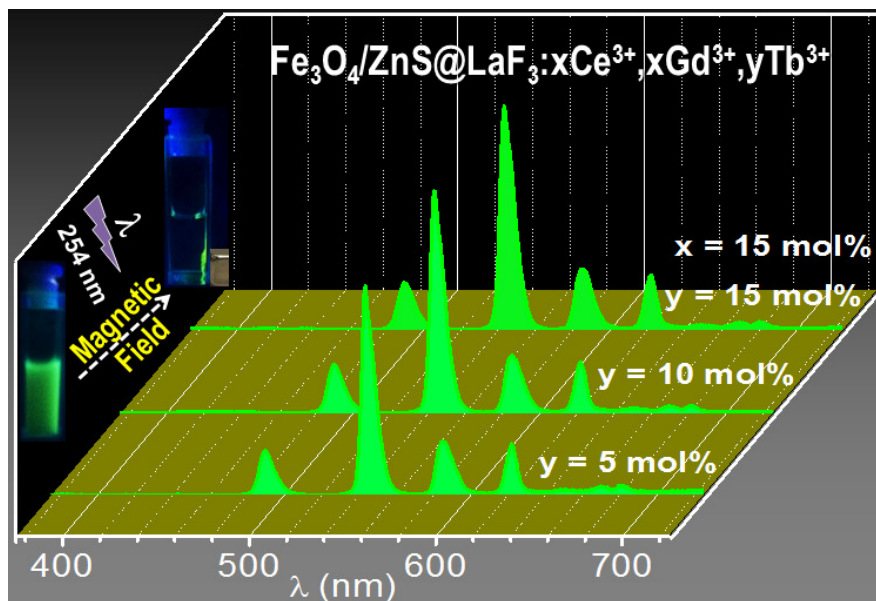
The bifunctional nanocomposite showing strong green emission of Tb^{3+} ion under UV lamp ($\lambda = 254$ nm), with and without external magnetic field.

The preparation of novel triply doped bifunctional $Fe_3O_4/ZnS@LaF_3:xCe^{3+},xGd^{3+},yTb^{3+}$ (x = 5; y = 5, 10 and 15 mol.%) nanocomposites with efficient optical and magnetic features have been reported. The ZnS semiconductor functionalized Fe_3O_4 particles were coated with $LaF_3:RE^{3+}$ (RE = Ce, Gd, Tb) materials via chitosan assisted co-precipitation method. The size of iron-oxide ~7.2 nm and trigonal structure of bifunctional nanostructure were confirmed from x-rays diffraction and high resolution transmission electron microscopy. The static magnetic measurements supported and manifested superparamagnetic behavior of the materials at 300 K. A broad emission band was observed in the blue region (400-550 nm) due to the sulphur vacancy on the surface of Fe_3O_4/ZnS nanocomposite. For triply doped bifunctional nanocomposite, the excitation spectra revealed broad absorption bands centered at around 270 nm, which is attributed to the $4f(^7F_{7/2}) \rightarrow 5d$ interconfigurational transition of the Ce^{3+} ion accompanied by narrow absorption lines arising from the 4f–4f intraconfigurational transitions of the Tb^{3+} ion. The emission spectra of the nanocomposites showed characteristic narrow emission lines assigned to the $^5D_4 \rightarrow ^7F_J$ transitions (J = 6-0) of the Tb^{3+} ion. The energy transfer process from the $Ce^{3+} \rightarrow Gd^{3+} \rightarrow Tb^{3+}$ ions was also presented and discussed. Further, the structural, photoluminescence and magnetic properties of $Fe_3O_4/ZnS@LaF_3:RE^{3+}$ suggested efficient candidature for the magnetic light converting molecular devices (MLMCDs) and high energy radiation detection.

5.1 Introduction

During last decade, the design and engineering of bifunctional nanosized materials by co-assembling magnetic and photonic features into a single entity nanostructure, have gained remarkable attention due to their promising applications in optoelectronics and scintillation of ionizing radiations.[47,122,156,187,188] These nanomaterials are also widely used as multifunctional biomarkers in various biomedical applications such as *in vitro* and *in vivo* labeling,[22,189] quantitative DNA analyses,[190] bioimaging,[191] and magnetic hyperthermia for cancer therapy.[13,192] Therefore, various approaches have been reported to design efficient multifunctional nanomaterials. Usually, the preparation methods of these bifunctional nanostructures include the coating or layer-by-layer deposition of rare earth (RE) phosphors or quantum dots on magnetic core nanoparticles[45,193,194] and polymer assisted encapsulation of magnetic nanoparticles with luminophores in single nanostructures.[28] The functionalization of Fe_3O_4 with fluorescent dyes or luminescent d transition metal complexes are other ways for the synthesis of bifunctional nanomaterials.[47,195,196]

Among the iron-oxide nanostructures, magnetite exhibits long range ordering of magnetic moment, high surface to volume ratio and low toxicity as compared to its parent bulk counterpart. However, the bare Fe_3O_4 nanoparticles are highly vulnerable to self-aggregation and air atmosphere that causes their partial oxidation to maghemite (γ-Fe_2O_3).[197,198] Usually, iron-oxide is strong luminescence quencher. This phenomena occurs *via* an energy transfer process; when a luminescent center (*e.g.*, RE^{3+} ion) comes into contact directly or proximity with the magnetic metal oxide surface (Fe_3O_4).[15,20] In order to overcome this drawback, the intermediate layers, spacers or energy barriers are usually introduced in between the iron-oxide nanoparticles and luminophores. Therefore, iron-oxide nanoparticles can be coated with organic macrocycles, polymers, silica or semiconductors before introducing the luminophores to prepare such bifunctional nanomaterials. It helps to retain their magnetic and luminescence features in same nanoentity. The magnetic properties of these bifunctional nanomaterials are originated directly by the iron-oxide nanoparticles in combination with the magnetic moments of the RE^{3+} ions.

Zinc sulfide (ZnS) is an important semiconductor and classical scintillating material with remarkable physical and chemical properties. The great advantages of ZnS material are: large energy band gap (3.72 eV), considerable excitonic binding energy (40 meV), fluorescent property, environment friendly nature, relatively lower price and simple synthesis procedure.[200]

Therefore, ZnS is a suitable luminophore to synthesize high-photo-stable fluorescent and magnetic Fe_3O_4/ZnS nanomaterials.[200–202] Besides, this nanocomposite structure may act as an energy barrier or separator between the Fe_3O_4 magnetic nanoparticles and RE^{3+} luminophores to lower luminescence quenching phenomena although being composite material. In this system, Fe_3O_4 acts as a semi metal with small band gap and can be expected to quench the luminescence of the ZnS due to leakage path provided by magnetite to excited electrons.[203] This may protect direct contact of magnetite with rare earth luminophores and lower quenching due to interaction between iron-oxide and LaF_3:RE^{3+} luminophores. The nanocomposite Fe_3O_4/ZnS does not affect much the magnetic characteristic. Thus magnetic-luminescent characteristics of Fe_3O_4/ZnS nanocomposite can be manipulated under external magnet field.

The luminescent RE^{3+} nanomaterials present remarkable optical characteristics mainly due to 4f energy level (shielded by externally filled 5s and 5p subshell) by exhibiting narrow emission bands from visible to near infrared range with relatively long lifetimes and high quantum yields.[83,177,204] The absorption and emission spectra of the 4f intraconfigurational transitions of the RE^{3+} ions retain more or less their atomic character and show narrow absorption and emission bands.[47,174] The optical energy transfer mechanism depends strongly on the selection of host lattice. As an example, the LaF_3 is considered as an ideal diamagnetic host matrix for exploitation of electronic transitions and magnetic contribution of dopant RE^{3+} ions,[205] the reason being the size compatibility with the other trivalent rare earth ions following the *Vegard's Law.* This rule establishes a limit of around 15% of the size of RE^{3+} to obtain complete solid solubility between the dopant and the host ion.[28,32,33] The LaF_3 matrix allows a high ionic character of the RE^{3+} and F^- bond leading to a wide band gap, low vibration energies (<350 cm^{-1}), minimal quenching of the electron-hole (e-h) and better chemical stability. These properties make it a versatile host matrix.[60,156,206] The very low vibration energy of the host matrix is an important factor as it protects the dopant ions from deactivation sources through nonradiative decays. This leads towards high emission quantum efficiency. The dopant RE^{3+} ions are selectively chosen to achieve efficient intramolecular energy transfer from sensitizers to the activator ions. These are primary criteria to obtain a highly luminescent nanomaterial.

One of the most intense emitting RE ions is Tb^{3+} ions with many distinct advantages.[35,209] It is paramagnetic at room temperature,[210] non-toxic, biocompatible, ultrasensitive (in vivo and in vitro), highly luminescent and monochromatic. The narrow emission bands of Tb^{3+} ion arising from 4f-4f transitions are independent of chemical environment. On the other hand, the Ce^{3+}

ion presents f-d interconfigurational transition (4f-5d) and can be used as a sensitizer in combination with Tb^{3+} activator, since it provides an easy indirect energy transfer pathway from Ce^{3+} to Tb^{3+} ions.[209,72] There are few reports that show the use of Ce^{3+} ion as a sensitizer in x-ray luminescence and also potential application for high energy radiation detection even in aqueous medium, where it is soluble.[72,71] The coexistence of the paramagnetic Gd^{3+} ($4f^7$) with Tb^{3+} and Ce^{3+} ions, having large energy gap (32000 cm^{-1}) between the $^8S_{7/2}$ and first excited $^6P_{7/2}$ energy level, supports the efficient energy transfer mechanism from Ce^{3+} to Tb^{3+} ions in LaF_3 host matrix in cascaded way. The Gd^{3+} ion has another unique characteristic. It is sensitive to neutron flux irradiation in radiation detection mechanism with highest stable neutron cross-section.[72,211]

In this work, the preparation, structural and morphological characterizations as well as photoluminescence and magnetic properties of the i) Fe_3O_4/ZnS and ii) bifunctional inorganic $Fe_3O_4/ZnS@LaF_3:xCe^{3+},xGd^{3+},yTb^{3+}$ (x = 5; y = 5, 10 and 15 mol.%) nanomaterials have been reported. The dc magnetic properties (M-H and ZFC/FC curves) were studied in order to analyze magnetic information over the final structure of the bifunctional nanocomposite. Moreover, the photoluminescence properties based on the excitation/emission spectral data and luminescence decay curves are also investigated and discussed in detail. The Fe_3O_4/ZnS together with the RE^{3+} ions doped LaF_3 luminescent materials makes the multistep synthesized nanocomposite applicable in downshift processes e.g., in high energy radiation detection as well in magnetic light converting molecular devices.

5.2 Experimental Section

5.2.1 Synthesis: The synthesis of green emitting bifunctional magnetic-luminescent $Fe_3O_4/ZnS@LaF_3:xCe^{3+},xGd^{3+},yTb^{3+}$ (x = 5; y = 5, 10 and 15 mol.%) nanomaterials have been performed according to the multistep synthesis protocol mentioned in chapter 3 (see section 3.1.3.2). However, a complete synthesis procedure has been provided in a following schematic diagram in Figure 5.1.

5.2.2 Instrumentation: The structural analyses have been performed utilizing PXRD, HRTEM and EDS (in STEM mode) techniques as mentioned in section 3.3.2 of Chapter 3. The dc magnetic measurements (M-H at 5 K and 300 K; and ZFC/FC in a field of 50 Oe) have been performed using SQUID magnetometer. The photoluminescence measurements (excitation/ emission and time decay curves for Tb^{3+} ions) have been performed using spectrofluorometer.

All the details are given in chapter 3.2. Further, CIE software has been used to determine the emission color chromaticity of the samples.
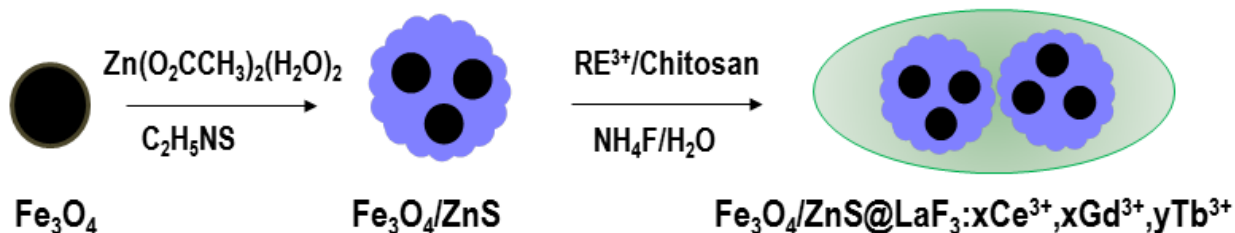
Figure 5.1: General synthesis scheme of $Fe_3O_4/ZnS@LaF_3:xCe^{3+},xGd^{3+},yTb^{3+}$ (x = 5; y = 5, 10 and 15 mol.%) bifunctional green emitting magnetic nanocomposites.

5.3 Results and Discussions

5.3.1 Morphological and structural analyses

5.3.1.1 Powder x-ray diffraction (PXRD): PXRD patterns of Fe_3O_4, Fe_3O_4/ZnS and $Fe_3O_4/ZnS@LaF_3:xCe^{3+},xGd^{3+},yTb^{3+}$ (x = 5; y = 5, 10 and 15 mol.%) nanocomposites have been presented in Figure 5.2. The average crystallite size was found as 7.2 nm for Fe_3O_4 nanoparticles showing cubic structure of the magnetite (iron (II/III) oxide, Fe_3O_4), corresponding to the reported reference pattern (ICDD PDF No. 19-0629).[39]

The PXRD pattern (Figure 5.2b) of the Fe_3O_4/ZnS nanocomposite were matched with reference ICDD PDF No. 12-0688 of the wurtzite ZnS hexagonal structure along with the minor peaks of Fe_3O_4 claiming composite structure. All the diffraction patterns of $Fe_3O_4/ZnS@LaF_3:xCe^{3+},xGd^{3+},yTb^{3+}$ nanocomposites with concentration x = 5; y = 5, 10 and 15 mol.% have been shown in Figure 5.2 c, d and e respectively. These diffraction peaks were indexed and matched with reference pattern ICDD PDF No 32-0483. It suggested trigonal structure (space group P-3c1, group number 165) of LaF_3 with small shifting, *vis-à-vis* existence of peaks of Fe_3O_4 and Fe_3O_4/ZnS nanosystems. The relative intensities of the XRD peaks of $LaF_3:xCe^{3+},xGd^{3+},yTb^{3+}$ were found much stronger and dominant in comparison to those from the Fe_3O_4 and Fe_3O_4/ZnS nanostructures. Further, it was observed that an increase in molar concentration of Tb^{3+} ions in the LaF_3 matrix, exhibited minor change in the profile of the diffraction peaks.
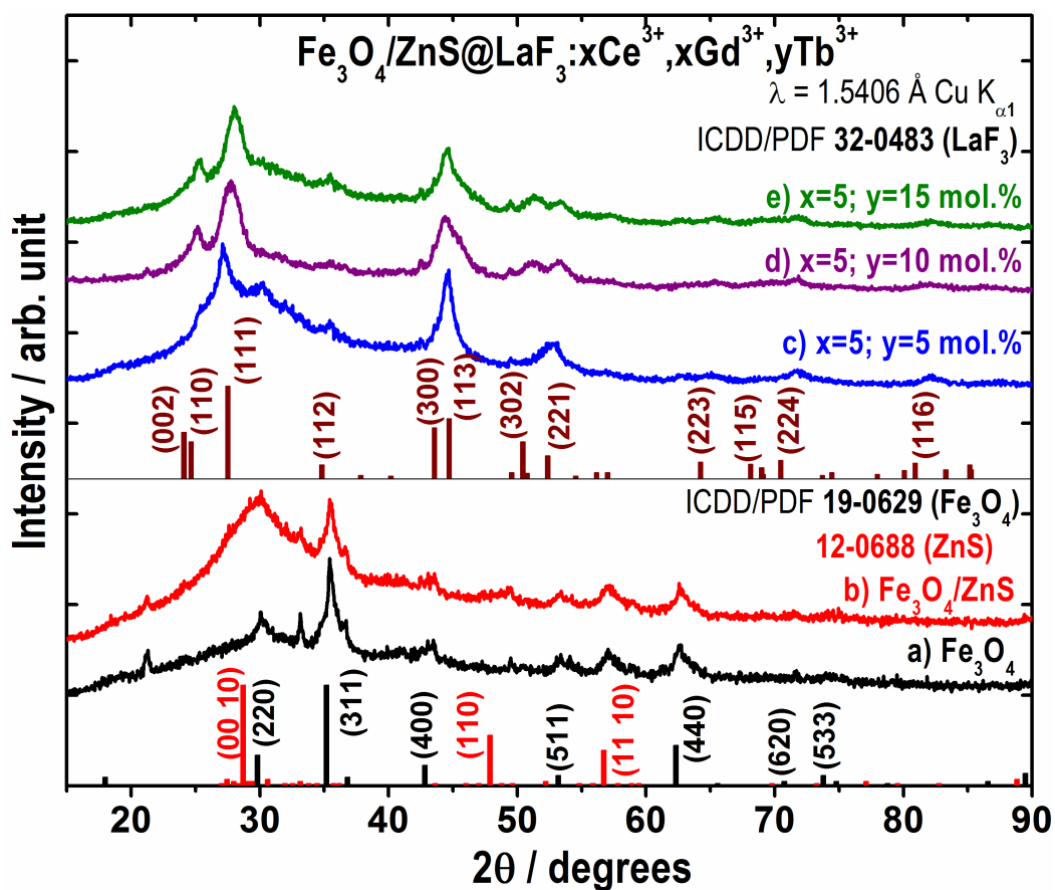
Figure 5.2: PXRD patterns of (a) Fe_3O_4; (b) Fe_3O_4/ZnS; (c, d, e) $Fe_3O_4/ZnS@LaF_3:xCe^{3+},xGd^{3+},yTb^{3+}$ (x = 5; y = 5, 10, 15 mol.%).

5.3.1.2 Transmission Electron Microscopy (TEM): The high resolution TEM image of the iron-oxide nanoparticles showed a majority of small particles (Figure 5.3a, left) with their size between 6 and 8 nm of spherical faceted shape. The inverse spinel structure of Fe_3O_4 has been confirmed from the Fast Fourier Transform (FFT) analysis, indexed along the [211] zone axis (ZA) (Figure 5.3a, right). Further, the existences of aggregated particles with average sizes of 30 nm were observed for the Fe_3O_4/ZnS material (Figure 5.3b, left). These particles showed spherical faceted polyhedral shapes and mass-thickness contrast. The Fe_3O_4/ZnS samples presented a mixture of the Fe_3O_4 cubic and the ZnS hexagonal structures showing d-spacing of (100) and (002) planes of the ZnS (highlighted in red) and (113) plane of the inverse spinel Fe_3O_4 structure, in yellow (Figure 5.3b right), corroborating through the PXRD pattern.
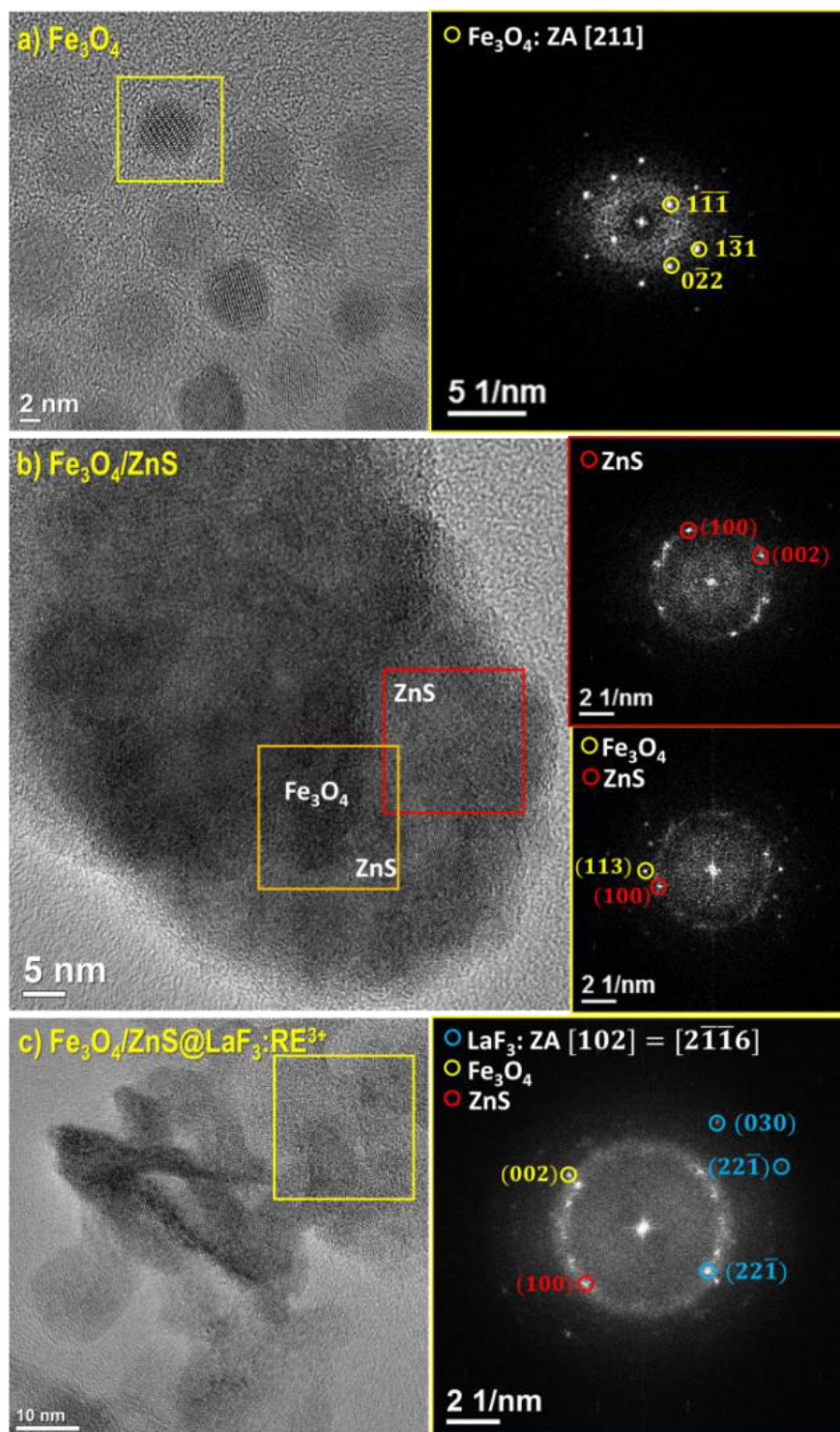
Figure 5.3: HRTEM images of (a) inverse spinel Fe_3O_4 (b) hexagonal Fe_3O_4/ZnS, (c), trigonal Fe_3O_4/ZnS@LaF_3:xCe^{3+},xGd^{3+},yTb^{3+} (x and y = 5 mol.%) samples acquired on JEM-2100F microscope. The regions of the images analyzed applying Fast Fourier Transforms (FFT) are highlighted.

The microstructure of $Fe_3O_4/ZnS@LaF_3:xCe^{3+},xGd^{3+},yTb^{3+}$ (x and y = 5 mol.%) nanoparticles was studied by HRTEM (Figure 5.3c, left), showing the presence of Fe_3O_4 (cubic), ZnS (hexagonal) and LaF_3 (trigonal structure). The Fast Fourier Transform (FFT) analysis showed the LaF_3 structure near the [102] zone axis, as well the presence of the (002) and (100) planes, which corresponds to Fe_3O_4 and ZnS structures, respectively (Figure 5.3c, right). The crystalline properties of all bifunctional nanocomposites indicated dimer like particles and are closer to the polycrystalline like structure.
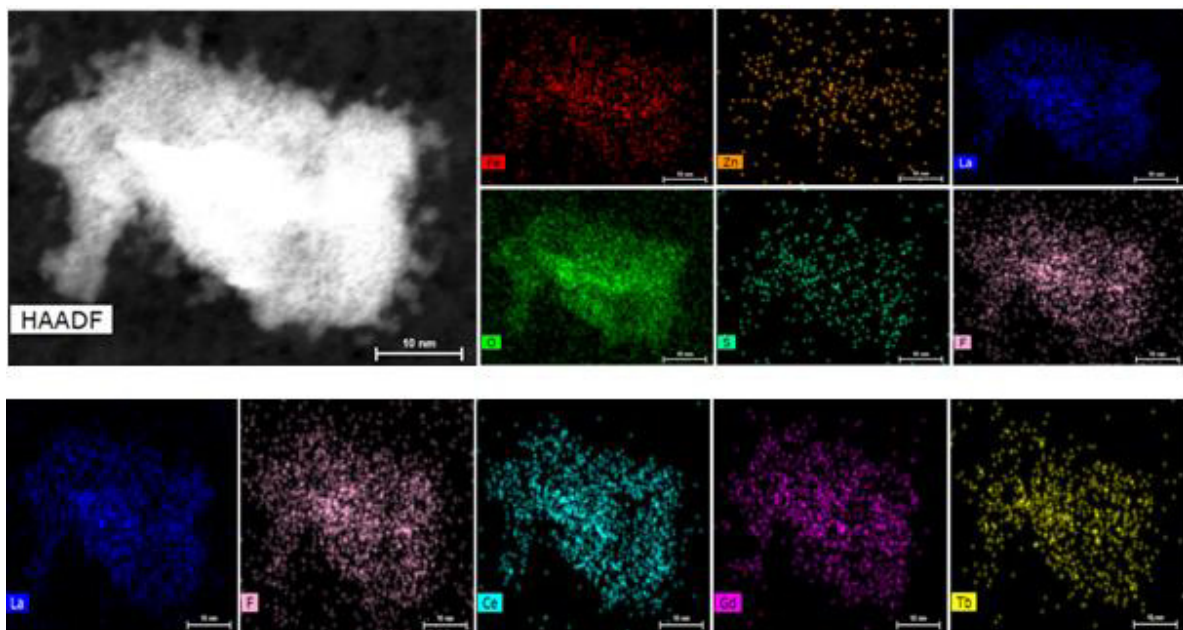
Figure 5.4: High angle annular dark field (HAADF) image and energy dispersive x-ray spectroscopy (EDS) elemental mappings, acquired in the Titan Cubed Themis 300 microscope, showing the homogeneous and uniform distribution of Fe, O, Zn, S, La, F elements (upper panel) and La, F, Ce, Gd and Tb (lower panel) for $Fe_3O_4/ZnS@LaF_3:xCe^{3+},xGd^{3+},yTb^{3+}$ (x = y = 5 mol.%) nanocomposite. All images have the scale bar of 10 nm.

5.3.1.3 Energy dispersive x-ray dispersive spectroscopy (EDS): High angle annular dark field (HAADF) and energy dispersive x-ray spectroscopy (EDS) analyses for elemental mapping (Figure 5.4) illustrate the homogeneous distributions of Fe, O, Zn, S, La, and F along with rare earth dopants. EDS spectra for $Fe_3O_4/ZnS@LaF_3:RE^{3+}$ (x = y = 5 mol.%) sample have been acquired for different spots and the electron beam was focused on agglomerate particles. The observed peaks confirm the existence of Fe, O, Zn, S, La, F, Ce, Gd and Tb

elements (Figure 5.5). The Cu and C peaks may be due to copper grids of ultrathin carbon film with Lacey carbon. The quantitative analysis of the mappings of the analyzed samples shows a difference in relation to the theoretical stoichiometry. The average % elemental composition analysis of lanthanides obtained by EDS spectra (Figure 5.5) for $Fe_3O_4/ZnS@LaF_3:xCe^{3+},xGd^{3+},yTb^{3+}$ (x and y = 5 mol.%) gives La (79.1 ± 2.1 %), Ce (7.6 ± 0.9 %), Gd (6.2 ± 1.3 %) and Tb (7.2± 2.2 %).
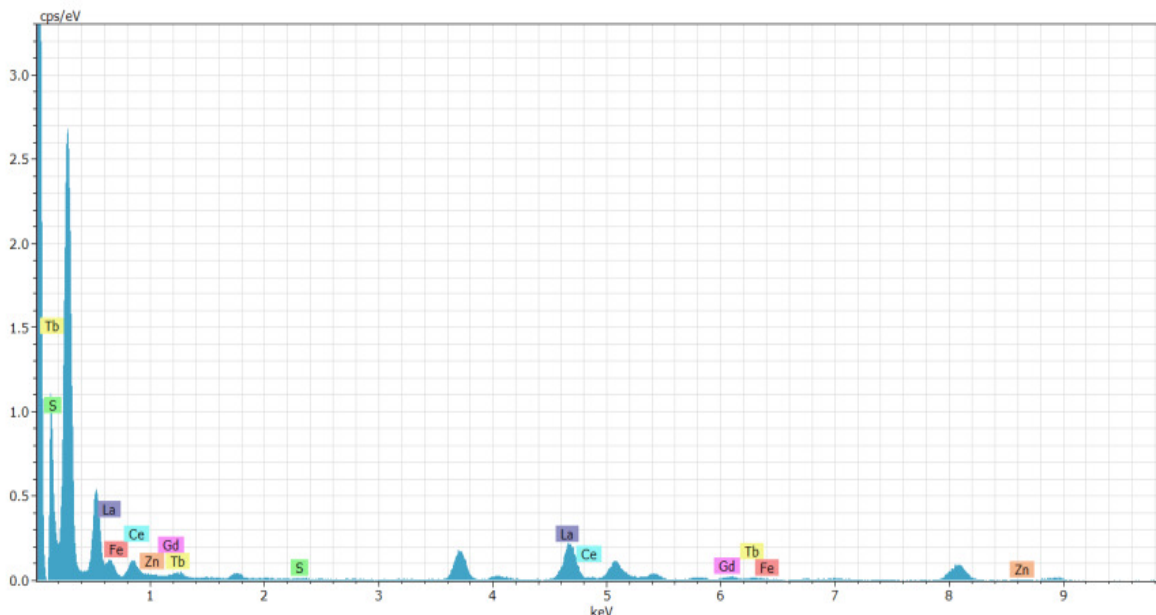
Figure 5.5: EDS spectrum for $Fe_3O_4/ZnS@LaF_3:xCe^{3+},xGd^{3+},yTb^{3+}$ (x = y = 5 mol.%) sample.

5.3.2 Photoluminescence (PL) Properties

5.3.2.1 Fe_3O_4/ZnS luminescence: Excitation spectrum (Figure 5.6a) of the Fe_3O_4/ZnS sample was recorded from 200-400 nm at 300 K, monitoring emission at 440 nm. It displayed a weak intensity broad absorption band centered at around 316 nm, which could be assigned to the band edge transition of the ZnS. The band gap of the ZnS semiconductor usually occurs in the range of 3.93–4.01 eV, which corresponds to the wavelength spectral range from 315 to 309 nm.[212] On the other hand, the emission spectrum of the Fe_3O_4/ZnS nanomaterial was recorded at 300 K, from 350-700 nm under excitation at around 316 nm assigned to the band edge transition of the ZnS (Figure 5.6b).

This emission spectrum revealed low intensity broad emission band centered at around 440 nm, which is usually originates due to the surface defect states such as sulfur vacancies located

at the surface of ZnS nanoparticles.[213] The optical data suggested the functionalization of Fe_3O_4 with ZnS and corroborated with the observed XRD and HRTEM analyses.
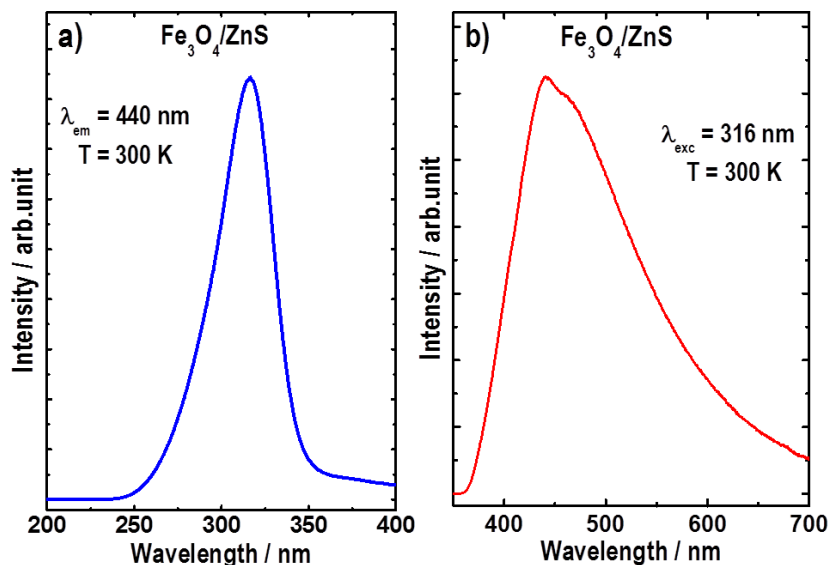
Figure 5.6: Luminescence spectra of Fe_3O_4/ZnS nanoparticles recorded at 300 K, (a) excitation spectrum, monitoring emission at 440 nm, and (b) emission spectrum under excitation at 316 nm which corresponds to the band edge transition of ZnS (3.9 eV).

5.3.2.2 Fe_3O_4/ZnS@LaF_3:xCe^{3+},xGd^{3+},yTb^{3+} green phosphors: The excitation spectra of the Fe_3O_4/ZnS@LaF_3:xCe^{3+},xGd^{3+},yTb^{3+} (x = 5; y = 5, 10 and 15 mol.%) nanophosphors were recorded from 200-470 nm at 300 K (Figure 5.7a), monitoring emission at 543 nm, assigned to the higher intensity $^5D_4 \rightarrow {}^7F_5$ transition of the Tb^{3+} ion. The excitation spectra of all nanomaterials presented high intensity broad absorption band centered at around 258 nm, corresponding to the $4f(^2F_{5/2}) \rightarrow 5d$ interconfigurational transition of the Ce^{3+} ion. Besides, the nanocomposite materials showed narrow absorption lines, assigned to the $4f^8$–$4f^8$ transitions of the Tb^{3+} ion such as: $^7F_6 \rightarrow {}^5L_{8,7,6}$ and $^5G_2$ (339 nm), $^7F_6 \rightarrow {}^5L_9$ and $^5G_4$ (351nm), $^7F_6 \rightarrow {}^5L_{10}$ (369 nm) and $^7F_6 \rightarrow {}^5G_6$ (377 nm). However, the relative intensities of these narrow absorption bands were very low in comparison to the strong broad band of the Ce^{3+} ion. This result indicated that the indirect excitation process of the Tb^{3+} ion *via* $4f(^2F_{5/2}) \rightarrow 5d$ interconfigurational transition of the Ce^{3+} ion, was more operative than under direct $4f^8$-$4f^8$ transitions of the Tb^{3+} ion in the nanophosphors.
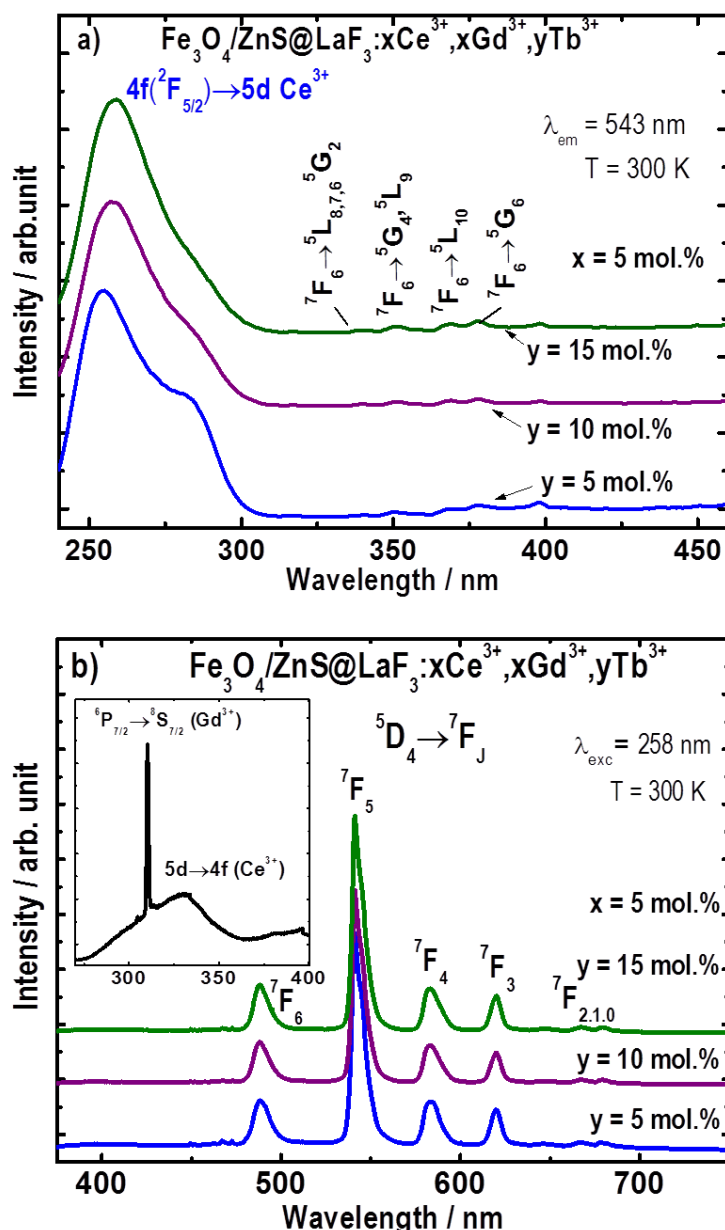
Figure 5.7: Luminescence spectra of Fe_3O_4/ZnS@LaF_3:xCe^{3+},xGd^{3+},yTb^{3+} nanophosphors, recorded at 300 K: (a) excitation spectra, monitoring emission at 543 nm assigned to the $^5D_4{\to}^7F_5$ transition and (b) emission spectra under excitation at 258 nm assigned to 4f ($^2F_{5/2}$)${\to}$5d interconfigurational transition of the Ce^{3+} ion (inset figure shows the amplified spectral range of the Ce^{3+} and Gd^{3+} transitions in the range 270 nm – 400 nm).

The emission spectra of the Fe_3O_4/ZnS@LaF_3:xCe^{3+},xGd^{3+},yTb^{3+} (x = 5; y = 5, 10 and 15 mol.%) bifunctional nanomaterials were recorded from 375-750 nm at 300 K (Figure 5.7b)

under excitation at 258 nm, assigned to $4f(^2F_{5/2}) \rightarrow 5d$ transition of the Ce^{3+} ion. The spectral range from 475-700 nm displayed narrow emission bands which have been assigned to the $^5D_4 \rightarrow ^7F_J$ transitions (J = 6, 5, 4, 3, 2, 1 and 0) of the Tb^{3+} ion. Further, the $^5D_4 \rightarrow ^7F_5$ transition at 543 nm was the most intense and dominant for all the $Fe_3O_4/ZnS@LaF_3:RE^{3+}$ nanophosphors. In addition, a very low intensity emission broad band was observed in spectra range of 270 to 400 nm (inset, Figure 5.7b). It was assigned to the $4f(^2F_{5/2}) \rightarrow 5d$ interconfigurational transition of the Ce^{3+} ion. However, a very narrow emission band at 310 nm in the same emission range was also assigned to the $^6P_{7/2} \rightarrow ^8S_{7/2}$ transition of the Gd^{3+} ion.[40] This result indicated that the Ce^{3+} ion has been an efficient luminescence sensitizer to the Tb^{3+} ion (luminescence activator) for these nanophosphors (Figure 5.7 and 5.8) through energy transfer (ET) process.
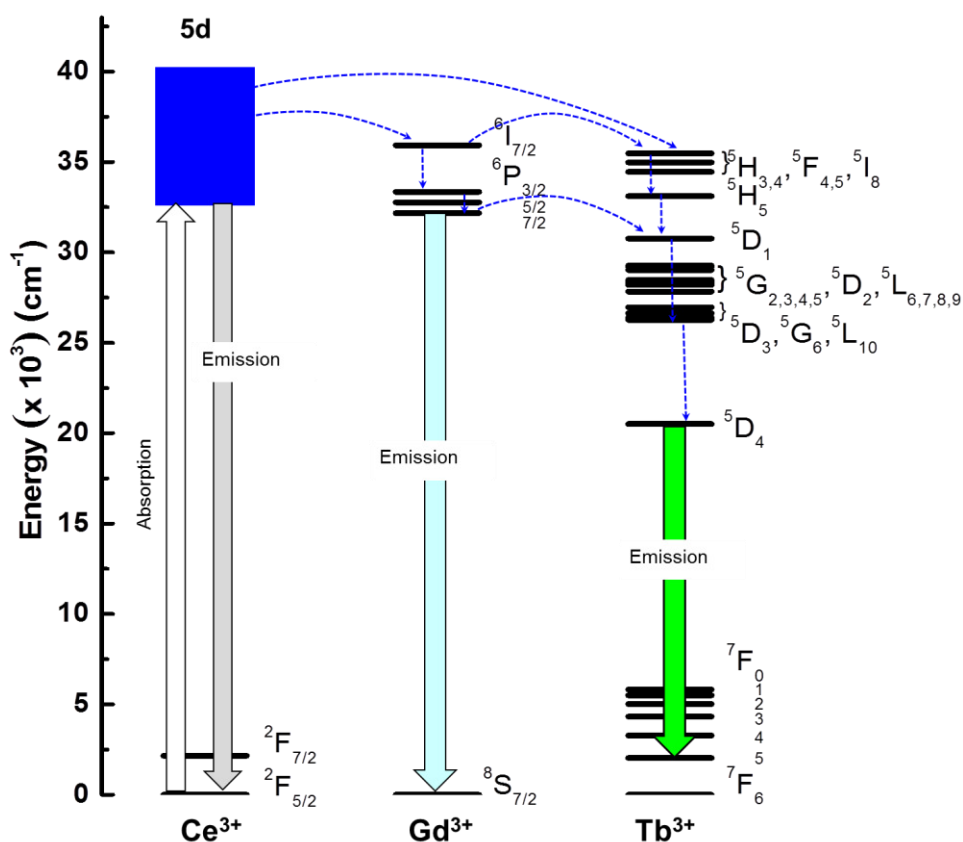
Figure 5.8: Partial energy level diagram of $Fe_3O_4/ZnS@LaF_3:xCe^{3+},xGd^{3+},yTb^{3+}$ nanophosphors presenting energy transfer (ET) processes from the sensitizer (Ce^{3+}) to the Gd^{3+} and Tb^{3+} activator ion. The dashed arrows represent nonradiative decays; and the grey, sky blue and green color downward arrows correspond to the radiative decay of the Ce^{3+}, Gd^{3+} and Tb^{3+} ions, respectively.

5.3.2.3 Energy transfer (ET) mechanism: From the excitation/emission data, the nonradiative ET pathways among the Ce^{3+}, Gd^{3+} and Tb^{3+} ions are described through schematic energy level diagram for the $Fe_3O_4/ZnS@LaF_3:xCe^{3+},xGd^{3+},yTb^{3+}$ samples (Figure 5.8). A simplified energy transfer process for these samples can be described as follows: (i) a strong absorption from the $^2F_{5/2}$ ground state to the 5d excited state of the Ce^{3+} ion leading to a weak emission from 5d to $^2F_{5/2}$ states; (ii) nonradiative energy transfer pathway from the 5d state of the cerium ion to $^6I_{7/2}$ excited state of the Gd^{3+} ion that decays nonradiatively to $^6P_{7/2}$ emitting level resulting weak UV emission assigned to the $^6P_{7/2}\rightarrow^8S_{7/2}$ transition, and (iii) a direct energy transfer from the 5d (Ce^{3+}) and $^6P_{7/2}$ (Gd^{3+}) states to the $4f^8$ intraconfigurational excited states of the Tb^{3+} ion. In this ET process, the Gd^{3+} ion provides another energy transfer pathway between sensitizer (Ce^{3+}) and activator (Tb^{3+}) ions.[214] However, the high intensity green emission line ($^5D_4\rightarrow^7F_5$) is dominated in the emission spectra of $Fe_3O_4/ZnS@LaF_3:RE^{3+}$ nanophosphors. This suggests that the $Fe_3O_4/ZnS@LaF_3:RE^{3+}$ nanophosphors are promising materials for green magnetic light converting molecular devices (MLMCDs).

5.3.2.4 Life time profiles: The lifetime values (τ) of the emitting $^5D_4$ level of Tb^{3+} ion were determined from the luminescence decay curves of the nanomaterials, which were measured at 300 K by monitoring emission at 543 nm of the $^5D_4\rightarrow^7F_5$ transition of Tb^{3+} ion and excitation at 258 nm. By fitting the curves with exponential function of $I(t) = I_0\exp(-t/\tau)$, it displayed mono-exponential decay behavior. The normalized luminescence decay curves of the $Fe_3O_4/ZnS@LaF_3:xCe^{3+},xGd^{3+},yTb^{3+}$ samples are shown in Figure 5.9. The lifetime (τ) values were found to be increased from 7.40 to 7.83 ms as the concentration of dopant Tb^{3+} ion was increased from 5 to 10 mol.%. However, this value decreased to 6.40 ms, as the concentration of dopant Tb^{3+} ion was increased to 15 mol.%, showing concentration quenching [215], which might be due to the cross relaxation process among the Tb^{3+} ions. This process depends on the interaction between two luminescent centers (Tb^{3+} ions) and quenches higher level emissions by cross relaxation. The cross relaxation in Tb^{3+} ions may occur as follow: Tb^{3+} ($^5D_3$) + Tb^{3+} ($^7F_6$) $\rightarrow$ Tb^{3+} ($^5D_4$) + Tb^{3+} ($^7F_0$).

5.3.2.5 CIE chromaticity: The emission color of green emitting nanomaterials was evaluated by *Commission Internationale de l'éclairage*-CIE chromaticity diagram (Figure 5.10). The overall emission color was calculated and expressed according to (x, y) CIE color coordinates, which has been marked as A (0.367, 0.513), B (0.361, 0.535) and C (0.384, 0.513) for the x =

5; y = 5, 10 and 15 mol.% samples, respectively and showing highest green emission intensity contribution of $^5D_4\rightarrow{}^7F_5$ transition of the Tb^{3+} ion (inset, Figure 5.10).
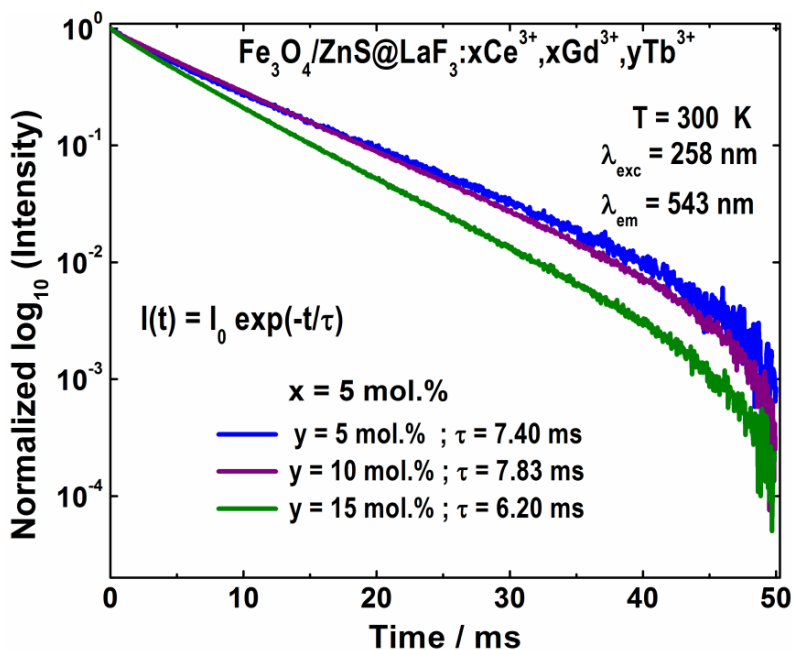
Figure 5.9: Normalized luminescence decay curves of $Fe_3O_4/ZnS@LaF_3$:xCe^{3+},xGd^{3+},yTb^{3+} (x = 5; y = 5, 10 and 15 mol.%) nanophosphors, monitoring excitation at 258 nm corresponds to the $4f(^2F_{5/2})\rightarrow5d$ interconfigurational transition of the Ce^{3+} ion and emission at 543 nm, assigned to the $^5D_4\rightarrow{}^7F_5$ transition of Tb^{3+} ion.
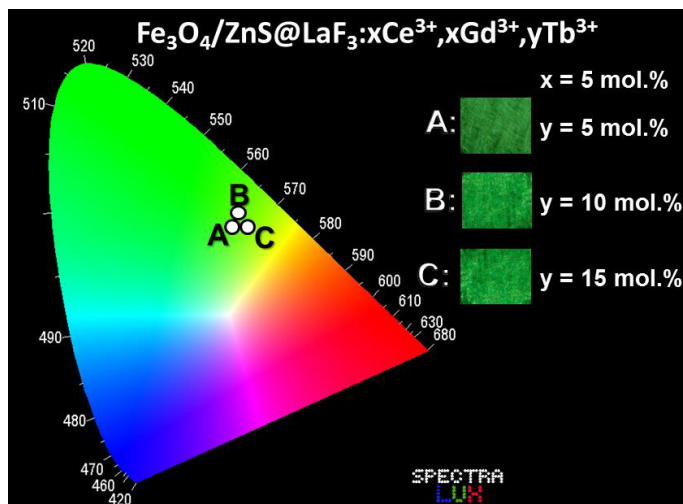
Figure 5.10: The CIE chromaticity diagram of green emitting $Fe_3O_4/ZnS@LaF_3$:xCe^{3+},xGd^{3+},yTb^{3+} (x = 5; y= 5, 10 and 15 mol.%) nanophosphors. Photographs of nanomaterials (inset), taken by a digital camera, displaying the green emission under UV irradiation lamp at 254 nm.

5.3.3 Magnetic Investigation

5.3.3.1 Magnetic hysteresis measurement: The dc magnetic properties using hysteresis loops (M-H curves) were measured by SQUID magnetometer at 300 K and 5 K. At 300 K, the hysteresis loops of Fe_3O_4, Fe_3O_4/ZnS and Fe_3O_4/ZnS@LaF_3:xCe^{3+},xGd^{3+},yTb^{3+} (x = 5; y = 5, 10 and 15 mol.%) nanomaterials showed superparamagnetic behavior with very low value of coercive field H_c (< 25 Oe) and remanence (Figure 5.11). The saturation magnetization (M_s) values were found 40.4 and 36.5 emu/g for Fe_3O_4 and Fe_3O_4/ZnS, respectively. The bifunctional Fe_3O_4/ZnS@LaF_3:xCe^{3+},xGd^{3+},yTb^{3+} samples showed M_s nearly 32.9 emu/g (x =5; y = 5 mol.%), 32.4 emu/g (x = 5; y = 10 mol.%) and 34.4 emu/g (x = 5; y=15 mol.%) (Figure 5.11a). This was attributed due to the variance in particle sizes distribution,[216] hence prolonged existence relaxation of nanostructures and non-collinear spin arrangement in the nanoentities.[217]
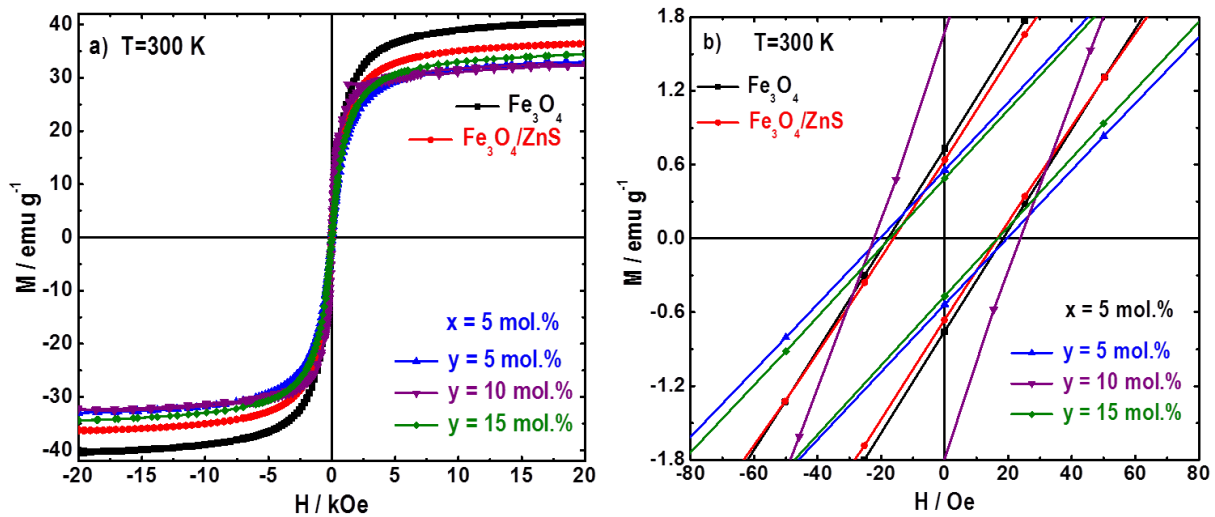
Figure 5.11: Magnetization per gram of iron oxide as a function of magnetic field (M-H) of Fe_3O_4, Fe_3O_4/ZnS and Fe_3O_4/ZnS@LaF_3:xCe^{3+},xGd^{3+},yTb^{3+} (x = 5; y = 5, 10 and 15 mol.%) samples, (a) at 300 K and (b) enlarged view of the low magnetic field regime at taken at 300 K.

The reduced value of M_s revealed the functionalization of Fe_3O_4 with ZnS and further grafting by LaF_3:xCe^{3+},xGd^{3+},yTb^{3+}. Moreover, the decreased value of M_s of iron-oxide from the bulk value (92 emu/g) was mainly due to coating of oleic acid over the Fe_3O_4 nanoparticles during the synthesis. The major contribution in magnetization was due to the iron-oxide nanoparticles. The mass fraction of the magnetic material attached is one of the factors that may affect the M_s to some extent.[218] The M_s of Fe_3O_4/ZnS was decreased due to contribution of low mass

fraction of the ZnS with Fe_3O_4. The overall magnetic contribution for magnetic green emitting nanomaterials was less than Fe_3O_4/ZnS by considering the mass contribution of magnetic-luminescent materials for x = 5; y = 5, 10 and 15 mol. %. The M_s of bifunctional nanocomposite varies from 32.4-34.4 emu/g and it showed very small increase in M_s value by increasing Tb^{3+} ion concentration (Figure 5.11 a). Although the M_s values of the bifunctional nanocomposites were lower when compared to Fe_3O_4 core nanoparticles, but still exhibited strong response to the external applied magnetic field.
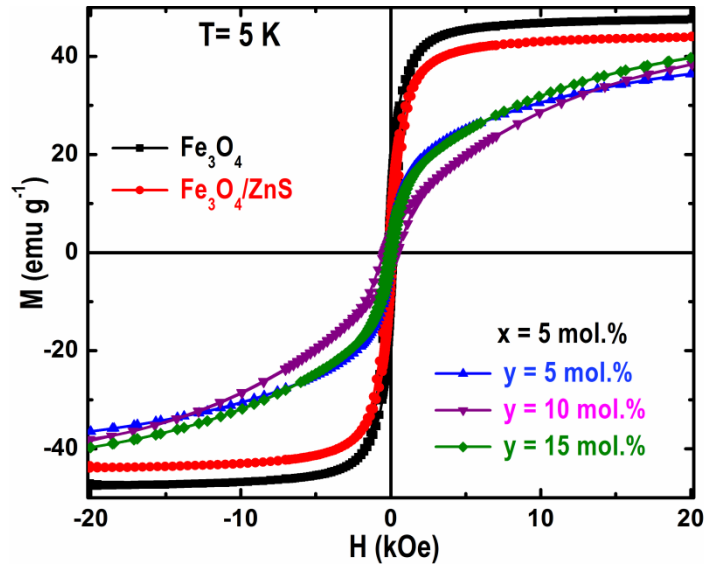
Figure 5.12: Magnetization per gram of iron oxide as a function of magnetic field for Fe_3O_4, Fe_3O_4/ZnS, and Fe_3O_4/ZnS@LaF_3:xCe^{3+},xGd^{3+},yTb^{3+} (x = 5; y = 5, 10 and 15 mol.%) samples at 5 K.

The saturation magnetization for Fe_3O_4 and Fe_3O_4/ZnS was found 47.50 and 44.01 emu/g, respectively at 5 K (Figure 5.12). The functionalization of semiconducting material ZnS with iron oxide did not affect magnetic property much. The higher value of saturation magnetization M_s compared to the values at 300 K, showed the dominant ferromagnetic nature of iron-oxide with probably some complex interaction among ions of Fe_3O_4/ZnS nanostructure and size-shape of the nanocomposites, produced during synthesis. After coating LaF_3:xCe^{3+}, xGd^{3+}, yTb^{3+} (x =5; y = 5, 10 and 15 mol.%) around Fe_3O_4/ZnS, saturation magnetization also increased to 36.42 , 38.54 and 39.63 emu/ g for x=5 and y = 5, 10 and 15 mol.% respectively in comparison to values at room temperature (Figure 5.12). Furthermore, increasing the concentration of Tb^{3+} ions in LaF_3:xCe^{3+}, xGd^{3+},yTb^{3+} showed a small magnetic contribution

of Tb^{3+} ion with variation in the coercivity value. This type of effect certainly indicated that their individual magnetic moment remained in a random fixed orientation without spontaneous magnetization switching i.e. they showed blocked regime behavior at low temperature.

5.3.3.2 ZFC/FC measurement: The measurement of temperature dependence magnetic property (M-T curves) under field cooling (FC) with an applied field of 50 Oe and zero field cooling (ZFC) from 5-300 K were performed for Fe_3O_4; Fe_3O_4/ZnS; and $Fe_3O_4/ZnS@LaF_3:xCe^{3+},xGd^{3+},yTb^{3+}$ (x = 5; y = 5, 10 and 15 mol.%) samples (Figure 5.13). The shapes of ZFC/FC curves are more like a collective assembly of nanoparticles with superparamagnetic nature at 300 K. It can be seen the differences between the ZFC profiles for all samples. For Fe_3O_4 nanoparticles, a maximum can be observed nearly 170 K, indicating its blocking temperature. Further, shifting in blocking temperature can be seen in Fe_3O_4/ZnS (Figure 5.13a) and $Fe_3O_4/ZnS@LaF_3:xCe^{3+},xGd^{3+},yTb^{3+}$ (x = 5; y = 5 and 15 mol.%) in Figure 5.13b below 300 K.
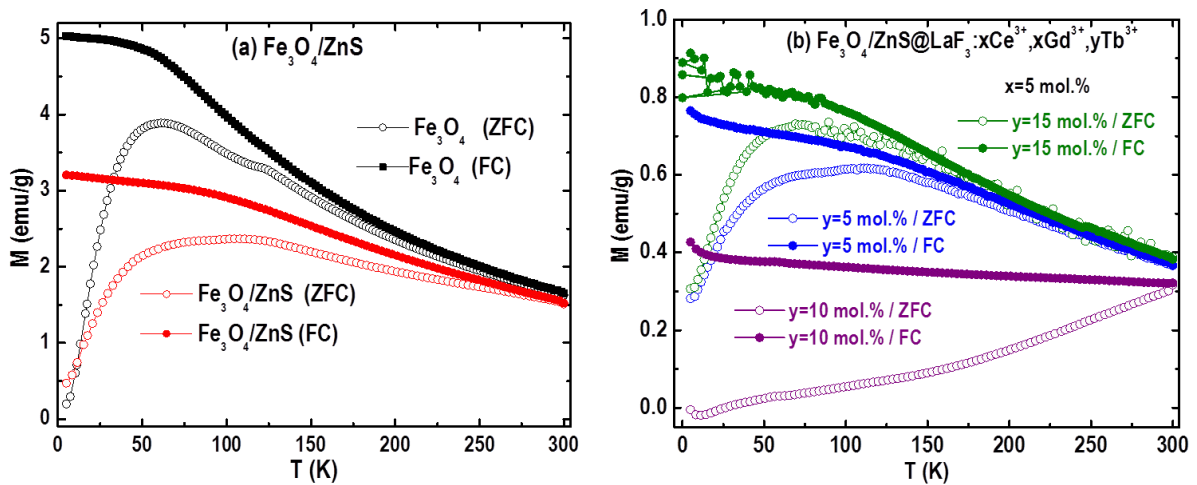
Figure 5.13: Zero field cooling (ZFC) and Field cooling (FC, at 50 Oe) measurements for the (a) Fe_3O_4 and Fe_3O_4/ZnS, and (b) $Fe_3O_4/ZnS@LaF_3:xCe^{3+},xGd^{3+},yTb^{3+}$ (x = 5; y = 5, 10 and 15 mol.%) samples.

However, the blocking temperature for sample $Fe_3O_4/ZnS@LaF_3:xCe^{3+},xGd^{3+},yTb^{3+}$ (x = 5; y = 10 mol.%) is not in the measured temperature range. It can be due to dipolar interaction among iron-oxide nanoparticles and aggregation of $Fe_3O_4/ZnS@LaF_3:xCe^{3+},xGd^{3+},yTb^{3+}$ (x = 5; y = 10 mol.%) nanoparticles. These changes in blocking temperature also indicate probable random sizes and shapes of materials. It is interesting to notice that the magnetization increase

for the ZFC and FC curves of the $Fe_3O_4/ZnS@LaF_3:xCe^{3+},xGd^{3+},yTb^{3+}$ (x = 5; y = 5, 10, 15 mol.%) samples in the low temperature range (Figure 5.13). This effect is due the paramagnetic contribution and higher magnetic moment of the Tb^{3+} ion, showing the non-negligible effect of Tb^{3+} ion on the magnetic properties.

5.3.4 Magnetophoretic Experiment

Combining the luminescence with magnetic characteristic together showed appreciable luminescent intensity from the nanomaterial under external magnetic field. It depicts the potential application of bifunctional nanomaterials for magnetic targeting and separation. The combination of magnetic and photoluminescence properties of green emitting magnetic nanocomposite has been shown in Figure 5.14, displaying successful alliance of magnetic-luminescent characteristic of the $Fe_3O_4/ZnS@LaF_3:RE^{3+}$ nanomaterial.
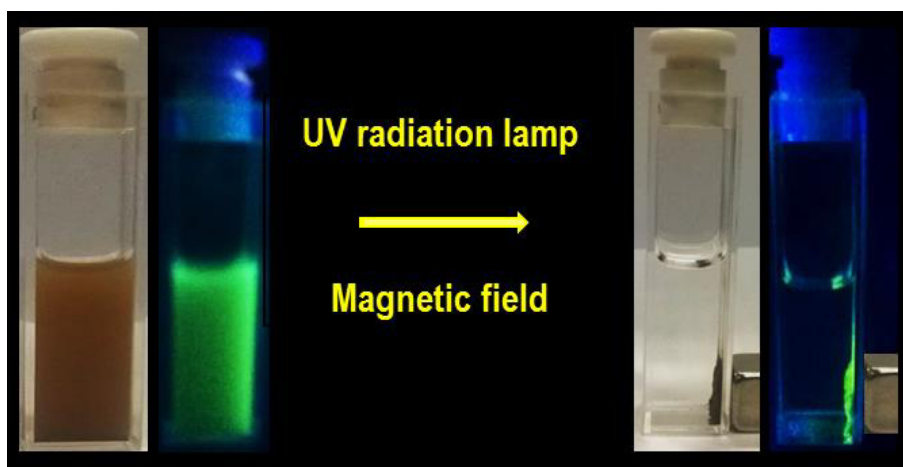
Figure 5.14: Digital photograph of $Fe_3O_4/ZnS@LaF_3$: $xCe^{3+},xGd^{3+},yTb^{3+}$ (x = 5; y = 15 mol.%) nanocomposite dispersed in ethanol without (left) and with external magnet (right) under UV irradiation at 254 nm.

In a cuvette, the material was dispersed in ethanol, displaying bright green emission under UV radiation. After applying the external bar magnet close to cuvette, all particles of the sample were moved quickly and stacked to a single place of the one side of the cuvette in clear solution of ethanol. This showed that the materials possessed strong magnetic characteristics. Besides, under exposure to the ultraviolet radiation of 254 nm, bright green light was perceived from the same corresponding place on the side wall of cuvette near magnet (Figure 5.14, right).

This complete procedure pointed out that these bifunctional nanoparticles owned clear strong magnetic and luminescent properties in conjugation. In brief, this nanocomposite can show better performance by tuning simultaneously magnetic and luminescence bifunctionality.

5.4 Conclusion

The luminescence and magnetic nanocomposites containing triply doped Fe_3O_4/ZnS@LaF_3:xCe^{3+},xGd^{3+},yTb^{3+} (x = 5; y =5, 10, 15 mol.%) were successfully prepared by multistep synthesis procedure. Employing ZnS as a spacer between direct linkage of Fe_3O_4 and green LaF_3:RE^{3+} phosphors played its role well. This bifunctional nanomaterial displayed good emission intensity from the $^5D_4 \rightarrow {}^7F_{6-0}$ transitions of Tb^{3+} ion when excited at the 4f$\rightarrow$5d *inter*configurational transition of Ce^{3+} and supported by Gd^{3+} ion. The luminescence decay profiles suggested probable concentration quenching for the $^5D_4 \rightarrow {}^7F_5$ transition of Tb^{3+} ion by cross relaxation. Structural and morphological studies using x-ray diffraction and HRTEM with EDS mappings in scanning TEM mode, supported by dc magnetic properties revealed the nanocrystalline, high magnetic saturation and superparamgnetic nature of the bifunctional nanocomposite at 300 K. As a result, this magnetic luminescent bifunctional nanocomposite may act as good candidates for the preparation of emitting layers in magnetic light converting molecular devices (MLCMDs) and radiation detection or in downshift applications through magnetic manipulation.

Chapter 6
Optical–Magnetic Characteristics for Dual Optical Window
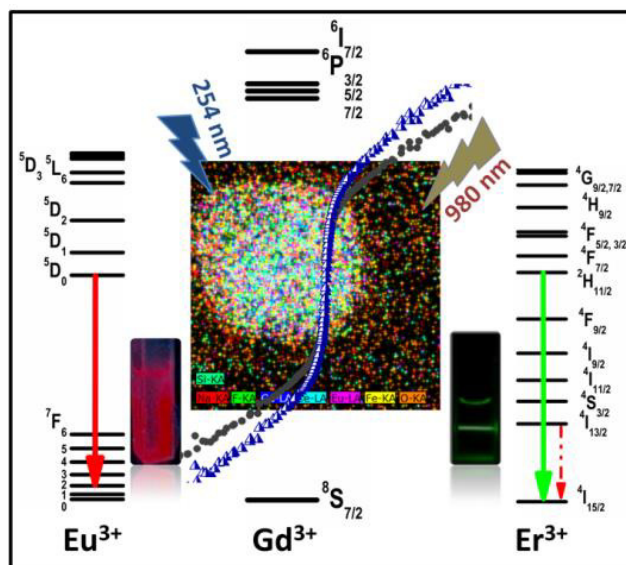
Red (Ce, Eu) and Green (Yb, Er) emission from superparamagnetic iron-oxide/SiO_2/$NaGdF_4$:RE^{3+} (Ce, Eu and Yb, Er) upon excitation by 254 nm ultraviolet light and 980 nm laser.

We report the microwave assisted thermolysis synthesis of binary doped optical-magnetic up/down converting β-$NaGdF_4$:RE^{3+} and iron-oxide/SiO_2/$NaGdF_4$:RE^{3+} (RE = Ce, Eu; Yb, Er) nanoparticles. The morphological characteristics of these systems were finely tuned from elongated rod-shaped nanoparticles in β-$NaGdF_4$:RE^{3+} to ovoidal nanoparticles for iron-oxide/SiO_2/$NaGdF_4$:RE^{3+}. The (Yb, Er) activated particles provided an excellent up/down conversion luminescence emission in visible (green) and mid-infrared optical windows, under excitation wavelength of 980 nm, whereas the (Ce, Eu) activated systems exhibited a strong red emission ($^5D_0{\rightarrow}^7F_2$ of Eu^{3+}) *via* Gd^{3+} sub-lattice upon excitation in the UV region. The magnetic hysteresis at 300 K for β-$NaGdF_4$:RE^{3+} showed typical signatures of a paramagnetic system, whereas the iron-oxide/SiO_2/β-$NaGdF_4$:RE^{3+} nanocomposites exhibited superparamagnetic behavior, along with the presence of a Curie-like component at high applied field, which was due to a paramagnetic contribution. The luminescence quenching effects induced by the presence of an iron-oxide phase have been validated by comparing the emission and life time decay curves of the β-$NaGdF_4$:RE^{3+} with those expressed by the iron-oxide/SiO_2/$NaGdF_4$:RE^{3+}. Owing to their excellent magnetic and optical responses, as witnessed in the dual optical window experiments, these new materials have high potentials for technological applications such as bio imaging and field detections.

6.1 Introduction

Multifunctional nanoparticles that are capable to merge together optical and magnetic properties into a single nanostructured material, became, in the last two decades, the target of intensive research efforts, because such materials can be easily implemented in a variety of industrial applications, from bio-clinical to communication technologies.[45,219,220,221,58] In order to achieve sustainable cooperation between optical and magnetic properties, two main synthetic routes have been so far explored for the successful assembly of such nanomaterials.[45,182,222–225] The most conventional approach (route (i)) relies on the combination of two distinct nonoentities, one magnetic and one luminophore nanoparticles, which are merged into a nanocomposite unit. Another approach (route (ii)) relies on the direct engineering of a single phase luminophore that is already magnetic. In both cases, the final target is the harmonious integration and modulation of the optical and magnetic properties into a functional nanomaterial, which can deliver, for example, an excellent platform for cell imaging.[23] In fact, optical imaging techniques offer improved high spatial resolutions, allowing the visualization of the cell structures. However, they have limited depth in imaging and poor quantitative accuracy, due to the absorption of light by tissues.[175] Magnetic imaging has no practical limitation in terms of depth but the spatial resolution is worse compared to the optical technique.[116] Hence, combination of multiple imaging (optical/magnetic) in multi-modality,[45,182,226,227] provides directly more information on the imaged object.

Despite the "*on paper*" simplicity on pursuing either route (i) or route (ii), the synthetic assembly of magnetic and optically active nanoparticles is a challenging task. This is due to several barriers that stand upon delivering materials in which magnetic and electrostatic interactions are finely controlled, and the hydrophobic/philic surfaces are careful engineered in a way to remain stable e.g., in biological media.[23] So far, optical/magnetic nanocomposites have been obtained via route (i) or (ii) by using as key-components in a large variety of systems, such as quantum dots, organic dyes, conjugated polymers, and rare earth complexes.[47,182,228,229] Following route (i), the synthetic methods include coating or layer-by-layer deposition of luminescence nanoparticle over the magnetic nanoparticles. Alternatively, the cross-linking of these two systems can be achieved by using other organic molecules that act as spacer between them, and the so obtained materials display the morphological organization of core-shell composites.[147] Moving to single phase material (route (ii)) containing magnetic and optical functionality (e.g. gadofluorophores: Gd containing

luminescence materials), their synthesis is relatively easier compared to route (i), and several examples can be found in the literature.[45,57,58,230,231] The control of the nanoparticle size and morphological evolution of the nanosystem is equally important, because size and morphology have large impact on tuning the material optical/magnetic performances as well as on the material biocompatibility.[232–234] The biocompatibility and strong magnetic property of iron-oxide nanoparticles have prompted us to employ this material in combination with luminophores, and then to investigate the resulting impacts on both luminescence proclivity and magnetic responses of the merged system.[23] The commonly explored luminophores are based on rare earth ions (RE^{3+}), which exhibit intense narrow intra 4f–4f luminescence bands in a wide range of hosts, covering UV to IR region that depends upon excitation wavelengths, presence of dopants, and chemical identity of the matrix.[60] Recent reports have demonstrated that optical-magnetic properties can be observed simultaneously in a single crystal or single phase fluorides by RE doping[1,5,23] such as in $NaGdF_4:RE^{3+}$ ($RE^{3+} = Ce^{3+}$, Eu^{3+}; Yb^{3+}, Er^{3+}). $NaGdF_4$ is, in fact, one of the most flexible host matrix.[39,57,58,231,235,236] Systems based on $NaGdF_4:RE^{3+}$ have the advantage to encode (i) low phonon energy (< 370 cm^{-1}), (ii) highly stable cross-sectional captor,[237] (iii) minimal quenching, leading to relatively long decay time of the excited emitting level, hence, to higher luminescence efficiency, and (iv) have the ability to prevent generation of participating phases even under heavy doping of other lanthanide ions. In this work, we report the synthesis and properties of a merged system that benefit from the use of combining iron-oxide and $NaGdF_4:RE^{3+}$ materials together. The synthesis is achieved *via* a microwave assisted thermolysis route to synthesize $NaGdF_4:RE^{3+}$ nanoparticles, followed by the use of a template route to assemble the iron-oxide/SiO_2/$NaGdF_4:RE^{3+}$ composite. Correlation between structure and morphological organization with the optical-magnetic properties of these materials has been carried out using different spectroscopic techniques. In particular, our work shines light on the physical principles that govern the changes in the intensity of the emission peaks and their lifetime variations promoted by the iron-oxide phase, the benefits obtained as well as the drawbacks encountered in these merged systems, so to draw a realistic portray of the possible implementation of similar materials in real world scenarios.

6.2 Experimental Section

The chemical reagents and the procedure to obtain $NaGdF_4:RE^{3+}$ and iron-oxide/SiO_2/$NaGdF_4:RE^{3+}$ nanocomposites are discussed in chapter 3 (section 3.1.3.3). The

dopant (RE^{3+} = 5 mol.% Ce^{3+} & 5 mol.% Eu^{3+}) and (RE^{3+} = 20 mol.% Yb^{3+} & 2 mol.% Er^{3+}) were used in $NaGdF_4$:RE^{3+} and iron-oxide/SiO_2/$NaGdF_4$:RE^{3+} nanomaterials. The synthesized materials were thoroughly characterized using Rietveld refinement of x-ray diffraction pattern, high resolution transmission electron microscopy techniques, Fourier transform infrared spectroscopy, and photoluminescence and dc magnetic measurements. The detailed description of instrumentation has been provided in chapter 3.

6.3 Results and Discussions

6.3.1 Crystallization behavior, structure and morphological evolution studies

The synthetic steps undertaken to produce $NaGdF_4$:RE^{3+} and the iron-oxide/SiO_2/$NaGdF_4$:RE^{3+} materials and their growth mechanism in 1-octadecene (1-ODE) and oleic acid (OA) solutions are schematically illustrated in Figure 6.1.
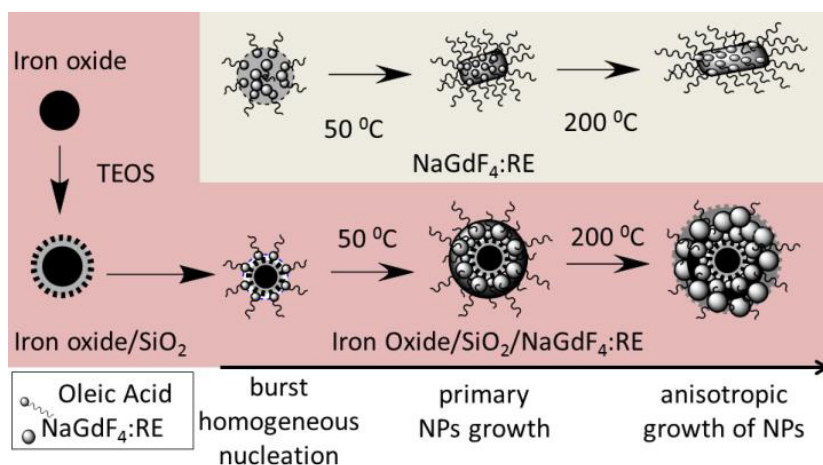
Figure 6.1: Schematic diagram for the synthesis of $NaGdF_4$:RE^{3+} and iron-oxide/SiO_2/$NaGdF_4$:RE^{3+} showing the proposed growth mechanism that occurs under microwave thermolysis.

6.3.1.1 Powder x-ray diffraction (PXRD): Figure 6.2 shows the PXRD patterns observed for the $NaGdF_4$:RE^{3+} and iron-oxide/SiO_2/$NaGdF_4$:RE^{3+} (RE^{3+} = Ce^{3+}, Eu^{3+} and Yb^{3+}, Er^{3+}). systems. From Figure 6.2c (iron-oxide/SiO_2/$NaGdF_4$:Ce^{3+} and Eu^{3+}) and Figure 6.2e (iron-oxide/SiO_2/$NaGdF_4$:Yb^{3+} and Er^{3+}), we observed that the diffraction peaks associated to the iron-oxide phase were very weak. This effect was due to the very small volume percentage and cross-section of the iron-oxide phase compared to the $NaGdF_4$ matrix. In addition, the recorded

patterns evidenced that similar diffraction peaks are observed in both samples ($NaGdF_4$:RE^{3+} and iron-oxide/SiO_2/$NaGdF_4$:RE^{3+}).
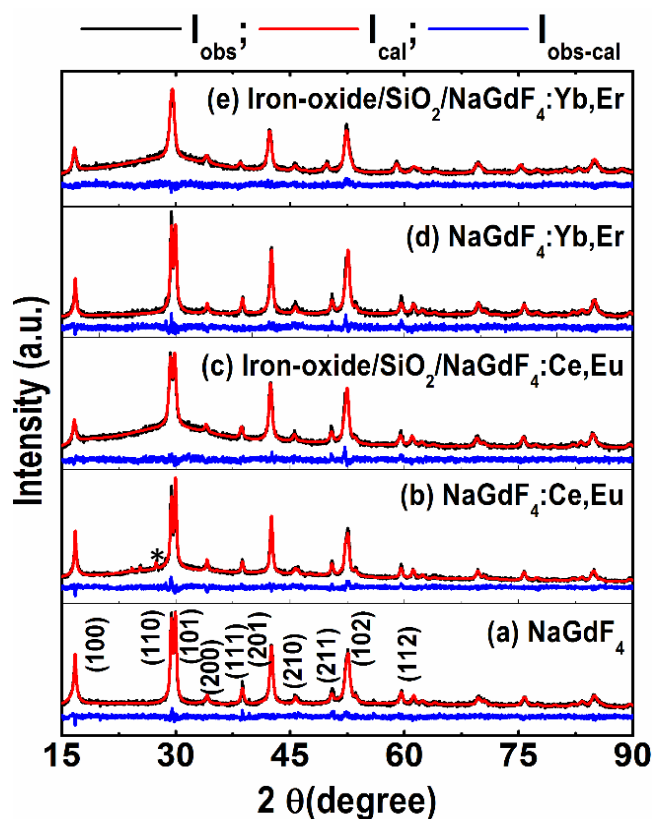
Figure 6.2: PXRD patterns and corresponding Rietveld fitting of (a) $NaGdF_4$ matrix; (b) $NaGdF_4$:Ce^{3+},Eu^{3+}; (c) iron-oxide/SiO_2/$NaGdF_4$:Ce^{3+},Eu^{3+}; (d) $NaGdF_4$: Yb^{3+},Er^{3+}; and (e) iron-oxide/SiO_2/$NaGdF_4$:Yb^{3+},Er^{3+} nanoparticles. * represents the GdF_3 phase.

All the XRD patterns shown in Figure 6.2 are in good agreement with the hexagonal phase β-$NaGdF_4$ (ICDD pattern 027-0699), and no secondary phases, as impurities, appeared in samples except existence of GdF_3 (~ 3%) in Figure 6.2b (marked as *). Following the incorporation of RE, the XRD patterns for the $NaGdF_4$ and iron-oxide/SiO_2/$NaGdF_4$: RE^{3+} (RE = Ce, Eu and Yb, Er) were only slightly weakened compared to those observed in neat $NaGdF_4$ shown in Figure 6.2a. This behavior indicates that the crystal structure is preserved after the incorporation of RE ions. The results are expected, because RE^{3+} (Ce, Eu and Yb, Er) have similar ionic radii of Gd^{3+}, following the Vegard's law.[147,237] The structural parameters obtained from the Rietveld analysis are collected together in Table 6.1 and clearly show that the hexagonal phase is preserved from the accuracy of the fitting (space group P6m/3). The enhanced intensity of the peak indicates that the preferential crystal growth occurs along (101)

121

direction in $NaGdF_4$: RE^{3+} (Ce^{3+}, Eu^{3+}) matrix (Figure 6.2 (a) and (b)), and along the (110) direction for $NaGdF_4$:RE^{3+} (Yb^{3+}, Er^{3+}) (see Figure 6.2 (d). The calculation of the crystallite sizes as given in Table 6.1, suggests that the pursued synthetic routes triggered the formation of large $NaGdF_4$:RE^{3+} particles (29-35 nm), but small iron-oxide/SiO_2/$NaGdF_4$:RE^{3+} (RE = Ce^{3+}, Eu^{3+} and Yb^{3+}, Er^{3+}) nanoparticles (15-20 nm). The Rietveld refinements analysis of $NaGdF_4$:RE^{3+} materials (Table 6.1) revealed, in addition, that during synthesis, alongside with large particles, also small particles are formed but to a minor extend; on the contrary, in the iron-oxide/SiO_2/$NaGdF_4$:RE^{3+} samples, a uniform statistical size distributions found to hold.

Table 6.1: Table obtained from the Rietveld refinements (lattice parameters, crystallite size and concentration of phases, strain, R_{wp} and goodness of fitting).

Samples	Phases	Lattice Parameters a, b, c (Å)	Conc. (%)	D (nm)	Strain (%)	R_{wp} (%)	GOF
NaGdF$_4$	Bigger	6.0442(5), 6.0442(5), 3.6071(3)	87(2)	29(1)	0.8(1)	4.8	1.2
	Smaller	6.096(7), 6.096(7), 3.70(5)	13(2)	7.1(7)	0.07(1)		
NaGdF$_4$:Ce,Eu	Bigger	6.0529(4), 6.0529(4), 3.6086(3)	89(2)	34(1)	0.06(1)	5.1	1.2
	Smaller	6.046(8), 6.046(8), 3.64(1)	8(2)	4.5(5)	0.02(1)		
	GdF$_3$	6.589(5), 7.007(3), 4.390(2)	3.0(3)	53(5)	0.02		
Iron-oxide/SiO$_2$/ NaGdF$_4$:Ce,Eu	Pure	6.0566(6), 6.0566(6), 3.6064(4)	100	19.1(4)	0.01	4.7	1.2
NaGdF$_4$:Yb,Er	Bigger	6.0496(6), 6.0496(6), 3.6080(4)	73(2)	32(1)	0.084(5)	5.9	1.2
	Smaller	6.085(5), 6.085(5), 3.609(5)	27(2)	6.6(7)	0.01		
Iron-oxide/SiO$_2$/ NaGdF$_4$:Yb,Er	Pure	6.0367(6), 6.0367(6), 3.6467(6)	100	16.2(3)	0.08(1)	5.0	1.1

6.3.1.2 Transmission electron microscopy (TEM): The morphological and structural characteristics of these materials were obtained by using TEM techniques. The TEM results shown in Figure 6.3 (a and b) indicate that the $NaGdF_4:Ce^{3+}$, Eu^{3+} nanomaterial contains a majority of rod shaped nanoparticles (~35 nm) with very few rods of average length ~ 15 nm, whereas iron-oxide/SiO_2/$NaGdF_4:RE^{3+}$ encode ovoidal shapes (Figure 6.3, d and e). The morphological differences suggests occurrence of an anisotropic growth of the nanoparticles.
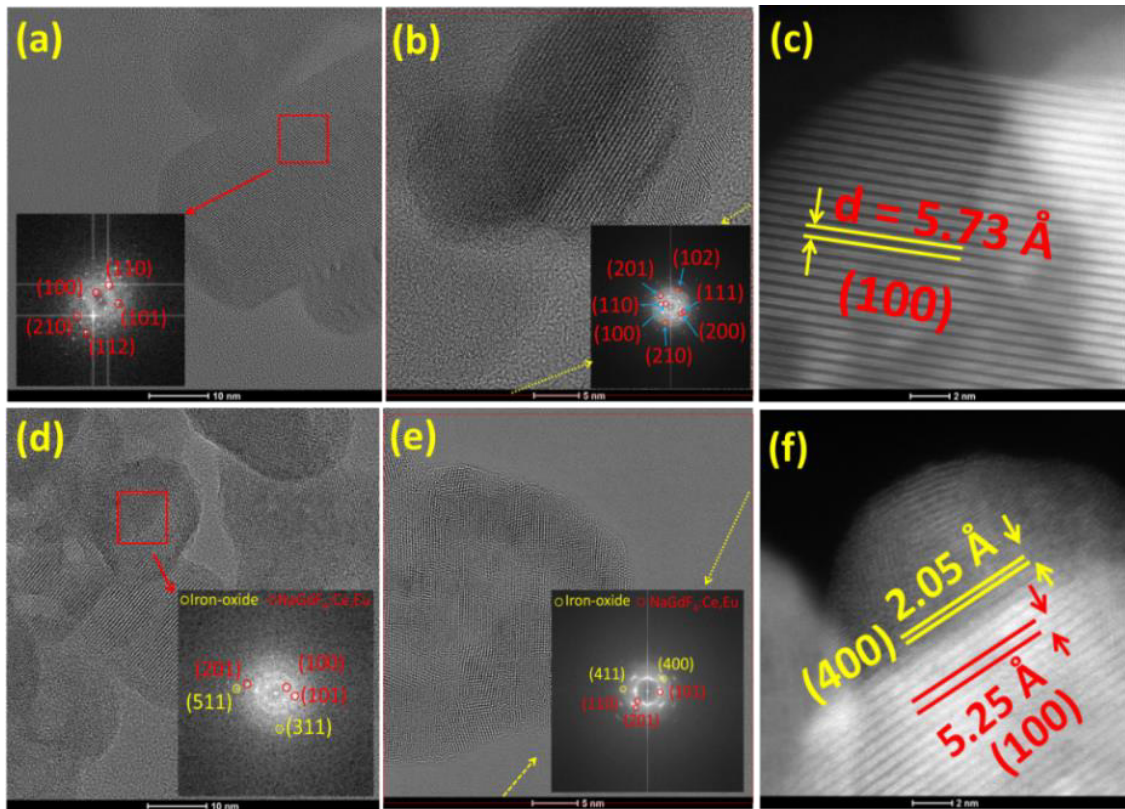
Figure 6.3: HRTEM images of (a-b) $NaGdF_4:Ce^{3+},Eu^{3+}$ and (d-e) iron-oxide/SiO_2/$NaGdF_4:Ce^{3+},Eu^{3+}$. The Fast Fourier transform of the highlighted areas are given as insets (in a, b, d, e). The insets (c) and (f) show the inter-plane distances (HAADF images) of the $NaGdF_4:Ce^{3+},Eu^{3+}$ and iron-oxide/SiO_2/$NaGdF_4:Ce^{3+},Eu^{3+}$ respectively. Yellow color is associated to the indexing of iron-oxide and the red color the indexing for $NaGdF_4:Ce^{3+},Eu^{3+}$. Scale bar (a and d): 10 nm; Scale bar (b and e): 5 nm; and Scale bar (c and f): 2 nm.

The fast Fourier transform (FFT) analyses showed that the diffraction of crystallographic planes with d-spacing of the hexagonal crystalline structure, according to the ICDD PDF no.

00-029-0699. FFT described in the insets of Figure 6.3 show the clear presence of (100), (110), (111), (200), (201) and (210) planes (inset, Figure 6.3a,b) in the $NaGdF_4:RE^{3+}$ material. The FFT shown Figure 6.3 (d and e) also reveals that the d-spacing calculations correspond to (400), (411), (511) and (311) planes of the Fe_3O_4, along with (110), (101), (100), (201) and (210) planes of $NaGdF_4:RE^{3+}$. Complementary high annular angular dark field (HAADF) images are given in Figure 6.3c and Figure 6.3f, which display the lattice fringes and interplanar distances. Additional TEM images of $NaGdF_4:Yb^{3+},Er^{3+}$ and iron-oxide/SiO_2/$NaGdF_4$:Yb^{3+},Er^{3+} are collected and reveals the occurrence of similar materials morphologies. Such structural properties have been further corroborated by their PXRD analysis (Figure 6.2d and Figure 6.2e, Table 6.1), thus, a similar anisotropic growth of the nanoparticles occurs for these systems as well.
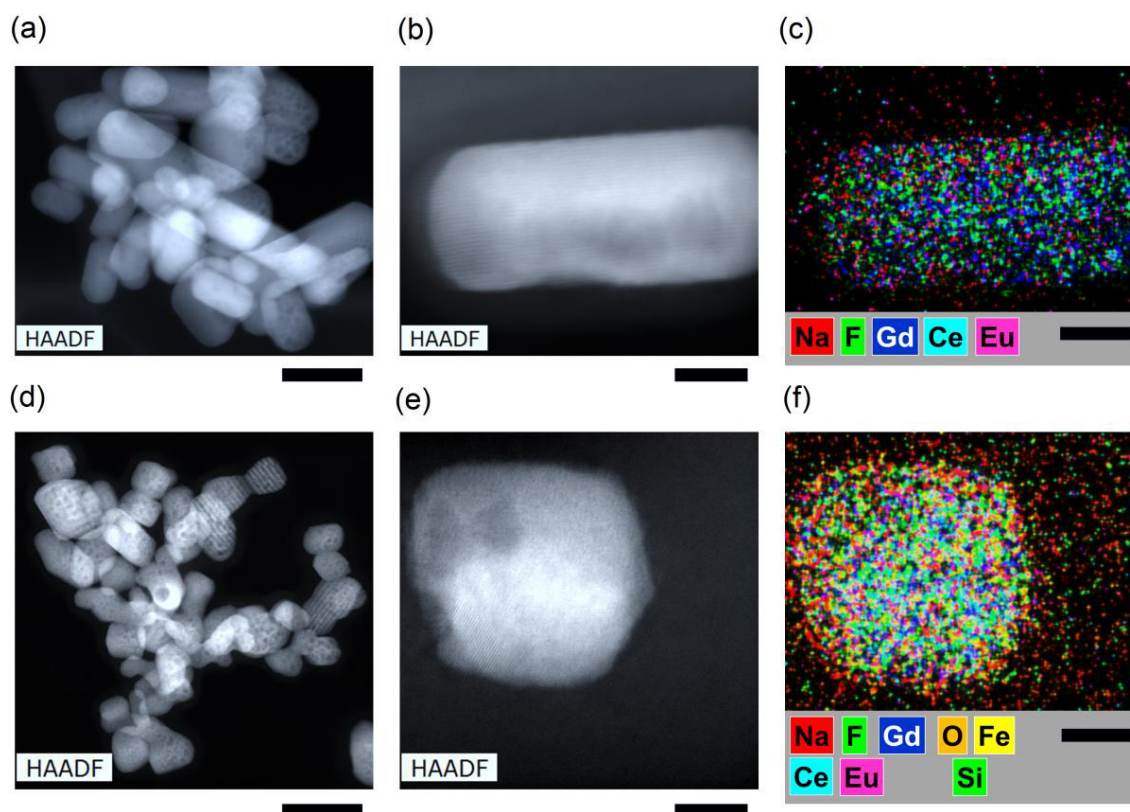
Figure 6.4: The high angle annular dark field (HAADF) images of the $NaGdF_4:Ce^{3+},Eu^{3+}$ (a, b) and the iron-oxide/SiO_2/$NaGdF_4:Ce^{3+},Eu^{3+}$ (d, e) nanocomposites; EDS elemental mappings for $NaGdF_4:Ce^{3+},Eu^{3+}$ are given in (c) and for iron-oxide/SiO_2/$NaGdF_4:Ce^{3+},Eu^{3+}$ in (f), showing the distribution of Fe, O, Si, Na, Gd, Ce, Eu and F elements. Scale bar (a and d): 20 nm; Scale bar (b, c, e and f): 9 nm

6.3.1.3 Energy dispersive x-ray spectroscopy (EDS): The spatial distributions of elements Fe, O, Si, Na, Gd, Ce, Eu and F in the synthesized materials were evaluated by HAADF and EDS mapping. Figure 6.4a,b shows HAADF images for $NaGdF_4:Ce^{3+},Eu^{3+}$ and Figure 6.4d,e the images obtained for the iron-oxide/SiO_2/$NaGdF_4:Ce^{3+},Eu^{3+}$. In the case of $NaGdF_4:Ce^{3+},Eu^{3+}$ the result indicates that exists an homogeneous distribution of the Ce, Eu, Na, Gd and F elements into the β-$NaGdF_4$ matrix (Figure 6.4c). The EDS images for the iron-oxide/SiO_2/$NaGdF_4:RE^{3+}$ nanocomposite (Figure 6.4f) also indicates the successful combination of three phases, iron-oxide, SiO_2, and $NaGdF_4:Ce^{3+},Eu^{3+}$ and show the Fe, Si, O, Ce, Eu, Na, Gd and F elemental spatial distribution. The calculated elemental % is collected together, for all the materials synthesized, and tabulated in Table 6.2 and Table 6.3.

Table 6.2: Chemical distribution of elements in $NaGdF_4:Ce^{3+},Eu^{3+}$ samples

	Spectrum 1		Spectrum 2		Spectrum 3	
Element	Wt%	Wt% Sigma	Wt%	Wt% Sigma	Wt%	Wt% Sigma
F	67.62	14.03	73.46	15.8	67.62	11.94
Na	12.48	02.21	8.63	1.17	14.03	2.32
Ce	4.27	0.44	3.74	0.42	3.38	0.39
Eu	2.04	0.25	1.97	0.23	1.64	0.20
Gd	13.56	1.05	12.20	1.01	13.23	1.06

Table 6.3: Chemical distribution of elements in iron-oxide/SiO_2/$NaGdF_4:Ce^{3+},Eu^{3+}$ samples

	Spectrum 1		Spectrum 2		Spectrum 3	
Element	Wt%	Wt% Sigma	Wt%	Wt% Sigma	Wt%	Wt% Sigma
F	59.12	12.54	58.99	12.78	61.76	10.23
Na	13.25	12.54	11.55	2.23	10.97	1.84
Ce	1.85	0.26	2.05	0.27	2.56	0.31
Eu	1.30	0.19	1.37	0.19	1.65	0.20
Gd	11.16	1.02	11.63	1.03	13.14	1.08
Si	0.45	0.18	0.54	0.20	0.43	0.14
Fe	0.71	0.10	0.96	0.10	0.90	0.10
O	12.16	3.19	12.88	3.50	8.60	1.72

6.3.1.3 Fourier transform infrared (FTIR) spectroscopy: The FTIR technique was employed to analyze further the $NaGdF_4:RE^{3+}$ (Fig. 6.5 a, b and d) and iron-oxide/SiO_2/$NaGdF_4:RE^{3+}$ nanostructured materials (Figure 6.5, c and e).[238] The presence of clear IR band at 3476 cm^{-1}, as shown in Figure 6.5 (panels a-e), was assigned to the vibrational stretching mode of surface O-H group. This band is weakened for the iron-oxide/SiO_2/$NaGdF_4$: RE^{3+} nanoparticles. The IR bands at 570 and 470 cm^{-1} are assigned to the Fe=O stretching and bending vibration mode, respectively, of iron-oxide, which are completely absent in the $NaGdF_4:RE^{3+}$ materials (Figure 6.5 a, b, and c).[129] A more sharp band, around 1100 cm^{-1}, is observed for the iron-oxide/SiO_2/$NaGdF_4:RE^{3+}$ composites (Figure 6.5, c and e), and originates from the Si-O-Si bonds, indicating the presence of silica shell coated on the surface of the iron-oxide cores. Although a similar band is observed in other samples ($NaGdF_4:RE^{3+}$) without Si (see Figure 6.5a and 6.5b), in those cases are associated with the presence of C-H bonds (oleic acid, OA).[237] The two strong bands centered at 1457 cm^{-1} and 1640 cm^{-1} are associated with the asymmetric and symmetric stretching vibrations of carboxylate anions.[237] The oleic acid was speculated to play an important role in growth and shape evolution.[239] The FTIR results indicate that the adhesion of OA on the surface of nanoparticles is not a merely physical adsorption but preferentially adsorbed onto certain crystallographic plane. Strong interaction may exist between the RCOO$^-$ and the RE atoms on the surfaces, and such effect possibly blocked the growth along the radial directions and accelerated the nanoparticle's growth rate along the axial direction.[239]

According to the Le Chatelier's principle, increasing the amount of OA in the solvent mixture would slow down the decomposition/desorption of oleate anions from the nanoparticles surfaces, thus strengthening the RCOO$^-$ and the RE atoms interactions, effect that could facilitate the anisotropic growth of the nanoparticles as observed through XRD and TEM analysis. In addition, the reduced decomposition rate of RE-RCOO$^-$ with increasing OA concentration enhances the binding effectiveness of the RCOO$^-$ group on the surfaces of the growing nanoparticles, which can in turn protect them from self-aggregation. This process finds its foundation in the XRD/TEM analysis of the $NaGdF_4:RE^{3+}$ and iron-oxide/SiO_2/$NaGdF_4:RE^{3+}$. Generally, with more oleic acid, the polarity of the solvent is enhanced and thereby increasing the solubility of NH_4F. Moreover, oleic acid is a weak acid and hence supports to dissolve even more F$^-$ ion through a NH_4F-HF pathway. As the ratio of 1-ODE:OA is higher for iron-oxide/SiO_2/$NaGdF_4:RE^{3+}$ as compared

to $NaGdF_4:RE^{3+}$, thereby it promotes the formation/dissolution of RE(oleate) in the solvent by increasing their mobility. As a result, there is an increase in the growth rate along the radial axis of nanoparticle against that occurring parallel to the axial direction. This leads to formation of ovoidal shape nanoparticles in case of iron-oxide/SiO_2/$NaGdF_4:RE^{3+}$ materials.
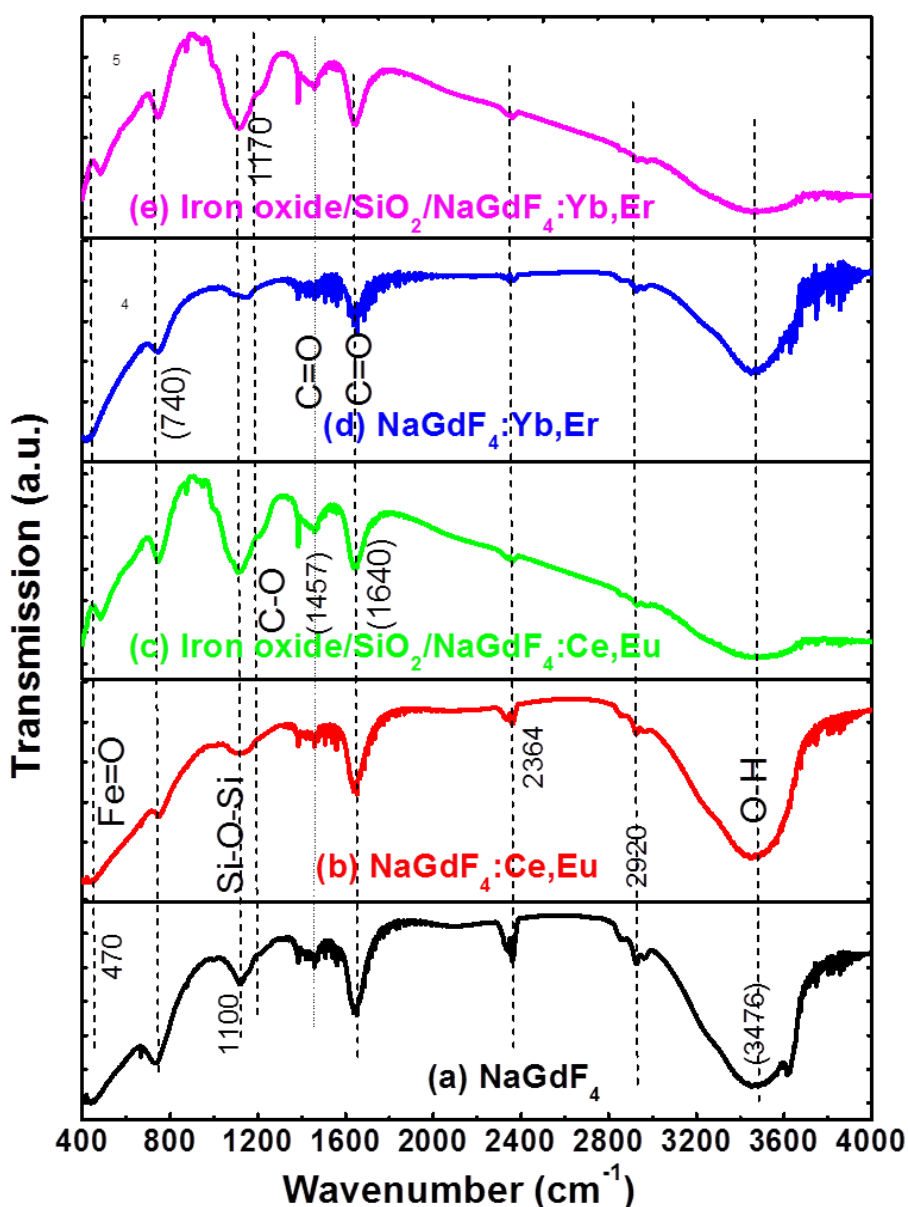
Figure 6.5: FTIR spectra of (a, b and d) $NaGdF_4:RE^{3+}$ and (c and e) iron- oxide/SiO_2/$NaGdF_4:RE^{3+}$ nanoparticles and (RE = Ce, Eu and Yb, Er).

6.3.2 Downconversion luminescence properties of Ce-Eu activated nanoparticles

The excitation spectra of $NaGdF_4:Ce^{3+},Eu^{3+}$ and iron-oxide/SiO_2/$NaGdF_4:Ce^{3+},Eu^{3+}$ nanoparticles were recorded in the range 200-500 nm at 300 K (Figure 6.6a), by monitoring the emission at 616 nm, which are assigned to the higher intensity $^5D_0 \rightarrow ^7F_2$ transition of the Eu^{3+} ion. The excitation spectra of $NaGdF_4:Ce^{3+},Eu^{3+}$ and iron-oxide/SiO_2/$NaGdF_4:Ce^{3+},Eu^{3+}$ presented a high intensity broad absorption band centered at around 254 nm, corresponding to the $4f(^2F_{5/2})$-5d interconfigurational transition of the Ce^{3+} ion. In addition, these materials showed a sharp intense narrow absorption lines at 271 nm and 392 nm, assigned to the $4f^8-4f^8$ transitions of the Gd^{3+} ($^6D_{7/2}$) and Eu^{3+} ($^5L_{6-8}$) ion, respectively. Additional secondary narrow absorption lines have also been detected, which are also assigned to the intraconfigurational 4f transitions, originating from the $^7F_0$ ground state to the following excited states of the Eu^{3+} ion:[237] $^5D_4$ (361 nm), $^5L_7$ (374 nm), and $^5D_2$ (464 nm). However, the intensities of these broad absorption bands are lower than those associated to the Ce^{3+}, Gd^{3+} and Eu^{3+} ($^5L_{6-8}$) cations. The presence and intensity of Ce^{3+} and Gd^{3+} excitation peaks in the excitation spectra indicate the existence of an energy transfer process being active from Ce^{3+} and Gd^{3+} to the Eu^{3+} luminescent ions. Excitation into the Ce^{3+} band at 254 nm yields weak and sharp emission of Gd^{3+} at 310 nm and weak emission of Ce^{3+} (300–400 nm), and strong emission of RE (Eu^{3+} ions) (400–700 nm) (red line) (Figure 6.6b).

The photoluminescence (PL) emission spectra (Figure 6.6b) of the same samples under excitation monitored at $4f(^2F_{5/2}) \rightarrow 5d$ along the interconfigurational transitions of the Ce^{3+} ion, show a number of characteristic intraconfigurational f–f transitions of Eu^{3+} which are associated with the transition from the excited level $^5D_0$ to the ground levels ^7F_J (J = 1, 2, 3 and 4) and are purely time dependent.[237] Furthermore, the weak emission lines from the level ^5D_J (J = 1, 2) to the ground levels ^7F_J (J = 1, 2, 3 and 4) are also observed. The other transitions, $^5D_0 \rightarrow ^7F_1$ (magnetic-dipole transition), $^5D_0 \rightarrow ^7F_3$, and $^5D_0 \rightarrow ^7F_4$, are found to be relatively weak for these samples.[81] The presence of electric dipole transition confirms that Eu^{3+} ions are located at sites without inversion symmetry. In other words, for the hexagonal structure of $NaGdF_4$, as stated above, cations usually occupy three different crystallographic sites, i.e., 1a, 1f, and 2h, among which 2h sites may normally be occupied by only sodium ions, 1a and 1f sites are occupied by Gd^{3+} ions. The point symmetry of la and lf sites is C_{3h}, which is a non-centrosymmetric system. Moreover, in terms of ionic sizes, the doped luminescent Eu^{3+} ions should occupy the 1a and 1f sites in the β-phase $NaGdF_4$.
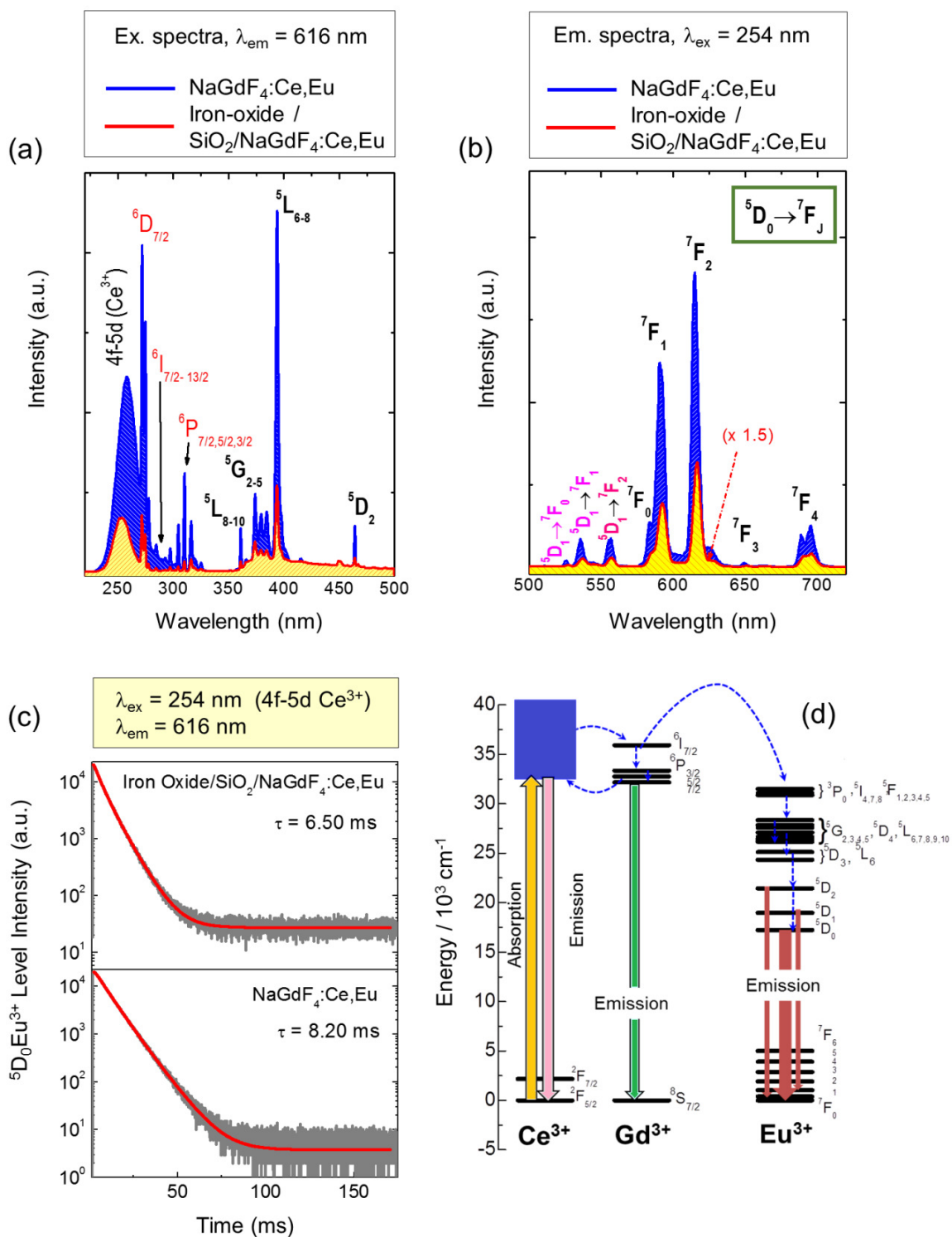
Figure 6.6: (a) excitation, (b) emission spectra, (c) time decay measurement of $^5D_0$ level of Eu^{3+} ion in optical magnetic $NaGdF_4$:Ce,Eu and iron oxide/SiO_2/$NaGdF_4$:Ce,Eu nanoparticles. An energy transfer mechanism ($Ce^{3+} \rightarrow Gd^{3+} \rightarrow Eu^{3+}$) is proposed in (d).

The related Judd-Ofelt parameters have been calculated (Table 6.4) and explained the observed reduction in the overall emission quantum efficiency, from 75 % to 42 %, the direct reasoning being the active participation of iron oxide in the quenching process.[47]

Table 6.4: Experimental intensity parameters (Ω_λ), lifetimes τ (Figure 6.6), emission coefficient rates A_{rad} and A_{nrad} as well as emission quantum efficiencies η for the $NaGdF_4:Ce^{3+},Eu^{3+}$ and iron-oxide/SiO_2/$NaGdF_4:Ce^{3+},Eu^{3+}$ nanophosphors.

Materials	Ω_2 $(10^{-20}\,cm^2)$	Ω_4 $(10^{-20}\,cm^2)$	A_{rad} (s^{-1})	A_{nrad} (s^{-1})	A_{tot} (s^{-1})	τ (ms)	η (%)
$NaGdF_4:Ce^{3+},Eu^{3+}$	2.1	2.7	158	51	209	8.20	75
Iron-oxide/SiO_2/$NaGdF_4:Ce^{3+},Eu^{3+}$	2.1	3.2	165	43	208	6.50	42

Emission decay curves of the samples are presented in Figure 6.6c. The obtained curves were fitted to bi-exponential decays, and provided good correlation coefficients. The derived two lifetimes, 8.20 ms and 6.50 ms for $NaGdF_4:Ce^{3+},Eu^{3+}$ and iron-oxide/SiO_2/$NaGdF_4:Ce^{3+},Eu^{3+}$ respectively, originate from the same ($^5D_0$) Eu^{3+} ions. The Eu^{3+} ions in $NaGdF_4:Ce^{3+},Eu^{3+}$ and iron-oxide/SiO_2/$NaGdF_4:Ce^{3+},Eu^{3+}$ nanophosphors occupy lattice sites inside the nanocrystals and on the surfaces, but the Eu^{3+} ions are surrounded by different environments in these two materials; thus, their lifetimes must be different, which is a direct evidence of the quenching induced by iron-oxide/SiO_2 phases, featuring a decrement of 20 %.[24] The derived lifetime values are known to be appreciable for Eu^{3+} in inorganic hosts but both are here shortened in the $NaGdF_4$ matrix.

Based on these data, the luminescence mechanism in the RE^{3+} doped β-$NaGdF_4:Ce^{3+},Eu^{3+}$ and iron-oxide/SiO_2/$NaGdF_4:Ce^{3+},Eu^{3+}$ nanoparticles can be derived (Figure 6.6d). The electronic transitions within $4f^n$ configurations of Eu^{3+} are strongly forbidden. However, the emission efficiency of Eu^{3+} can be greatly improved by exciting a sensitizer ion (i.e., Ce^{3+}) with an allowed electronic transition, which transfers the excitation energy to the activator (i.e., Eu^{3+}).[237] During the emission process, the excitation energy is first absorbed by the 4f–5d transition of Ce^{3+}, then transferred to the Gd^{3+}, migrates over the Gd^{3+} sub-lattices and finally to the Eu^{3+}, where the energy is released in the form of fluorescent emissions.[237]

6.3.3 Up/downconversion luminescence properties of Yb-Er activated nanoparticles

The visible upconversion luminescence spectra of the optical-magnetic $NaGdF_4$:Yb^{3+},Er^{3+} and iron-oxide/SiO_2/$NaGdF_4$:Yb^{3+},Er^{3+} under infrared excitation (980 nm) are shown in Figure 6.7a. The green luminescence between 510-570 nm can be assigned to the ($^2H_{11/2}$, $^4S_{3/2}$)$\rightarrow$$^4I_{15/2}$ transition. A red emission is observed between 650 and 680 nm, originating from the $^4F_{9/2}$$\rightarrow$$^4I_{15/2}$ transition, which is weak (~38%) compared to green lines. Additionally, the blue emission, which is attributed to the $^4G_{11/2}$$\rightarrow$$^4I_{15/2}$ (~378 nm) and $^2H_{9/2}$$\rightarrow$$^4I_{15/2}$ (~411 nm) transitions of Er^{3+} ions, are also observed. The green emission line intensity of iron-oxide/SiO_2/$NaGdF_4$:Yb^{3+},Er^{3+} nanoparticles is approximately 50% of $NaGdF_4$:Yb^{3+},Er^{3+}. All these spectra and transitions fall in the visible region. Furthermore, a down conversion in the infrared red region was also observed after excitation of the nanoparticles at 980 nm (Figure 6.7a, inset). The emission at 1535 nm is assigned to the $^4I_{13/2}$$\rightarrow$$^4I_{15/2}$ transition of Er^{3+} and the emission intensity of iron-oxide/SiO_2/$NaGdF_4$:Yb^{3+},Er^{3+} is found 1.5 times less strong than the emission intensity of $NaGdF_4$:Yb^{3+},Er^{3+} nanoparticles which assigned to the same transition. These results were validated from the time decay analysis of $^4I_{13/2}$$\rightarrow$$^4I_{15/2}$ transition of Er^{3+}; upon excitation at 980 nm, the life time of this emitting level decreased from 1.70 ms to 1.45 ms (Figure 6.7b). In conclusion, the surface properties and crystallinity of $NaGdF_3$:Yb^{3+},Er^{3+} nanoparticles severely impact the different energy level transition of the doped ions, thus induce different emission intensity of red, green and blue light.

The possible upconversion (UC) and downconversion (DC) mechanisms for the Yb^{3+} and Er^{3+} doped $NaGdF_4$ nanoparticles are discussed hereafter on the basis of the energy level diagram presented in Figure 6.7c. Under 980 nm excitation, the Yb^{3+} ions are excited from the $^2F_{7/2}$ level to the $^2F_{5/2}$ level and then transfer their energies to the nearby Er^{3+} ions. The upper levels $^4G_{11/2}$, $^4F_{7/2}$, and $^4F_{9/2}$ of Er^{3+} ions are mainly populated by the following processes: (i) energy transfers (ETs) between Yb^{3+} and Er^{3+} ($^2F_{5/2}$$\rightarrow$$^2F_{7/2}$: $^4I_{15/2}$$\rightarrow$ $^4I_{11/2}$, $^4I_{13/2}$$\rightarrow$$^4F_{9/2}$, and $^4I_{11/2}$$\rightarrow$$^4F_{7/2}$), (ii) the excited state absorption of the pump radiation from the $^4I_{11/2}$ and $^4I_{13/2}$ levels, and (iii) the cross relaxation between Er^{3+} ions, as depicted in Figure 6.7c. Additionally, it can be seen from Figure 6.7c that the UC emissions are all related to the population of the $^4I_{11/2}$ level of Er^{3+} ions.

With the addition of cores iron-oxide/SiO_2, the population of the $^4I_{11/2}$ level decreases due to the phonon-assisted ET from Er^{3+} ions to semi-metal iron oxide.
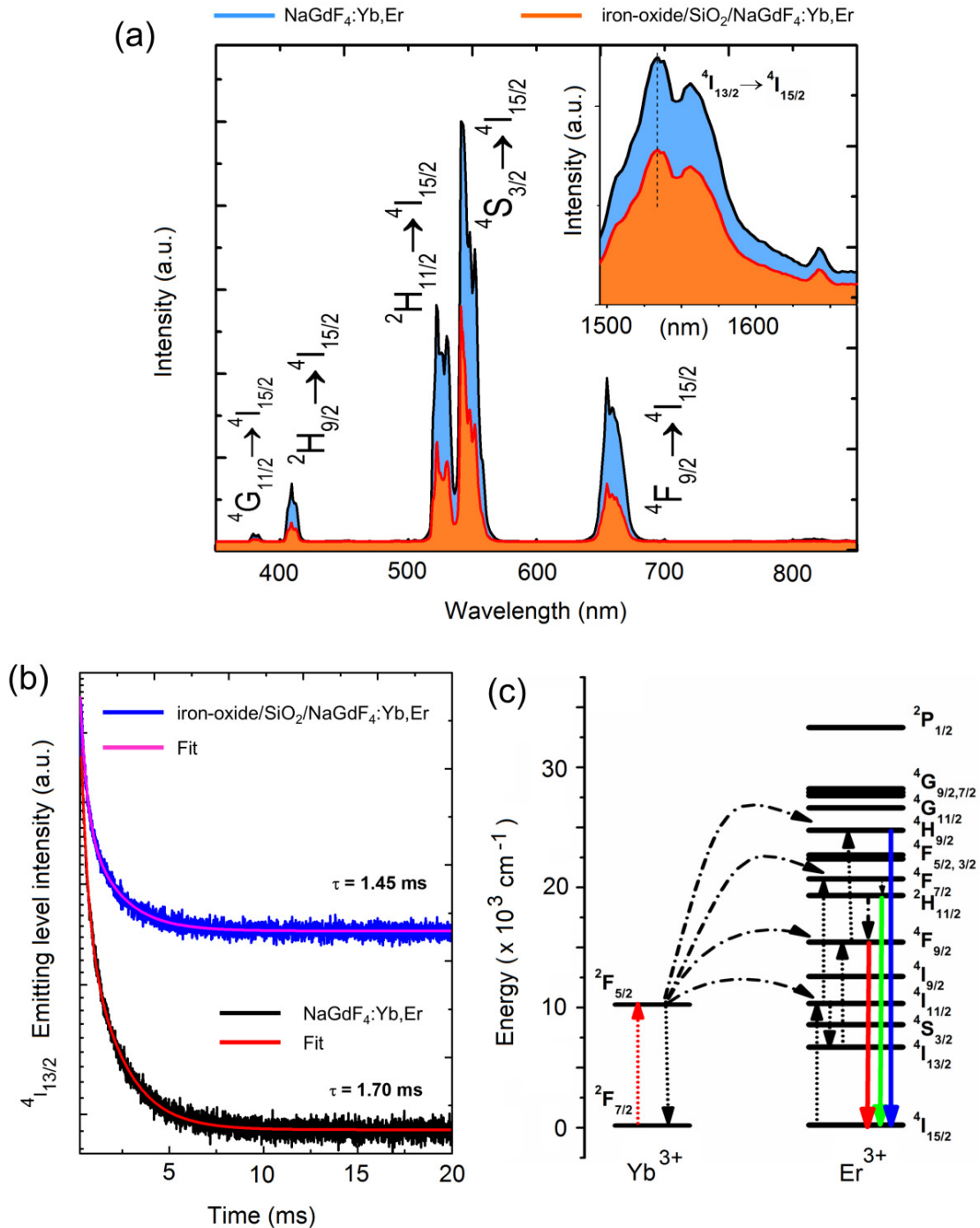
Figure 6.7: (a) Emission spectra, (b) lifetime decay curves in IR region for $NaGdF_4$:RE^{3+} (RE^{3+} = Yb^{3+}, Er^{3+}) and iron-oxide/SiO_2/$NaGdF_4$:RE^{3+} (RE^{3+} = Yb^{3+}, Er^{3+}) nanoparticles, and (c) proposed energy transfer diagram from Yb^{3+} to Er^{3+}.

Additionally, because the energy mismatch between $^4F_{9/2} \rightarrow ^4I_{9/2}$ (Er^{3+}) and iron oxide is small, the ET from Yb^{3+} ions to Er^{3+} ions can occur more effectively. As a result, the red emission from the $^4F_{9/2}$ level was quenched heavier than that of the green emissions from the $^2H_{11/2}$ and $^4S_{3/2}$ levels, due to the light absorption by iron-oxide/SiO_2 in the red region (see FTIR, Figure 6.5) as shown in Figure 6.7(c).

The change in intensity and life of emitting level, as observed in Figure 6.6 and Figure 6.7, is mainly due to a significant change of nonradiative centers on the surface of iron-oxide/SiO_2/$NaGdF_4$:RE^{3+} (RE = Ce, Eu and Yb, Er) nanoparticles, upon shielding effect of the protective shell. Iron-oxide and iron-oxide/SiO_2 materials may provide a leakage path to the radiative electron from the emitting level when they are in sub-nanoscopic proximity to the luminescence center. Hence, the probability of absorption of the emitting radiation is increased and thereby the quenching phenomenon occurs. Additionally, the increased emission intensity may also result from the suppressed quenching induced by the outer shell material, namely the inherent emission of luminescent $NaGdF_4$:RE^{3+} nanoparticles. Another probable reason is the participation of O-H ions (see Figure 6.5 c and d) as well as the overall system morphology.

6.3.4 The CIE chromaticity and magnetophoretic separation: The emission color of red emitting and green-emitting iron-oxide/SiO_2/$NaGdF_4$:RE^{3+} (RE^{3+} = Ce^{3+}, Eu^{3+} and Yb^{3+}, Er^{3+}) nanomaterials was evaluated by plotting the CIE chromaticity diagram (see Figure 6.8). The overall emission color was calculated and expressed according to the (x, y) CIE color coordinates, which has been marked as A (0.5966, 0.3722), B (0.5834, 0.3646), C (0.3412, 0.6026) and D (0.3272, 0.6206). The red emission color was mainly due to the highest emission intensity contribution of the $^5D_4$ - $^7F_5$ transition of the Eu^{3+} ion and green emission is due $^4S_{3/2} \rightarrow ^4I_{15/2}$ transition of Er^{3+} ion.

Magnetophoretic separation: In addition to magnetophoretic separation in magnetic field gradients, the particles are expected to align themselves with the external magnetic fields, due to their magnetic shape anisotropy with orientation and shape dependent properties. The magnetic nanoparticles alignment and their magnetic manipulation *in situ* is an additional property that can be exploited for the development of sensors, such as those related to the diagnostics of diseases down to cellular level. To illustrate better this concept, one simple experiment was carried out (Figure 6.8, right panel). The material was dispersed in hexane and placed in a quartz cuvette, displaying bright red emission under UV radiation (for iron-oxide/SiO_2/$NaGdF_4$:Ce^{3+},Eu^{3+}) and bright green emission under 980 nm laser irradiation (for

iron-oxide/SiO$_2$/NaGdF$_4$:Yb^{3+},Er^{3+}). After placing the external bar magnet close to the cuvette, the particles moved in approximately 30 seconds and stacked together on the side of the cuvette, making a clear hexane solution. Besides, upon exposure to radiation, bright red emission (at UV excitation for iron-oxide/SiO$_2$/NaGdF$_4$:Ce^{3+},Eu^{3+}) or green light (at 980 nm for iron-oxide/SiO$_2$/NaGdF$_4$:Yb^{3+},Er^{3+}) were observed from the same corresponding place on the side wall of the cuvette near the magnet (Figure 6.8, right panel). This simple experiment clearly indicates that these bifunctional nanoparticles encode not only luminescence properties but also strong magnetic responses.
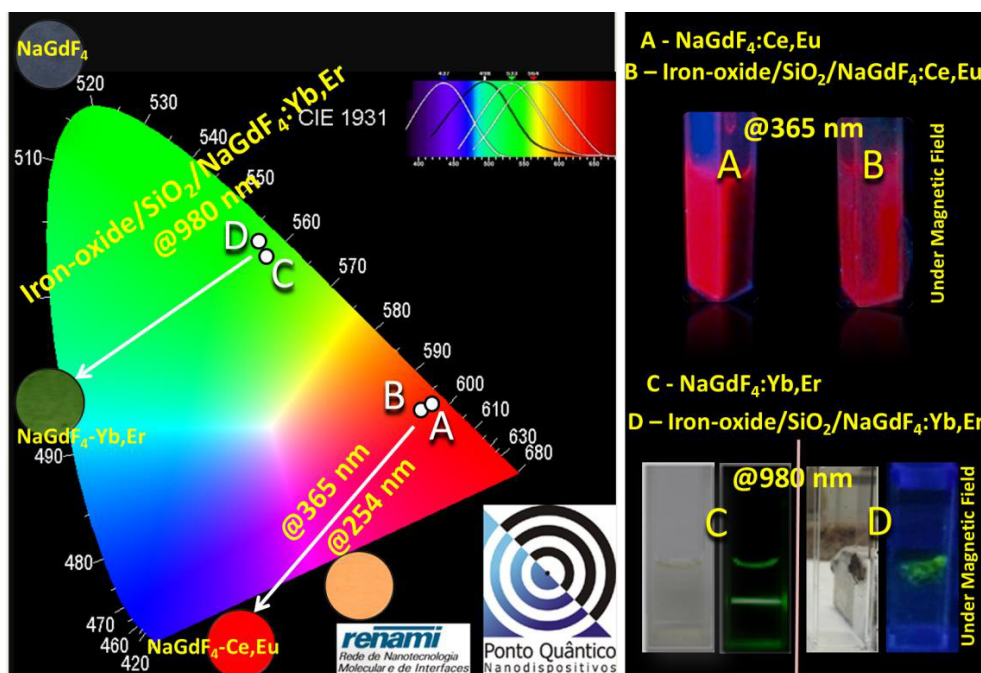
Figure 6.8: CIE chromaticity diagram of optical magnetic NaGdF$_4$:RE^{3+} and iron oxide/SiO$_2$/NaGdF$_4$:RE^{3+} (RE^{3+} = Ce^{3+}, Eu^{3+} and Yb^{3+}, Er^{3+}) nanoparticles (left panel) and illustration of simultaneous magnetic-luminescence characteristics (magnetophoretic) of iron-oxide/SiO$_2$/NaGdF$_4$:RE^{3+} (right panel). Ce, Eu ions activated nanoparticles are red emitting, and Yb, Er activated nanoparticles are green emitting.

6.3.5 Magnetic investigation of NaGdF$_4$:RE^{3+} and iron-oxide/SiO$_2$/NaGdF$_4$:RE^{3+} nanoparticles

To elucidate the magnetic properties of these systems, the magnetization loops for NaGdF$_4$:RE^{3+} and iron-oxide/SiO$_2$/NaGdF$_4$:RE^{3+} nanoparticles were recorded at 300 K (Figure 6.9a). The observed MH curve (magnetization *vs.* field) for NaGdF$_4$:RE^{3+}

nanoparticles indicated that these systems are paramagnetic with susceptibilities values of 0.8 x 10^{-2} (NaGdF$_4$), 1.38 × 10^{-2} (NaGdF$_4$:Ce^{3+},Eu^{3+}) and 1.06 × 10^{-2} (NaGdF$_4$:Yb^{3+},Er^{3+}), expressed in physical unit of emug^{-1}Oe^{-1}. On the other side, the sample iron-oxide/SiO$_2$/NaGdF$_4$:RE^{3+} (RE = Ce, Eu and Yb, Er) showed superparamagnetic behavior at 300 K, with negligible coercive field. The saturation magnetization of iron-oxide/SiO$_2$/NaGdF$_4$:RE^{3+} nanocrystals was ~ 1.2 emu/g. Compared to the susceptibility expressed by the same volume of reference iron oxide, there is a large decrease in the saturation magnetization for iron-oxide/SiO$_2$/NaGdF$_4$:RE^{3+} nanoparticles.[147] This effect can be explained by the concomitant presence of interlocked physical effects:[240] (i) the presence of thick shells and the organic coating (diamagnetic) on the iron-oxide nanoparticles, (ii) the large non-magnetic contribution to the weight of the sample, and (iii) the emergence of exchange couplings phenomena arising from the ordered core surrounded by disordered shell, because of the size of iron oxide core less than 5 nm (size-reduction effects).
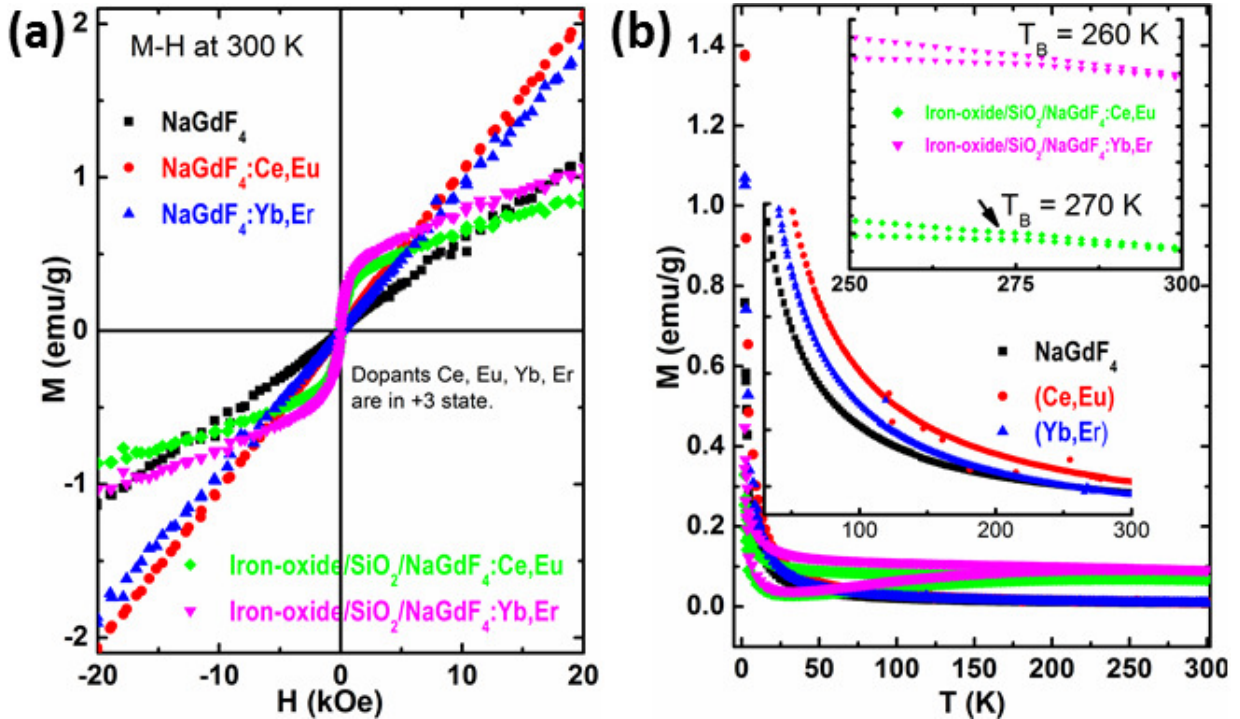
Figure 6.9: (a) The magnetic hysteresis loops taken at 300 K, and (b) Zero field cooling and field cooling (ZFC/FC) magnetization versus temperature data at 100 Oe of NaGdF$_4$:RE^{3+} and iron-oxide/SiO$_2$/NaGdF$_4$:RE^{3+} (RE^{3+} = Ce^{3+}, Eu^{3+} and Yb^{3+}, Er^{3+}) nanoparticles.

The temperature dependence (from 2 K to 300 K) of the magnetization was measured under an applied field of 100 Oe using ZFC/FC procedures, and the results are shown in Figure 6.9b. The ZFC and FC curves for iron-oxide/SiO$_2$/NaGdF$_4$:RE^{3+} merged at high temperatures (very close to 300 K) but bifurcated already at T > 250 K, indicating that the samples were superparamagnetic already at temperatures close to room temperature.

6.4 Conclusion

In this work, we described a microwave assisted thermolysis route that leads to the synthesis of NaGdF$_4$:RE^{3+} and iron-oxide/SiO$_2$/NaGdF$_4$:RE^{3+} nanosystems. These materials encoded both optical and magnetic properties, and exhibited red and green emissions. The various processes of excitation/emission, energy transfer mechanism through Gd-sublattice mediated energy migration, UV down conversion, NIR up/down conversion and lifetime analysis, have been discussed and explained in detail. For the iron-oxide/SiO$_2$/NaGdF$_4$:RE^{3+} nanoparticles in particular, we found that the decrease in luminescence intensity and life time of the emitting levels were promoted by the iron oxide core but were not totally quenched. Therefore, using Gd based matrices, the combination of efficient up/downconversion mechanism coupled with the paramagnetic properties of Gd^{3+} in NaGdF$_4$:RE^{3+} and iron-oxide/SiO$_2$/NaGdF$_4$:RE^{3+} nanoparticles resulted in the formation of new types of multifunctional nanomaterials. The synthetic strategy presented, it's easy to carry-out protocol and the diverse system morphologies obtained could be used as an inspiration to tailor further the properties of similar materials; for example, other Gd based nanoparticles doped with different activators, in order to achieve efficient dual-mode luminescence effects and to expand the library of available materials for biomedical applications in UV and IR optical window as well as for smart field detection.

Chapter 7
Scintillation Experiment using Ionizing Radiation Source

7.1 Introduction

The detection of ionization radiation has been intensively investigated for over 6 decades due to its broad applications in areas closely related to society. These include scientific research in high energy physics, astrophysics, radiochemistry, nuclear physics, medical research,[241] and so on.[242,243] Industrial facilities also use x-rays,[244] γ-rays, neutrons, electron beams, or ion beams for diagnostics or characterization, especially in the commercial nuclear energy sector, and medical and dental diagnostics involving digital imaging.[241,244,245] In addition, cutting-edge radiation detection technology is increasingly demanded in non-proliferation and national security applications where better energy resolution attained by semiconductors is not mandatory.[246–248]

Most of these areas require the detection of various radiations with high spectroscopic resolution, rapid throughput and ease of operation, reliability, high sensitivity, and low cost. Modern detection system generally consists of detecting materials and assisting instrumentation. The scintillator is the active component and usually located at the interface between the ionizing radiation source and the electronic detection chain.[249] The advancement of instrumentation has partially satisfied aforementioned requirements in radiation detection, though the development of new radiation detection materials is in great demand to address current challenges and future opportunities. Capability to detect a wide variety of radiations including γ- and x-rays, charged particles and neutrons, the great variety in size and constitution of different specific scintillators make them as the best choice in different applications.[250]

7.1.1 Parameters of scintillating material: Performance of any scintillation detector depends largely on the physio-chemical properties of the material. However, the ideal material should possess the following properties. [69,249,251]

- **Decay lifetime**: The time required for emission intensity to drop from some 100 % level to 1/e of that quantity (~ 37 %), where e is Euler's number. Faster decay times

- **Linearity:** A measure of the proportionality of detector response with incident energy. For scintillators, this is generally defined as some number of photons per keV deposited. Poor linearity affects the precision of spectroscopic measurements, limiting detector operations to some particular region where the scintillator response is still proportional.

- **Wavelength matching:** The ability to tune the secondary photon output to the most sensitive (or lowest) noise regions of the accompanying Photo Multiplier Tube (PMT). Wavelength-shifters can increase the total luminescent output, each stage in the energy transfer chain may exhibit changes in pulse shape that make process modelling or consistent measurements difficult to achieve.

- **Materials stability:** Qualities of the scintillator in terms of resistance to large radiation dosages and environmental factors such as photobleaching, vibrational sensitivity, hygroscopicity limit the detector's useful lifetime. This should be considered as a financial modifier when designing low-cost installations.

- **Structure:** The physical qualities, other than stability, which recommend or discourage a material for a particular project. These include the maximum production size and shape of a scintillator block, the effective density for absorbing the targeted radiation type (s), and the clarity of the material to emitted secondary photons.

No material simultaneously meets all these criteria, and the choice of a particular scintillator is always a compromise among these and other factors and the optimization of these parameters largely contributes to improving detector efficiency. The ability of a detector system to distinguish between radiation from threatening and non-threatening sources depends on its capability to unambiguously resolve radioisotope-decay energy signatures.

Since the discovery of NaI(Tl) crystal, as an standard scintillation material, significant effort has been put into the research and development of new scintillators for detection of nuclear radiation.[252,253] Discovery of Bismuth Germanate (BGO) scintillator, CsF, Ge-detectors, [9]B, [3]He, plastic detectors, and BaF_2 brought new perspectives for scintillation detection. Numerous chemical compounds were studied as potential scintillators crystals, such as Gd_2SiO_5(GSO), Lu_2SiO_5(LSO), $YAlO_3$:Ce (YAP), $LuAlO_3$:Ce (LuAP), $PbWO_4$ (PWO), CeF_3, etc., and are proposed for different applications in physics, medicine, etc.[69,74,249,254,255] Except these

materials, several different approaches are used for design of radiation detecting materials such as plastic scintillators, dyes, and liquid scintillators. These materials are still used commercially.[256,257]

NaI single crystals are used for gamma radiation detection but can also be used to detect slow neutrons due to isotope ^{127}I. This crystal and CsI(Tl) are among the most widely used commercial scintillating materials, even with increased application of plastics for large format installations.[7] However, recently developed LaBr$_3$ (Ce) scintillators may eventually replace NaI(Tl) for spectroscopic identification. This lanthanide compound has high light yield of 63,000 photons/MeV and energy resolution of 2.9 % for 662 keV gamma radiation. The blue-shifted emission peak at 380 nm matches well with sensitive peak of most PMTs.[258] These crystals have even greater luminescence, shorter decay times, and higher resolution. However, the main challenge with the lanthanides is the difficulty in growing large size crystals. The bulk single crystal scintillators are difficult and expensive to produce, there is little flexibility for exploring and adjusting their chemical composition, or looking for alternative dopants and crystal shapes. These crystals also have drawbacks such as anisotropy in thermal and mechanical properties and hygroscopicity, and the lack of ruggedness and design flexibility pose more restrictions on these bulk scintillators, greatly reducing their ability to face the rigors of an uncontrolled environment. More interesting researches are now focused on lanthanides to resolve such issues.[247,252,259–263]

7.1.2 Lanthanides and need of nanoparticle scintillator

The lanthanide elements (Z = 57 – 71) are a group of elements that share similar chemical properties with outer electron configurations composed of 5d and 4f electron shells. This similarity means that the series forms similar crystalline structures and therefore substituting between them in crystalline lattices does not lead to degradation of the overall structure of the crystal.[12] Furthermore lanthanides are also used for radiation detection and on a macro-scale, traditionally lanthanides have been exploited as detector media, because of the large cross section for either neutrons or gamma/x-rays.[255] Neutron counting has been accomplished by exposing a dysprosium foil to a neutron flux, and then using a Geiger counter, to count the beta decays that result from the transmutation of the dysprosium into holmium. LaBr$_3$(Ce), CeF$_3$ and other crystal scintillators doped with rare earth ions are already in trend.[74,255,256,264] There has been an effort to create nanoscale crystals which can then be encapsulated and protected

from the environment, making these types of detectors much more durable than current macro-scale crystal based systems.

Nanocrystals offer many benefits. The engineering of nanostructure materials with tunable optical and scintillating properties is an issue that can offer new alternatives and solutions to the constraints discussed above. Compared with their bulk counterparts, nanocrystalline colloidal scintillators are comparatively easy to produce, flexible, and potentially less expensive than single crystal scintillators.[74,256,257,262] The nanocrystal size is much smaller than the wavelengths of excitation and emission being studied and therefore cause minimal scattering, allowing for the device to be optically clear. The nanocrystalline size and ability to functionalize their surface, chemistry allows us to incorporate them into several ways such as different polymers (carbon), dyes, colloidal form, powders etc. This allows them to be made more rugged, protecting the crystalline structure. Carbon based polymers add benefit of thermalizing the neutrons. Further to meet all the parameters, selection of such material for nanoscale design and engineering becomes very important.[1,12,13] Embedded nanocrystals with a large neutron cross section (Gd, Cd, Li etc.) based detectors are also used to enhance their ability to detect certain types of neutron radiation. This is just a narrow look at a few applications that can be found for lanthanide containing nanocrystals, and there is an ever growing list of applications.

A single crystal detector is only sensitive to medium boundaries at a limited surface area and optical coupling is aided by the application of optical grease. Further, coatings of teflon tape or reflective material increase the quantity of incident light that is eventually directed into the PMT. For an assembly of nanoparticles, even those in polymers or other matrices, each inter-particle gap represents at least two transitions in materials of disparate refractive indices; this often leads to a visible loss of transparency and the scattering of light throughout the material. The result of this is that nanoparticle samples must produce an immense number of scintillation photons to overcome the scattering and trigger an appropriate count from the PMT and multichannel analyser. Many inorganic scintillators require a high-temperature synthesis route, reducing their capability of accepting surface modifications. Without adjustment of their outer bonding structures, the particles aggregate in monomer precursors, curing into an opaque product, or one with a very low nanoparticle loading level, and subsequently dim luminescence.

In this work, we focused on the nanoscintillators themselves, without considering interaction with a matrix, in which these particles may be embedded.[261] Due to their intrinsic structural and optical properties, lanthanum fluoride (LaF_3) nanocrystals proved to be a good host for scintillating response to gamma and neutron irradiation,[74,250] with potential impact in detection and spectroscopy applications.[265] The most remarkable pros of LaF_3 regarding scintillation application are following.[237]

- Its large solubility for all of lanthanide ion groups, which gives versatility for ad-hoc engineering design.
- Minimal quenching of the electron-hole (e-h) excited states due to its low energy phonons and guest ion rattling modes.
- Its chemical stability, which has an advantage against the classic and more recent hygroscopic counterparts when exposed to open air conditions (such as NaI, $LaBr_3$).

However, there are some drawbacks to lanthanide halide detectors such as

- Internal radioactivity of some lanthanides that contributes to spectral counts.
- A poor low-energy response that can cause detector resolution to be lower than that of NaI (TI) below 100 keV.

The selection of dopants becomes very important in optically inactive LaF_3 matrix. We have prepared two types of LaF_3 matrix: (i) $LaF_3:Ce^{3+},Gd^{3+},Eu^{2+/3+}$ and (ii) $LaF_3:Ce^{3+},Gd^{3+},Tb^{3+}$. In scintillation mechanism, generally two terms are being used namely activators and wavelength shifters. Among the fastest activator centers known for gamma ionizing radiation detection through inelastic collisions, are Ce^{3+}, Eu^{2+}, Pr^{3+}, and Nd^{3+} ions.[244,250,261] Although Ce^{3+}(or Eu^{2+}) center exhibits light output emission wavelengths in the UV-Visible range of 300 nm to 550 nm in different crystalline environments of hosts. Therefore Ce^{3+} or Eu^{2+}centres are more convenient because they satisfy both requirements; here namely sharp decay time, and soft UV-Visible output light emission that can be matched with the sensitivity of available photocathodes of PMTs.

The co-doping ion mechanism of these scintillators can be a way to enhance the light yield output. Natural wavelength-shifters of the group of the lanthanide ions (such as co-doping acceptors Tb^{3+}, Yb^{3+}, Eu^{3+}) can be used to enhance the light yield through a down-conversion process, i.e., through energy transfer between donor and acceptor centres.

With the aim to make the nanoscintillator sensitive to neutron radiation, gadolinium (Gd) is a suitable ion for neutron conversion due to its superior thermal neutron absorption cross-section

mainly because of the neutron absorption produced in ^{157}Gd.[74,248,263] After the neutron capture in ^{157}Gd, the ^{158}Gd isotope emitting prompt gamma rays, internal conversion electrons, and x-rays. Hence doping of Ce and Gd may find its potential in both neutron detection and gamma ray spectroscopy.

7.1.3 Neutron detectors

There are different types of detectors (^{6}Li, ^{9}B, ^{3}He, ^{157}Gd etc.) available to detect neutrons although we are discussing only two main types namely helium and gadolinium detectors.

 (i) Helium detectors: The detection process is based on the reaction

^{1}n + ^{3}He → ^{1}H (0.573 keV) + ^{3}H (0.191 keV)   (7.1)
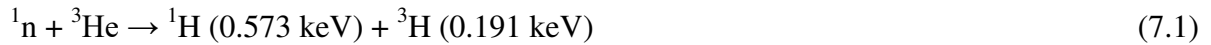
For the thermal neutrons, the cross-section for this reaction is 5330 barns and it is known as the best neutron detector. The interaction of ^{3}He with neutrons can be explained as: the daughter products of the reaction move in opposite directions and produce an output pulse proportional to 0.764 keV. This pulse can be detected and distinguished easily from signals created by gamma rays or other types of ionizing radiation. This makes ^{3}He an ideal detector for thermal neutrons. Because of this, detectors based on ^{3}He are superior to other detectors. However, the issues involved with these detectors are: (a) required electronics to actively monitor the detector, and (b) the availability and cost of ^{3}He.[266]

(ii) Gadolinium detector: The detectors usually take advantages of high cross-section capture reactions, inducing charged ions easily separable from recoil electrons. Though gadolinium and cadmium isotopes have the highest capture cross-sections for thermal neutrons, prompt gamma rays from the radioactive capture cannot be easily discriminated from natural background gamma rays.[259] Indeed, the capture of a neutron by ^{157}Gd forms a ^{158}Gd* nucleus within an excited state. The return to a fundamental state of energy is promptly mediated by the emission of gamma rays. However, gadolinium-based detectors have been developed to address alternative neutron measurement. The first approach consists in loading gadolinium into scintillation detectors such as the Gd doped HfO_2 or the LGB (lithium gadolinium borate) crystal.[248] The reaction associated with the de-excitation of a Gd nucleus follows the absorption of thermal neutron nuclear reactions:

^{155}Gd + ^{1}n→^{156}Gd*→^{156}Gd + γ + X + ICe$^-$ + Ae$^-$ (7.2)

^{157}Gd + ^{1}n→^{158}Gd*→^{158}Gd + γ + X + ICe$^-$ + Ae$^-$ (7.3)
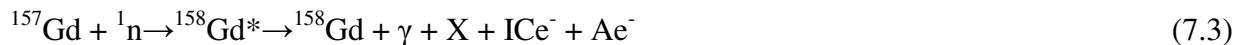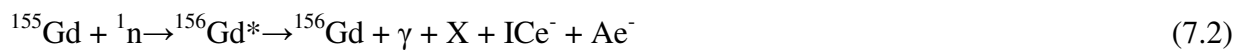
where the gamma rays labeled as γ; x-rays as X, internal conversion electron as ICe$^-$ and Auger

electrons as Ae⁻ are known as electron source term. Table 7.1 summarizes major data set for selected isotopes with high thermal neutron source.

Table 7.1 Data for isotopes with high thermal neutron cross sections

Target Isotope	Cross section (barns)	Natural abundance	Target half-life	Reaction	Reaction Product	Product half-life	Final product
Xe-135	2665000	0%	9.14 hours	(n,γ)	Xe-186	Stable	
Gd-157	**253000**	**24.80%**	**Stable**	**(n,γ)**	**Gd-158**	**Stable**	
Gd-155	**60700**	**14.80%**	**Stable**	**(n,γ)**	**Gd-156**	**Stable**	
Sm-149	40520	13.80%	Stable	(n,γ)	Sm-150	Stable	
Gd-153	40520	0%	240 days	(n,γ)	Gd-154	Stable	
Cd-113	20720	12.22%	Stable	(n,γ)	Cd-114	Stable	
Rh-105	15840	0%	35.4 hours	(n,γ)	Rh-106	30 s	Pd-106
Sm-151	15140	0%	90 years	(n,γ)	Sm-152	stable	
Eu-152	12790	0%	13 years	(n,γ)	Eu-153	Stable	
Eu-151	9184	47.80%	1.7E18 y	(n,γ)	Eu-151	13 years	Sm-152
He-3	5330	0.000137%	Stable	(n,γ)	H-3	12.3 years	He-3
B-10	3840	19.80%	Stable	(n,γ)	Li-7	Stable	
Eu-155	3760	0%	4.7 years	(n,γ)	Eu-156	15.9 hours	Gd-156
Dy-165	3530	0%	2.3 hours	(n,γ)	Dy-166	81.6 hours	Er-166
Hg-196	3078	0.15%	Stable	(n,γ)	Hg-197	64 hours	Au-197
Os-184	3000	0.02%	Stable	(n,γ)	Os-185	94 days	Re-185
Dy-164	2653	28.18%	Stable	(n,γ)	Dy-165	2.3 hours	Ho-165
Li-6	940	7.59%	Stable	(n,γ)	H-3	12.3 years	He-3

7. 2 Testing and experimental preparation

Evaluating a newly synthesized material for radiation flux from [241]AmBe involves several stages of characterization and analysis. The most important of these is luminescence performance, tested through ultraviolet (UV) excitation. The second aspect of important concern is the structural and compositional scrutiny, whereas the third one is the visual transparency, and confirmation of performance with radiation activation. All experiments related to structural/morphological/photoluminescence characteristics of the LaF_3: Ce, Gd, Eu are discussed in chapter 4. LaF_3 nanocrystals doped with $Ce^{3+}(Eu^{2+})$ as the activator centre

(donor), $Eu^{2+/3+}$ as the wavelength-shifter center (acceptor), and Gd^{3+} as the neutron captor agent is selected for the scintillation experiment. The motivation behind this work was to maximize the out coming scintillating light at the desired wavelength range close to the maximum sensitivity of the photocathode's material, $\lambda \sim (450 \pm 50)$ nm and to detect the radiation (gamma/neutron). The use of Eu^{3+} as wavelength-shifter is supported by the previous work.[265] Following subsections explain the preparation before the radiation detection experiments under irradiation of high energy. Figure 7.1 shows the schematic diagram of the whole experimental setup, consisting of nuclear electronics, Photo Multiplier Tube (PMT) and standard NaI (Tl) scintillator or nanoparticles sample.
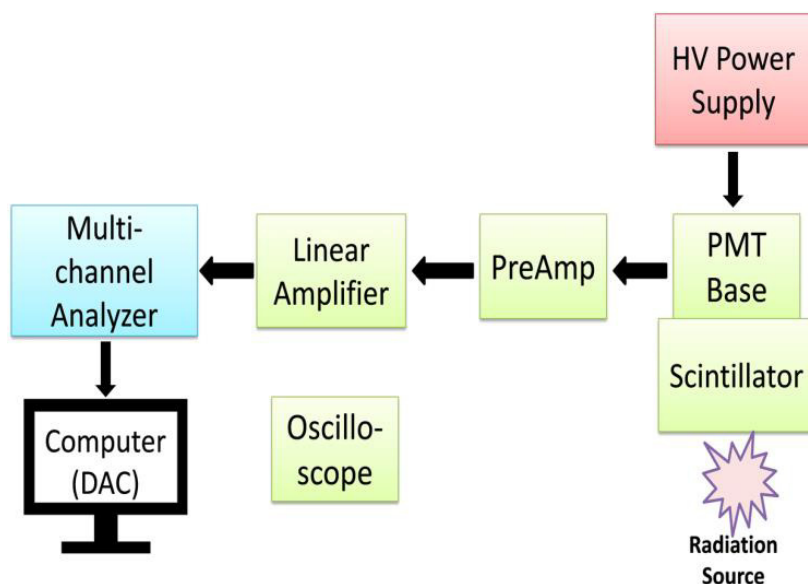
Figure 7.1: Block diagram for a scintillation detector system.

7.2.1 Shielding chamber: A lead chamber was designed to protect from radiation as shown in Figure 7.2. A thick polyethylene slab was used inside the lead chamber close to walls to reduce the neutron flux outside the shielding chamber. The purpose of shielding is to reduce the background count rate of a measurement system as well. Shielding reduces the background count rate by absorbing some of the components of cosmic radiation and radiations emitted from materials in the surroundings of the measurement system. Ideally, the material used for shielding should itself be free of any radioactive material that might contribute to the background. In practice, this is difficult to achieve as most construction materials contain at

144

least some naturally radioactive species (such as ^{40}K, members of the uranium and thorium series, etc.).
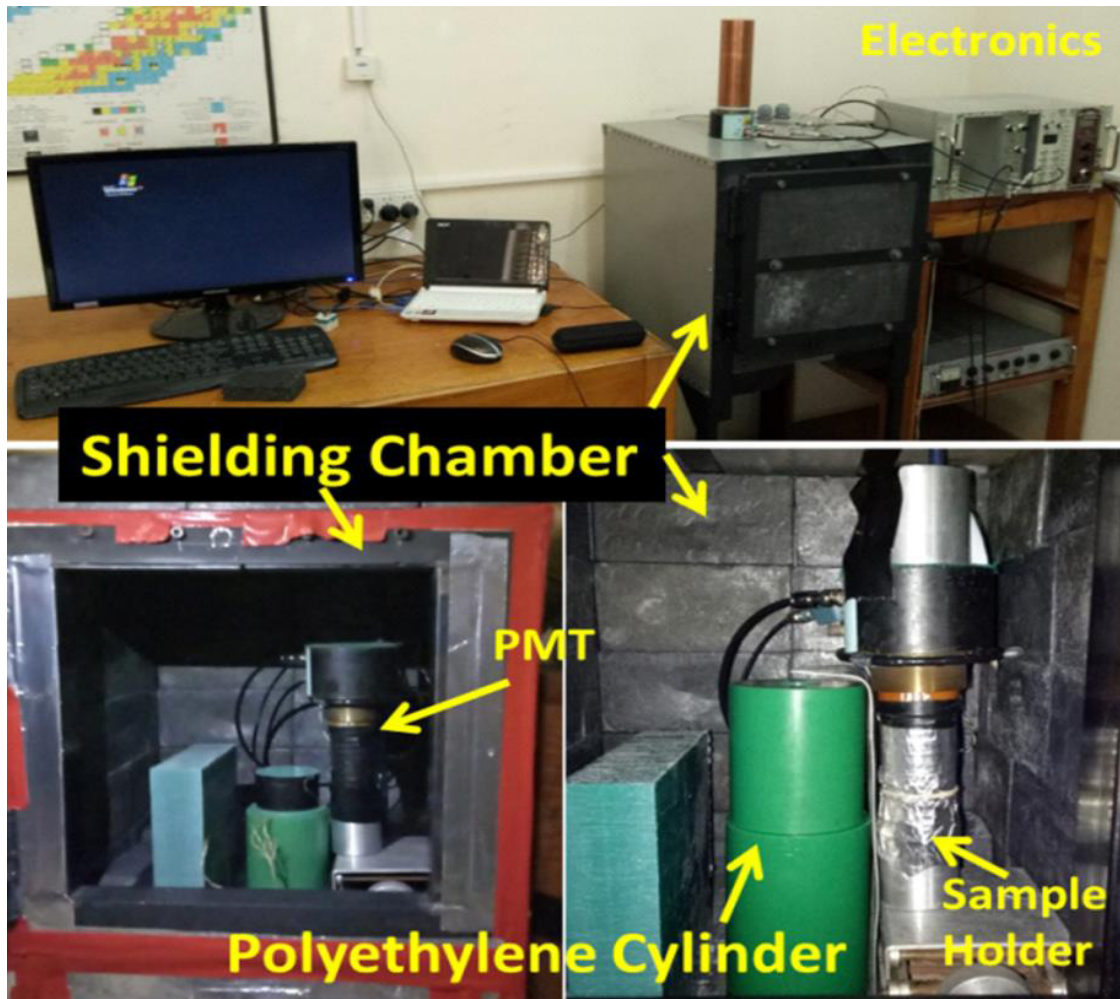
Figure 7.2: A complete experimental conditions for the experiment, showing engineering of shielding chamber, electronics involved, physical experimental condition, sample holder.

7.2.2 Standard detector and sample holder: The scintillation detector is illustrated in Figure 7.3. Our detector has a 2×2 inch cylindrical NaI(Tl) scintillation crystal which is activated with about 1 part in 10^3 thallium impurities. Through various processes, a gamma ray passing into the crystal may interact with it creating many visible and ultraviolet photons (scintillations). This detector has been used to calibrate the overall instrumentation. The standard size and shape of a sample holder has been prepared using standard volume of NaI(Tl) scintillators.

Aluminium (Al) has been chosen to fabricate sample holder (cane) because, (a) it is transparent to gamma and neutron irradiation, and (b) it is the cheapest available material in the laboratory.
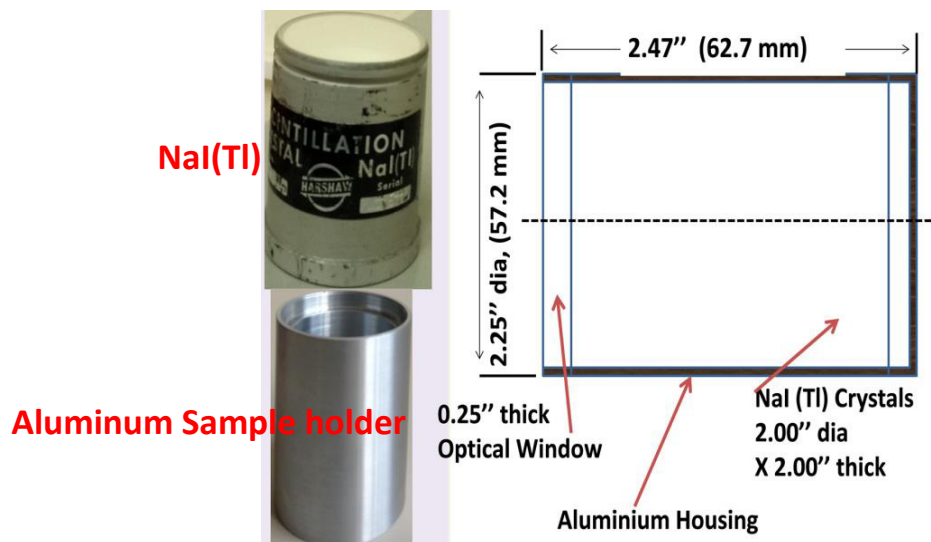
Figure 7.3: Hasshay NaI(Tl) commercial scintillator. The left top image is Hasshay packaged scintillating crystal. On the right is the schematic provided by the manufacturer, in their specification sheet. The left bottom image is Aluminum sample holder made in laboratory and it contains equal volume as Hasshay NaI(Tl) scintillator.

7.2.3 Real experimental setup used: Scintillation events have been detected using aluminum cane as sample holder (prepared by considering the active volume of NaI(Tl) crystal) with a Hamamatsu R7449 quartz-window bi-alkali photomultiplier tube (PMT) at a bias of 1000 V with peak at 420 nm. The electronic signal from the PMT was processed using Ortec 113 preamplifier, Ortec 570 amplifier, pulse shaper, and Ortec Illusion 25 multichannel analyzer. Data were analyzed using Ortec Maestro-32 software on Windows operating system.[267] The cane that contained LaF_3:5%Ce, 5% Gd, y%Eu (y = 10 mol. %) nanoparticles solution was fixed with PMT in reverse order by teflon tape to improve light collection and to avoid evaporation of solvent. A Cd sheet has been used to stop thermal neutrons. The polyethylene cylinder was used as moderator and reduces the energy of fast neutrons emitted by the source, thereby turning them into thermal and epithermal neutrons. The radioactive source was placed in this polyethylene cylinder and kept 10 cm away in lateral direction from the centre of

sample holder. All measurements were taken over a fixed live time (counts per live time (counts/s)). All these experiments were carried out at Bariloche Atomic Centre, Argentina.

7.2.4 Electronics used: The instruments used and tested to perform scintillation experiments are high voltage power supply, Preamplifier, linear amplifier, Multichannel analyzer (MCA), Photomultiplier tube (PMT). The specifications of the electronics utilized during the experiment are mentioned below.

- ORTEC Model 556 High Voltage Power Supply is a standard double width NIM module that provides either polarity of output voltage from 50 V to 3000 V, 0 to 10 mA.

- Canberra Model 556A Acquisition Interface Module (AIM)

- The ORTEC Model 579 wideband Fast filter Amplifier with Gated Baseline Restorer.

- Model 8701 ADC is a 100 MHz Wilkinson analog to digital converter designed to provide a full 8192 channels of resolution in a wide range of applications.

- A multichannel analyzer (MCA) is an electronic instrument which can collect the entire spectrum at once. MCA consists of an analog-to-digital convertor (ADC), memory, and a method of display. The ADC is a specialized type which measures only the maximum height of the pulse corresponding to a radiation event. Since it takes a finite amount of time to measure a pulse, the MCA must close off its entrance to further pulses to prevent correct measurement of the one it is working on. This processing period is called "dead time" and must be accounted for.

- A photomultiplier tube (PMT) is a device that creates an electric charge in proportion to the amount of light energy that it receives. The charge is typically integrated throughout some critical time period and is taken as a measure of the input light energy.

7.2.5 Sample preparation: Oleic acid coated LaF_3:Ce, Gd, Eu nanoparticles were dispersed and tested in several non-polar solvents. Toluene was found to be the best solvent and a fixed concentration (0.65, 0.85, and 1; in mg/mL) of nanoparticles was prepared by dispersing in toluene and ultrasonication for 1 hour. However, the stability of dispersion was its best for 5-6 hours only. The samples were prepared using 100 mL of toluene to fill completely the active volume of the sample holder (aluminum cylindrical cane). All testings were done with neutron source with and without Cd sheet. 1 mm Cd sheet works as the stopper for the thermal neutrons, but fast neutrons emitting from the source penetrate this Cd sheet (neutron captor

cross section for Cd is 20700 barns). To increase the number of thermal neutrons/slow neutrons, the neutron source was kept in a polyethylene cylinder that increases the number of neutrons falling on the sample holder. A teflon tap was used to tie the PMT and sample holder to make better optical coupling. The ^{241}AmBe source was kept 10 cm away from the centre line of sample holder/PMT

7.2.6 Specification of radiation source: A medium intense neutron source of ^{241}AmBe (10^6 neutron/s), purchased from Spectrum Technologies, has been used in current spectrum to test LaF$_3$:5%Ce^{3+}, 5%Gd^{3+}, y%Eu$^{2+/3+}$ nanocrystals for scintillation experiments. Untagged gamma and tagged-neutron are yielded from ^{241}AmBe radiation source. Very low-activity mono-energetic gamma source (^{60}Co and ^{137}Cs) has also been used, that were purchased from Spectrum Technologies during installation of electronics and calibration of standard crystal scintillators NaI(Tl).

7.3 Results and discussion

A better response and well resolved spectra were obtained from the sample for a concentration of 1 mg/mL. In case of irradiation of ^{241}AmBe radiation source, three sets of measurements were taken for the colloidal sample of nanocrystals. These measurements were repeated several times, for different times of irradiations and the results obtained were plotted as counts/second versus channel number. Before, starting the actual experiment, the background was measured and then later on subtracted from the experimental data. The major contribution comes from the electrical/electronic noises along with background signals due to activated shielding chamber and other materials inside. Average background counts limited around 200 channels and only a few counts were observed beyond 200 channels. The neutron source ^{241}AmBe was placed in the detection array, inserted in its hydrogenated moderator cylinder (polyethylene), allowing majority of slow/thermal neutrons which were stopped using 1 mm thick Cd Sheet. The sample holder contained the nanoparticles dispersed in toluene. The experiments were carried out for ~ 240 minutes. The average spectrum was plotted in counts (per live time) versus channel number. Few counts were observed. The same procedure was repeated without Cd sheet. It allowed all the emitted neutrons directly on the sample holder containing nanoparticles dispersed in toluene, after moderated by polyethylene cylinder. The experiments were also performed for ~ 240 minutes. The average spectrum was plotted in counts (per live

time) versus channel. Clear distinctions from the previous steps were observed. The results after background subtraction are shown in Figure 7.4.

The ^{241}AmBe source has low energy gamma emissions along with high energetic decaying neutrons (fast & slow neutrons) of great energy. The measured pattern of ^{241}AmBe with the moderator and without Cd sheet showed higher absolute counts when compared with moderator and with Cd sheet. Therefore, considering that the ^{241}AmBe gamma ray contribution is approximately the same in both experiments (with and without Cd sheet), it is possible the contribution of some lower energy gamma rays from the moderator due to the de-excitation of H atoms which have captured a neutron.
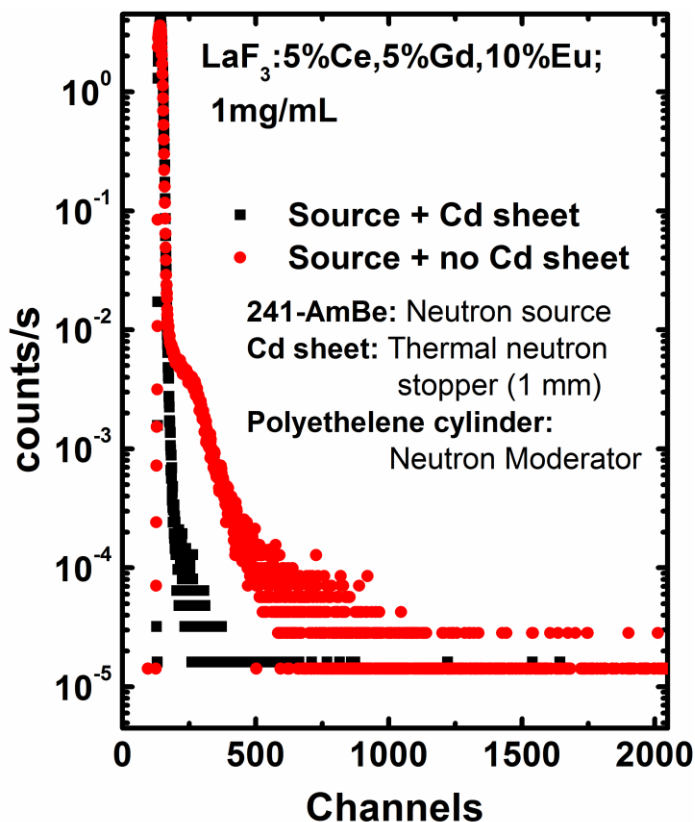
Figure 7.4: An average spectra of count versus channel (counts were measured per live time in second) upon irradiation of high energy from ^{241}AmBe source.

Furthermore, when Cd sheet is present there, it may also emit gamma radiation, upon interaction with thermal neutrons and also contribute in scintillating activity. However the important observation was a great decrease in counting rate detected from the Gd-containing nanoparticles (LaF$_3$:5%Ce^{3+},5%Gd^{3+},10%Eu$^{2+/3+}$), using the ^{241}AmBe source with the use of

Cd material, in comparison with the counts detected from without stopping of thermal neutron situation (Figure 7.4, radiation source with Cd sheet)). Even without moderator/stopper material some counts can be seen over background with a similar shape of that observed for thermal neutrons due to the moderation of fast neutrons mainly in the host of the sample (background). The larger change in count rates in Gd containing nanoparticles is mainly due to the absorption and detection of thermal neutrons followed by the emission of conversion electrons with energies up to about 1 MeV. Also the high counting at lower pulse heights (lower channel numbers) in Figure 7.4 depicts the well-known wall effect in neutron detectors. For this sample concentration, a minimal wall effect can be produced in the walls of the sample container (when the electrons emitted after the nuclear reaction reach the walls of the container).[265,268,269] Another more probable possibility is consistent with the small size of each nano detecting particle, as the energy brought to play by each neutron capture reaction is partially lost when the resulting electrons during transfer of energy reach the surface of the individual nano detector. This happens because those electrons lose kinetic energy through interactions with other electrons, which will play their role in the scintillating mechanism. This process is abruptly ended when they reach the surface. Thus, smaller the detector volume, greater is the wall effect. As a consequence, the apparent observation of wall effect may tend to yield further evidence of neutron detection in the studied system.

7.4 Conclusion

To summarize, we have tested colloidal nanoparticles $LaF_3:Ce^{3+},Gd^{3+}, Eu^{2+/3+}$ for high energy radiation detections. We have observed that the PMT is sensitive at around 450 nm which is due to superposition of short lived Eu^{2+} (350-550 nm) along with long lived Eu^{3+} emission. Interestingly, the colloidal nanoparticles under irradiation of ^{241}AmBe source have clearly differentiated the detection of mainly the thermal neutrons along with gamma radiation. Finally our experimental investigation has provided an opportunity explaining the real potential candidature for the radiation detection and possible alternatives to replace the traditional materials.

Chapter 8
Conclusion and Future Perspective

8.1 Conclusion

The objective of the present thesis was to develop magnetic–luminescent bifunctional nanoparticles using wet chemical routes to explore and improve the luminescence and magnetic properties for application in radiation detection. To realize, we have presented (i) $LaF_3:RE^{3+}$ (RE = Ce, Gd, Eu), (ii) $LaF_3:RE^{3+}$ and iron-oxide/ZnS@$LaF_3:RE^{3+}$ (RE = Ce, Gd, Tb), and (iii) $NaGdF_4:RE^{3+}$ and iron-oxide/SiO_2/$NaGdF_4:RE^{3+}$ (RE = Ce, Eu; and Yb, Er) nanoparticles. The major results obtained during the development of such bifunctional nanomaterials are summarized below.

(i) $LaF_3:RE^{3+}$ (RE= Ce, Gd, Eu) nanoparticles

- ➢ The polyol synthesis of triply doped LaF_3 along with in-depth investigation of energy transfer mechanism, photoluminescence and magnetic characteristics have been described.

- ➢ The presence of Eu^{2+} cations on the increasingly doped system, $LaF_3:xCe^{3+},xGd^{3+},yEu^{3+,}$ had a profound effect on the witnessed color of the fluoride luminescence, which spread from blue-white to red as a result of the band $4f^6 5d^1/4f^7$ transitions of Eu^{2+}.

- ➢ The Judd-Ofelt parameters were fully calculated and showed the greatest efficiency (85 %) of the $LaF_3:xCe^{3+},xGd^{3+},yEu^{3+}$ (x= 5, y= 10 mol.%) system.

- ➢ Besides optical properties, the reported materials $LaF_3:xCe^{3+},xGd^{3+},yEu^{3+,}$ were magnetically active, and exhibited paramagnetic behavior in the temperature range of from 2 to 300 K.

(ii) Iron-oxide/ZnS@$LaF_3:RE^{3+}$ (RE = Ce, Gd, Tb) nanoparticles

- ➢ The luminescence and magnetic nanocomposites containing triply doped Fe_3O_4/ZnS@$LaF_3:xCe^{3+},xGd^{3+},yTb^{3+}$ (x = 5; y =5, 10, 15 mol.%) were successfully prepared by multistep synthesis procedure.

- ➢ This bifunctional nanomaterial displayed good emission intensity from the $^5D_4 \rightarrow {}^7F_{6-0}$ transitions of Tb^{3+} ion when excited at the $4f \rightarrow 5d$ interconfigurational transition of Ce^{3+}

and supported by Gd^{3+} ion. The luminescence decay profiles suggested probable concentration quenching for the $^5D_4 \to ^7F_5$ transition of Tb^{3+} ion by cross relaxation mechanism.

➢ Structural and morphological studies using XRD and HRTEM with EDS mappings in scanning TEM mode, supported by dc magnetic measurements revealed the nanocrystalline, high magnetic saturation and superparamagnetic nature of the bifunctional nanocomposite at 300 K.

➢ The demonstration of the simultaneous strong green emission under control of field by bar magnet, profound the claim "action at distance" characteristic which means that nanoparticles can be manipulated by an external magnetic force. This provides tremendous advantages in many applications

(iii) $NaGdF_4:RE^{3+}$ and iron-oxide/SiO_2/$NaGdF_4:RE^{3+}$ ($RE^{3+} = Ce^{3+}$, Eu^{3+}; and Yb^{3+}, Er^{3+}) nanoparticles

➢ A new approach for microwave assisted thermolysis route was used to prepare $NaGdF_4:RE^{3+}$ and iron-oxide/SiO_2/$NaGdF_4:RE^{3+}$ nanosystems, which encoded both optical and magnetic properties, and exhibited red ($RE^{3+} = Ce^{3+}$, Eu^{3+}) and green ($RE^{3+} = Yb^{3+}$, Er^{3+}) emissions.

➢ The various processes of excitation/emission, energy transfer mechanism through Gd-sublattice mediated energy migration, UV down conversion, NIR up/down conversion and lifetime analysis have been discussed.

➢ The combination of efficient up/downconversion mechanism coupled with the paramagnetic properties of Gd^{3+} in $NaGdF_4:RE^{3+}$ and iron-oxide/SiO_2/$NaGdF_4:RE^{3+}$ nanoparticles resulted in the formation of new types of multifunctional nanomaterials.

➢ The illustration of "action at distance" characteristic shows strong red (green) emission under an external magnetic field and nanoparticles can be manipulated by an external magnetic force.

(iv) Scintillation experiments using ionizing radiation source

➢ We have tested successfully the colloidal nanoparticles $LaF_3:Ce^{3+}, Gd^{3+}, Eu^{2+/3+}$ for high energy radiation detections.

➢ Under irradiation of ^{241}AmBe source have clearly differentiated the detection of mainly the thermal neutrons along with gamma radiation.

> Our experimental investigation has provided an opportunity explaining the real potential candidature for the radiation detection and possible alternatives to replace the traditional materials.

In brief, this thesis provides a platform to understand the combinatorial investigation of magnetic and luminescence characteristics of nanoscaled bifunctional systems. Several characterization techniques were used to understand and explore these bifunctional materials. The simultaneous light emission from nanoparticles under an external magnetic field provides the potential application of such magnetic-luminescent bifunctional nanoparticles in the field of biomedical applications, smart field sensing devices, and magnetic light converting molecular devices. Finally, bifunctional luminophores were tested for scintillation application which further encouraged in development of nanodetectors for high energy radiation.

8.2 Future Perspective

Although there are many exciting potential applications for such bifunctional nanomaterials, and researchers are mainly interested in biomedicals at clinical levels and sensor devices, considerable challenges and issues remain to be resolved. For example, heterogeneity of nanomaterials remains a major problem and it is hard to precisely control the number of functional materials on the surface of nanoparticles that have precise composition, uniform surface modification and reproducible functionalization. Therefore, it is necessary to further explore multifunctional magnetic-luminescent nanoparticles for designing successful application oriented materials.

We believe that the research pursued in this dissertation project lays the groundwork for others in the field of nanomaterial synthesis and applications. The most important part of the future research is developing such nanomaterials combining enhanced magnetic and optical properties, which could make these materials a better choice for various technological applications. We would like to mention following points to further expand this work keeping in view future prospective.

> The valuable insights gained from the preparation of several bifunctional nanoparticles with precise control of size/shape can be extended to synthesize other Ln-fluoride based bifunctional nanoparticles, using different core-shell/shell or composite templates for different (alkali) rare earth fluoride based matrices. One may select suitable co-dopants by using different synthesis techniques to achieve rainbow color tunability. Also,

investigating hybrid nanoparticles with magnetic entities and lanthanides, one can explore novel physical phenomenon such as magntoluminescnce (creating luminescence using external magnetic energy) and magnetoacoustic.

- ➤ The materials containing magnetic nanoentity along with luminescence materials have possibility to explore magnetic light converting molecular devices (MLCMDs) by applying external magnetic field. On the other hand, controlling the luminescence under external pulsating magnetic field in lanthanide based luminophores may have very exciting results related to applications in telecommunications and aircraft-guidance. Few reports suggest the sensitivity of luminescence to the magnetic field that may enable the application of such nanomaterials in smart remote sensing and biomedicine. Besides, several biomedical/bioclinical applications these nanomaterials have great scope in solar energy conversion, bar-codes and other security tags and in forensic sciences.

- ➤ The one most important objective of design and development of such materials were "Demonstration of nuclear radiation nanodetectors based on colloidal nanoparticles with unprecedented performance: biomedical application". Hence, testing of bifunctional materials for scintillation application will be more rigorous and quantitative in terms of designing nanoscintillators as detectors for homeland security applications and equally to design magnetic-radioluminescent nanomaterials for tissue imaging and tomography.

Chapter 9
Bibliography and References

1　C. N. R. Rao, H. S. S. Ramakrishna Matte, R. Voggu and A. Govindaraj, *Dalton Trans.*, 2012, **41**, 5089–5120.

2　L. M. Liz-Marzán and P. V. Kamat, in *Nanoscale Materials*, Kluwer Academic Publishers, Boston, pp. 1–3.

3　S. K. Sharma, *Complex magnetic nanostructures : synthesis, assembly and applications*, Springer International Publishing, Cham, 2017.

4　Sarveena, N. Shrivastava, M. Singh and S. K. Sharma, in *Complex Magnetic Nanostructures*, Springer International Publishing, Cham, 2017, pp. 225–280.

5　W. Wu, Q. He and C. Jiang, *Nanoscale research letters*, 2008, **3**, 397–415.

6　M. Mikhaylova, D. K. Kim, N. Bobrysheva, M. Osmolowsky, V. Semenov, T. Tsakalakos and M. Muhammed, *Langmuir*, 2004, **20**, 2472–7.

7　P. N. Prasad, *Nanophotonics*, Wiley, 2004.

8　L. K. Joseph, K. R. Dayas, S. Damodar, B. Krishnan, K. Krishnankutty, V. P. N. Nampoori and P. Radhakrishnan, *Spectrochimica Acta-Part A: Molecular and Biomolecular Spectroscopy*, 2008, **71**, 1281–1285.

9　G. Chen, H. Ågren, Y. Ohulchanskyy, P. N. Prasad, H. Agren, T. Y. Ohulchanskyy and P. N. Prasad, *Chem. Soc. Rev.*, 2015, **44**, 1680–1713.

10　J. Bao, W. Chen, T. Liu, Y. Zhu, P. Jin, L. Wang, J. Liu, Y. Wei and Y. Li, *ACS Nano*, 2007, **1**, 293–298.

11　C. B. Murray, C. R. Kagan and M. G. Bawendi, *Annual Review of Materials Science*, 2000, **30**, 545–610.

12　P. D. Howes, R. Chandrawati and M. M. Stevens, *Science*, 2014, **346**, 1247390–1247390.

13　A. Espinosa, R. Di Corato, J. Kolosnjaj-Tabi, P. Flaud, T. Pellegrino and C. Wilhelm, *ACS Nano*, 2016, **10**, 2436–2446.

14　S. Laurent, D. Forge, M. Port, A. Roch, C. Robic, L. Vander Elst and R. N. Muller, *Chemical Reviews*, 2008, **108**, 2064–2110.

15　D. Ling, N. Lee and T. Hyeon, *Accounts of Chemical Research*, 2015, **48**, 1276–1285.

16 H. Dong, S.-R. Du, X.-Y. Zheng, G.-M. Lyu, L.-D. Sun, L.-D. Li, P.-Z. Zhang, C. Zhang and C.-H. Yan, *Chemical Reviews*, 2015, **115**, 10725–10815.

17 G. Wang, Q. Peng and Y. Li, *Accounts of Chemical Research*, 2011, **44**, 322–332.

18 C.-T. Yang and K.-H. Chuang, *MedChemComm*, 2012, **3**, 552.

19 L. Sun, Y. Qiu, T. Liu, H. Peng, W. Deng, Z. Wang and L. Shi, *RSC Advances*, 2013, **3**, 26367–26375.

20 L. Sudheendra, G. K. Das, C. Li, D. Stark, J. Cena, S. Cherry and I. M. Kennedy, *Chemistry of Materials*, 2014, 26(5), 1881–1888.

21 P. Perna, D. Maccariello, C. Rodrigo, J. L. F. Cuñado, M. Muñoz, J. L. Prieto, M. A. Niño, A. Bollero, J. Camarero, and R. Miranda, *Appl. Phys. Lett.*, 2014, **104**, 202407-4.

22 J. B. Magnetic nanoparticle biosensorsHaun, T. J. Yoon, H. Lee and R. Weissleder, *Wiley Interdisciplinary Reviews: Nanomedicine and Nanobiotechnology*, 2010, **2**, 291–304.

23 L. Zhang, W.-F. Dong and H.-B. Sun, *Nanoscale*, 2013, **5**, 7664–84.

24 A. J. Kell, M. L. Barnes, Z. J. Jakubek and B. Simard, *Journal of Physical Chemistry C*, 2011, **115**, 18412–18421.

25 R. K. Singh, K. D. Patel, J.-J. Kim, T.-H. Kim, J.-H. Kim, U. S. Shin, E.-J. Lee, J. C. Knowles and H.-W. Kim, *ACS Applied Materials & Interfaces*, 2014, **6**, 2201–2208.

26 C. Su, *Journal of Hazardous Materials*, 2017, **322**.

27 T.-D. Nguyen and T.-H. Tran, *RSC Advances*, 2014, **4**, 916–942.

28 C. Kaewsaneha, P. Tangboriboonrat, D. Polpanich and A. Elaissari, *ACS Applied Materials and Interfaces*, 2015, **7**, 23373–23386.

29 N. Chekina, D. Horák, P. Jendelová, M. Trchová, M. J. Beneš, M. Hrubý, V. Herynek, K. Turnovcová and E. Syková, *Journal of Materials Chemistry*, 2011, **21**, 7630.

30 S. Comby, E. M. Surender, O. Kotova, L. K. Truman, J. K. Molloy and T. Gunnlaugsson, *Inorganic Chemistry*, 2014, **53**, 1867–1879.

31 R. Blandford, Y. Yuan, M. Hoshino and L. Sironi, *Space Science Reviews*, 2017, **207**, 291–317.

32 L. Tong, J. Shi, D. Liu, Q. Li, X. Ren, and H. Yang, *Journal of Physical Chemistry C*, 2012, **116**, 7153-7157.

33 J. Li, B. Arnal, C.-W. Wei, J. Shang, T.-M. Nguyen, M. O'Donnell and X. Gao, *ACS Nano*, 2015, **9**, 1964–1976.

34 C. T. Kuo, H. S. Peng, Y. Rong, J. Yu, W. Sun, B. Fujimoto and D. T. Chiu, *Analytical*

Chemistry, 2017, **89**, 6232–6238.

35 S.-Y. Yu, H.-J. Zhang, J.-B. Yu, C. Wang, L.-N. Sun and W.-D. Shi, *Langmuir*, 2007, **23**, 7836–7840.

36 L. Sun, Z. Wang, J. Z. Zhang, J. Feng, J. Liu, Y. Zhao and L. Shi, *RSC Advances*, 2014, **4**, 28481–28489.

37 R. Kas, E. Sevinc, U. Topal and H. Y. Acar, *J. Phys. Chem. C*, 2010, **114**, 7758–7766.

38 L. U. Khan and Z. U. Khan, in *Complex Magnetic Nanostructures*, Springer International Publishing, Cham, 2017, pp. 121–171.

39 C. Zhong, P. Yang, X. Li, C. Li, D. Wang, S. Gai and J. Lin, *RSC Advances*, 2012, **2**, 3194.

40 H. He, M. Y. Xie, Y. Ding and X. F. Yu, *Applied Surface Science*, 2009, **255**, 4623–4626.

41 H. Peng, G. Liu, X. Dong, J. Wang, J. Xu and W. Yu, *Journal of Alloys and Compounds*, 2011, **509**, 6930–6934.

42 G. Jie and J. Yuan, *Analytical Chemistry*, 2012, **84**, 2811–2817.

43 G. H. Du, Z. L. Liu, Q. H. Lu, X. Xia, L. H. Jia, K. L. Yao, Q. Chu and S. M. Zhang, *Nanotechnology*, 2006, **17**, 2850–2854.

44 T. Wu, H. Pan, R. Chen, D. Luo, H. Zhang, Y. Shen, Y. Li and L. Wang, *Journal of Rare Earths*, 2016, **34**, 71–76.

45 F. Zhang, G. B. Braun, A. Pallaoro, Y. Zhang, Y. Shi, D. Cui, M. Moskovits, D. Zhao and G. D. Stucky, *Nano Letters*, 2012, **12**, 61–67.

46 J. Fang, M. Saunders, Y. Guo, G. Lu, C. L. Raston and K. S. Iyer, *Chemical Communications*, 2010, **46**, 3074.

47 L. U. Khan, H. F. Brito, J. H??ls??, K. R. Pirota, D. Muraca, M. C. F. C. Felinto, E. E. S. Teotonio and O. L. Malta, *Inorganic Chemistry*, 2014, **53**, 12902–12910.

48 D. Wang, J. He, N. Rosenzweig and Z. Rosenzweig, *Nano Letters*, 2004, **4**, 409–413.

49 K. C. Barick, A. Sharma, N. G. Shetake, R. S. Ningthoujam, R. K. Vatsa, P. D. Babu, B. N. Pandey and P. A. Hassan, *Dalton Trans.*, 2015, **44**, 14686–14696.

50 J. Shen, L.-D. Sun, Y.-W. Zhang and C.-H. Yan, *Chemical Communications*, 2010, **46**, 5731.

51 S.-Y. Yu, H.-J. Zhang, J.-B. Yu, C. Wang, L.-N. Sun and W.-D. Shi, *Langmuir*, 2007, **23**, 7836–7840.

52 D. Ling, N. Lee and T. Hyeon, *Accounts of Chemical Research*, 2015, **48**, 1276–1285.

53 J. Choi, Y. Jun, S.-I. Yeon, H. C. Kim, J.-S. Shin and J. Cheon, *Journal of the American*

Chemical Society, 2006, **128**, 15982–15983.

54 M. Srinivasan, M. Rajabi and S. A. Mousa, *Nanomaterials (Basel, Switzerland)*, 2015, **5**, 1690–1703.

55 J. Gao, H. Gu and B. Xu, *Accounts of Chemical Research*, 2009, **42**, 1097–1107.

56 X. Li, D. Zhao and F. Zhang, *Theranostics*, 2013, **3**, 292–305.

57 Y. Zhang, Q. Xiao, H. He, J. Zhang, G. Dong, J. Han and J. Qiu, *Journal of Materials Chemistry C*, 2015, 3–8.

58 Y. Liu, D. Wang, J. Shi, Q. Peng and Y. Li, *Angewandte Chemie - International Edition*, 2013, **52**, 4366–4369.

59 D. Peng, Q. Ju, X. Chen, R. Ma, B. Chen, G. Bai, J. Hao, X. Qiao, X. Fan and F. Wang, *Chemistry of Materials*, 2015, **27**, 3115–3120.

60 J.-C. G. Bunzli and C. Piguet, *Chemical Society Reviews*, 2005, **34**, 1048–1077.

61 V. Muhr, S. Wilhelm, T. Hirsch and O. S. Wolfbeis, *Accounts of Chemical Research*, 2014, **47**, 3481–3493.

62 F. Auzel, *Chemical Reviews*, 2004, **104**, 139–174.

63 J. Ren, G. Jia, Y. Guo, A. Wang and S. Xu, *Journal of Physical Chemistry C*, 2016, **120**, 1342–1351.

64 X. Chen, Y. Liu and D. Tu, *Lanthanide-Doped Luminescent Nanomaterials*, Springer-Verlag Berlin Heidelberg, 2014.

65 G. Yi and G.-M. Chow, *Chemistry of Materials*, 2007, **19**, 341–343.

66 R. Yadav, S. K. Singh, R. K. Verma and S. B. Rai, *Chemical Physics Letters*, 2014, **599**, 122–126.

67 J. T. van Wijngaarden, S. Scheidelaar, T. J. H. Vlugt, M. F. Reid, and A. Meijerink, *Physica. Review B,* 2010, **81**, 155112.

68 H. Chander, *Materials Science and Engineering R: Reports*, 2005, **49**, 113–155.

69 M. Nikl, *Measurement Science and Technology*, 2006, **17**, R37–R54.

70 L. G. Jacobsohn, K. B. Sprinkle, S. A. Roberts, C. J. Kucera, T. L. James, E. G. Yukihara, T. A. DeVol and J. Ballato, *Optical materials*, 2012, **33**, 136–140.

71 Y. Liu, W. Chen, S. Wang, A. G. Joly, S. Westcott and B. K. Woo, *Journal of Applied Physics*, 2008, **103,** 063105.

72 J. Zhou,, M. Yu, Y. Sun, X. Zhang, X. Zhu, Z. Wu, D. Wu, and F. Li, B*iomaterial,* 2011*,* **32,** 1148-*1156*.

73 P. Retif, S. Pinel, M. Toussaint, C. Frochot, R. Chouikrat, T. Bastogne and M. Barberi-Heyob, *Theranostics*, 2015, **5**, 1030–1044.

74 G. Lee, N. Savage, B. Wagner, Y. Zhang, B. Jacobs, H. Menkara, C. Summers and Z. Kang, *Journal of luminescence*, 2014, **147**, 363–366.

75 D. Wisniewski, S. Tavernier, A. J. Wojtowicz, M. Wisniewska, P. Bruyndonckx, P. Dorenbos, E. van Loef, C. W. E. van Eijk, L. A. Boatner,. *Nuclear Inst. and Methods in Physics Research, A*, 2002, **486**, 239–243.

76 J. Lucas, P. Lucas, T. Le Mercier, A. Rollat and W. Davenport, *Rare Earths: Science, Technology, Production and Use*, Elsevier Inc., 2014.

77 J. G. Bunzli and S. V Eliseeva, in *Springer Series on Fluorescence*, Springer-Verlag Berlin Heidelberg 2011, 1–45.

78 J. Vuojola and T. Soukka, *Methods and Applications in Fluorescence*, 2014, **2**, 12001.

79 C. J. Raub, *Handbook on the physics and chemistry of rare earths, volume 21*, Elsevier 1997.

80 JCG Bünzli, *Accounts of Chemical Research*, 2006, **39**, 53–61.

81 K. Binnemans, *Coordination Chemistry Reviews*, 2015, **295**, 1–45.

82 J. claude G. Bünzli, *Inorganica Chimica Acta*, 1987, **139**, 219–222.

83 K. Binnemans, *Chemical Reviews*, 2009, **109**, 4283–4374.

84 J. S. Shi and S. Y. Zhang, *Journal of Physical Chemistry B*, 2004, 18845–18849.

85 G. H. Dieke and R. A. Satten, *American Journal of Physics*, 1970, **38**, 399–400.

86 G. H. Dieke, H. M. Crosswhite and B. Dunn, *Journal of the Optical Society of America*, 1961, **51**, 820.

87 P. Hänninen and H. Härmä, Eds., *Lanthanide Luminescence*, Springer Berlin Heidelberg, Berlin, Heidelberg, 2011, vol. 7.

88 P. Dorenbos, *Journal of Luminescence*, 2007, **122**–**123**, 315–317.

89 K. N. Shinde, S. J. Dhoble, H. C. Swart and K. Park, *Phosphate Phosphors for Solid-State Lighting*, 2012, **174**, 41–60.

90 X. Chen, Y. Liu and D. Tu, *Lanthanide-doped luminescent nanomaterials : from fundamentals to bioapplications*, Springer-Verlag Berlin Heidelberg, 2014.

91 L. Armelao, S. Quici, F. Barigelletti, G. Accorsi, G. Bottaro, M. Cavazzini and E. Tondello, *Coordination Chemistry Reviews*, 2010, **254**, 487–505.

92 (a) F. Auzel, *Chemical Reviews*, 2004, **104**, 139–174. (b) B. Zhou, B. Shi, D. Jin and X.

Liu, *Nature Nanotechnology*, 2015, **10**, 924-936.

93 Q. Y. Zhang and X. Y. Huang, *Progress in Materials Science*, 2010, **55**, 353–427.

94 S. Ye, F. Xiao, Y. X. Pan, Y. Y. Ma and Q. Y. Zhang, *Materials Science and Engineering R: Reports*, 2010, **71**, 1–34.

95 S. S. Skourtis, C. Liu, P. Antoniou, A. M. Virshup and D. N. Beratan, *Proceedings of the National Academy of Sciences of the United States of America*, 2016, **113**, 8115–20.

96 T. Miyakawa and D. L. Dexter, *Physical Review B*, 1970, **1**, 2961–2969.

97 U. H. Kynast, M. M. Lezhnina and H. Kätker, *Solid State Phenomena*, 2005, **106**, 93–102.

98 V. . Makhov, N. . Khaidukov, N. Y. Kirikova, M. Kirm, J. . Krupa, T. . Ouvarova and G. Zimmerer, *Journal of Luminescence*, 2000, **87**–**89**, 1005–1007.

99 S. V. Vladimirov, V. S. Kaftanov, A. F. Nilov, Y. A. Semenov, V. T. Smolyankin, V. I. Ushakov, O. A. Goronkov, E. N. Zvonarev, O. I. Kozlov, V. P. Mashirev, V. V. Shatalov, T. T. Basiev, V. A. Konyushkin, V. V. Osiko, A. G. Papashvili and V. N. Skvortsov, *Atomic Energy*, 2001, **90**, 55–62.

100 P. A. Tanner, *Chemical Society Reviews*, 2013, **42**, 5090.

101 Y. Tosaka and S. Adachi, *Journal of Luminescence*, 2014, **156**, 157–163.

102 I. D. Hughes, M. Däne, A. Ernst, W. Hergert, M. Lüders, J. Poulter, J. B. Staunton, A. Svane, Z. Szotek and W. M. Temmerman, *Nature*, 2007, **446**, 650–653.

103 R. J. Elliott, *Magnetic properties of rare earth metals,* Plenum Press, 1972.

104 S. Kern and P. M. Raccah, *Journal of Physics and Chemistry of Solids*, 1965, **26**, 1625–1628.

105 J. S. Smart and J. H. Van Vleck, *Physics Today*, 1966, **19**, 77–78.

106 A. K. Zvezdin, V. M. Matveev, A. A. Mukhin and A. I. Popov, *Moscow, Izdatel'stvo Nauka, 1985, 296 p. In Russian.*, 1985.

107 I. Sharifi, H. Shokrollahi and S. Amiri, *Journal of Magnetism and Magnetic Materials*, 2012, **324**, 903–915.

108 X. Liu, K. Huang, S. Zhou, P. Zhao, U. Meridor, A. Frydman and A. Gedanken, *Journal of Magnetism and Magnetic Materials*, 2006, **305**, 504–508.

109 S. K. Sharma, *Exchange bias : from thin film to nanogranular & bulk systems*, CRC Press, 2017.

110 N. T. K. Thanh, N. Maclean and S. Mahiddine, *Chemical Reviews*, 2014, **114**, 7610–7630.

111 G. Jürjens, A. Kirschning and D. A. Candito, *Nat. Prod. Rep.*, 2015, **32**, 723–737.

112 S. Gai, C. Li, P. Yang and J. Lin, *Chemical Review*, 2014, **114**, 2343-2389.

113 B. Liu, W. Xie, D. Wang, W. Huang, M. Yu and A. Yao, *Materials Letters*, 2008, **62**, 3014–3017.

114 L. G. Jacobsohn, C. J. Kucera, T. L. James, K. B. Sprinkle, J. R. DiMaio, B. Kokuoz, B. Yazgan-Kukouz, T. A. DeVol and J. Ballato, *Materials*, 2010, **3**, 2053–2068.

115 O. V. Kharissova, B. I. Kharisov, V. M. Jiménez-Pérez, B. Muñoz Flores and U. Ortiz Méndez, *RSC Advances*, 2013, **3**, 22648.

116 S. Laurent, D. Forge, M. Port, A. Roch, C. Robic, L. V Elst, R. N. Muller, L. Vander Elst and R. N. Muller, *Chemical Reviews*, 2008, **108**, 2064–2110.

117 B. Liu, D. Wang, W. Huang, M. Yu and A. Yao, *Materials Research Bulletin*, 2008, **43**, 2904–2911.

118 R. G. Chaudhuri and S. Paria, *Chemical Reviews*, 2012, **112**, 2373–2433.

119 F. N. Tenorio Gonzalez, A. M. Bolarín Miró, F. Sánchez De Jesús, C. A. Cortés Escobedo and S. Ammar, *Journal of Magnetism and Magnetic Materials*, 2016, **407**, 188–194.

120 F. Fievet, J. P. Lagier, B. Blin, B. Beaudoin and M. Figlarz, *Solid State Ionics*, 1989, **32–33**, 198–205.

121 G. Cravotto and D. Carnaroglio, *Microwave Chemistry*, Walter de Gruyter GmbH & Co KG, Bostan, 2017.

122 O. Chen, L. Riedemann, F. Etoc, H. Herrmann, M. Coppey, M. Barch, C. T. Farrar, J. Zhao, O. T. Bruns, H. Wei, P. Guo, J. Cui, R. Jensen, Y. Chen, D. K. Harris, J. M. Cordero, Z. Wang, A. Jasanoff, D. Fukumura, R. Reimer, M. Dahan, R. K. Jain and M. G. Bawendi, *Nature Communications*, 2014, **5**, 5093.

123 F. Zhang, G. B. Braun, A. Pallaoro, Y. Zhang, Y. Shi, D. Cui, M. Moskovits, D. Zhao and G. D. Stucky, *Nano Letters*, 2012, **12**, 61–67.

124 S. Ge, X. Shi, K. Sun, C. Li, C. Uher, J. R. Baker, M. M. Banaszak Holl and B. G. Orr, *The Journal of Physical Chemistry C*, 2009, **113**, 13593–13599.

125 X. Yu, J. Wan, Y. Shan, K. Chen and X. Han, *Chemistry of Materials*, 2009, **21**, 4892–4898.

126 K. Sankar, J. B. Plumley, B. a. Akins, T. a. Memon, N. J. Withers, G. a. Smolyakov and M. Osinski, 2009, **7189**, 718909-718909–12.

127 F. Li, C. Li, X. Liu, T. Bai, W. Dong, X. Zhang, Z. Shi and S. Feng, *Dalton Trans.*, 2013, **42**, 2015–2022.

128 F. Wang, R. Deng and X. Liu, *Nature Protocols*, 2014, **9**, 1634–1644.

129 S. Santra, R. Tapec, N. Theodoropoulou, J. Dobson, A. Hebard and W. Tan, *Langmuir*, 2001, **17**, 2900–2906.

130 B. Manning and A. Ichimura, 2006.

131 V. K. Pecharsky and P. Y. Zavalij, *B9-Fundamentals of Powder Diffraction and Structural Characterization of Materials*, 2005.

132 Brucker AXS (2008):TOPAS V4:General profile and structure analysis software for powder diffraction data.-User's manual, Brucker AXS, Karlshruhe, Germany.

133 A. C. Larson and R. B. Von Dreele, *Los Alamos National Laboratory Report*, 2004, LAUR 86-748.

134 R. L. Fagaly, In *Wiley Encyclopedia of Electrical and Electronics Engineering*, John Wiley & Sons, Inc., 2016.

135 F. L. Bregolin, P. Franzen, H. Boudinov, U. S. Sias and M. Behar, *Journal of Luminescence*, 2014, **153**, 144–147.

136 A. I. Figueroa, In *Complex magnetic nanostructures : synthesis, assembly and applications, Springer International Publishing, Cham, 2017*.

137 D. Koziej, *Chemistry of Materials*, 2016, **28**, 2478–2490.

138 T. D. Dunbar, W. L. Warren, B. A. Tuttle, C. A. Randall and Y. Tsur‖, Journal of Physical Chemistry B, 2004, **108** (3), 908–917

139 R. D. Teo, J. Termini and H. B. Gray, *Journal of Medicinal Chemistry*, 2016, **59**, 6012–6024.

140 R. Liu, M. Buchert, S. Dittrich, A. Manhart, C. Merz and D. Schüler, *Digest of Technical Papers - IEEE International Conference on Consumer Electronics*, 2011, 286–290.

141 M. Osinski, J. B. Plumley, N. J. Withers, B. A. Akins, G. Medina, A. C. Rivera and G. A. Smolyakov, *ICONN 2010 - Proceedings of the 2010 International Conference on Nanoscience and Nanotechnology*, 2010, 189–192.

142 P. E. Healy, F. Application and P. Data, 2007, **2**.

143 G. Barnard, P. Myslinski, J. Chrostowski and M. Kavehrad, *IEEE Journal of Quantum Electronics*, 1994, **30**, 1817–1830.

144 F. Leonberger, W. H. Glenn and G. A. Ball, Continously tunable single-mode rare-earth doped pumped laser arrangement, *US Patent US 5317576 A,* 1994.

145 G. F. de Sá, O. L. Malta, C. de Mello Donegá, a. M. Simas, R. L. Longo, P. a. Santa-Cruz

and E. F. da Silva, *Coordination Chemistry Reviews*, 2000, **196**, 165-195.

146 L. Sun, X. Ge, J. Liu, Y. Qiu, Z. Wei, B. Tian and L. Shi, *Nanoscale*, 2014, **6**, 13242–13252.

147 N. Shrivastava, L. U. Khan, Z. U. Khan, J. Vargas, O. Moscoso-Londoño, C. Ospina, H. F. Brito, Y. Javed, M. C. F. C. Felinto, A. S. de Menezes, M. Knobel and S. K. Sharma, *J. Mater. Chem. C*, 2017, 2282–2290.

148 Y. Wang, G. Zhu, S. Xin, Q. Wang, Y. Li, Q. Wu, C. Wang, X. Wang, X. Ding and W. Geng, *Journal of Rare Earths*, 2015, **33**, 1–12.

149 L. G. Jacobsohn, a. Toncelli, K. B. Sprinkle, C. J. Kucera and J. Ballato, *Journal of Applied Physics*, 2012, **111**, 74315.

150 R. Naccache, Q. Yu and J. A. Capobianco, *Advanced Optical Materials*, 2015, **3**, 482–509.

151 T. K. Srinivasan, B. S. Panigrahi, A. K. Arora, B. Venkatraman and D. Ponraju, *Radiation Physics and Chemistry*, 2014, **99**, 92–96.

152 C. Liu, Y. Hou and M. Gao, *Advanced Materials*, 2014, **26**, 6922–6932.

153 R. Lv, G. Yang, Y. Dai, S. Gai and P. Yang, *Nanoscale*, 2014, **6**, 14799.

154 E. A. Radzhabov, *Optics and Spectroscopy*, 2016, **121**, 482–486.

155 T. K. Srinivasan, B. S. Panigrahi, A. K. Arora, B. Venkatraman and D. Ponraju, *Radiation Physics and Chemistry*, 2014, **99**, 92–96.

156 C. Lorbeer and A. V. Mudring, *Journal of Physical Chemistry C*, 2013, **117**, 12229–12238.

157 Y. Liu, D. Tu, H. Zhu and X. Chen, *Chemical Society Reviews*, 2013, **42**, 6924.

158 E. M. Rodrigues, R. D. L. Gaspar, I. O. Mazali and F. a. Sigoli, *J. Mater. Chem. C*, 2015, **3**, 6376–6388.

159 M. M. Lezhnina, T. J??stel, H. K??tker, D. U. Wiechert and U. H. Kynast, *Advanced Functional Materials*, 2006, **16**, 935–942.

160 T. Grzyb and S. Lis, *Journal of Rare Earths*, 2009, **27**, 588–592.

161 M. Y. Xie, L. Yu, H. He and X. F. Yu, *Journal of Solid State Chemistry*, 2009, **182**, 597–601.

162 P. Dorenbos, *Chemistry of Materials*, 2005, **17**, 6452–6456.

163 E. Sarantopoulou, S. Kobe, Z. Kollia, B. Podmiljšak, P. . McGuiness, G. Dražić and a. . Cefalas, *Journal of Magnetism and Magnetic Materials*, 2003, **267**, 182–190.

164 D. R. Cooper, K. Kudinov, P. Tyagi, C. K. Hill, S. E. Bradforth and J. L. Nadeau, *Physical*

chemistry chemical physics : PCCP, 2014, **16**, 12441–53.

165 R.E. Kroona,, H. C. Swart, O.M. Ntwaeaborwa, and H.A.A. Seed Ahmed, *Physica B*, **2014**, 439, 83–87..

166 G. Liu and B. Jacquier, S*pectroscopic Properties of Rare Earths in Optical Materials* S Springer Berlin Heidelberg, 2005.

167 A. B. Parmentier, P. F. Smet and D. Poelman, *Materials*, 2013, **6**, 3663–3675.

168 S. Li, X. Zhang, Z. Hou, Z. Cheng, P. Ma and J. Lin, *Nanoscale*, 2012, **4**, 5619–26.

169 X. Li, F. Zhang and D. Zhao, *Chemical Society reviews*, 2015, **44**, 1346–1378.

170 B. Yan, *RSC Advances*, 2012, **2**, 9304.

171 D. Chen and Y. Wang, *Nanoscale*, 2013, **5**, 4621.

172 S. H. M. Poort, A. Meyerink and G. Blasse, *J. Phys. Chem. Solids*, 1997, **58**, 1451–1456.

173 J. C. R. Aquino, F. H. Arago, P. Hidalgo, R. Cohen, L. C. C. M. Nagamine, J. A. H. Coaquira and H. F. Brito, *Journal of Nanoparticle Research*, 2014, **16**, 1–9.

174 H. F. Brito, O. L. Malta, M. C. F. C. Felinto and E. E. S. Teotonio, *Luminescence phenomena involving metal enolates. In The Chemistry of Metal Enolates. ZABICKY, J., Ed.; John Wiley & Sons Ltd.; England*, 2009, 131–184.

175 J. C. G. Bünzli, *Journal of Luminescence*, 2016, **170**, 866–878.

176 T. Grzyb, A. Szczeszak, Z. Śniadecki, B. Idzikowski and S. Lis, *Journal of Alloys and Compounds*, 2016, **686**, 489–495.

177 J.-C. G. Bünzli, *Coordination Chemistry Reviews*, 2015, **293**–**294**, 19–47.

178 L. Chen, C. C. Lin, C. W. Yeh, and R. S. Liu, *Materials*, 2010, **3**, 2172-2195.

179 T. K. Srinivasan, B. Venkatraman, D. Ponraju and A. K. Arora, *World Journal of Nano Science and Engineering*, 2012, **2**, 201–205.

180 P. K. Nampoothiri, M. N. Gandhi and A. R. Kulkarni, *Materials Chemistry and Physics*, 2017, **190**, 45–52.

181 R. A. Sá Ferreira, S. S. Nobre, C. M. Granadeiro, H. I. S. Nogueira, L. D. Carlos and O. L. Malta, *Journal of Luminescence*, 2006, **121**, 561–567.

182 H. Chen, D. C. Colvin, B. Qi, T. Moore, J. He, O. T. Mefford, F. Alexis, J. C. Gore and J. N. Anker, *Journal of materials chemistry*, 2012, **22**, 12802–12809.

183 G. Srinet, P. Varshney, R. Kumar, V. Sajal, P. K. Kulriya, M. Knobel and S. K. Sharma, *Ceramics International*, 2013, **39**, 6077–6085.

184 J. A. Sampaio, M. C. Filadelpho, A. A. Andrade, J. H. Rohling, A. N. Medina, A. C.

Bento, L. M. Silva, F. C. G. Gandra, L. A. O. Nunes and M. L. Baesso, .

185 L. C. V. Rodrigues, J. Hölsä, H. F. Brito, M. Maryškoe, J. R. Matos, P. Paturi, R. V. Rodrigues, and M. Lastusaari, *Journal of Luminescence*, 2016, **170**, 701-706.

186 K. Van den Eeckhout, P. F. Smet and D. Poelman, *Materials*, 2010, **3**, 2536–2566.

187 L. U. Khan, D. Muraca, H. F. Brito, O. Moscoso-Londoño, M. C. F. C. Felinto, K. R. Pirota, E. E. S. Teotonio and O. L. Malta, *Journal of Alloys and Compounds*, 2016, **686**, 453–466.

188 G. Konstantatos and E. H. Sargent, *Nature nanotechnology*, 2010, **5**, 391–400.

189 F. Ye, Å. Barrefelt, H. Asem, M. Abedi-Valugerdi, I. El-Serafi, M. Saghafian, K. Abu-Salah, S. Alrokayan, M. Muhammed and M. Hassan, *Biomaterials*, 2014, **35** (12), 3885-94.

190 A. Son, A. Dhirapong, D. K. Dosev, I. M. Kennedy, R. H. Weiss and K. R. Hristova, *Analytical and Bioanalytical Chemistry*, 2008, **390**, 1829–1835.

191 O. S. Wolfbeis, *Chem. Soc. Rev. Chem. Soc. Rev*, 2015, **44**, 4743–4768.

192 D. Shi, M. E. Sadat, A. W. Dunn and D. B. Mast, *Nanoscale*, 2015, **7**, 8209–8232.

193 S. Gai, P. Yang, C. Li, W. Wang, Y. Dai, N. Niu and J. Lin, *Advanced Functional Materials*, 2010, **20**, 1166–1172.

194 H. Kim, M. Achermann, L. P. Balet, J. A. Hollingsworth and V. I. Klimov, *Journal of the American Chemical Society*, 2005, **127**, 544–546.

195 Y.-S. Lin, S. Wu, Y. Hung, Y. Chou, C. Chang, M. Lin, C. Tsai and C.-Y. Mou, *Chemistry of Materials*, 2006, **18**, 5170–5172.

196 L. Zhang, B. Liu and S. Dong, *Journal of Physical Chemistry B*, 2007, **111**, 10448–10452.

197 X. Hong, J. Li, M. Wang, J. Xu, W. Guo, J. Li, Y. Bai and T. Li, *Chemistry of Materials*, 2004, **16**, 4022–4027.

198 W. Wu, Q. He and C. Jiang, *Nanoscale Research Letters*, 2008, **3**, 397–415.

199 C.-J. Yu, S.-M. Wu and W.-L. Tseng, *Analytical Chemistry*, 2013, **85**, 8559–8565.

200 A. Roychowdhury, S. P. Pati, S. Kumar and D. Das, *AIP Conf. Proc*, 2013, **1512**, 246–247.

201 L. Liu, W. Jiang, L. Yao, X.-W. Yang, B.-H. Chen, S.-X. Wu and F.-S. Li, *Journal of Nanoscience and Nanotechnology*, 2014, **14**, 5047–53.

202 C. Zhang, B. Pu, Z. Mo and C. Jiang, *Micro & Nano Letters*, 2014, **9**, 171–174.

203 M. Stefan, C. Leostean, O. Pana, M. L. Soran, R. C. Suciu, E. Gautron and O. Chauvet, *Applied Surface Science*, 2014, **288**, 180–192.

204 A. S. Borges, J. D. L. Dutra, R. O. Freire, R. T. Moura, J. G. Da Silva, O. L. Malta, M. H. Araujo and H. F. Brito, *Inorganic Chemistry*, 2012, **51**, 12867–12878.

205 J. M. D. Coey, *Magnetism and Magnetic Materials*, Cambridge University Press, 2010.

206 W. T. Carnall, G. L. Goodman, K. Rajnak and R. S. Rana, *The Journal of Chemical Physics*, 1989, **90**, 3443–3457.

207 X. Sun, Y. W. Zhang, Y. P. Du, Z. G. Yan, R. Si, L. P. You and C. H. Yan, *Chemistry - A European Journal*, 2007, **13**, 2320–2332.

208 A. R. Denton and N. W. Ashcroft, *Physical Review A*, 1991, **43**, 3161–3164.

209 F. N. Sayed, V. Grover, S. V. Godbole and A. K. Tyagi, *RSC Adv.*, 2012, **2**, 1161–1167.

210 E. Sarantopoulou, S. Kobe, Z. Kollia, P. J. McGuiness and A.-C. Cefalas, *IEEE Transactions on Magnetics*, 2003, **39**, 3426–3428.

211 S. Ruebel and M. Stuemke, Pub. No. US 2010/0041620A1, vol. 1, no. 60, p. 11, 2004.

212 B. Poornaprakash, D. Amaranatha Reddy, G. Murali, N. Madhusudhana Rao, R. P. Vijayalakshmi and B. K. Reddy, *Journal of Alloys and Compounds*, 2013, **577**, 79–85.

213 Y. Jiang, X. M. Meng, J. Liu, Z. Y. Xie, C. S. Lee and S. T. Lee, *Advanced Materials*, 2003, **15**, 323–327.

214 L. Liu, N. Zhang, Z. Leng, Y. Liang, R. Li, L. Zou and S. Gan, *Dalton Trans.*, 2015, **44**, 6645–6654.

215 J. Lian, X. Sun and X. Li, *Materials Chemistry and Physics*, 2011, **125**, 479–484.

216 Q. A. Pankhurst and R. J. Pollard, *Physical Review Letters*, 1991, **67**, 248–250.

217 P. M. A. de Bakker, E. De Grave, R. E. Vandenberg, L. H. Bowen, R. J. Pollard and P. R.M., *Phys. Chem. Minerals*, 1991, **18**, 131–143.

218 B. Poornaprakash, K. Naveen Kumar, U. Chalapathi, M. Reddeppa, P. T. Poojitha and S.-H. Park, *Journal of Materials Science: Materials in Electronics*, 2016, **27**, 6474–6479.

219 S. S. Lucky, K. C. Soo and Y. Zhang, *Chemical Reviews*, 2015, 115.

220 Z. Fan, M. Shelton, A. K. Singh, D. Senapati, S. A. Khan and P. C. Ray, *ACS Nano*, 2012, **6**, 1065–1073.

221 L. Cheng, C. Wang, X. Ma, Q. Wang, Y. Cheng, H. Wang, Y. Li and Z. Liu, *Advanced Functional Materials*, 2013, **23**.

222 G. Tian, X. Zhang, Z. Gu and Y. Zhao, *Advanced Materials*, 2015, **27**.

223 P. C. Ray, S. A. Khan, A. K. Singh, D. Senapati and Z. Fan, *Chemical Society Reviews*, 2012, **41**, 3193.

224 S. Yu, L. Fu, Y. Zhou and H. Su, *Photochemical & photobiological sciences*, 2011, **10**, 548–553.

225 F. Bi, X. Dong, J. Wang and G. Liu, *RSC Adv.*, 2015, **5**, 12571–12577.

226 L. W. Yang, Y. Y. Zhang, J. J. Li, Y. Li, J. X. Zhong and P. K. Chu, *Nanoscale*, 2010, **2**, 2805–2810.

227 C. Liu, Z. Gao, J. Zeng, Y. Hou, F. Fang, Y. Li, R. Qiao, L. Shen, H. Lei, W. Yang and M. Gao, *ACS Nano*, 2013, **7**, 7227–7240.

228 L. Zhang, Y.-S. Wang, Y. Yang, F. Zhang, W.-F. Dong, S.-Y. Zhou, W.-H. Pei, H.-D. Chen and H.-B. Sun, *Chemical Communications*, 2012, **48**, 11238.

229 A. Xia, Y. Gao, J. Zhou, C. Li, T. Yang, D. Wu, L. Wu and F. Li, *Biomaterials*, 2011, **32**, 7200–7208.

230 P. Chen, Z. Zhong, H. Jia, J. Zhou, J. Han, X. Liu and J. Qiu, *RSC Advances*, 2016, **6**, 7391–7395.

231 Y. Chan, J. P. Zimmer, M. Stroh, J. S. Steckel, R. K. Jain and M. G. Bawendi, Advanced Materials, 2004, 16, 2092-2097.

232 C. Yang, L. Ma, S. Wu, X. Yu and H. Liu, *Journal of Materials Science: Materials in Electronics*, 2016, **27**, 11720–11725.

233 F. Li, C. Li, X. Liu, T. Bai, W. Dong, X. Zhang, Z. Shi and S. Feng, *Dalton transactions (Cambridge, England : 2003)*, 2013, **42**, 2015.

234 Lin and Q. Wang, *Chemical Engineering Journal*, 2014, **250**, 190–197.

235 Y. Liu, D. Tu, H. Zhu, R. Li, W. Luo and X. Chen, *Advanced Materials*, 2010, **22**, 3266–3271.

236 H. S. Jang, K. Woo and K. Lim, *Optics Express*, 2012, **20**, 17107–17118.

237 N. Shrivastava, L. U. Khan, J. M. Vargas, C. Ospina, J. A. Q. Coaquira, G. Zoppellaro, H. F. Brito, Y. Javed, D. K. Shukla, M. C. F. C. Felinto and S. K. Sharma, *Phys. Chem. Chem. Phys.*, 2017, **19**, 18660–18670.

238 C. Liu, H. Wang, X. Zhang and D. Chen, *J. Mater. Chem.*, 2009, **19**, 489–496.

239 G. A. Kumar, C. W. Chen, J. Ballato, andR. E. Riman, *Chemistry of Materials., 2007, 19 (6), 1523–1528*

240 H. Zhu, J. Tao, W. Wang, Y. Zhou, P. Li, Z. Li, K. Yan, S. Wu, K. W. K. Yeung, Z. Xu, H. Xu and P. K. Chu, *Biomaterials*, 2013, **34**, 2296–2306.

241 A. Kamkaew, F. Chen, Y. Zhan, R. L. Majewski and W. Cai, *ACS Nano*, 2016, **10**, 3918–

3935.

242 C. Ronda, H. Wieczorek, V. Khanin and P. Rodnyi, *ECS Journal of Solid State Science and Technology*, 2016, **5**, R3121–R3125.

243 S. M. Pellegrin, C. Whitney and C. G. Wilson, *Journal of Microelectromechanical Systems*, 2010, **19**, 1207–1214.

244 T. M. Demkiv, O. O. Halyatkin, V. V. Vistovskyy, A. V. Gektin and A. S. Voloshinovskii, *Journal of Applied Physics*, 2016, **120**, 144301.

245 W. V Mayneord, *British Journal of Applied Physics*, 1953, **4**, 353–358.

246 T. Gupta, *Radiation, ionization, and detection in nuclear medicine*, Springer, 2013.

247 E. A. McKigney, R. E. Del Sesto, L. G. Jacobsohn, P. A. Santi, R. E. Muenchausen, K. C. Ott, T. M. McCleskey, B. L. Bennett, J. F. Smith and D. W. Cooke *Nuclear Instruments and Methods in Physics Research Section A: Accelerators, Spectrometers, Detectors and Associated Equipment*, 2007, **579**, 15–18.

248 M. Flaska, S. A. Pozzi and J. B. Czirr, in *2008 IEEE Nuclear Science Symposium Conference Record*, IEEE, 2008, pp. 3376–3380.

249 F. WILKINSON, in *Emission Tomography*, Elsevier, 2004, pp. 229–254.

250 (a) J. S. Neal, L. A. Boatner, M. Spurrier, P. Szupryczynski and C. L. Melcher, *Nuclear Instruments & Methods in Physics Research Section A*, 2007, **579**, 19-22. (b) R. B. James, A. Burger and L. A. Franks (eds.), International Society for Optics and Photonics, 2007, **6706**, 67061A.

251 M.Moszyński, *Nuclear Instruments and Methods in Physics Research Section A: Accelerators, Spectrometers, Detectors and Associated Equipment*, 2003, **505**, 101–110.

252 *Nuclear Instruments and Methods in Physics Research Section A: Accelerators, Spectrometers, Detectors and Associated Equipment*, 2007, **572**, 774–784.

253 T. INADA, *Journal of Nuclear Science and Technology*, 1968, **5**, 287–291.

254 A. N. Caruso, *Journal of Physics:Condensed Matter*, 2010, **22**, 443201.

255 TakayukiYanagida, *Optical Materials*, 2013, **35**, 1987–1992.

256 L. G. Jacobsohn, C. J. Kucera, K. B. Sprinkle, S. A. Roberts, E. G. Yukihara, T. A. DeVol and J. Ballato, in *IEEE Nuclear Science Symposuim & Medical Imaging Conference*, IEEE, 2010, pp. 1600–1602.

257 W. Lawrence and Vivek Nagarkar, US Patent, *US9151668 B1, US 13/349,329*, 2012

258 P.Dorenbos, *Nuclear Instruments and Methods in Physics Research Section A:*

Accelerators, Spectrometers, Detectors and Associated Equipment, 2002, **486**, 208–213.

259 J. Dumazert, R. Coulon, V. Kondrasovs, K. Boudergui, G. Sannié, J. Gameiro, S. Normand Laurence Méchin, Advancements in Nuclear Instrumentation Measurement Methods and their Applications, Apr 2015, Lisbonne, Portugal. HAL Id : hal-01195882

260 S. Pan, Q. Wang, H. Li, X. Chen and G. Ren, *Radiation Measurements*, 2016, **88**, 7–13.

261 P. Guss, R. Guise, D. Yuan, S. Mukhopadhyay, R. O'Brien, D. Lowe, Z. Kang, H. Menkara and V. V. Nagarkar, *Journal of Applied Physics*, 2013, **113**, 64303.

262 L. G. Jacobsohn, K. B. Sprinkle, S. A. Roberts, C. J. Kucera, T. L. James, E. G. Yukihara, T. A. DeVol and J. Ballato, *Journal of Nanomaterials*, 2011, **2011**, 1–6.

263 Teng-Kuan Tseng, *Luminescent oxide nanocomposite: synthesis, characterization and scintillation application,* Thesis, University of Florida, 2010.

264 Mitsuru Nenoi (ed.), *Current Topics in Ionizing Radiation Research*, InTech, 2012.

265 Krishnaprasad Sankar, *Synthesis and Characterization of Ceriumdoped Lanthanum Halide Colloidal Nanocrystals,* Thesis, The University of New Mexico, 2008.

266 R. T. Kouzes, K. E. Conlin, J. H. Ely, L. E. Erikson, W. J. Kernan, A. T. Lintereur, E. R. Siciliano, D. L. Stephens, D. C. Stromswold, R. M. Van Ginhoven and M. L. Woodring, .

267 H. Kluge and K. Weise, *Radiation Protection Dosimetry*, 1982, **2**, 85–93.

268 F. D. Amaro, C. M. B. Monteiro, J. M. F. Dos Santos and A. Antognini, *Scientific reports*, 2017, **7**, 41699.

269 S. M. Carturan, T. Marchi, G. Maggioni, F. Gramegna, M. Degerlier, M. Cinausero, M. D. Palma and A. Quaranta, *Journal of Physics: Conference Series*, 2015, **620**, 12010.

Curriculum Vitae

Navadeep Shrivastava
Doctoral Student in Condensed Matter Physics
Functional Nanomaterials Laboratory
Post-Graduate Program in Physics (PPGF)
Federal University of Maranhão
São Luís - MA, 65080-805, Brazil
E-mail: enavadeep@gmail.com

List of Publications in Peer Reviewed Journals: Contribution in Thesis

1. Navadeep Shrivastava, L. U. Khan, Z U. Khan, J. M. Vargas, O. Moscoso-Londoño, Carlos Ospina, H. F. Brito, Yasir Javed, M. C. F. C. Felinto, A. S. Menezes, Marcelo Knobel and S. K. Sharma, *Building block magneto-luminescent nanomaterials of iron-oxide/ZnS@LaF$_3$:Ce^{3+},Gd^{3+},Tb^{3+} with green emission*, **Journal of Material chemistry C**, *2017*, 5, 2282-2290. **DOI:** 10.1039/c6tc05053k (Full Article).

2. Navadeep Shrivastava, L.U. Khan, J. M. Vargas, Carlos Ospina, Jose Coaquira, Giorgio Zoppellaro, H.F. Brito, Yasir Javed, Dinesh Shukla, M.C.F.C. Felinto and S. K. Sharma; *Efficient Multicolor Tunability of Ultrasmall Ternary doped LaF$_3$ Nanoparticles: Energy Conversion and Magnetic Behavior*, **Physical Chemistry and Chemical Physics**, *2017,* 19 18660-18670, **DOI:** 10.1039/C7CP02235B. (Full Article).

3. Navadeep Shrivastava, Uelson Rocha, , Diego Muraca, Wagner Silva, Carlos Jacinto, Rajesh Kumar, and S. K. Sharma, *Insight into Dual-Modality of Triply doped Magneto-Luminescent Iron-oxide@NaGdF$_4$:RE^{3+} (RE = Ce, Tb, Dy) Nanoparticles*; **Materials Letters**, *2017,* Article in Press, (DOI: 10.1016/j.matlet.2017.11.037) (Communication)).

4. Navadeep Shrivastava, Uelson Rocha, Diego Muraca, Carlos Jacinto, Sergio Moreno, J. M. Vargas, and S. K. Sharma, *Magnetic Up/Down Converting Fluorescent NaGdF$_4$:Ln^{3+} and Fe$_x$O$_y$@ NaGdF$_4$:Ln^{3+} Nanoparticles*; Accepted, **AIP advances,** *2017* (Full Article).

5. Navadeep Shrivastava, Uelson Rocha, Carlos Ospina, Wagner F. Silva, Diego Muraca, Rajesh Kumar, A. S. De Menezes, Carlos Jacinto, Giorgio Zoppellaro, and S. K. Sharma, (2017), Optical-magnetic characteristics for dual optical window: a case of NaGdF4:RE3+ and Fe$_x$O$_y$/SiO$_2$/NaGdF$_4$:RE^{3+} nanoparticles, **Submitted**, (Full Article).

List of Publications of Book Chapters: Contribution in Thesis

1. Sarveena, **Navadeep Shrivastava**, M. Singh, and S. K. Sharma, Multifunctional Magnetic Nanostructures: Exchange Bias Model and Applications; In S.K. Sharma (ed.), Complex Magnetic Nanostructures; Springer International Publishing AG 2017, DOI: 10.1007/978-3-319-52087-2_7ISBN: 978-3-319-52086-5.

2. Navadeep Shrivastava, Sarveena, M. Singh and S. K. Sharma, *An introduction to magnetism at nanoscale: An Overview*; In *S.K. Sharma (ed.)*, Exchange Bias: From Thin Film To Nanogranualar To Bulk Systems, CRC press series in Materials Science and Engineering, Taylor and Francis, 2017; ISBN: 978-1-4987-9723-8).

Participation in Conferences during Ph.D.

1. 62nd Annual Conference on **Magnetism and Magnetic Materials conference**, 6-10 November, 2017, Pittsburgh, USA

2. 16th **Brazilian Material Research Society** (B-MRS), 10-14 September, 2017, Gramado, Brazil.

3. 18th **International Conference of Luminescence** (ICL), 28 August -1 September 2017, João Pessoa, Brazil

4. Spring Meeting of **European Material Research Society** (E-MRS), 22-26 May, 2017, Strasbourg, France.

5. 15th **Brazilian Material Research Society** (B-MRS), 25-29 September, 2016, Campinas, Brazil.

Awards and Recognition

1. Travel Grant of USD $750.00 by IEEE to participate in 62nd MMM conference, 2017 in Pittsburgh, USA.

2. Bernhard Gross Award for Best Oral Contribution in Symposium B, at Brazilian-MRS (XVI SBPMAT meeting), 2017, Gramado, RS, Brazil.

3. Best Poster Award and Cash Prize of 100 Euro in Symposium O, at Spring Meeting of EMRS-2017, Strasbourg, France.

4. International Travel grant (2017) by State Funding Agency FAPEMA to attend scientific conference spring meeting of European Material Research Society (E-MRS) 2017 in Strasbourg, France.

5. Short Stay International Fellowship (3 Months) in 2017 by State Funding Agency, FAPEMA-Brazil, for scientific collaboration at Institute of Belseiro, Bariloche Atomic Center, Argentina (IB-CAB, CNEA).

6. Short Stay National Fellowship (3 Months) in 2016 by State Funding Agency, FAPEMA-Brazil, for scientific collaboration at Institute of Chemistry, University of Sao Paulo (IQ-USP).

PAPER

Building block magneto-luminescent nanomaterials of iron-oxide/ZnS@LaF$_3$:Ce^{3+},Gd^{3+},Tb^{3+} with green emission†

Navadeep Shrivastava,[ab] L. U. Khan,[b] Z. U. Khan,[c] J. M. Vargas,[d] O. Moscoso-Londoño,[e] Carlos Ospina,[f] H. F. Brito,[b] Yasir Javed,[g] M. C. F. C. Felinto,[h] A. S. Menezes,[a] Marcelo Knobel[ef] and S. K. Sharma*[a]

The preparation of novel triply-doped bifunctional Fe$_3$O$_4$/ZnS@LaF$_3$:xCe^{3+},xGd^{3+},yTb^{3+} (x = 5; y = 5, 10 and 15 mol%) nanocomposites with efficient optical and magnetic features has been reported. The ZnS semiconductor functionalized Fe$_3$O$_4$ particles were coated with LaF$_3$:RE^{3+} materials *via* a chitosan-assisted co-precipitation method. The size of iron oxide ∼7.2 nm and trigonal structures of bifunctional nanostructures were confirmed through X-ray diffraction and high-resolution transmission electron microscopy. The static magnetic measurements supported and manifested the superparamagnetic behavior of the materials at 300 K. A broad emission band was observed in the blue region (400–550 nm) due to the sulphur vacancy on the surface of the Fe$_3$O$_4$/ZnS nanocomposite. For a triply doped bifunctional nano-structure, the excitation spectra revealed broad absorption bands centered at around 270 nm, which were attributed to the 4f(^{7}F$_{7/2}$) → 5d interconfigurational transition of the Ce^{3+} ion accompanied by narrow absorption lines arising from the 4f–4f intraconfigurational transitions of the Tb^{3+} ion. The emission spectra of the nanocomposites showed characteristic narrow emission lines assigned to the ^{5}D$_4$ → ^{7}F$_J$ transitions (J = 6–0) of the Tb^{3+} ion. The energy transfer process from the Ce^{3+} → Gd^{3+} → Tb^{3+} ions has also been presented and discussed. Furthermore, the structural, photoluminescence and magnetic properties of Fe$_3$O$_4$/ZnS@LaF$_3$:RE^{3+} suggested that it may be an efficient candidate for magnetic light-converting mole-cular devices (MLMCDs) and high energy radiation detection.

PAPER

Efficient multicolor tunability of ultrasmall ternary-doped LaF$_3$ nanoparticles: energy conversion and magnetic behavior†

Navadeep Shrivastava, [ab] L. U. Khan,[bc] J. M. Vargas,[d] Carlos Ospina,[c] J. A. Q. Coaquira, [e] Giorgio Zoppellaro, [f] H. F. Brito,[b] Yasir Javed,[g] D. K. Shukla,[h] M. C. F. C. Felinto[i] and Surender K. Sharma [*a]

Luminescence-tunable multicolored LaF$_3$:xCe^{3+},xGd^{3+},yEu^{3+} (x = 5; y = 1, 5, 10, and 15 mol%) nanoparticles have been synthesized *via* a low cost polyol method. Powder X-ray diffraction and high-resolution transmission electron microscopy studies confirm the hexagonal phase of the LaF$_3$:xCe^{3+},xGd^{3+},yEu^{3+} nanophosphors with average sizes (oval shape) ranging from 5 to 7 nm. Energy-dispersive X-ray spectroscopy analyses show the uniform distribution of Ce^{3+}, Gd^{3+}, and Eu^{3+} dopants in the LaF$_3$ host matrix. The photoluminescence spectra and electron paramagnetic resonance measurements guarantee the presence of Eu^{2+}, corroborated through DC susceptibility measurements of the samples displaying paramagnetic behavior at 300 K, whereas weak ferromagnetic ordering is shown at 2 K. The non-radiative energy transfer processes from the 4f(^{2}F$_{5/2}$) → 5d state (Ce^{3+}) to the intraconfigurational 4f excited levels of rare earth ions and simultaneous emissions in the visible region from the 4f^{6}5d^1 (Eu^{2+}) and ^{5}D$_0$ (Eu^{3+}) emitting levels, leading to overlapped broad and narrow emission bands, have been proclaimed. The energy transfer mechanism proposes involvement of the Gd^{3+} ion sub-lattice as the bridge and finally trapping by Eu$^{2+/3+}$, upon excitation of the Ce^{3+} ion. The calculation of experimental intensity parameters ($\Omega_{2,4}$) has been discussed and the highest emission quantum efficiency (η = 85%) of the Eu^{3+} ion for the y = 10 mol% sample is reported. The advantageous existence of the Eu^{2+}/Eu^{3+} ratio along with variously doped nanomaterials described in this work, results in tunable emission color in the blue-white-red regions, highlighting the potential application of the samples in solid-state lighting devices, scintillation devices, and multiplex detection.

Insight into dual-modality of triply doped magnetic-luminescent iron-oxide/NaGdF$_4$:RE^{3+} (RE = Ce, Tb, Dy) nanoparticles

Navadeep Shrivastava [a], Uelson Rocha [b], Diego Muraca [c], Wagner Silva [b], Carlos Jacinto [b], Rajesh Kumar [d], S.K. Sharma [a,*]

[a] Federal University of Maranhão, São Luís, MA, Brazil
[b] Federal University of Alagoas, Maceió, AL, Brazil
[c] University of Campinas, Campinas, SP, Brazil
[d] Department of Physics, JCDAV College Dasuya, Punjab, India

ABSTRACT

Green emitting iron-oxide@NaGdF$_4$:RE^{3+} (RE = 5%Ce, 5%Tb, 5%Dy) nanoparticles have been synthesized using microwave assisted solvothermal method. The Rietveld analysis of powder X-ray diffraction and high-resolution transmission electron microscopy provides an average crystallite size ($\sim$20 nm) and the hexagonal crystal structure. Magnetic hysteresis loops at 300 K display superparamagnetic behavior along with paramagnetic feature for the reference NaGdF$_4$:RE^{3+}, further validated through magnetization versus temperature curves taken in an external magnetic field of 100 Oe. The photoluminescence investigation of the nanoparticles, suggest a down-converting energy transfer. The excitation spectra consist of a dominant broad band at around 254 nm due to Ce^{3+}(4f–5d) along with f-f transitions due to Gd^{3+}, Tb^{3+} and Dy^{3+} ions. The strong emission color lines due to characteristic transitions of Tb^{3+} ($^5D_4 \rightarrow {}^7F_J$, J = 6–3), and Dy^{3+} ($^4F_{9/2}$–$^6H_{15/2}$, $^6H_{13/2}$), were observed. The luminescence quenching in iron-oxide/NaGdF$_4$:RE^{3+} through leakage path provided by iron-oxide to excite electrons has been confirmed and explained by comparing the time decay analysis.

© 2017 Published by Elsevier B.V.